HIGH SPEED PHOTOGRAPHIC STUDIES OF BLAST WAVE IMPACT PHENOMENA

By

NOORI SABIH AL-MALIKY
(B.Sc,Basrah Univ.,Iraq)

A thesis submitted in partial fulfilment of the requirements
for the award of the degree of
Master of Philosophy
of the
Loughborough University of Technology

Superviser:Dr. D.J. Parry

ACKNOWLEDGMENTS

I sincerely thank my supervisor, Dr. D J Parry for his guidance, consistent encouragement and advice throughout the project period as well as the thesis preparation.

Also my thanks to professor K Zeibeck for his provision of laboratory facilities and his kindness and help.

My thanks to Dr. Gerry Swallowe for his assistance, and Mrs. P Dawson, Dr. P Dixon, Miss. Debby Smith, Mr. Zeng and Mr. N Zayer for their assistance and friendship.

I would like also to thank the ministry of Higher Education in Iraq for their financial support.

Finally it is my pleasure to thank my parents who spent their life sponsoring, advising, and looking after me during my studies, and my brothers and sisters for their encouragement.

ABSTRACT

An exploding wire technique (EWT) is described, which provides high rates of loading by producing cylindrical blast waves of high reflection pressure with short duration. These waves have been used for internal impact of hollow polymeric cylindrical specimens. The EWT overcomes the small size restrictions of other high strain rate testing methods like the Split– Hopkinson pressure bar technique and drop weight.

The experimental work of this thesis has been involved in generating and studying cylindrical blast waves produced in atmospheric pressure air by exploding a copper wire, which is instantaneously vaporized by passing a rapid discharge current from a 13.2 μF capacitor of stored energy of up to 8 kJ. Measurements of the electrical characteristics of the exploding wire circuit have also been made by using a thick wire, which does not explode.

Schlieren photography has been used in conjunction with a high speed image converter camera at a framing rate of 10^6 f/s to study the exploding wire phenomenon by recording the blast waves. The blast waves have been observed to expand in a cylindrically symmetric manner, with Mach numbers up to 15. These waves provide uniform internal loading of hollow cylindrical specimens, the behaviour of which can then be studied under these impact conditions.

Studies have been carried out on high density polyethylene (HDPE) thin-wall cylinders subjected internally to the impact of the explosion. The outer surface displacements, velocities, and hoop strains have been determined up to and beyond fracture from high speed photographs. Velocities up to 500 m/s , and strain rates up to 10^4 s^{-1} have been measured, with fracture hoop strain of up to 180%. These fracture strains are always less than the quasi-static values quoted by the supplier.

Preliminary investigations have also been carried out on freely expanding rings of HDPE to study the tensile stress-strain behaviour of the material. The freely expanding ring technique has the advantage of enabling the specimen stress to be obtained directly from the photographs of the expansion. The technique requires a thin ring to be placed as a sliding fit on a thick-walled cylindrical specimen. This protects the ring from the high temperature of the explosion and enables free flight of the ring to take place after the explosion inside the cylider. From the ring deceleration in the absence of a driving pressure the true stress can be found. Ring velocities up to 150 m/s, true strains up to 30%, and strain rates of about 10^4 s^{-1} have been measured. The stress/strain behaviour shows the increase of the flow stress when the strain rates increases from quasi-static rates of 10^{-3} s^{-1} to 10^4 s^{-1} or 10^5 s^{-1} of dynamic tests.

CONTENTS

Page No.

CHAPTER 1
INTRODUCTION

1.1 General introduction

The exploding wire technique is one of a few methods which are available for mechanical testing of materials at high rates of loading. These methods include:

1) drop weight and pendulum methods for strain-rates of about $100s^{-1}$.

2) the split Hopkinson-Davies pressure bar which is capable of strain-rates of about 10^3 s^{-1}. This method (Parry 1988) suffers from several limitations, amongst which is the need for small-sized test samples.

3) the exploding wire technique, which is a different method from the previous methods of loading. The explosion of a wire is used to produce cylindrical blast waves of high reflection pressure (greater than 1 kbar), low risetime (less than 1 μsec) and short duration ($\approx 5\mu s$).

The exploding wire technique is used for studying a range of materials at high pressure and very high rates of loading up to and including fracture.

High speed photography is generally the means used to record the phenomenon of wire explosion. The exploding wire phenomenon is similar to that of a plasma sheath which forms around a wire that is exploded in a vacuum, but in general the explosion of a wire is done at atmospheric pressure if high pressures are required.

The present application of wire explosions is in generating blast waves with high impact reflected pressures to be used for loading a cylindrical specimen. This work investigates the behaviour of the specimen material under high rates of loading at high strain-rates (up to 10^4 s^{-1}). In addition, current experimental work at

Loughborough University is described which deals with the measurement of the characteristics of the exploding wire circuit by using a thick wire.

1.2 Material properties

1.2.1 Elasticity

Materials are said to be elastic if deformations disappear completely on removal of load (Megson 1980). All known engineering materials are linearly elastic within certain limits of stress, so that strain within these limits, is directly proportional to stress. The ratio of stress to strain is constant and time-independent (Ritchie 1965). This is called instantaneous or Hookean elasticity. At longer times the ratio of stress to strain does not depend on time, the strains may become large but they are recoverable if the load is removed. This is called delayed elasticity, slow elasticity, or high elasticity. At even longer times, some of the strain becomes irrecoverable showing that the material has deformed in part like a liquid rather than a solid, and that is called flow.

A wide range of elastic properties of polymers depend upon the structure and the testing conditions (Kinloch 1983). Figure (1.1) shows the variation of Young's modulus (E) with temperature for an amorphous polymer. At low temperatures the polymer is glassy with a relatively high modulus (about 10^9 Nm^{-2}). The modulus falls rapidly in the region of T_g (glass transition temerature) where the polymer is viscoelastic and the modulus is very rate- and temperature - dependent.

At a sufficiently high temperature the polymer becomes rubbery. If it is cross-linked, then the modulus remains approximately constant

with increasing temperature at about 10^6 Nm^{-2} otherwise it flows like a viscous liquid.

From linear theory of elasticity, the stress-strain relation for isotropic materials with changes in the temperature (Bisplinghoff 1965) is

$$\epsilon_{mn}=\frac{1}{E}\left[(1+\nu)\sigma_{mn}-\nu\delta_{mn}\sigma_{rr}\right]+\alpha\delta_{mn}\Delta T$$

where ϵ_{mn}= linear strain tensor,
E = Young's modulus,
ν = Poisson's ratio,
σ_{mn}= stress tensor,
δ_{mn}= Kronecker delta,
σ_{rr}= sum of normal stresses,
α = thermal expansion coefficient,
and ΔT = change in temperature.

For polythene of $\alpha=2.5\times10^{-4}$ $^0C^{-1}$, if the temperature is increased by 10 ^0C, the last term of the above equation will give a normal strain of 0.25%. But for copper which has $\alpha=17\times10^{-6}$ $^0C^{-1}$, the last term equals to 0.017% for the same change of temperature.

The elastic behavior of polymers reflects the deformation of the structure on a molecular level. In the high modulus polymer fibers and crystals the deformation takes place essentially through bending and stretching of the aligned polymer backbone bonds which requires high forces.

1.2.2 Plasticity

When materials are subjected to increasing load (Ahmad 1988), they may reach a point before fracture occurs where, on release of stress, the specimen no longer returns to its original shape. The stress at

which this phenomenon begins is called the elastic limit of the material. For metals at temperatures below about half the absolute melting temperature, the permanent deformation may be assumed to be reached almost immediately, and hence to be independent of time. Time-independent deformation which remains on release of load is called plastic deformation. Figure (1.2) shows these processes.

A material is perfectly plastic if no strain disappears after the removal of load. Ductile materials are elastoplastic and behave in an elastic manner until the elastic limit is reached after which they behave plastically. When the stress is relieved the elastic component of the strain is recovered but the plastic strain remains as a permanent set. The elastic deformation represents a temporary change in the distance between atoms or molecules but plastic deformation represents a permanent change in their relative position (Roark 1954).

1.2.3 Viscoelasticity

Some materials at high temperature, and polymers under most conditions, continue to increase their deformation with time even at constant stress. This phenomenon is called creep (Ahmad 1988). At temperatures and stress levels at which creep occurs, if a deformation is applied and held constant, a stress will develop with the application of the deformation and then fall off with increasing time. This decrease of stress is known as stress relaxation. This type of behaviour is characteristic of polymeric materials, which possess properties which are a combination of those of a viscous fluid and an elastic solid. These are known as viscoelastic materials.

Materials such as polymers respond to external forces in a manner intermediate between the behaviour of an elastic solid and a viscous liquid, and their mechanical properties are dependent on the conditions of testing, such as the rate of application of load, temperature, and amount of strain.

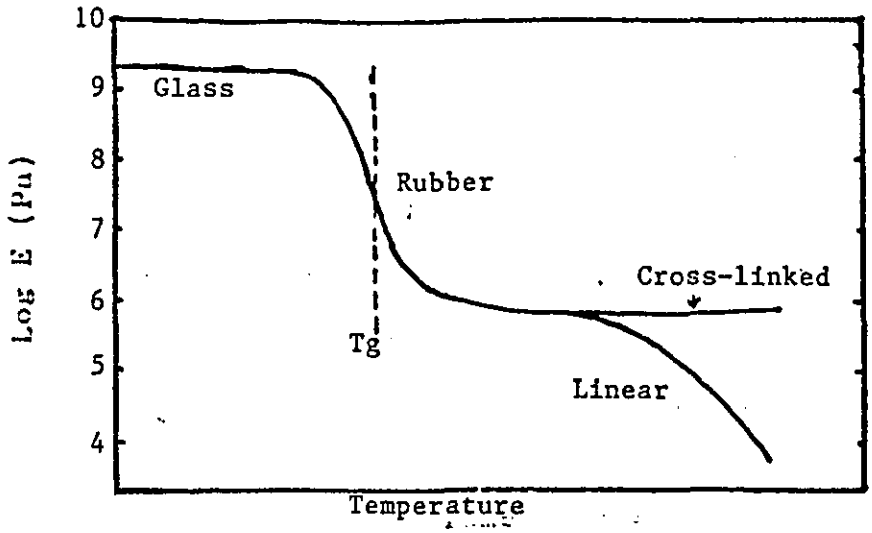

Figure (1.1) Typical varaition of Young's modulus E, with temperature for polymer, (Kinloch A.J. 1983).

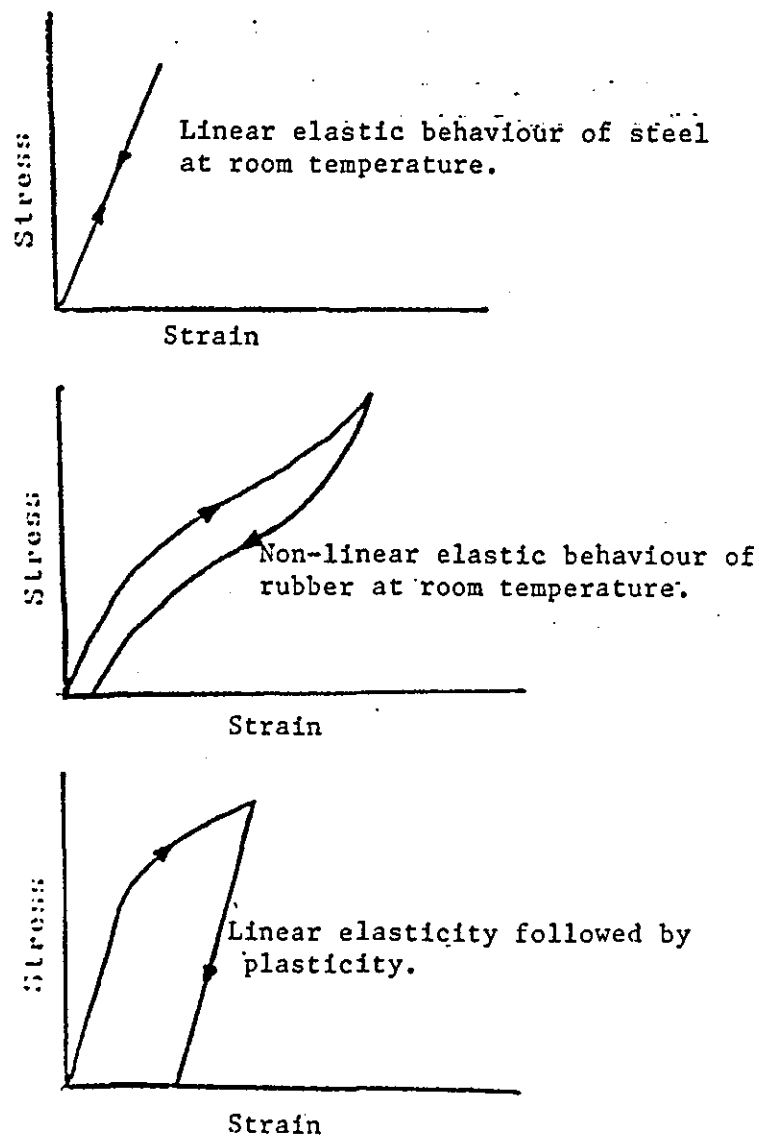

Figure(1.2) Elastic and plastic behaviours of materials.

A polymer can show all the features of a glassy, brittle solid or an elastic rubber, or a viscous liquid, depending on the temperature and time scale of measurement. At low temperatures, the polymer may be glass-like with Young's modulus of 10^{10} – 10^{11} Pa and may break or flow at strains greater than 5%. At high temperatures the same polymer can behave like rubber with a modulus of 10^{7} – 10^{8} Pa, withstanding large extensions (≃ 100%) without permanent deformation.

As mentioned above, one aspect of the mechanical behaviour of polymers is the way in which their response to an applied stress or strain depends upon rate or time period of loading (Young 1983). Elastic materials obey Hooke's law that the stress is proportional to strain, whereas viscous materials such as liquids, tend to obey Newton's law that the stress is proportional to strain-rate and is independent of the strain. The behaviour of some materials like polymers can be thought of as being somewhere between that of elastic solids and liquids. At low temperatures and high rates of strain they display elastic behaviour, but at high temperatures and low strain rates they behave in a viscous manner like liquids. Therefore such materials are termed viscoelastic as they display both viscous and elastic type of behaviour. The prefix "visco" implies that the material has some of the features of a viscous liquid, so that its properties are time dependent (Ritchie 1965).

CHAPTER 2
EXPLODING WIRE TECHNIQUE

2.1 A survey of exploding wire studies

There was, until Chace (1964), no previous review of exploding wires to which we may refer. The first paper on exploding wires was read before the Royal Society of London in December of 1773, the year before the first continental congress met in Philadelphia. The author Edward Naire, invented a static machine which he used to charge 64 Leyden jars with which he exploded an iron wire of 0.15 mils (1mil=0.025mm) diameter. Forty years later Singer and Crosse reported on exploding wires. This work about destructive and driving forces foreshadowed electric guns.

In the 1920's Dr. John A. Anderson, who may be called the father of scientific exploding wire study produced high temperatures from the explosion of the wires. He developed a rotating mirror camera and time – resolved spectroscope, estimated the temperature, and made a general study of the phenomenon. Muller (1937) observed the cylindrical blast wave which is produced by an exploding wire by using an optical method. He used a Schlieren Kerr cell technique to record the explosion which ... resulted from an energy of 12 joules per centimetre. He followed the shock wave out to a distance of 3 cm from the wire.

Lin S.C. (1954) analyzed the cylindrical shock wave and got a simple result that could be used for estimating the propagation and decay of the disturbance behind the cylindrical shock wave produced by the explosion of a long thin wire.

Bennett (1958) used high resolution rotating mirror streak camera photography to follow the primary shock travel for several centimetres away from the wire. Jones and Gallet (1962) used microwave Doppler techniques for the same purpose.

Bennett and Marvin (1962) did measurements and analysis of high current tubular shunts and transient skin effects in exploding wire circuits by using Laplace transform methods. He assumed that the exact solution can be obtained, as well as an approximate solution which allows estimates to be made of the errors expected, and to minimize the skin effect, the tubular shunt must be thin. At the same time Bennet had measured the temperature behind the head of the shock wave generated by an exploding wire by employing blast wave theory. He also did estimates of thermal-ionization times for electron–atom and electron–ion collisions showing that local thermal equilibrium should be well approximated everywhere except near the arc boundary. Also (1964) he solved the equation of the power input to the exploding wire as a function of change of temperature and for energy input after neglecting radiation, hydrodynamic, and skin effects.

The outward propagation of cylindrical shock waves produced by exploding wires was shown to be radially symmetric along the axis of the wire and accurately reproducible (Fyfe and Ensminger 1964–1966). The response of the specimen to this loading was obtained by a measurement of the time variation of the outer surface displacement using an optical method. Good agreement with the corresponding theory for the case of elastic waves confirmed the validity of this type of measurement and the authors have since used the method to study the propagation of blast waves (Fyfe and Swift 1969).

Fyfe and Ensminger (1964) used a cylindrical geometry for emphasizing the measurement because of the following advantages:

i) the ability to observe directly the specimen response,

ii) a greater area of the specimen is available for measurements, and

iii) there is a closer approximation to one dimensional displacements.

Ensminger and Fyfe (1966) have used an exploding wire technique to produce a high amplitude stress wave incident on the inner surface of a hollow cylindrical specimen. In the same year Edelson and Korneff (1966) observed that the under water wire explosion presents a more orderly structure than the explosion in air.

In 1968 Ryszard Malewski developed a new device with fast response time for current measurement in exploding wire circuits.

Bennett published a paper in 1970 for establishing some geometrical techniques and mathematical relations upon which subsequent analyses of the metal flow in the exploding wire are based. This paper shows the resulting fringe contours for both single and multiple fringe cases of gas and electron distribution around the exploding wire, and compares these fringe contours with some actual interferograms.

Swift and Fyfe (1970), carried out two distinct types of experiments using the exploding wire technique to examine an elastic/viscoplastic constitutive theory in a radial cylindrical configuration. One examines the plane strain plastic response of hollow cylinders subjected to an internal finite-rise-time pressure pulse; the other examines the decay behaviour of the cylindrical elastic precursor associated with high stress level impact loading. They considered the viscoplastic strain-rate function in a linear and an exponential form.

Vlostos (1973) said that a hard X-ray radiation of short duration could be produced by the explosion of thin tungsten wires in a vacuum but the recrystallization of the wire may have reduced the X-ray output.

Schmit and Fyfe (1973) used exploding wire techniques to study the dynamic fracture of thick hollow cylinders.

Schofer, Seydel and Jager (1977) recorded the pressure profiles of shock waves of underwater wire explosions by using piezoresistive pressure probes at different distances from the wire.

Forrestal, Duggin, and Butler (1980) applied an explosive loading technique to study the uniform plastic expansion and fracture initiation of 304 stainless steel cylinders.

Hwangbo, Kong, and Lee (1980) observed the inhomogeneous process in underwater copper wire explosions induced by a capacitor discharge.

Nakamura and Tsuno (1980) used a Schlieren system with high sensitivity and a high speed camera to measure high velocity flow propagating through gases due to a shock wave produced by the explosion the of the wire in air.

Isuzugawa and Fujimura (1982) proposed a simulation model considered to be appropriate to the behaviour of the copper wire heated by the passing of an impulse current until the wire's temperature reaches boiling point at atmospheric pressure when it violently evaporates the wire.

Ron, Rohatgi, and Rau (1983) used an exploding wire to trigger a vacuum gap to measure the rise time of the gap.

So-Young and Kim (1984) employed oscillographic recordings and Schlieren-streak photography to observe the current dwell, explosion, and arc discharge stages.

Griffiths, Parry, and Stewardson (1986) used an exploding wire as a method for impact loading to study materials at high pressures and very high rates of loading up to and inducing fracture. This method produces a radial stress wave of high amplitude (>2kbar) and short risetime (<2 μsec) in a hollow cylindrical specimen of 10 cm length and 5 cm outside diameter.

Suhara (1986) initiated an arc discharge by the method of exploding a wire in a static short gap between two electrodes. This method was done to describe the V–I characteristics of the discharge and to calculate the arc duration time of opening electrical contacts in inductive circuits.

Yakimura (1987) gave an estimation of pressure and of energy of shock waves produced by a thin wire disintegation during the vaporization stage of the wire. He compared the results obtained in air explosions with those for underwater explosions .

Lee (1988) measured the profiles of underwater shock wave pressure, current, and voltage for exploding aluminium, aluminium–lithium alloy, and copper wires in water when an inductive energy store was discharged through the wire.

In the Physics department at Loughborough University an Imacon high speed camera is used with a Schlieren technique for optical studies of blast waves produced by exploding copper wires of various lengths and diameters connected to a 13.2 μF capacitor charged to a range of voltages. Studies are also being made of the material properties of cylindrical materials under impact loading from the blast waves.

2.2 Exploding wire theory

The wire explosion mechanism (Pollard 1966) has not been fully understood. The phenomenon in general is accepted as being a combination of several physical processes. Some parts of the processes (Ahmad 1985) have no explanation, while others have been explained by a number of theories .

A typical current waveform, as shown in Figure (2.1,B) for the basic exploding wire circuit of Figure (2.1,A), shows that before the explosion occurs (Ahmad 1985) the current follows a damped sine wave shape.

(A)

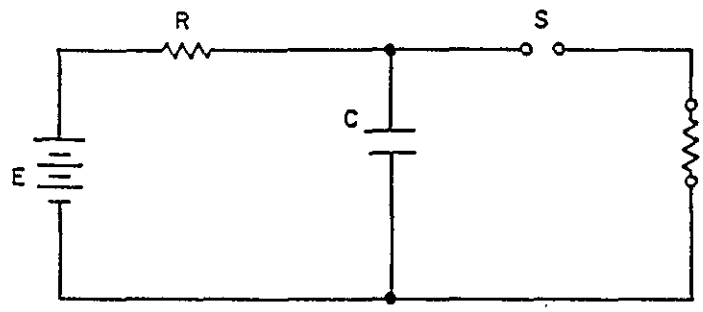

(B)

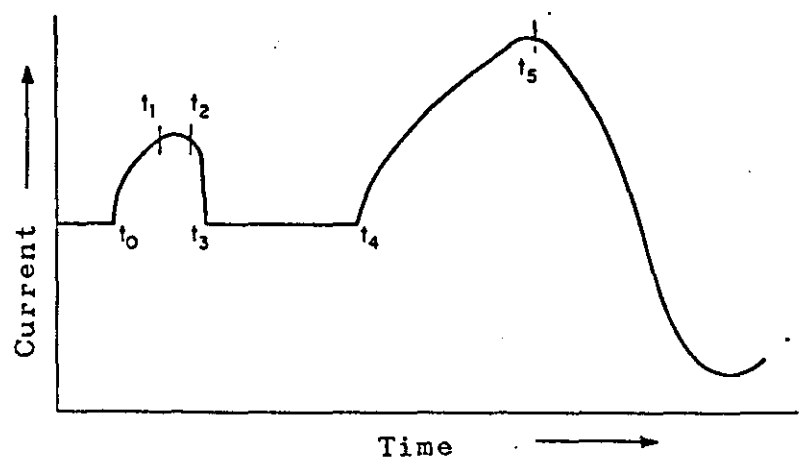

Figure (2.1) (A) Basic exploding wire circuit.
(B) A typical current waveform of EW circuit.

The explosion phenomenon (Pollard 1966) consists of the following behaviour. At t_0 the switch is closed and voltage is applied to the wire. The current, controlled by RCL characteristics of the circuit, causes the wire temperature to rise thus heating it up to its melting point and beyond. This stage of the process occurs in less than a microsecond. The physical shape of wire is maintained by inertia and magnetic pressure. As the heating of the wire increases the temperature rises reaching the boiling point. However, equilibrium boiling does not occur at this time because the temperature must reach a level to supply not only the heat of vaporization but also the energy to overcome the phase – change barrier. The temperature of the wire at t_1 to t_2 is sufficiently high to cause the violent explosion. The explosive vaporization, or transplosion, causes the metal of the wire to transform into colloidal form, which is a continuous phase of liquid metal interspersed with a discontinuous phase of metal vapour. This colloidal form has a profound effect on the electrical properties of the wire. Now suddenly the electrodes are connected only by a gas with a number of metallic particles floating in it. The conductivity drops to low level in the interval between t_2 and t_3.

During the interval t_3 to t_4 a period of low conductivity occurs the so–called dwell or pause time, in which (Lavrentyuk 1987) the current falls practically to zero. The current continues to flow at relatively constant low rate due to conduction by only a limited number of ions or electrons. The voltage related to dwell current is called dwell voltage which has an exponential relation (So-Yong and Kim 1984) with the dwell period.

The rapid change of the condensed phase (liquid) to gas develops a momentary high density in the gas so that the current carriers moving in the field between the wire terminals do not acquire sufficient energy between collisions to produce impact ionization. This case is

analogous to conduction by thermionic or field emission. The high density state is instantaneous. Therefore expansion of the gas is retarded only by its mass inertia and the pressure of the atmosphere around the wire.

In a very short time at t_4 the pressure of the gas has dropped, the mean free path has increased giving rise to extensive ionization by impacting current carriers which cause avalanching to occur with attendant rise in current to a level typified by point t_5. The current level is controlled by RLC parameters in the circuit. The interval between t_4 and t_5 is the restrike or reignition stage of exploding wire phenomenon .

The persistence of the dwell-time between t_3 and t_4 is dependent on the energy available from the capacitor C. The duration of the dwell period will be greater as the residual energy increases.

The phenomenon described above is for the case of copper wires. Different type of wire (Ahmad 1985) might undergo different phenomena. For some wires you may get the dwell current without restrike. The current values will also depend on the type of wire.

2.3 Shock waves from exploding wires

The velocity of wave propagation in solids is a function of $\partial\sigma/\partial\epsilon$ (Ahmad 1988), the gradient of the curve of the stress against the strain. For most solids this is constant upto the proportionality limit and then decreases. If $\partial\sigma/\partial\epsilon$ increases with strain beyond the elastic limit then large strains travel faster than the earlier small ones, so that a pulse acquires a steep front as the later waves catch up. The gradient of this step is limited by dissipative forces such as viscosity and thermal conduction, which become more important as the pressure gradient becomes steeper. The wave under these conditions is known as a shock wave, and it can be studied in a similar manner to shock waves in fluids.

Dilatational waves of large amplitudes can also produce a shock front since the compressibility of solids increases at high pressure. The velocity of dilatational waves is given by the following formula (Kolsky 1953)

$$c_d = \sqrt{((k+[4/3]\mu)/\rho)}$$

where c_d is the dilatational or irrotational wave propagation velocity, k is the bulk modulus, μ is the rigidity modulus, and ρ is the density of the solid medium.

The wire explosion can generate a shock wave with cylindrical symmetry surrounding the wire due to the passage of heavy current pulse.

As mentioned in Section 2.1 various methods have been used in the measurements of exploding wire phenomenon. The optical methods commonly used include the Schlieren technique with high speed cameras.

The main purpose of using an exploding wire in the present work is to generate a shock wave with high amplitude which can be used for loading different materials for testing their behaviour under impact loading.

Fyfe and Ensminger (1964) have investigated the symmetry of an exploding wire inside polyethylene and aluminium cylinders to examine the deformation caused by the shock wave. Also in 1966 they used an exploding wire inside a hollow cylinder to measure stress-strain relationship by measuring the outer surface displacements.

The present work as will be described in the next chapters is measuring the shock wave velocity, energy, and the exploding wire efficiency as well as determining reflecting pressure of shock waves

produced by exploding wires. Further work was done in using the shock waves for loading a polyethylene cylindrical specimen to study its behaviour under these impact conditions.

CHAPTER 3
HIGH SPEED PHOTOGRAPHY

3 High speed photography

The photography of very rapid dynamic events such as shock waves from explosions, and electrical discharges needs short exposure durations to see the behaviour of these phenomena. A special photographic technique, which is called high speed photography, is required.

3.1 Introduction to high speed cameras

In the measurement of pico-, nano-, or micro-second ultra high speed phenomena, high speed cameras (Shin-Ichi 1979) are essential instruments which are used in many laboratories. These cameras (Zukas 1982) are the most widely used instruments for studying dynamic mechanical events such as impact and explosions because of (a) investigator familiarity with related conventional cameras, (b) availability of practical equipment, and (c) enormous information storage rates achievable.

High speed cameras have considerably exceeded the data recording rates of normal cameras but the principal advantages offered by high speed imaging technology are in the area of extending the time-resolving capabilities.

The resolution time of high speed cameras approaches 10^{-13} s (100 fs), and cameras are available with resolution time near 10^{-12} s (1 ps). The time resolution limit of these current photoinstruments is 500 billion times faster than that of the human's vision which can resolve 0.05 s.

The object's motion during the exposure period causes blurring that reduces resolution especially in the direction of the object motion. Very short exposure time is required for reducing this observation difficulty for dynamic events.

The critical factor determining exposure time requirements for producing usable images is the time for the observed object to cross the field of view. The ratio between this time and the exposure time determines the resolution limit of the resultant image imposed by motion blurring as:

$$R_0 = \frac{X_i}{\tau_i \cdot U}$$

where R_0 is the total resolution of the observed object (in line pairs); U is the object velocity; X_i is the width of the observed area; and τ_i is is the exposure time.

Figure (3.1) shows the exposure time requirements for observing various types of dynamic events.

When the photographs (George 1952) were taken at high speed, initially one of the primary problems was to move the film rapidly at the correct speed without it vibrating, breaking or becoming abraded.

There are several techniques used to solve these problems. These are described next.

3.1.1 Optical-mechanical methods

These methods can be divided (Zukas 1982) into two types of photography which are high speed cine photography, or framing photography, and streak photography.

1) High speed cine photography

The familiar, so called cine, camera incorporates a mechanism for transporting unexposed film from one spool through an enclosure where exposure takes place while the film is immobilized, and collecting

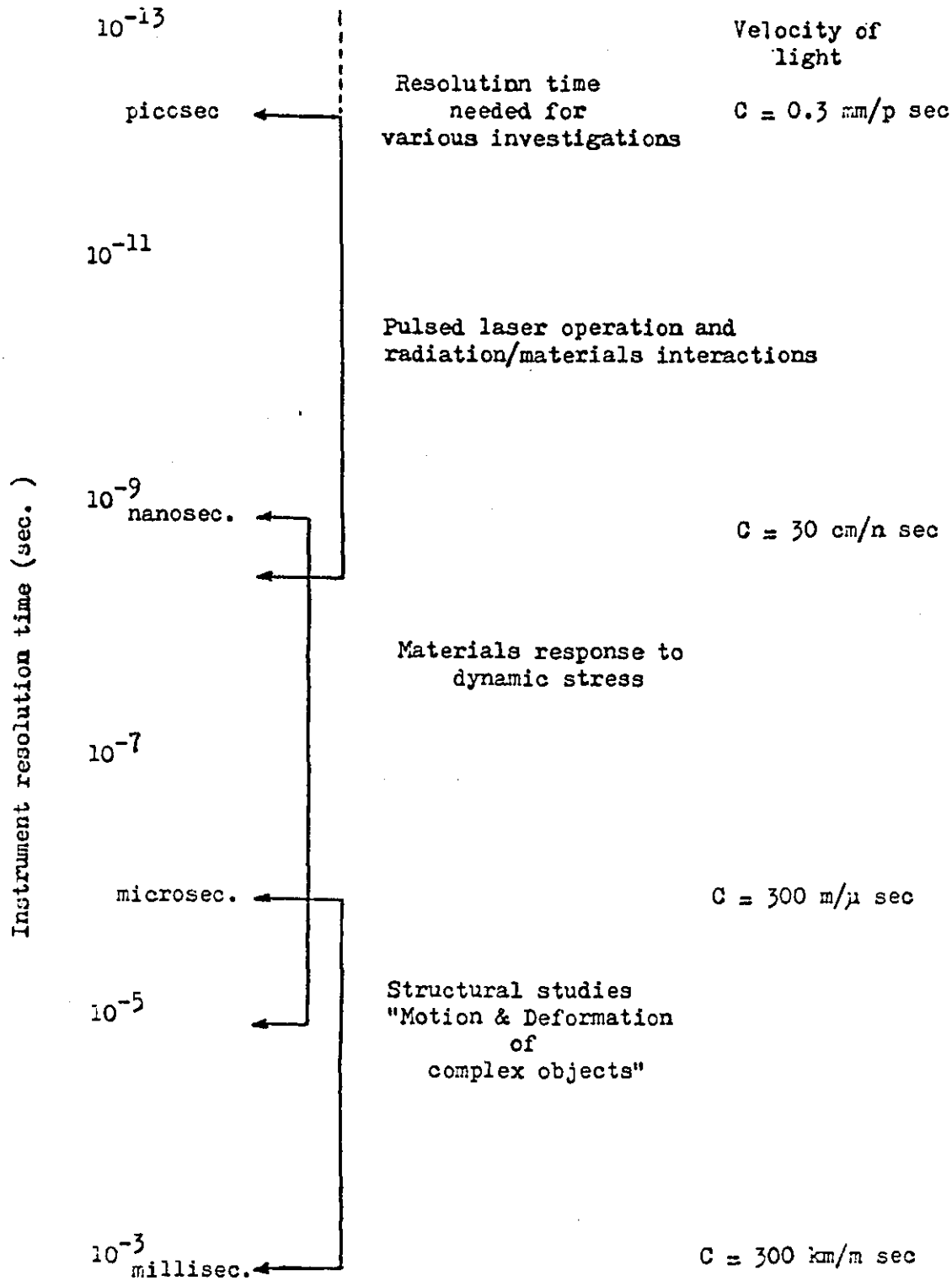

Figure (3.1) Exposure time requirements for observing various types of dynamic events.

the exposed film on another spool. If this is done at speeds above 50 frames per second, it can reasonably be termed a high-speed camera.

a) Intermittent motion cameras

This type (Zukas 1982) of camera is operated with a mechanism that rapidly advances the film one frame at a time and stops it while a rotary shutter produces an exposure. The process is then repeated until the camera is turned off or the film supply is exhausted. The frame sequences speed of this type can be up to 500 f/s. The exposure time for each frame is near 20% of the interframe time, so that 400 μs duration exposures may be accomplished with framing rates of 500 f/s.

The film advance and shuttering mechanisms place little restraint on the use of objective lenses, so that almost any focal length and F/no. aperture may employed. A colour film is often used to produce spectacular image sequences that can be viewed with motion picture projectors.

b) Rotating prism cameras

The rotating-prism type is one in which the film is moved continuously, an optical/mechanical mechanism being built in to the camera such that the image moves at the same speed as the film and so gives records which are not smeared. Instruments of this type can be operated successfully at speeds of up to 40,000 frames per second. Figure (3.2) shows a simple diagram of the optical/mechanical operation of rotating prism camera.

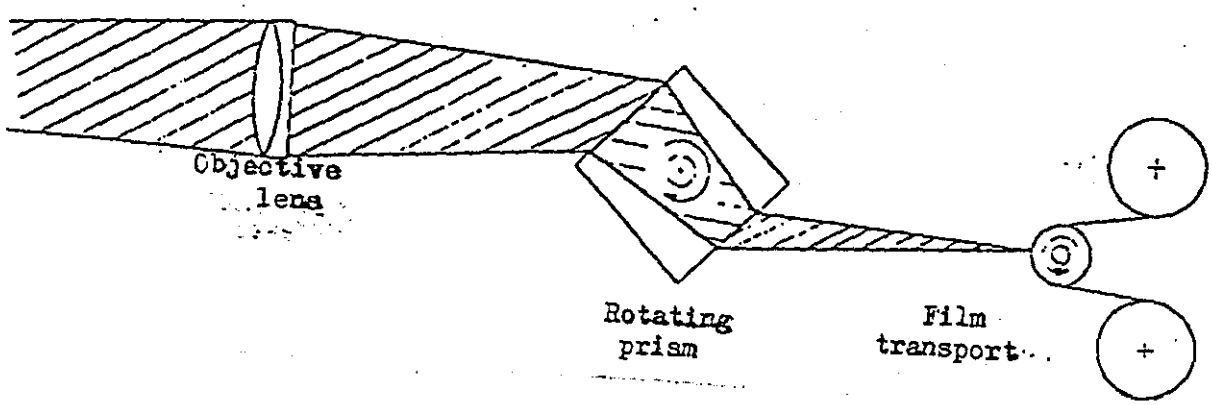

Figure (3.2) Rotating prism camera.

c) Rotating drum cameras

Rotating prism cameras have been improved progresively. The limitation on the speed of the rotating prism camera caused by peak film speed and centrifugal burst strength of the prisms (Zukas 1982) can be overcome to some extent by mounting a relatively short strip of film (attached on the inside surface the high speed rotating drum) and replacing the prism mechanism for image motion composition with a rotating mirror assembly.

The drum containing the film is accelerated to maximum velocities several times higher than those achieved by reel to reel mechanism during several tens of seconds of torque application. Drum cameras are capable of operating at framing rates near 10^5 frames per second with exposure time near 4 μs.

The disadvantages of rotating drum cameras are: the number of frames that can be taken during an individual operation is limited, the format does not lend itself to motion picture projection without laborious reprinting of the individual frames onto a single strip of film, the F/no. of the optics system and the back focal distance of the lens are restricted even more severely than for rotating prism camera, and the use of multiple mirrors in the optical path reduces the optical sensitivity of the camera below that predicted by the F/no. and effects image quality.

d) Rotating -mirror cameras

Rotating mirror cameras contain a very high speed rotating mirror (usually turbine-driven) which deflects the incoming light onto a stationary strip of film via a series of fixed relay lenses. Cameras of this type can work at rates of up to about 2×10^5 f/s with exposure time down as low as 50 ns to be achieved. This type of camera was invented before the World War II (Zukas 1982), and provided a big improvement to the field of high speed photography.

e) Cranz–Schardin spark camera

This type of camera (Zukas 1982) like the rotating mirror cameras opened the possibility for taking ultra high speed cine sequences many years ago, of high speed dynamic mechanical events. It is a cine version of focused shadowgraph cameras as shown in Figure (3.3). A number of spark gaps are mounted in a plane containing the camera objective lens. Firing the spark gaps sequentially produces a cine sequence of images of the event under observation by using separate objective lenses for each spark gap. The advantage of this type is that the framing rate may be adjusted independently of the exposure time for each frame. The disadvantages are the strict limitation to take shadowgraph images, each frame having a field of view slightly different from the others, which complicates extraction of quantitative motion data from the photograph to some extent. The framing format is not suitable for motion picture projection unless the relatively difficult job of reprinting the frames in a standard strip sequence is accomplished.

2) Streak photography

In this type of photography the object of interest will be imaged onto the surface of a continuously moving film transport or the object will be swept onto the film by moving its image by using moving reflector such as rotating mirror shutters.

a) Reel to reel streak cameras

The simplest (Zukas 1982) of this type is the smear streak camera which consists of an objective lens that images the object of interest onto the moving film. Such types can be used for recording a light emitting event such as the beam of a cathode ray tube (CRT) with the sweep circuitry disabled, the film motion providing the sweep action so that voltage variations with time can be resolved for

extended time periods. Some types of these cameras employ an objective lens such as shown in Figure(3.4); the rest have been developed to employ a relay lens and a narrow slit aperture.

As shown in Figure (3.5 a,b) the relay lens images the slit across a moving film so that continuous illumination of the slit produces a stripe from one end of the film to the other which are motor-driven film transports with the objective lens mounted in front of the film gate.

The resolution time of such cameras is basically the time required for the slit image to traverse the resolution limit of the relay lens operating in conjunction with the film, $\sim$ 0.2 μs, and can be shortened by increasing the velocity of the film transport. Typical peak speeds of about 300 m/s can be achieved with this type producing resolution times as short as 70 ns.

b) Rotating mirror streak camera

A rotating mirror cine camera can be used as a streak camera by replacing the stationary relay lenses by a slit and single relay lens in front of the camera, so the rotating mirror can sweep the image directly on the film surface without passing through relay lens. This type can resolve 10^{-9} seconds. Figure (3.6) shows the operation of a rotating mirror streak camera. The prismatic mirror is spun at high speed by an air or helium-driven turbine (Hyzer 1962).

These cameras can be used to study the explosions, and rapid movement of small mechanical parts that is beyond the range of intermediate speed cameras.

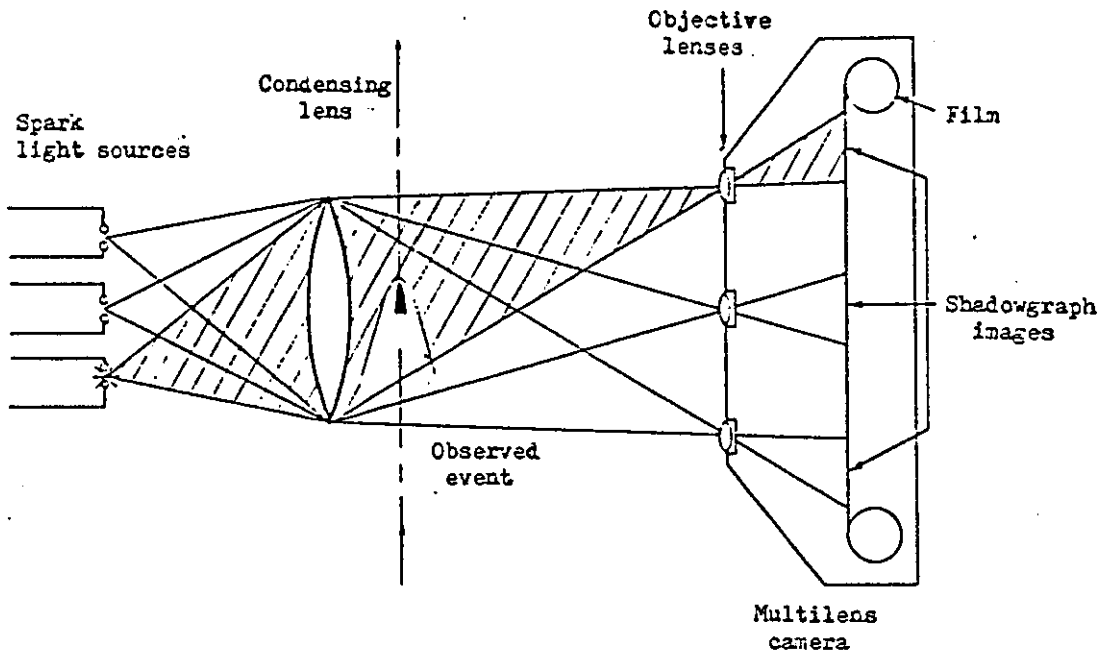

Fig (3.3) Cranz-Schardin multiframe spark-shadowgraph camera

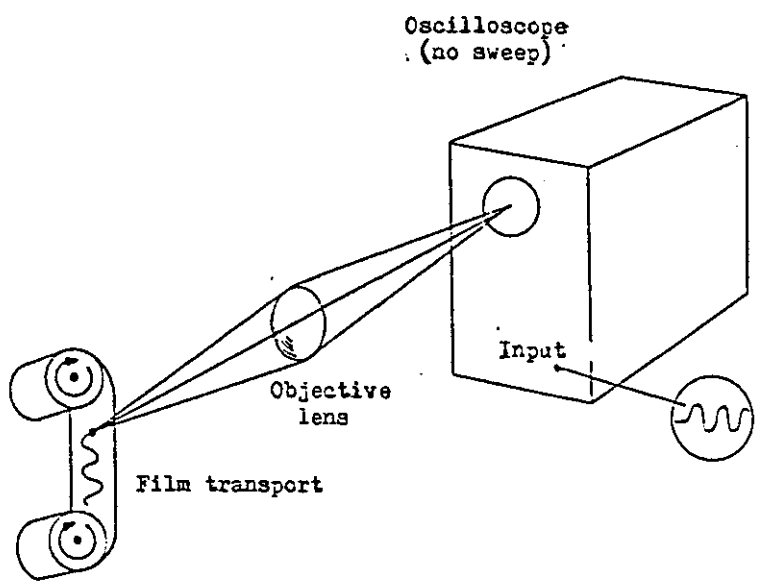

Fig (3.4) Smear-camera concept for recording extended sweep duration from an oscilloscope.

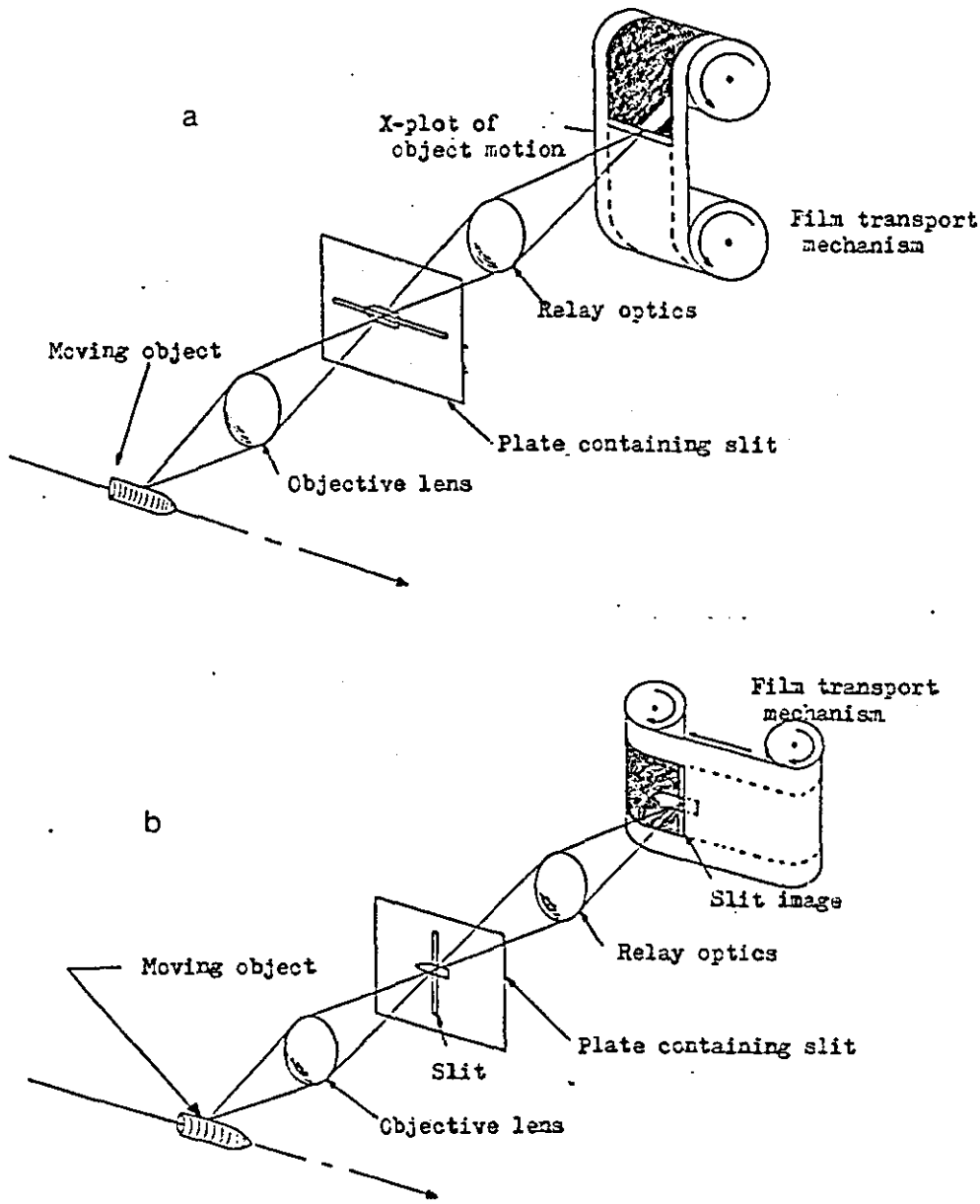

Figure (3.5) a; Streak-camera concept operating in parallel slit mode.
b: Streak-camera concept operating in perpendicular slit mode.

Typical top speeds for the slit image moving across the film plane are limited to 30 km/s because of system defocusing caused by unavoidable mirror distortion developing at rapid rates. This distortion is enough to offset the greater potential time resolution produced by the increase in slit image speed.

Rotating streak cameras are restricted to using high F/no. optics (>F/10) because of the large separation required between the relay lens and the film.

The rotating prism camera can also be [illegible] a streak camera with 10^{-7} s resolution time by removing the prism and leaving the image swept directly onto the moving film. The rotating drum cameras primarily use the same mode with resolution times of about 10 ns.

3.1.2 Electro-optical methods

a) Electronic framing cameras

These cameras (Hyzer 1962) have been used since the mid-1950s. The high speed camera systems are based on various designs of image-converter and image-intensifier tubes. Many of these systems have proved to be successful and are in wide use today in fields such as nuclear physics, electrical discharges, lasers, detonation, shock and fractures.

The electronic framing cameras (Zukas 1982) have become important during the 20th century because of their greater efficiency in use of light and their ultra-high speed framing rate capabilities.

The vital part of high speed electronic cameras is the electron-image tube, as shown in Figure (3.7). The tube uses the Kerr cell shutter method which will be described in the next section, except that two sets of opposing deflection plates are used to deflect the relatively small images of the photocathode onto different regions of a large

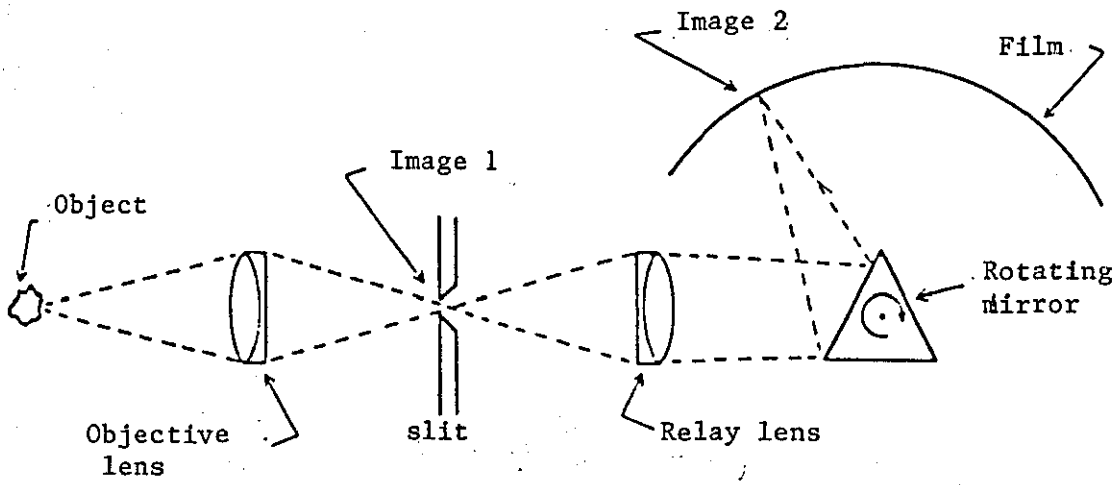

Figure (3.6) Operation of a rotating mirror-streak camera.

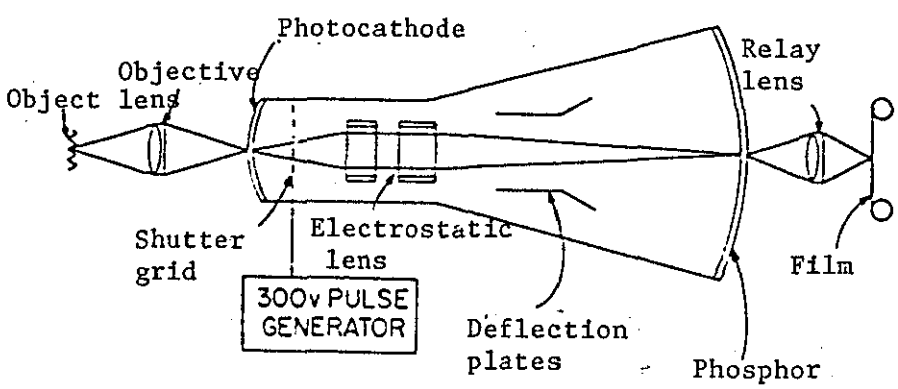

Figure (3.7) Electrostatically focused image tube with image-deflection capability.

phosphor screen. The images move from point to point producing image sequences at up to about 3×10^9 f/s. Electronic framing cameras can be subdivided into two types:

a) The single-picture camera, which is the simplest electro-optical device usable in a high-speed camera, is the proximity-focused diode tube. The tube which is shown in Figure (3.8) consists of an evacuated bulb containing a plane photoemissive surface or photocathode, deposited on a transparent entry window which is held parallel and close to the photocathode. When a positive pulse (usually 10 kV or more in amplitude) is applied between screen and photocathode, the tube acts as a shutter with an open time equal to the pulse duration.

b) Multi-framing cameras consist of an electro-optical tube fitted with additional electrodes to enable the electron beam to be switched both on and off at appropriate times to give a repetitive shutter action. The beam is deflected and suitably synchronized to the shutter action, to give a sequence of stationary positions on the screen of the tube. One example of multiple-framing camera is the image converter camera which is shown in Figure (3.9) which can be operated in framing mode at speeds of up to 2×10^7 frames per second at which rate each exposure is of 10 ns duration.

b) High speed electronic streak cameras

High-speed streak cameras (Shin-Ichi 1979) play a very important role in the diagnostics of laser pulses, laser-induced plasmas researches, etc. Electronic streak cameras (Zukas 1982) are capable of operating at much lower light levels than mechanical cameras because of their fast optics, and optical amplification. They can resolve times of about 1ns.

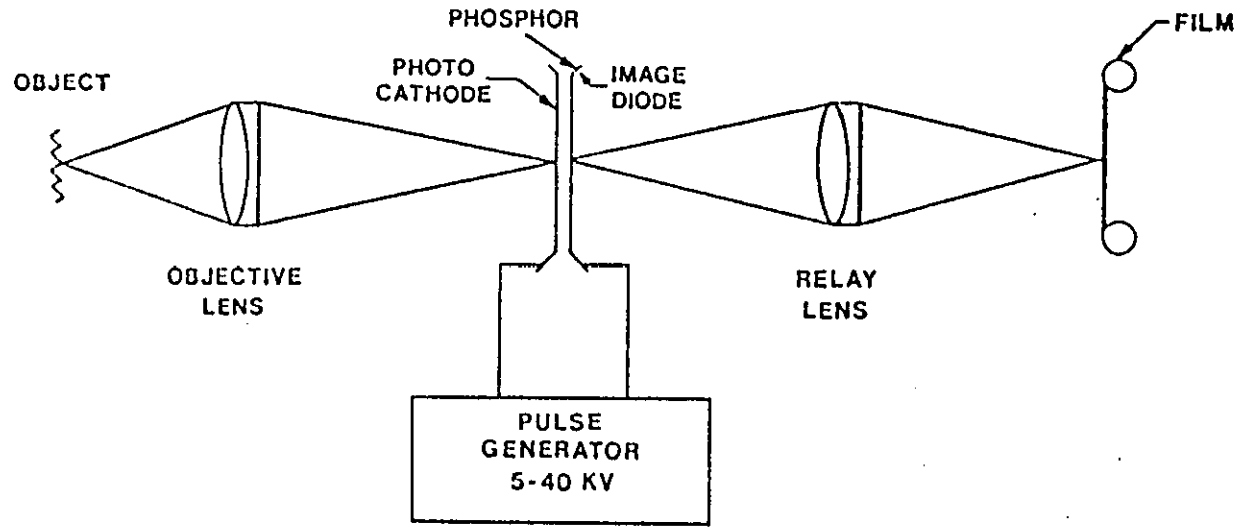

Figure (3.8) Single-frame electronic camera using a proximity-focused image tube.

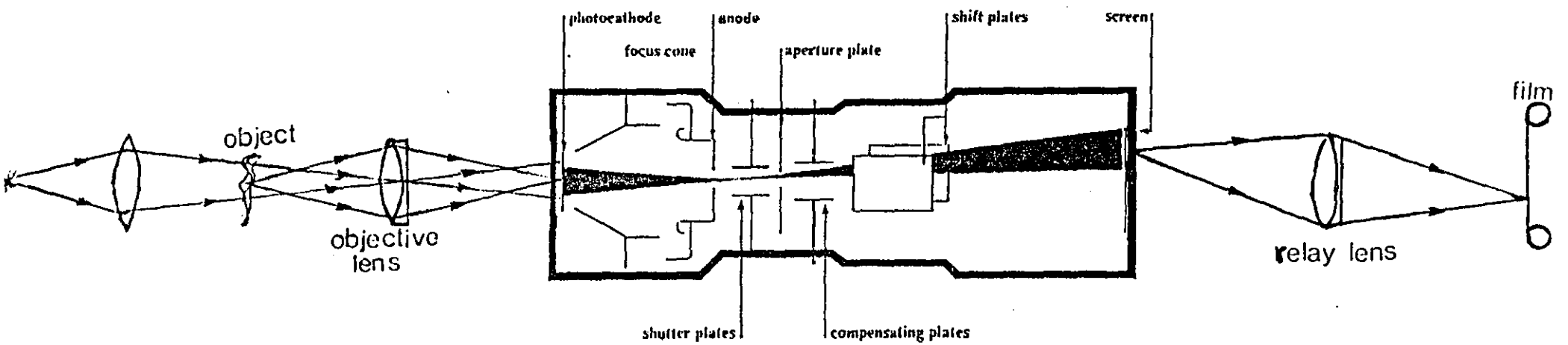

Figure (3.9) Multiple framing camera.

These cameras use electron – image tube similar to the tube which is used in electronic framing cameras but without shuttering the electron beam into frames. The electron cloud generated at the photocathode is accelerated towards the phosphor screen by the anode and is focused on it by an electrostatic lens system. It passes between one set of deflecting plates on which a linearly increasing ramp is applied. The deflection of the image across the phosphor screen is continuous and travels at a constant velocity.
The electronic streak cameras can resolve 10^{-13} s (100 fs), and they have intrinsic optical gains of up to a few hundred when the output tube is coupled to film or other photosensitive media.

It is important to obtain a linear output representation of the input photo-intensity. The range of linearity must be adequate to permit input peak amplitude variations to occur. Two important factors affect linearity. One is the linearity of output current from the photocathode of the streak image converter tube, relative to the input photo-intensity. The other factor affecting linearity is space-charge saturation near the cathode.

c) Electronic X–ray high speed cameras

X-ray high-speed image-converter cameras (ICC) of two different types have been developed (Huston 1978). In the first one, soft x-ray radiation is used to illuminate the photocathode surface of a large x–ray intensifier tube which converts the x–rays into visible light with the aid of a 0.5 ns response time plastic scintillator. In this tube the scintillator screen mounted on the front surface of the tube converts the x–rays to visible light which is then converted to an electron–image analogue at the photocathode surface. The electrons from the photocathode are then focused electrostatically onto a small diameter output phosphor after being accelerated by 30 kV voltage.

The framing rates of this type exceeds 5×10^4 f/s, and the advantage of using it is that the image on the output phosphor is approximately 10,000 times brighter than the image falling on the photocathode because of the geometric demagnification and the effects of energetic electrons striking the phosphor.

The second type of camera incorporates a photocathode which is sensitive to the visible and x-ray radiation which come from the x-ray flash. Its calculated temporal resolution approaches 5-7 ps.

These cameras were employed for studies of x-ray radiation emitted by laser plasma.

3.2 High speed shutters

The classification of high speed cameras sometimes depends on the shutter system because the shutter is considered as the heart of the camera.

Many cameras determine the effective exposure time for producing images by pulsing a light source. This method can not be used when a self-luminous event is photographed using its own light, or when exposure times shorter than those available with pulsed light sources are required. So mechanical shutters have been developed to be operated at exposure times down to 10^{-4} seconds, and electronic shutters have been developed also, starting with Kerr-cell shutter, for shorter exposures.

3.2.1 Electro-optical shutters

Electro-optical shutters became available in 1925, when Karolus succeeded in making a fully effective electro- optical shutter capable of extremely short exposure times. The electro-optical effect had been discovered by Kerr in 1875, but the problems of using it as a shutter to control a light beam had been great and the

achievement of Karolus was a considerable one. The effect is produced when a strong electric field is applied to certain isotropic liquids or solids. Under the correct conditions, the material becomes doubly refracting and is thus able to rotate the plane of polarization of light passing through it. In the Kerr cell (George 1952) an isotropic liquid is employed which becomes non isotropic under the application of a powerful electric field.

The Kerr cell which is shown in Figure (3.10) has two filters placed with their planes of polarization at right angles, so that normally no light is transmitted. When a sufficiently powerful pulse is applied across the electrode plates in the cell, the plane of polarization is turned so that light can pass through the system for a fraction of a second. This phenomenon (Ralph 1959) is known as the Kerr effect. If an electro-optical cell of this nature is placed between two sheets of a polaroid (polarizing filter) the arrangement constitutes an extremely rapid light shutter which can be made to respond to high-voltage pulses of less than 10^{-8} seconds duration of maximum transmission through the second polaroid. When the voltage is zero the shutter is closed. The exposure time is the duration of the applied pulse. In the Kerr cell a voltage of (20-50) KV is needed. The transmission efficiency of the Kerr–cell is below 20 per cent.

The practicability of the technique depends upon the purity and optical clarity of the material used, upon the availability of an efficient polarizer and analyzer to use with it, and upon the evolution of a circuit for producing a high-voltage pulse of suitably short duration. As no mechanical parts are involved, exposures can be extremely short.

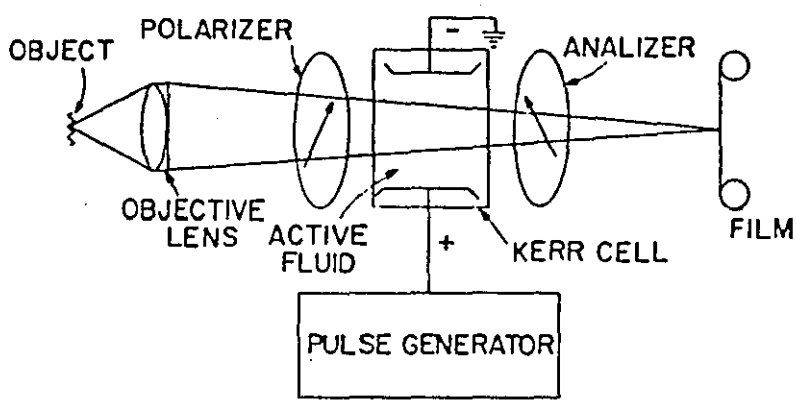

Figure (3.10)Schematic diagram of a Kerr-cell optical shutter.

3.2.2 Optical-mechanical shutters.

a) Moving lens shutters

The most obvious method is to move the lens during the period of exposure (George 1952). In this case the lens and film should move together at the same speed. Figure (3.11) shows the rotating lens shutter.

b) Moving-mirror shutters

These types of shutters depend on rotating reflectors such as in the mirror drum shutter which is shown in figure (3.12), and the single rotating mirror which is shown in Figure (3.13).

The framing rate of the camera depends on the speed of rotation of the reflector mirror in these shutters.

c) Rotating plane prism shutters

This type of shutter (Figure 3.14) depends on the rotating movement of the transparent plane prism. The film should be moved at the same speed as the prism.

d) Also there is another type of high-speed shutter, the "Gas Motor Gun", which is a simple and efficient rapid opening shutter, is capable of opening an area about 7.5 mm square in under 0.5 ms. The gas motor is designed to push a simple aperture plate rapidly out of the way to let the light come in through the aperture to reach the camera (McVeagh & Newbreg).

3.2.3 Image converter shutters

The modern system for producing electronic shutters is by using electron-image tubes which vary in their methods of focusing and shuttering. These tubes are evacuated and consist of a photocathode where the optical images are focused on, and a phosphor screen against which the electrons are accelerated by high electrostatic potential. These two parts are separated by some distance and use electrostatic lenses to provide the required electron focusing and shuttering by applying appropriate voltages on sets of deflection plates.

There are two types of image converter tube shutter as in section (3.1.2):

a) the single frame shutter which is shown in figure (3.8) is the simplest and contains a photocathode and phosphor screen connected to a pulse generator which gives a high potential difference (usually between 5 and 20 kV).

b) the multiple frame shutter tube, which employs electrostatic lenses between the photocathode and the phosphor screen (Figure (3.9)). These lenses do the focusing and shuttering of the images as will be described in Chapter 4. Finally this tube has a good optical gain and can be operated with exposure times down to 10^{-9} seconds.

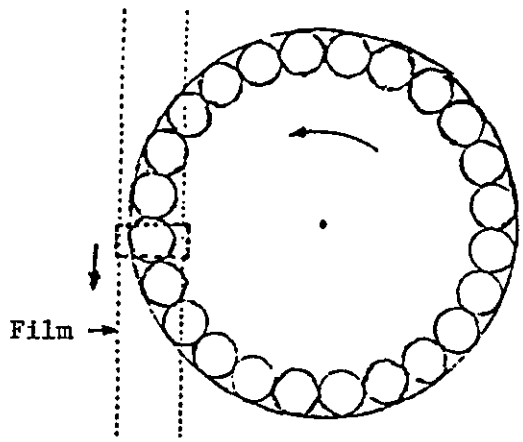

Figure (3.11) Rotating lens sutter .

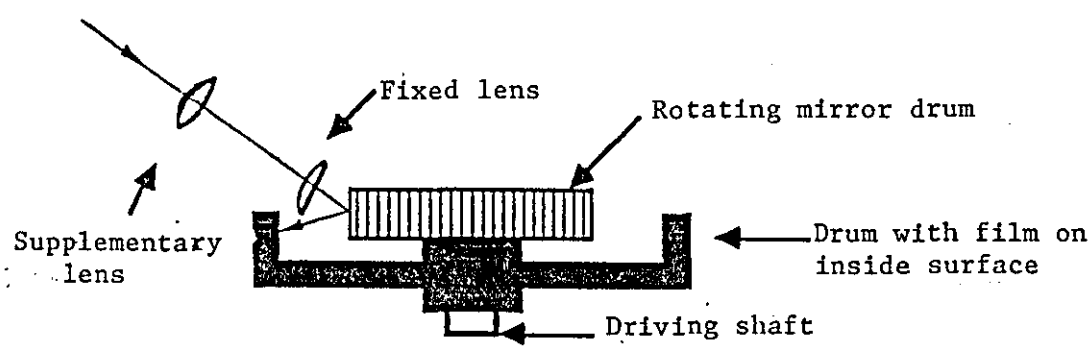

Figure (3.12) Rotating mirror drum camera .

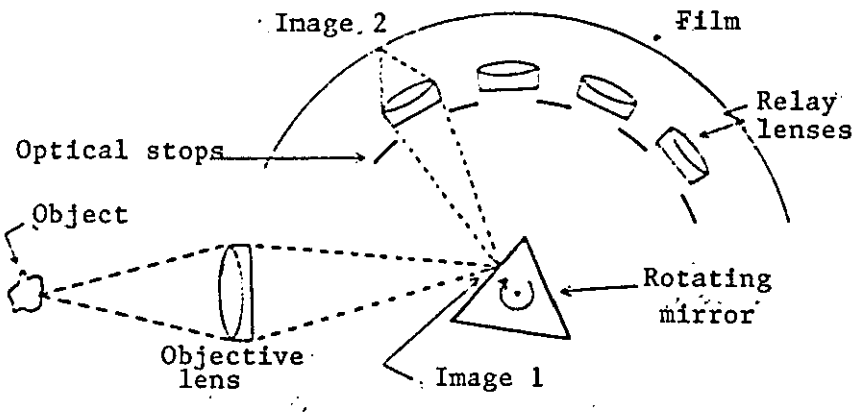

Figure (3.13) Rotating mirror shutter for cine photography

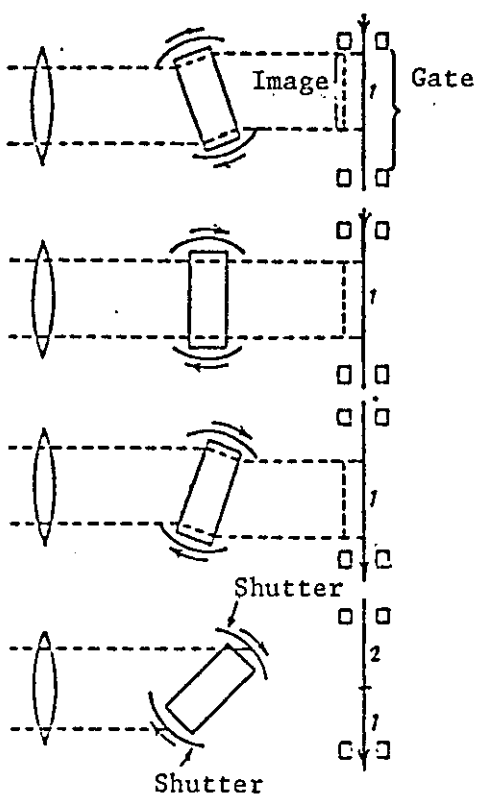

Figure (3.14) Rotating plane prism shutter .

3.3 The shadowgraphic technique

Methods of experimental flow analysis can be used which involve the use of additives to the fluid. This has several disadvantages, including inertia effects, pollution of the fluid, and deviation of the flow pattern by the very presence of the additive or indicator (Hyzer 1962). The shadowgraphic method depends only on the density variations within the fluid which is under study. The refractive index (n) for a gas or vapour was found by Gladstone and Dale to be related to its density (ρ) by the law (Dirwish 1979)

$$k\rho = (n-1)$$

where k is Gladstone-Dale constant. Light travels at a speed inversely proportional to the refractive index of the medium through which it is passing. Thus, if a light-wave of given form enters a region in which the density varies it will travel slowest through zones of high density and high refractive index. If these density variations are perpendicular to the direction of travel of the wavefront, there will be a deviation of the beam which will cause a variation in illumination over a screen placed in the light beam (Ralph 1959).

This effect is utilized in the shadowgraphy method for determining the positions and shapes of shock waves (Dirwish 1979). In the shadowgraphy system (Hyzer 1962), a point source of light, usually a short duration spark, is used to illuminate a screen or photographic plate. If the medium between the spark and the plate is free of disturbance, the plate will be evenly illuminated. However when a disturbance is produced in the medium by the passage of a high-velocity projectile or by a heated object, density gradients occur throughout the affected area and cause the rays of light to be deviated to produce corresponding changes in plate illumination. It can be shown that the variation in illumination on the screen is

proportional to the second derivative of the fluid density normal to the ray through the disturbance, ie, $\partial^2/\partial y^2$ The shadowgraphy method is sensitive only to high-density gradients of the type that accompany severe shock waves and is not applicable to low-energy disturbances that easily fall within the sensitivity range of the Schlieren technique (to be described in the next section). The resolution and sensitivity obtained by the spark method are:

1) inversely related to the diameter of the spark,

2) directly related to the distance between the disturbance and the photographic plate. The advantage of shadowgraph method is its simplicity in the study of intense shocks. The principal disadvantages of the conventional unfocused shadow method of shock wave photography are the requirements for:

1) complete darkness during the test,

2) a large film size approximating that of the area to be studied. Figure (3.15) shows a diagram of a shadowgraph system which includes a DC power supply to a capacitor which feeds the spark gap after the trigger pulse from the trigger part, and a photographic plate. When the projectile passes through the light beam it will block the beam to the photo tube for a moment and that causes a sudden pulse to go into the amplifier and inductance coil to produce a suitable pulse to trigger the flash. This illuminates the plate enabling the projectile and wave front to be seen as dark regions. Two methods of using shadowgraphy:

1) Unfocused shadowgraph

This method is (Zukas 1982) used with the oldest single frame technique. An open sheet of film is placed close to the object, and small diameter pulsed light source such as an electronic flash or electrical spark gap is mounted behind the object. By using very

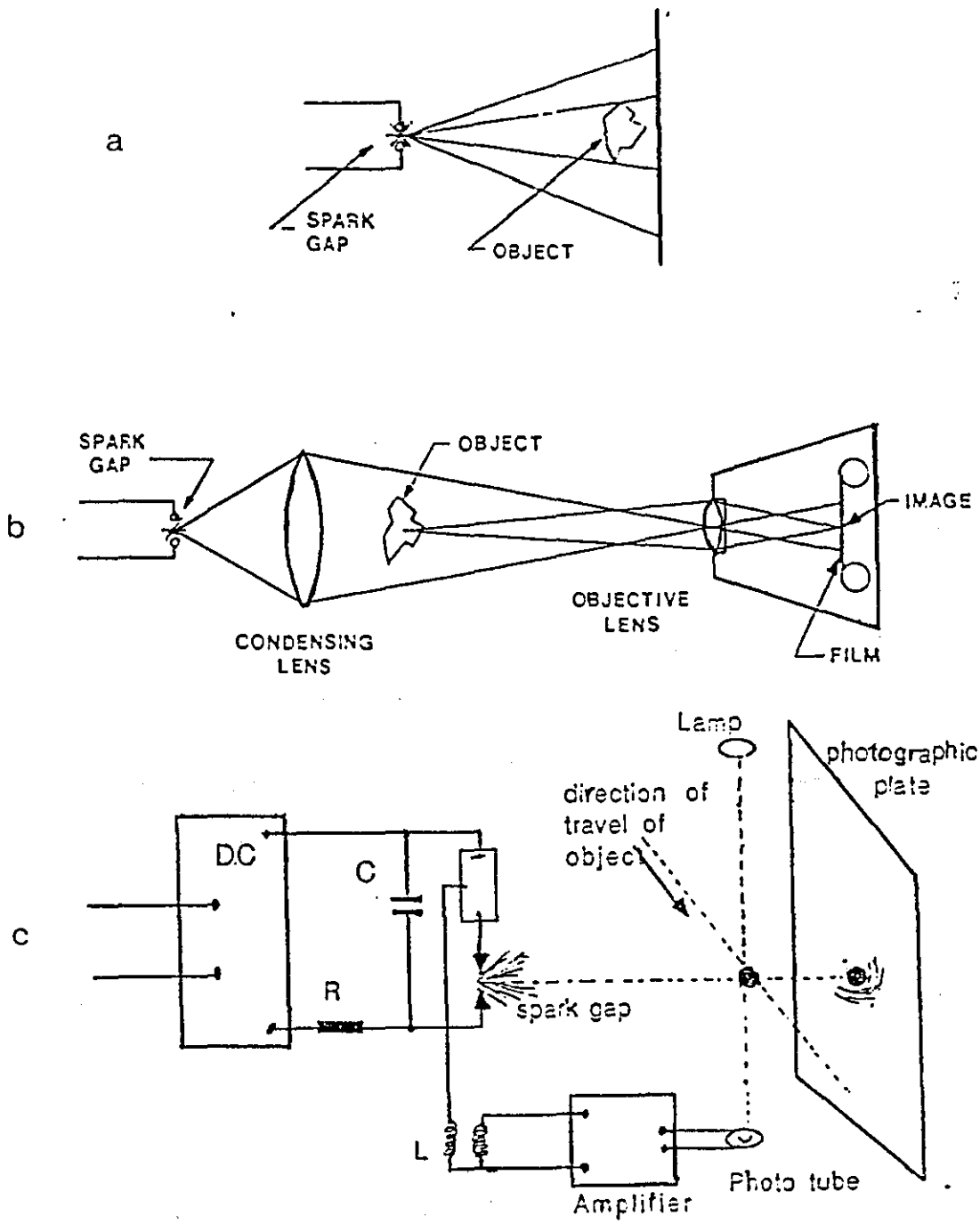

Figure (3.15) Shadowgraph setups for taking images of moving objects; a, unfocused; b, focused; c, complete unfocused shadowgraph system.

simple spark circuits the system can give an exposure time of 10^{-6} s duration, which recently has been reduced to be 10^{-11} s by using the pulsed laser. Figure (3.15 a) shows unfocused shadowgraph optics.

2) Focused shadowgraph

The disadvantage of the unfocused shadowgraph is its requirements of nearly total darkness, and the placing of the film close to the object can damage the film if the event under study is violent enough. Because of these difficulties a focused shadowgraph system which is shown in Figure (3.15) can be used. The film is loaded in an ordinary camera which is focused on the object. A condenser lens placed between the object and the spark images a small light source on iris of the camera lens after passing through the object area.

In this system the effective diameter of the camera objective lens is the diameter of the light source image focused by the condensing lens rather than the iris diameter. Because the image is small, the effective F/no. of the camera lens is high, and produces a substanial depth of field.

3.4 Schlieren photography

The simple Schlieren system (Ahmad 1988) which is shown in Figure (3.16) includes a point source of light behind a small circular aperture, a simple single lens and another circular aperture in front of the camera. This method (Lipson 1964) is equivalent to cutting off half the transform including the central peak of the light by deviating the light because of the differences in the medium density.

Also it displays (Brown 1965) the density gradient in the fluid. Observation of details of the flow of air or other gases about a high velocity body requires making visible (or detectable) the variation of refractive index associated with the small changes of pressure created as a result of the flow. As indicated previously, the refractive index of a gas is related to density ρ by

$$n-1 = k\rho$$

where k is the Gladstone-Dale constant, and ρ is the gas density. This can be written as

$$\frac{n-1}{\rho} = \frac{n_0-1}{\rho_0}$$

or $$n-1 = (n_0-1)\frac{\rho}{\rho_0} = C\frac{\rho}{\rho_0}$$

where C is a quantity, which for air in visible light ranges from about 2.9×10^{-4} to about 2.98×10^{-4}. When light passes through (Ahmad 1985) a gas in which there is a variation of density, and therefore of refractive index, it will suffer from deflections given by:

$$\theta = t\frac{\partial n}{\partial y}$$

where θ is the angle of refraction, and t is the width of the disturbance. We can express the above equation as:

$$\theta = t\frac{C}{\rho_0}\frac{\partial \rho}{\partial y}$$

or

$$\theta = kt\frac{\partial \rho}{\partial y}$$

where $$k = \frac{C}{\rho_0}$$

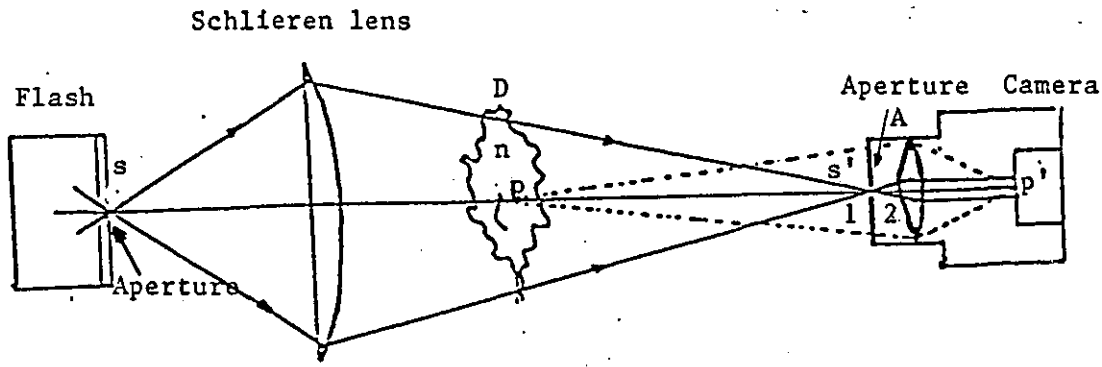

a) Typical simple Schlieren system arrangement.

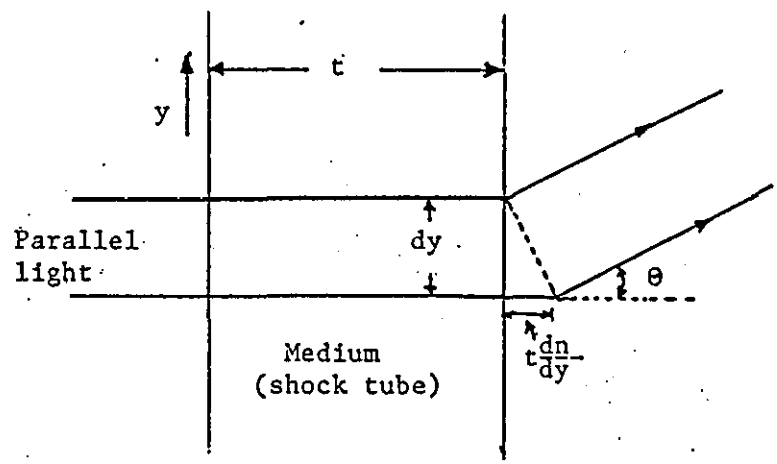

b) The deviation of a light beam by refractive index gradient.

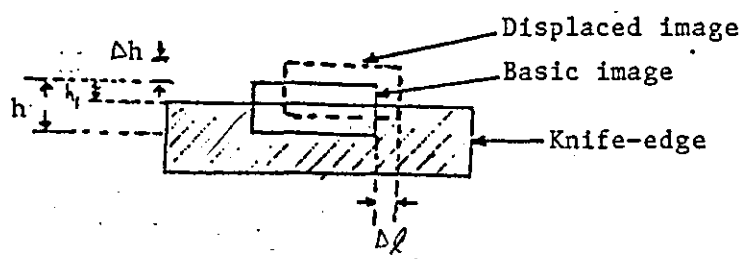

c) Knife-edge effect.

Figure (3.16) Schlieren photography method.

Since the value of $k\rho_0$ is, in general, small, deviation is also small unless $\partial\rho/\partial y$ is very large.

The system which makes use of small deflections obtained when $\partial\rho/\partial y$ is not very large is known as a Schlieren system (Parry 1976). In Figure (3.16) if the circular aperture A in front of the camera lens is moved up into the focused beam at s, the screen illumination is reduced in such a way that the screen darkens evenly, since all the light which reaches s' has come in a evenly distributed manner from the whole Schlieren lens area. The aperture placed at positions 1 or 2 would produce uneven darkening.

Consider the effect of a disturbance at D situated so that it and the camera screen are conjugate planes. Point p is imaged at p' and any rays leaving p will be focused at p'. Thus, when a change in n at p deflects the ray in any direction, it partly misses A but still focuses at p'; a darker stop is recorded at p, larger in illumination than the surrounding screen. The Toepler Schlieren method, (as it is known) therefore records changes in n gradients through changes of illumination on a screen.

3.5.1 Electronic flash

The use of special equipment and techniques (Quick 1972) is necessary for high speed photography. The exposure rate of high speed cameras normally requires greater illumination of a non luminous object than is normal in standard cinematography. The light must be of greater contrast for high speed work to make the action more apparent.

In many respects the operation of an electronic flash bulb is identical to a lightning flash where electrical energy is accumulated slowly in the cloud-earth system and is suddenly released in a terrific surge of electrical power. The air is quickly heated by the lighting stroke and a flash of light of high instantaneous brilliance and short duration is produced (Edgerton 1953). The single

electronic flash has a very high peak light output, but usually a very short duration, so that the camera shutter has no other function than to keep out any ambient light that may be present. The electrical energy is obtained from a rectified mains power system, or from a battery, and stored in an electrical capacitor until the flash is desired. The capacitor is the equivalent element to the cloud - earth energy storage system of the lightning stroke.The amount of the energy which is stored is given by

$$W = \frac{1}{2} CE^2 \quad \text{watt-second (Joule)}$$

where C is the capacitance of the capacitor (in farads) and E is the voltage to which the capacitor is charged before the flash. However, the light output of a flash unit depends not only on the amount of the stored energy but also upon the efficiency of the flash tube.

Basically the flash system (Wakefield 1952) includes a capacitor which is slowly charged by a suitable source and then discharged rapidly through the tube by means of a triggering circuit.

The triggering action should take place while the camera is ready to take the photograph of the event, so synchronization between the flash and the camera is required to ensure that the camera shutter is fully open when the flash output is fully effective (Wakefield 1952). The best way to do this with a flash which is not connected directly with the camera is by using a photodiode pointing at the flash to trigger the camera.

3.5.2 Electronic flash duration

There is no standard definition of duration for an electronic flash, but the common definition is that the duration is the time between half peak points on the rising and falling portions of the light output curve.

The duration of the flash is an important criterion in motion analysis when a blur-free image is required. The flash duration (Ralph 1959) is determined by several factors which include:

a) flash-tube design;
b) capacitor size;
c) capacitor voltage;
d) values of resistance and inductance in the flash-tube circuit.

In most practical cases the total output duration is much longer than described in the above definition because of the long decay time of the light after glow characterizing the discharge. The duration might be more realistically based on one-tenth of the peak value. Simple flash guns have a half-peak output of about 1000 μs; such devices are not suitable for many scientific applications, where the subject moves at high speed, e.g. photographing shock waves.

The flash duration can be measured or estimated by the following ways:

a) by using a photodetector connected to an oscilloscope to record the flash output as a function of time. The above definition can then be used to establish the half-peak duration,
b) from the relationship $T = d/v$ (Edgerton 1979), where T is the appropriate flash duration in seconds, d is the blur of subject movement, and v is the velocity of the subject, and

c) by using the equation $i = I_{max}\, e^{-t/RC}$ (Hyzer 1962), where i is the flash tube current (amp), R is the flash tube resistance (ohms), t is the time (seconds), and C is the capacitance (farads). The duration T in seconds based on a light level half of the peak can then be

calculated from the equation as $T = 2RC/3$ assuming negligible risetime. The resistance can be calculated by using the initial capacitor voltage E in volts, and the maximum instantaneous discharge current I_{max} to give

$$R = E/I_{max}$$

Alternatively, the resistance is given by

$$R = \rho L/A$$

where ρ is the xenon plasma resistivity (ohm-cm), L is the arc length and A the cross-sectional area. From Edgerton (1979),

$$\rho = 1.13(J)^{\frac{1}{2}}$$

where J is the current density (amp/cm^2).

Hence $$R = 1.13L(iA)^{\frac{1}{2}}$$

where i is the instantaneous discharge current.

Flash tubes are operated most commonly in one of the following two types of discharge circuits: capacitor discharge, and inductor-capacitor discharge. The first type is the simplest flash circuit in common use the flash tube acting as its own switch. The advantage of introducing an air-core inductor-capacitor discharge circuit is to:

a) reduce the peak current of the simple capacitor discharge

b) lengthen the pulse duration

c) increase the life of the flash tube, the flash duration in this type being given by $T=\pi(LC)^{\frac{1}{2}}$ (Edgerton 1979).

3.6 Conclusion

High speed photography is required for investigating rapid events which were previously unseen by the scientists, such as the movement of fast small mechanical particles, shock waves generated by explosion and impact loading, plasma behaviour, and electrical discharges. Resolution time of the high speed cameras can approach 10^{-13} s, and the speed rate can be ranged from 500 f/s for intermittent motion camera, to 3×10^{9} f/s for the electronic camera which can be operated with exposure time down to 1 ns.

The flash output that is required for such photography should be powerful with a short duration.

In this chapter several types of high speed camera have been described as well as electronic flash, shadowgraph and Schlieren techniques.

An image converter camera which will be described specifically in Chapter 4 is used in the present work in association with Schlieren photography and a xenon electronic flash, which will also be described in Chapter 4. These devices are suitable for the demands of the present work, which requires a short duration flash and high speed camera as well as Schlieren photography which is used to show the disturbance caused by the explosion clearly and hence to measure the shock wave expansion.

CHAPTER 4

DESCRIPTION OF EQUIPMENT

4.1 High speed photography equipment

Figure (4.0) shows general diagram of equipment which is used in the present measurements and for synchronizing the whole system.

4.1.1 Imacon Camera

The Imacon is a high speed image converter camera (Al-maliky 1989). It can be operated in both multiple framing and streak modes. The framing rate can be varied from 2.5×10^4 to 2×10^7 frame/sec as determined by interchangeable plug-in modules. In the streak mode, the image is swept across the film with sweep rate range from millisecond/cm to nanosecond/mm.

The Imacon camera uses an electric field for deflecting an electron beam in a CRT (cathode ray tube) as previously described in Chapter 3, by means of deflecting plates mounted inside the tube, the shutter of the camera being, effectively, an electric oscillating field. The Imacon makes use of a special image tube which has three pairs of deflector plates in the drift space between anode and screen. In the framing mode the first pair of plates act as shutter plates and, when a sinusoidal oscillation is applied to them, deflect the electron beam up and down across an aperture slit. Figure (4.1) shows the tube and the signals across the plates.

The electron beam can only get through the aperture plate when it passes through this narrow slit and this effects repetitive shuttering. However, this produces blurred pictures on the phosphor screen. The beam comes from the photocathode which is supplied with a negative potential of 20 kV from a stabilized EHT generator mounted within the camera. When the light is incident on the photocathode it causes it to emit an electron beam from the inside surface of the photocathode and this beam is focused by the focusing cone (at negative potential) and accelerated by the anode which is earthed.

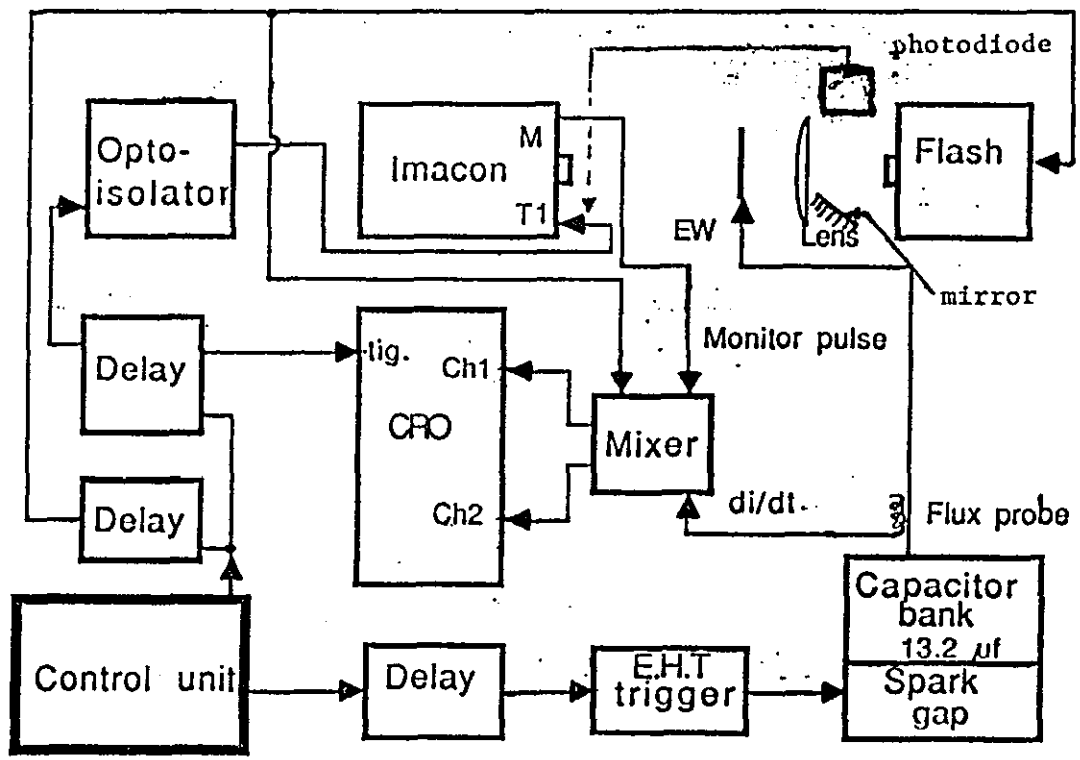

Figure (4.0) Block digaram of the present set up for synchronisation and measurements.

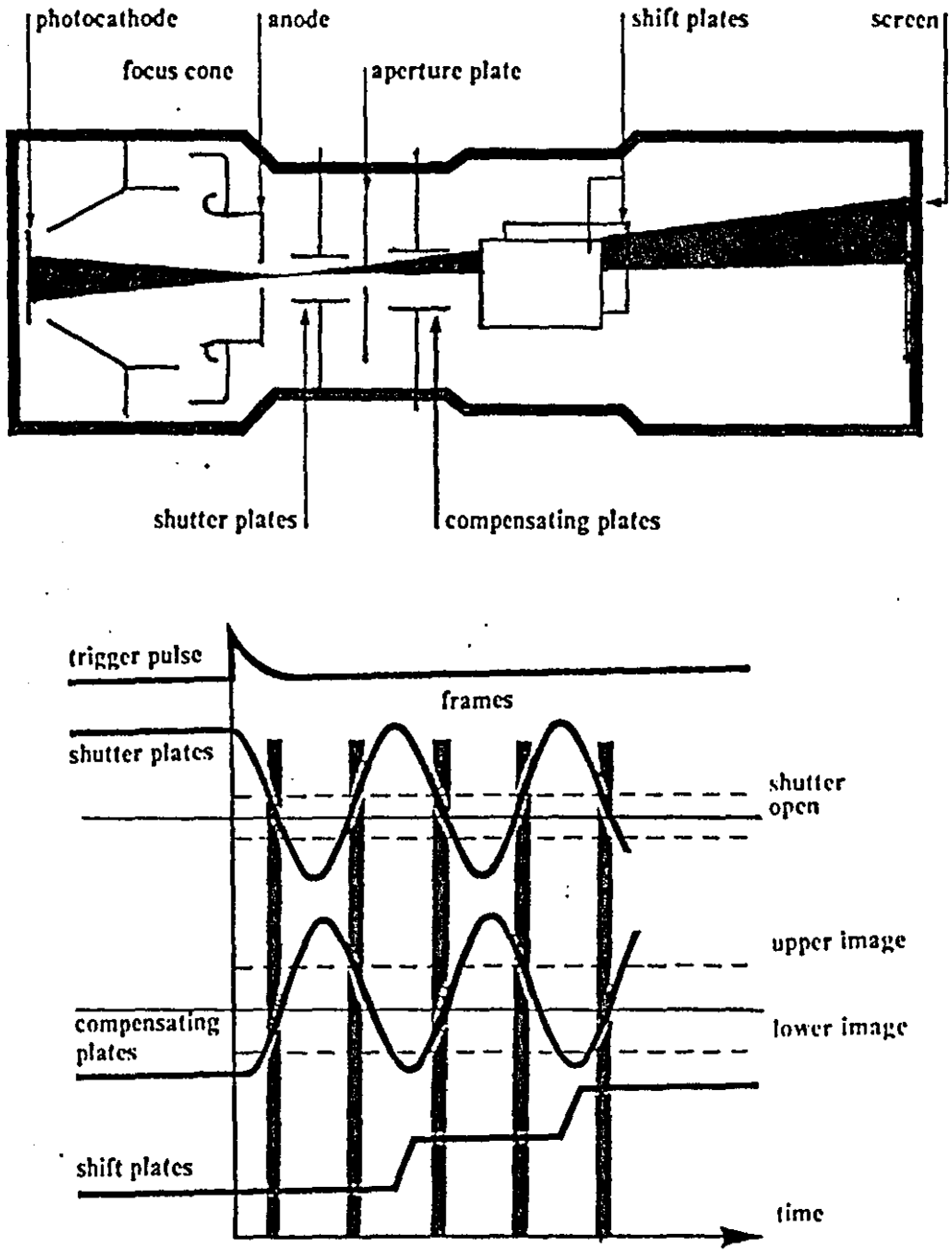

Figure (4.1) Image converter tube and the signals across its plates

In front of the camera there is an objective lens which forms an image of the event on the photocathode. At the rear of the camera there is a combined mirror/relay lens system for focusing the screen images on to a camera back containing 3000 ASA polaroid film.

The exposure time is related to the framing rate of the camera. It equals 0.2/framing rate, i.e. one - fifth of the total time between each two frames. The image resolution is 10 line pairs/mm for exposure times down to 0.1 μs (2×10^6 f/s), and 5 line pairs/mm for shorter times.

When the camera is switched on and put on focus mode, an image is formed on the photocathode. The resulting electron beam is focused by the focusing cone. The beam then passes through the shutter plates which now have zero voltage, after acceleration by the anode (with zero voltage, but positive relative to the cathode voltage). The electron beam then falls on the screen, and the image on the screen is focused by adjusting the objective lens. After focusing, in order to use the camera to photograph a moving event, the camera is put on operating mode. This lets the shutter deflect the electron-beam up to prevent it passing through the aperture. When an external pulse is applied to the oscillator, the oscillator makes the shutter deflect the beam down, which lets the beam pass through. The compensating plates then shift the beam up to make the upper image on the screen, which is the first image on the picture. After this half cycle the shutter deflects the beam upward to do the lower image in the same way and so on. The compensating plates are used to shift the beam up and down to produce the lower and upper images; this is why the Imacon is referred to as a multiple framing camera. The shift plates shift the electron-image horizontally after each upper and lower image; that means it steps horizontally after every second exposure, thus, forming two rows of images on the screen such as shown in Figure (4.2). The framing speed of the camera depends on the plug in modules used (e.g. 10^5, 5×10^5, 10^6, 10^7 f/s).

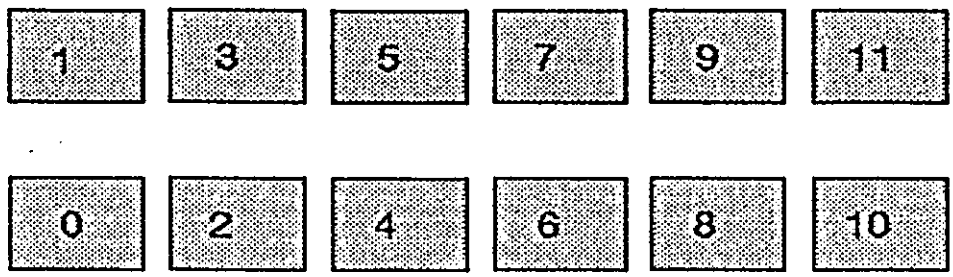

Fig (4.1) Framing sequences of high speed Imacon camera.

The camera back was originally made for Polaroid roll film (type 47) with speed of 3000 ASA. However we have modified it to use flat pack film (type 667, ISO 3000/36°) by changing the original back to a suitable back for the flat film. The reasons for this modification are the easier availability of the flat film, the lower film cost, and the better quality.

4.1.2 Flash unit

The flash source is of type HL03 (20 or 50 μs duration). The unit as shown in Figure (4.3) contains high voltage capacitors which can be discharged by triggering the lamp. It gives a maximum energy of 240 joules per flash. The intrinsic delay of the unit between the triggering pulse and the flash output is dependent on the operating voltage and the triggering pulse amplitude and risetime.

The flash can be triggered by a positive pulse of 20 – 200 V applied to the 'pos –pulse' socket or by pressing the 'Test' push button as shown in Figure (4.4).

The flash source is housed in a rectangular box. A limiting aperture of variable diameter is placed in front of the source to allow the light to come out from the lamp almost as a point source, which is important for a Schlieren system. The small diameter aperture gives a better defined light beam through the event and better sensitivity. At the back of the source there are the operating systems. The charging indicator is scaled from 0 to 3 kV, with the scale between 2.5 and 3 kV coloured in red. This means that if the voltage is more than 2.5 kV the flash might trigger by itself. Beside the scale there is the regulator which is connected to the variac transformer to adjust the charging voltage. In the lower part there is the test push-button which is used to trigger the flash manually. To trigger

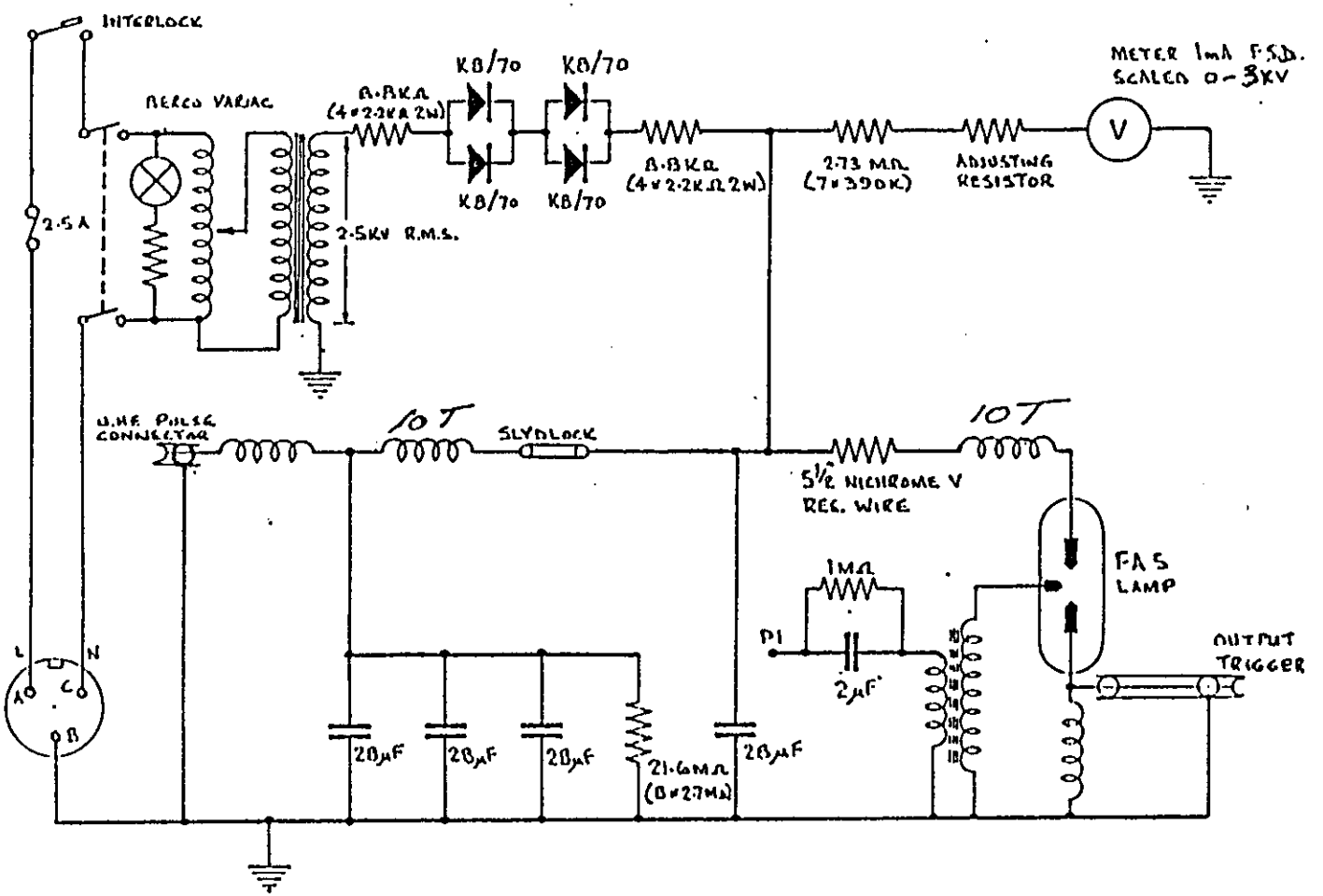

Figure(4.3)Discharge circuit diagram of HL105 Xenon flash.

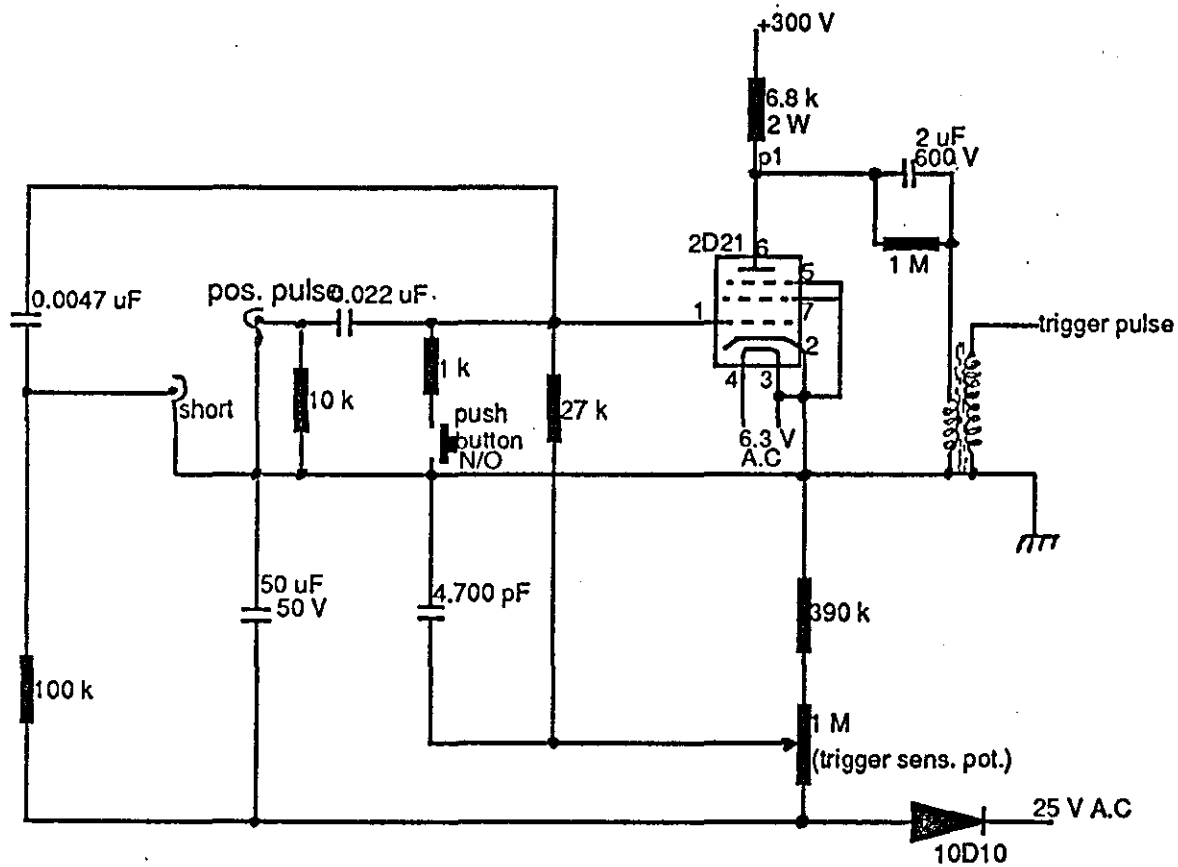

Figure (4.4) Trigger circuit of the flash unit.

the flash remotely a positive-pulse of about (20-200) volts can be applied to the 'pos.pulse' socket; the rate of rise of this pulse should be greater than 10 V/μsec. Alternatively, a -10 V pulse can be applied to the '-ve pulse' socket.

4.1.3 The trigger photodiode

The photodiode and its associated circuit are housed in a die-cast metallic box. In front of the box there is a slot to allow the light to come into the box onto the cell. The circuit diagram is shown in Figure (4.5). When the light strikes the photocell (A) it conducts and allows a pulse through the 0.01 μF capacitor (B) which switches on an avalanche transistor in an emitter arrangement. The output pulse is used for triggering the camera when the flash output reaches a suitable level for photohgraphy.

4.1.4 Lite Mike detector

The main part of the Lite Mike (Dirwish 1979) is the photodiode (D) which acts as a current generator where the current depends linearly on the intensity of the received light. The circuit diagram of the Lite Mike is shown in Figure (4.6). This detector was used to measure the flash output amplitude and duration, as will be described in Chapter 5.

4.1.5 The opto–isolator trigger unit

One feature of the Imacon camera is the ability to trigger it by an electrical signal derived from the event. Initially a photodiode detector was used to catch the light from the explosion itself to produce a suitable pulse to trigger the camera. One disadvantage of this system is the difficulty of pointing the detector in the right direction, and the impossibility of varying the triggering time delay. To avoid these problems, the opto-isolator circuit is now

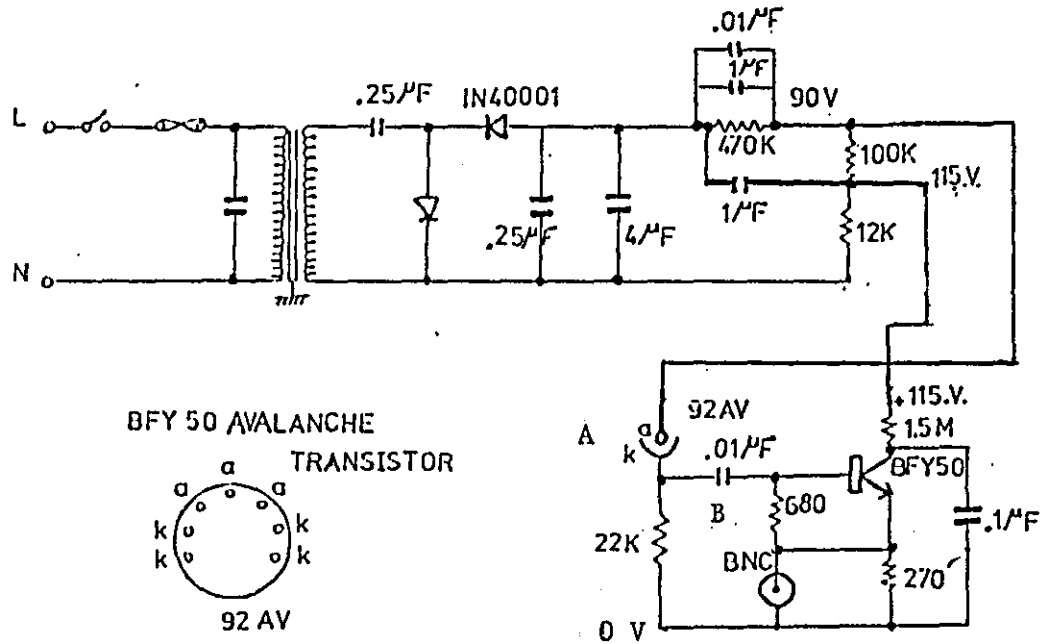

Figure (4.5) Circuit diagram of trigger photodiode unit.

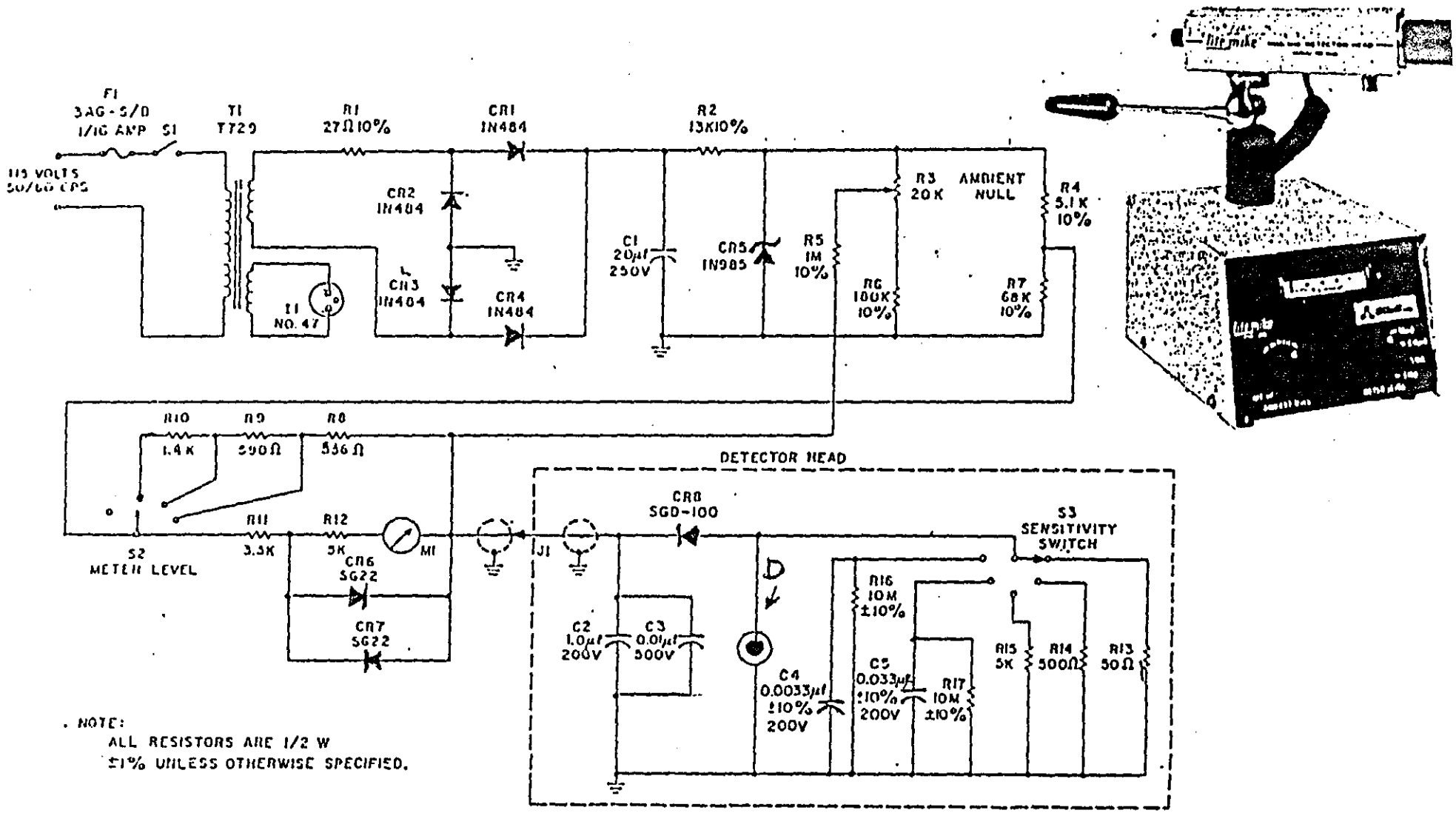

Figure(4.6)Lite-Mike circuit diagram.

used which is shown in Figure (4.7). It can give a similar pulse for triggering the camera but with variable delay times by using a pulse generator.

A pulse of (5 - 20)V applied to the input 10 kΩ resistor will open the transistor T1 to allow current to pass through it to earth causing the diode D1 to emit light. This light will be received by the diode D2 which then generates a pulse which is applied to IC1. By the voltage +5 V IC1 gives output pulse to IC2 which in the same way will give a very short rise time pulse to the base of the transistor T2 to open it. An 80 V signal will appear across the 1 kΩ resistor as a sharp pulse with a rise time of 0.3 μsec, and +80 V peak. This pulse is sufficient to trigger the camera.

4.1.6 The pulse generators and the oscilloscope

The system includes two pulse generator units as shown in Figure (4.8). One is a Venner pulse generator which is used for triggering the flash unit by using a +18 V, 5μsec width, and 1 μsec delay pulse which is itself used as a reference pulse in the oscilloscope record. The second pulse generator is a Farnell double pulse generator with two separate channels. One channel is used to trigger the oscilloscope with a +26 V, 5 μsec width pulse without delay, and the second one is used to trigger the Opto-isolator unit by a +10 V, 0.3μsec width pulse with variable delays (usually a 20 μsec delay) and a rise time of 0.02 μsec.

A dual beam oscilloscope Tektronix type 556 is employed to display the di/dt, Imacon monitor, and the pulse generators signals in both of its channels. Also a flat film Shackman scope camera is used to record the signals and the screen grid of the oscilloscope.

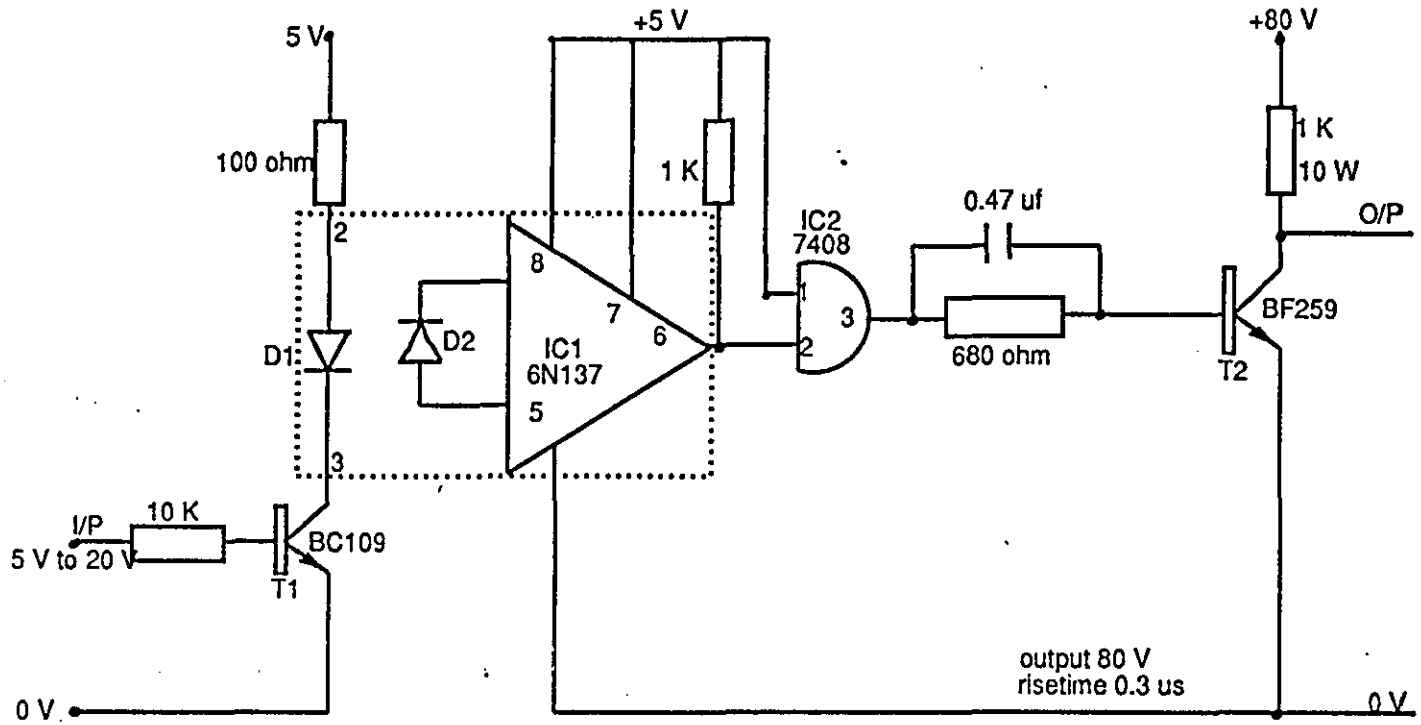

Figure (4.7) Opto-isolator trigger unit.

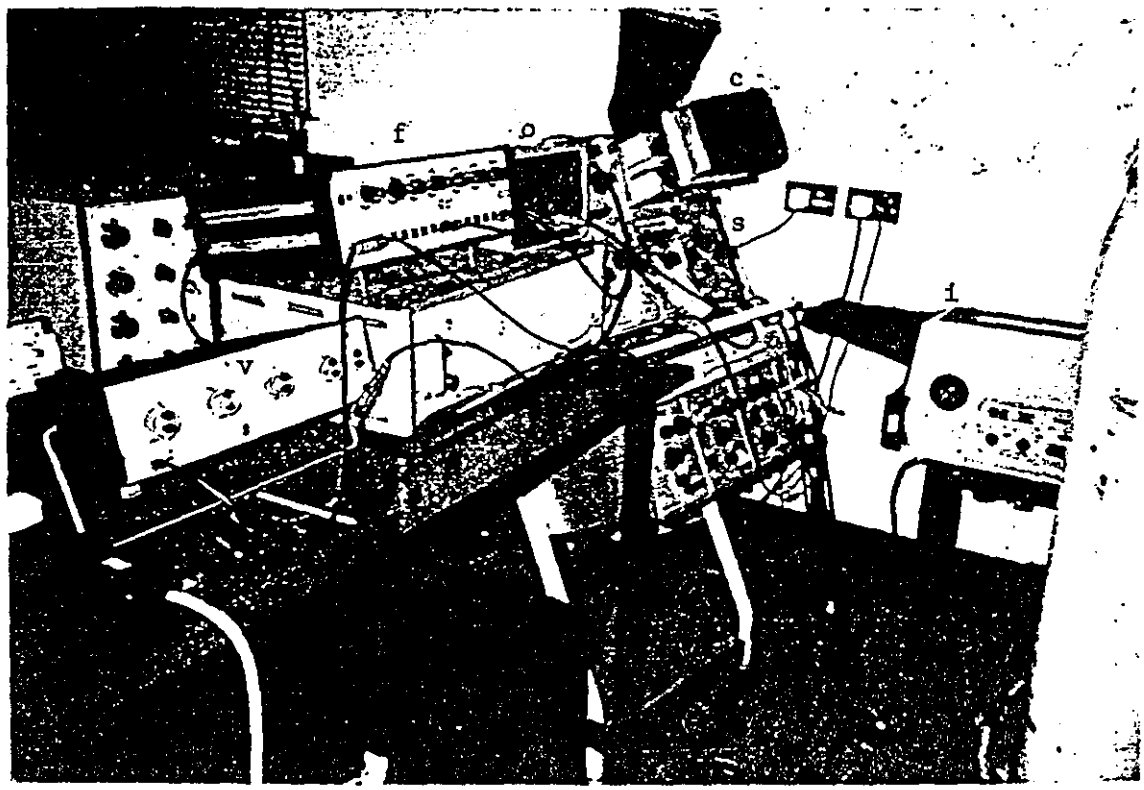

Figure (4.8) General view of high speed photography system
i- Imacon camera, s- Tektronix oscilloscope,
c- Scope camera, f- Farnell pulse generator,
v- Venner pulse generator, o- Opto-isolator
trigger unit.

A new storage Philips oscilloscope has recently been used (instead of the Tektronix oscilloscope) is association with Graphtek 8 colour pen digital plotter to record the signals and the screen grid of the oscilloscope.

4.2 Exploding wire equipment

Figure (4.9) shows that the exploding wire system can be divided into two parts, the outer part in the main laboratory controlling the second part which is inside a separate room. The inner part, which is called the exploding wire laboratory, includes the charger unit, the bank, and the flash as shown Figure (4.10). This room also includes a Schlieren setup of xenon flash, lens and trigger photodiode as shown in Figure (4.11). The charger contains the variac transformer which is supplied by mains A.C power supply through the fortress safety and mode selector switches. The variac is followed by a D.C charging unit which charges the condenser bank through a series of high resistors of 100 kΩ in total in series with 10 rectifiers by using the charge contactor switch. This switch is controlled by the control unit in the main laboratory by means of a position sensor and a two-ways valve which employs pressurized dry air. The same charging cable is connected to two switches which are moved by another valve which is similar to the first one. These switches, called earth or dump switches, are used for bleeding any residual charge on the bank to earth after the experiment.

Discharging the bank requires a fast and low inductance switch; therefore the exploding wire system employs a spark gap switch which is triggered by a separate high voltage pulse supplied to the third electrode in the gap to ionize the air between the main electrodes and so cause a rapid discharge.

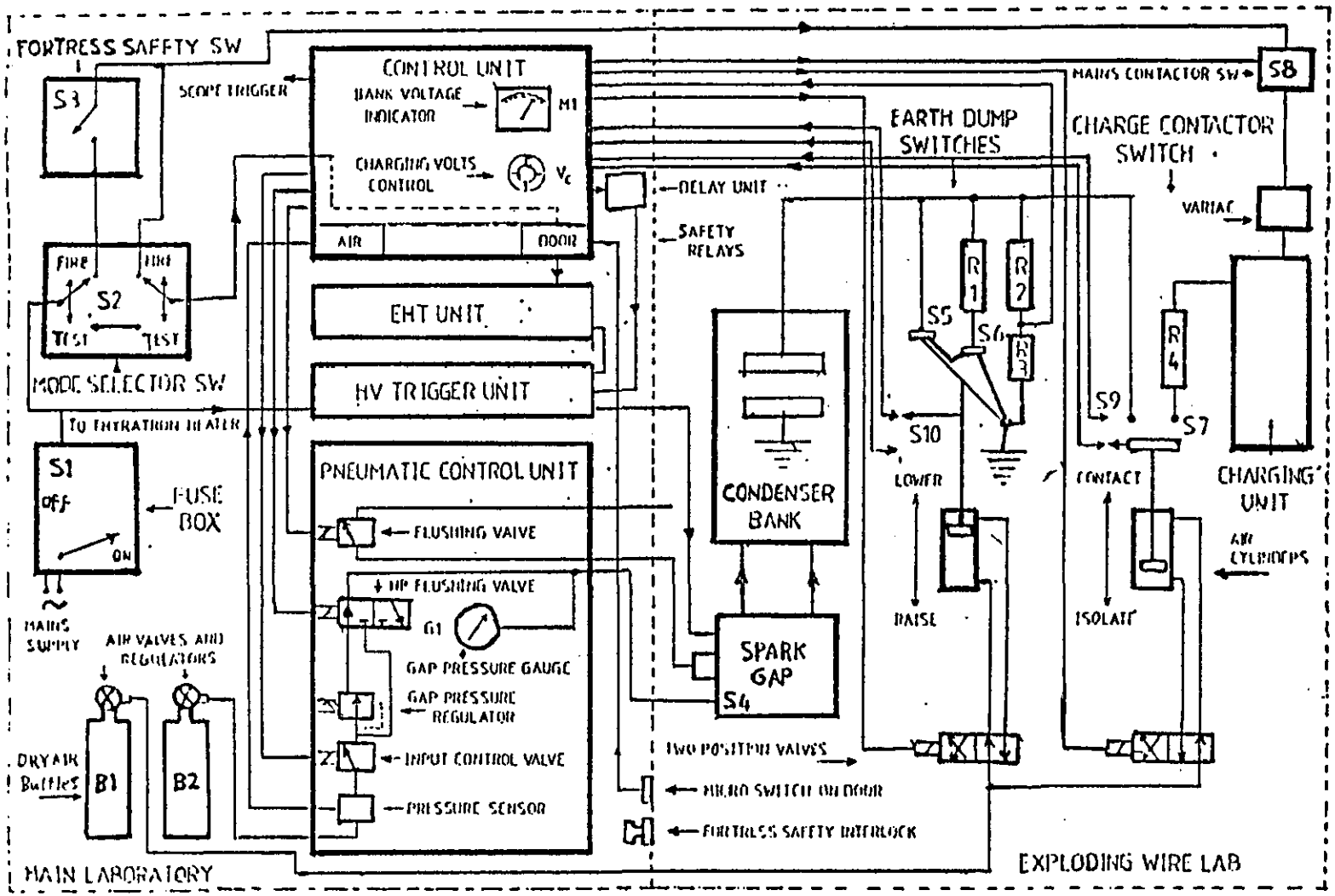

Figure(4.9)Condenser bank charging control and safety system,

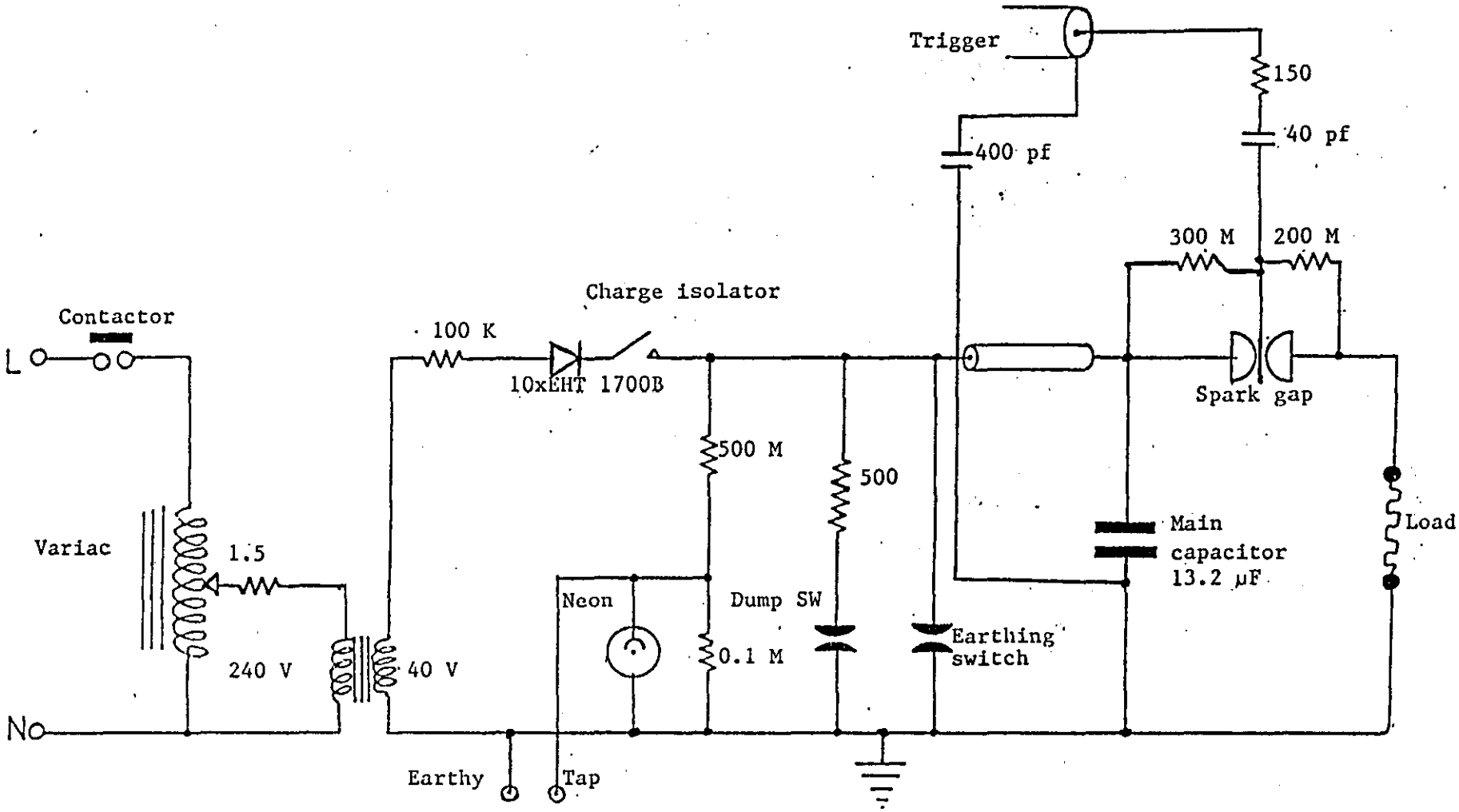

Figure (4.10) H.V. capacitor bank.

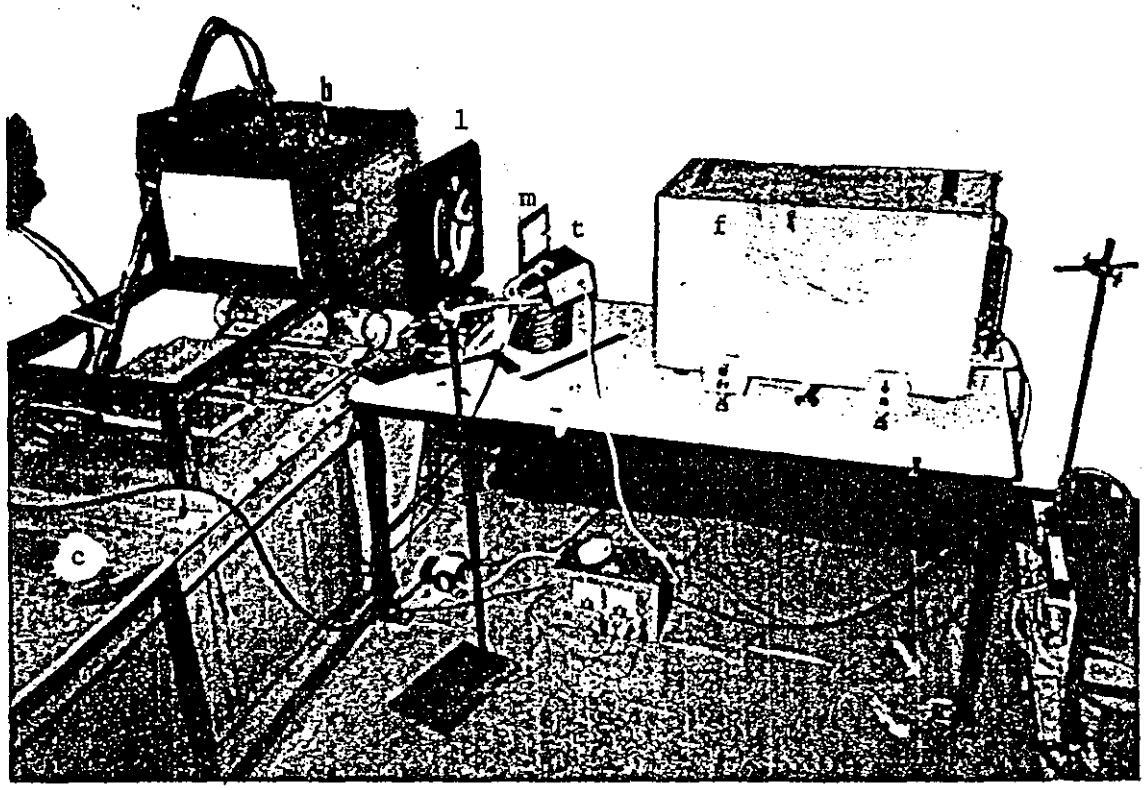

Figure (4.11) General view of the optical set-up inside EW room
f- Xenon flash, t- Trigger photodiode,
m- Mirror, l- Schlieren lens, b- EW and bank terminals box, c- Capacitor.

The second part of the laboratory is the main laboratory outside the explosion room. The most important feature here is the control unit that controls all the system. It controls the bank charging voltage, the triggering of the spark gap (using the E.H.T and H.V trigger units) and the pneumatic control unit. It also controls the triggering of the high speed camera, the flash, and the oscilloscope through the pulse generators.

The pneumatic system is supplied by pressurized dry air from two bottles .

4.2.1 Power supply

The power supply (Figure (4.12)) is an 80 kV, 8kVA single phase transformer with variac control which feeds a chain of 10 rectifiers through . 14 resistors in series, of 100 kΩ in total and 180 W each, to limit the current. The output voltage can be varied up to 50 kV to charge the capacitor by using the variac in the primary of E.H.T transformer. The charger includes dump and charge isolating switches operated by pneumatic rams, and a potentiometer to sense the voltage; by this part of the voltage we can measure the actual voltage by a digital voltmeter after multiplying by the ratio 1050 which is the the potential divider ratio of 1050:1.

The charging unit is operated by push buttons on the control unit. The bank charging voltage can be set at the control unit, and when the voltage reaches the set value the charging unit is isolated from the capacitor automatically.

The safety feature of the unit is the ability to discharge or dump the capacitor charge by short circuiting the capacitor through a switched low resistance (500 Ω). The system is connected to an independent earth strap for safety reason.

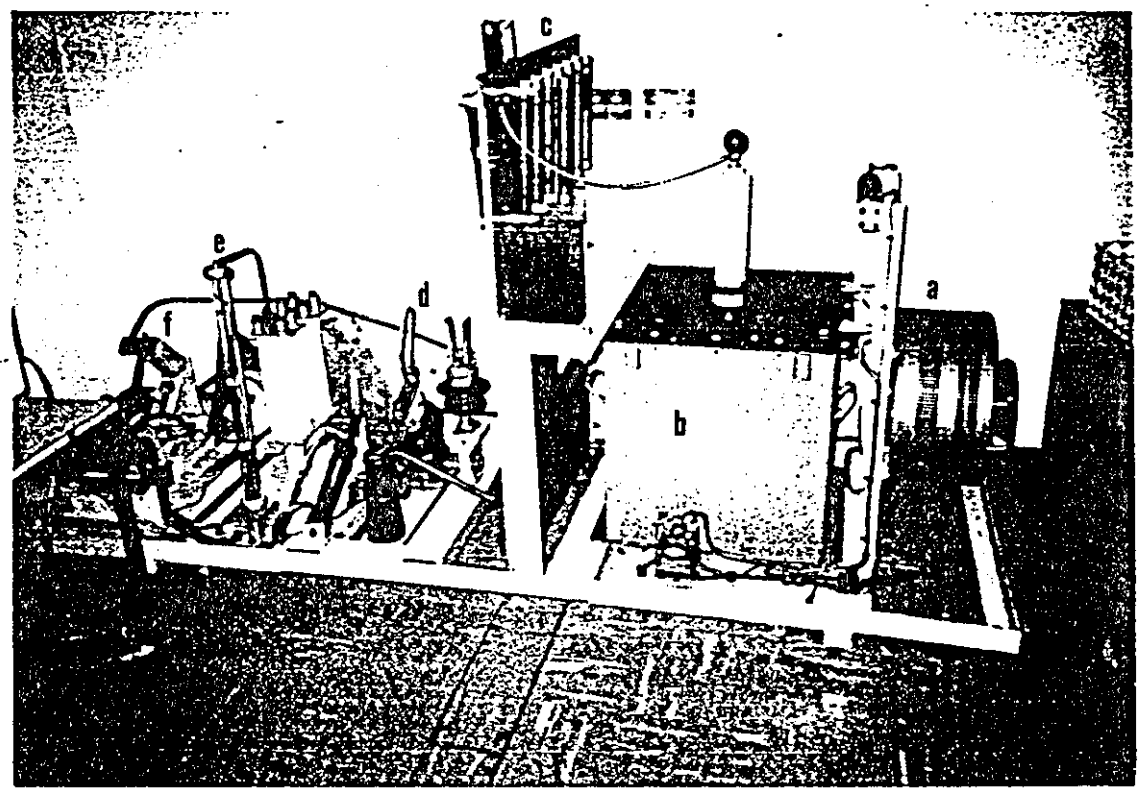

Figure (4.12) A view of the charging system
a- Variac, b- DC transformer, c- Resistance,
d- Charging switch, e- Potential divider,
f- Earthy dump switch.

4.2.2 The bank unit

The capacitor bank, which is shown in Figure (4.13) (Ahmad 1985), is of 13.2 μF a combined inductance of 30 nH, and a maximum current rating of 500 kA peak. It can be supplied to a maximum voltage and energy of 40 kV (10 kJ).

The capacitor windings (Stewardson 1984) use an oil/paper dielectric system, and are housed in a metallic rectangular case with dimensions of (1.12×0.4×0.39 m). The capacitor elements are connected in parallel to H.T terminals in the centre of an insulating lid to obtain a low inductance configuration by using external parallel plate transmission lines.

This design contains also an additional transmission line between the case and the high voltage connections to allow the spark gap and the load to be placed at opposite ends of the bank.

The top aluminium plate is taken to earth. It makes a good electrical connection to the rest of the case, and screens the high voltage connections.

4.2.3 Spark gap

The spark gap which is shown in Figure (4.14) consists of a three – electrode distortion pressurized air gap. It is mounted at the end of the capacitor. The main two electrodes are discs separated by insulation sheets but joined in the centre by an air gap. A third electrode (trigger electrode) is inserted through the discs and should be set to 60% of the travel from bottom electrode and 40% from the top one.

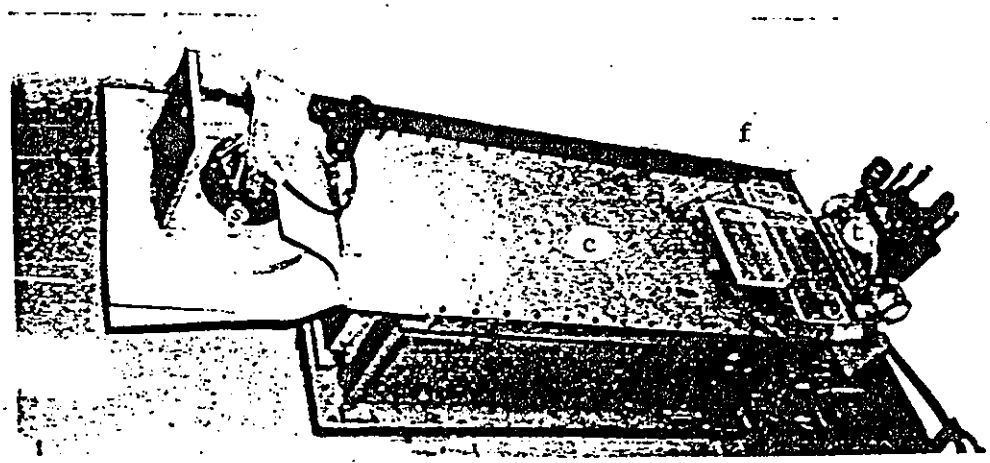

Figure (4.13) Capacitor bank (c), Spark gap (s),
Bank terminals (t), and Flux probe (b).

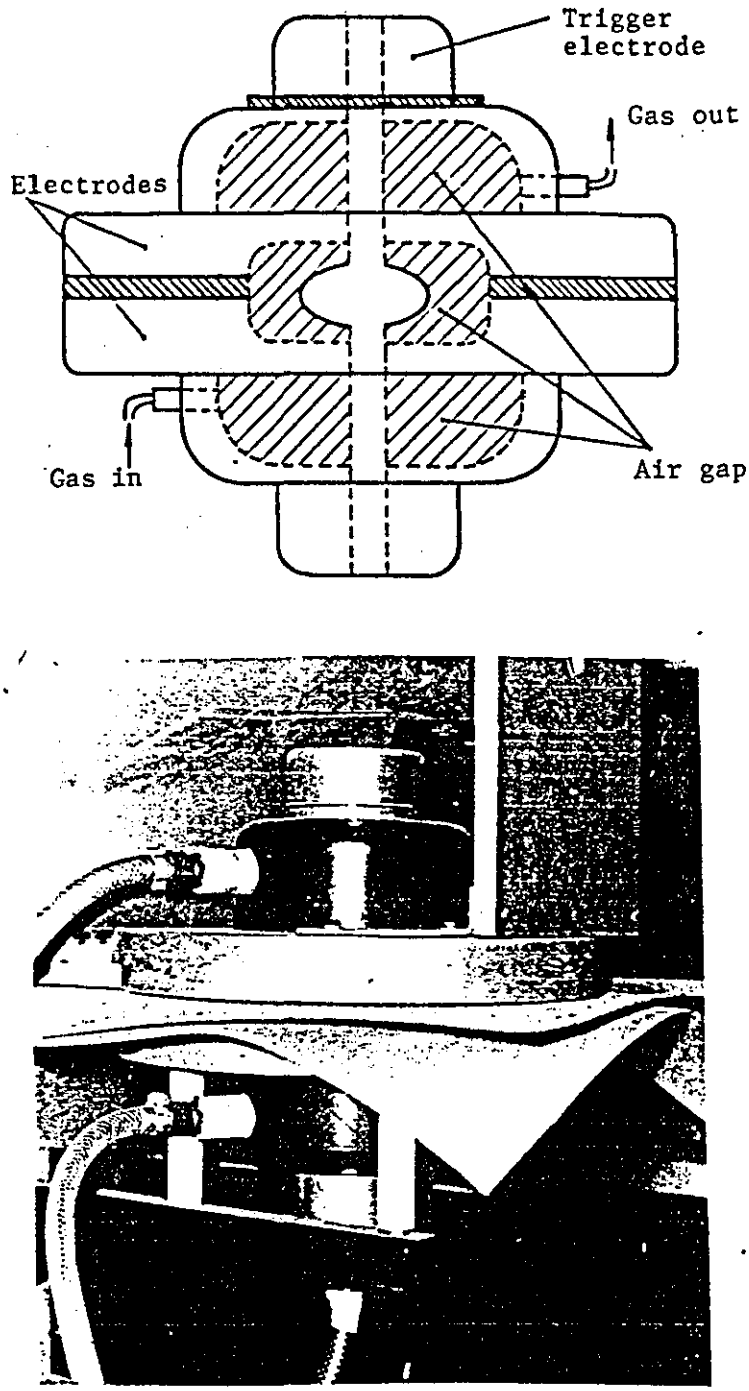

Figure (4.14) Spark gap unit.

The electrodes are covered by two insulating lids. When a voltage pulse is applied to the trigger electrode, the spark gap breaks down between the two main electrodes rapidly.

The clean dry air which used to pressurize the gap and the products of the arc must be removed immediately after firing by flushing with dry air; this is done automatically by the control unit. The gap pressure should be set by the pneumatic control unit between 8 p.s.i and 14 p.s.i at the voltages of 20 kV and 30 kV respectively.

The following are the manufacturer's rating for the spark gap only:
inductance = 16 μH
operating voltage = 15 – 60 kV
peak current = 550 kA
maximum operating pressure = 6.5 atmospheres
maximum Coulombs /discharge (c/d) =15
electrode life max. = 1.3×10^5 d/c
min. = 3×10^4 d/c
for capacitor with spark gap:
measured capacitance = 13.2 μF
max. voltage = 40 kV
inductance of capacitor /spark gap = 45 nH
life = 3×10^4 shots at 50 kV
50% reversal

stored energy kJ	40 kV	50 kV
	10	15
max. voltage reversal	70%	50%

4.2.4 Thyratron and trigger pulse generator

The trigger pulse generator and thyratron are shown in Figure (4.15) and 4.16) respectively. The single thyratron unit is connected to the spark gap by 10 m long cable for carrying the triggering pulse to the spark gap. The thyratron is operated by a controlled rectifier control signal to start conduction. When a suitable current pulse is passed through the thyratron, conduction is achieved. The output pulse from the trigger unit generator is +200 V for about 1μs followed by -200 V for about 1.5 μs applied onto a load connected to the thyratron. The thyratron acts as a virtual short circuit. The output is -10 kV, which doubles to be -20 kV down the cable to trigger the spark gap. The cable must be 10 m long or more to provide adequate width and energy in the pulse to be applied to the trigger electrode of the spark gap.

4.2.5 Control unit

To operate and control all the equipment which is associated with the system and because of the danger of the high voltage, a good control system must be used. So the control unit, shown in Figure (4.17), plays a very important role in the operation of the exploding wire system.

A nine push-button control unit placed outside the discharge room controls the operation of the charge and discharge sequence of the bank as shown in Figure (4.18). It contains indicator lamps showing the mode of the interlock circuits and the conditions in the firing sequence. Also it includes 16 relays to operate the pneumatic valves and ensure fail safe operation. The set volts control is used to determine the charging voltage which can be read on a meter. The circuit diagram is shown in Figure (4.19).

The control unit senses the bank voltage so that when it reaches the set value an isolating relay is operated disconnecting the charging unit from the bank. It is easy to start and stop charging and to lower or raise the earth in case of emergency.

4.2.6 Delay Unit

It is most important to get the timing right to study the explosions. It is necessary to trigger the camera at least 2 μsec before the explosion (see Chapter 5), and the (50 μs duration) flash about 18 - 20 μsec before the camera to enable the flash to reach a suitable output for photography. Therefore, a delay unit has to be used to delay the explosion by delaying the triggering pulse from the control unit to the E.H.T generator to trigger the spark gap after a set delay time.

Figure (4.20) shows the circuit diagram for the delay unit. It consists of two IC units which control the delay by the use of several resistors and capacitors. Three external control knobs vary the delay, and one switched input socket is used for either a 5 or 250 V pulse. The latter pulse is attenuated and then limited by a zener diode to a value of 5.1 V. This pulse is applied to the input of the first IC to give a delayed pulse to the second IC which triggers the transistor to let the +5.1 V pass through to induce a pulse in the pulse transformer.

This pulse opens the thyristor to let a +200 V pulse reach the output socket through the positive or negative pulse switch. The +200 volts pulse comes from the mains power supply after modifying it from AC to DC by the shown rectifier circuit in Figure (4.20).

4.2.7 The pneumatic control system

The pneumatic system is provided by two-position valves and cylinders on the charging unit inside the exploding wire room. It is supplied by pressurized air at 80 p.s.i from the bottle B1 which is shown in Figure (4.9). The second bottle B2 supplies the spark gap with air at a pressure of 60 p.s.i to pressurize and flush the gap.

A pressure sensor at the input to the unit operates a relay interlock in the control unit and when all the interlocks are made and S10 is operated by raising the dump switch, the input control valve is opened allowing air to go to the spark gap (S4) via the H.P flushing valve. The pressure gauge(G1) and the regulator are used to set the gap pressure.

The H.P flushing valve leads the set pressure to the spark gap (S4), and it is opened after the firing for a set period by a timed relay to clean the gap of the arc products.

The flushing is done automatically but the H.P flush can be operated manually by depressing the H.P flush push button on the control unit to allow the H.P flushing valve to direct the full pressure from the bottle to the gap.

4.2.8 Mixing Unit

Figure (4.21) shows the circuit diagram of the mixing unit which is used for attenuating the many pulses which are displayed together on the oscilloscope screen even though the oscilloscope has two channels only. The Venner pulse generator pulse is recorded on both of the channels of the oscilloscope at the same time for accurate alignment of the traces. The Venner pulse is attenuated by 18.95 toward Ch1 and 6.32 toward Ch2. The oscilloscope is triggered externally by a 23V pulse with zero delay from the Farnell pulse generator.

The I/P2 is the input of the camera monitor pulses. These pulses are then attenuated by 8.89 for display on the CRO.

The input I/P3 is for the di/dt pulse, which comes from the flux probe, for display on the CRO. An attenuation of 47 is used to protect the CRO input. A part of the di/dt pulse is also picked up by Ch1 by the mixing resistors of the Venner input.

The 124 Ω resistor is used to attenuate the monitor pulses which go to the CRO to be reduced to a small value. The 47.3 Ω resistor is used to prodect the camera monitor by reducing the di/dt pulse which comes through the 150 Ω and 2.16 kΩ resistors. It also protects the camera from the pickup pulse which comes from the trigger input of the flash unit by reducing it to a small value. The flash unit is usually triggered by the same pulse from the Venner pulse generator which is used as a reference pulse. So the 47.3 Ω resistor is a protector for the monitor of the camera from any high voltage pulses from the flash unit trigger input circuit or the di/dt pulse from flux probe.

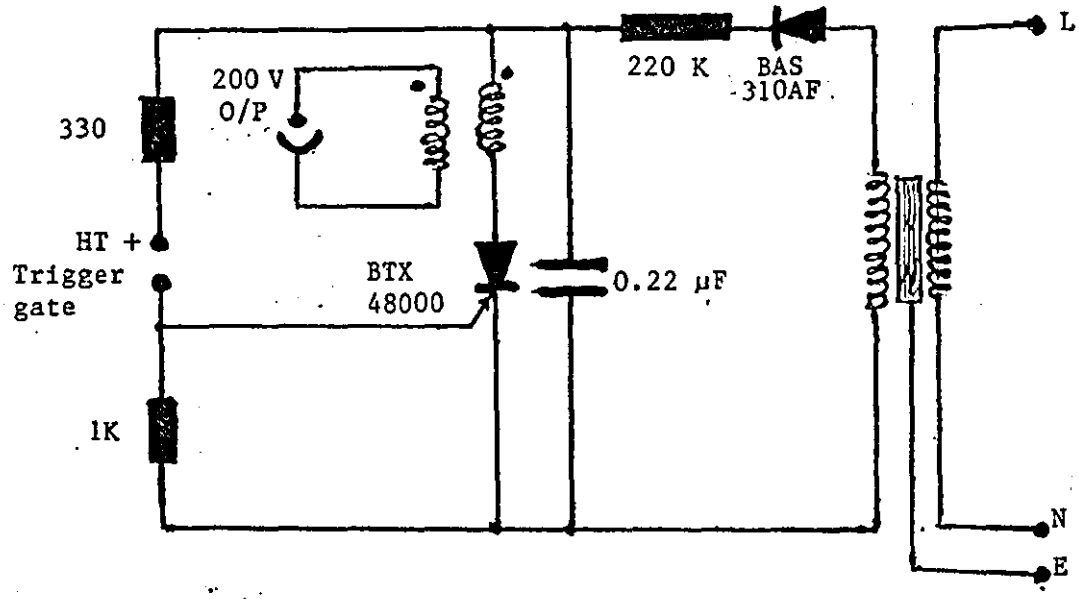

Figure (4.15) Trigger pulse generator.

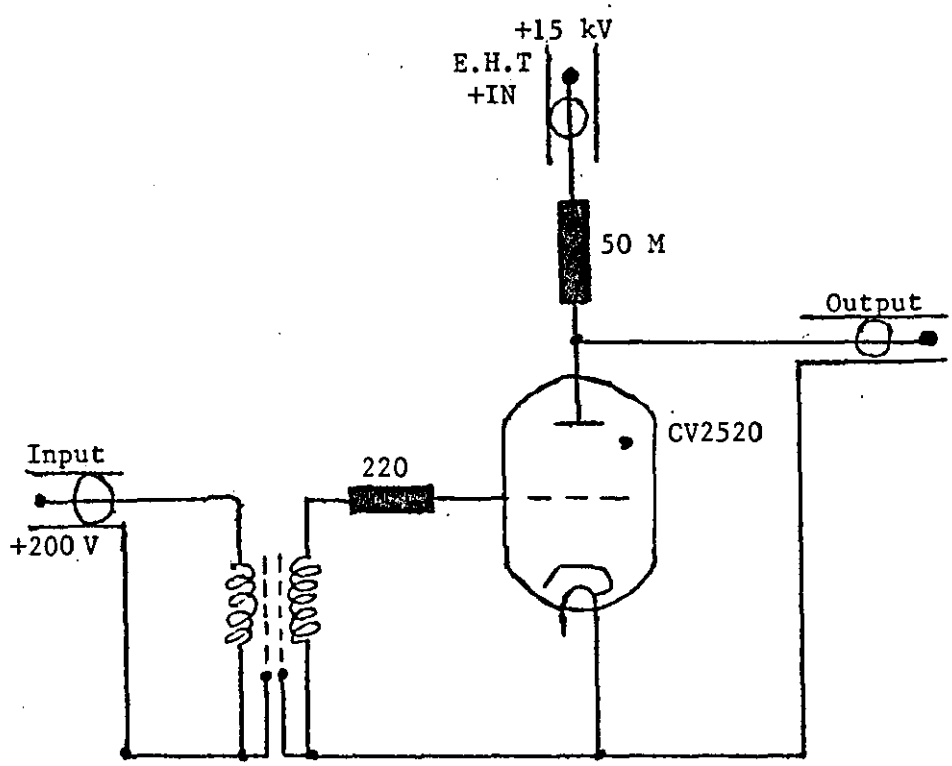

Figure (4.16) Single thyratron unit type 80041

a- control unit
b- delay-time unit
c- gas cylinder
d- pressur gauge
e- thyratron & pulse generator

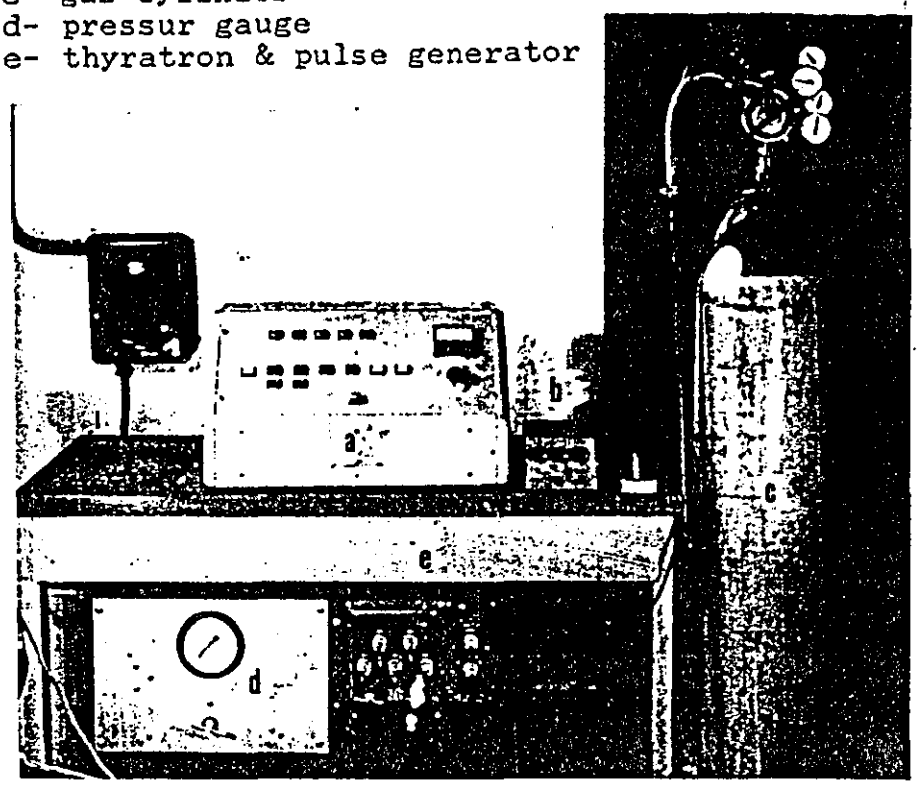

Figure (4.17) General view of the control system.

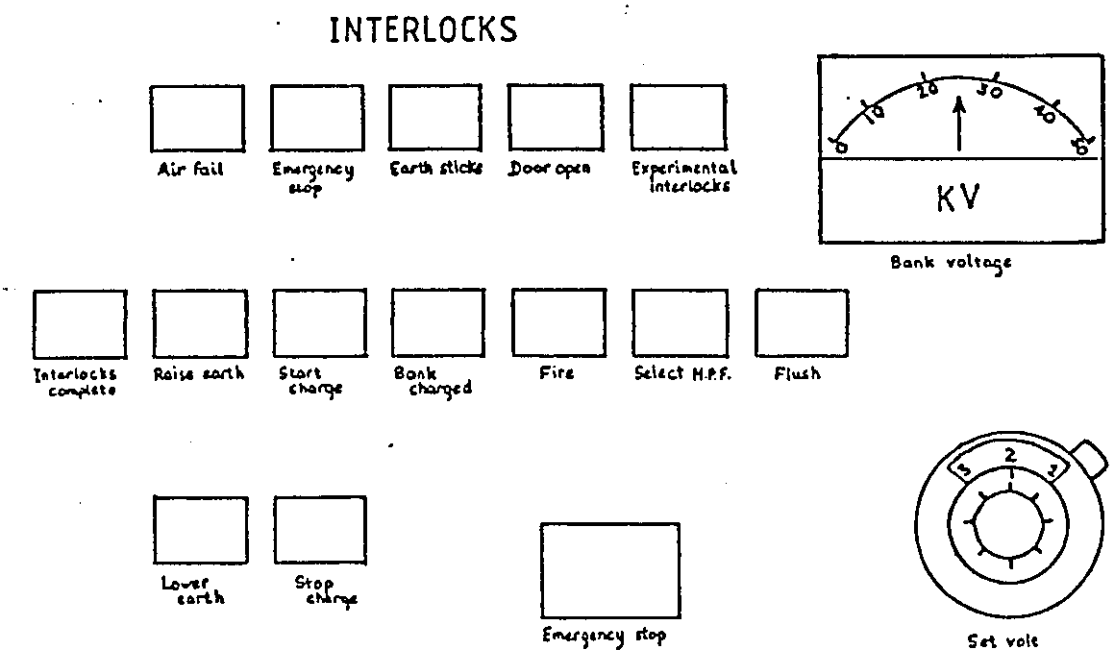

Figure (4.18) Diagram of the control system.

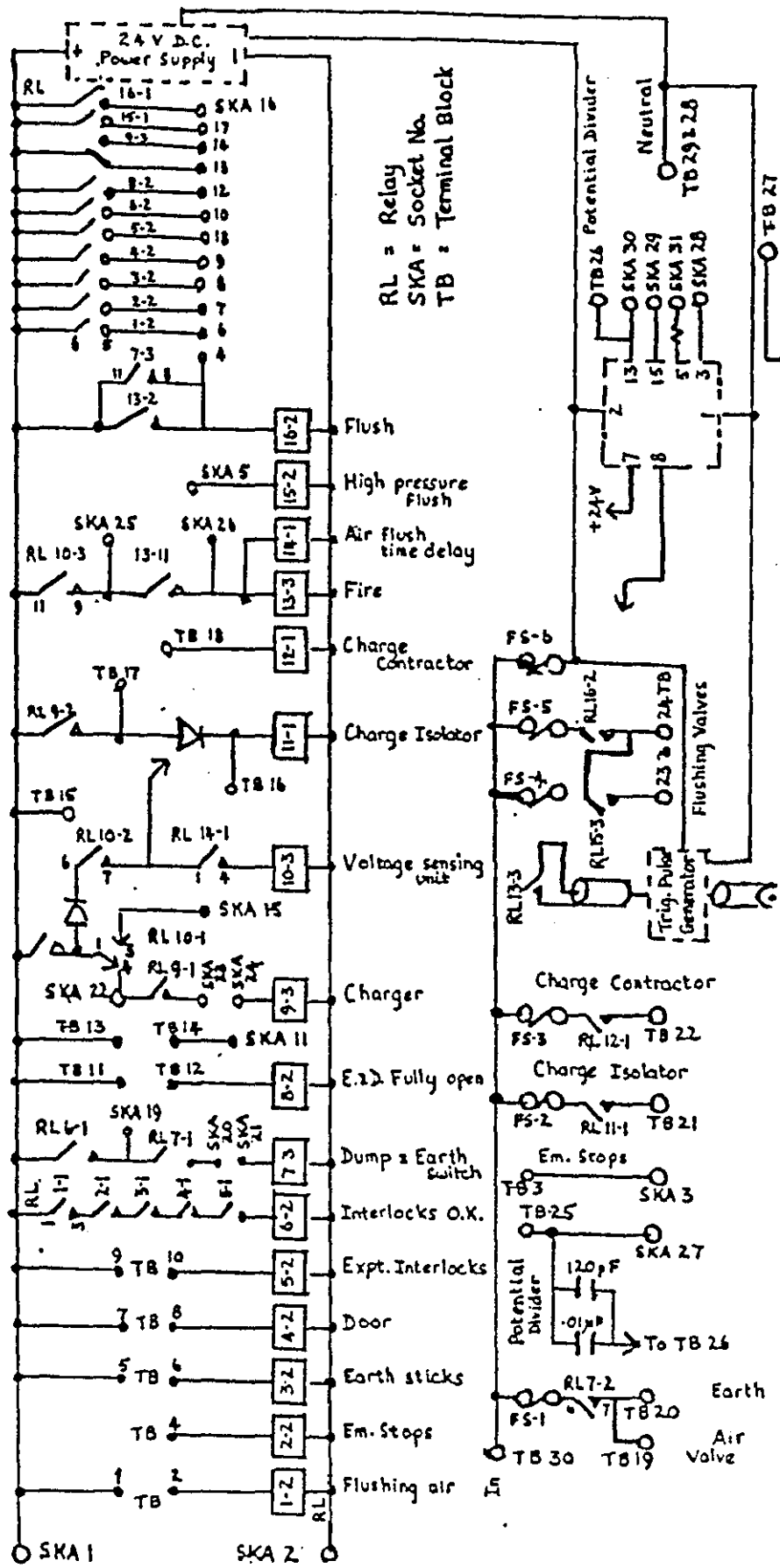

Figure (4.19) Circuit diagram of the control units.

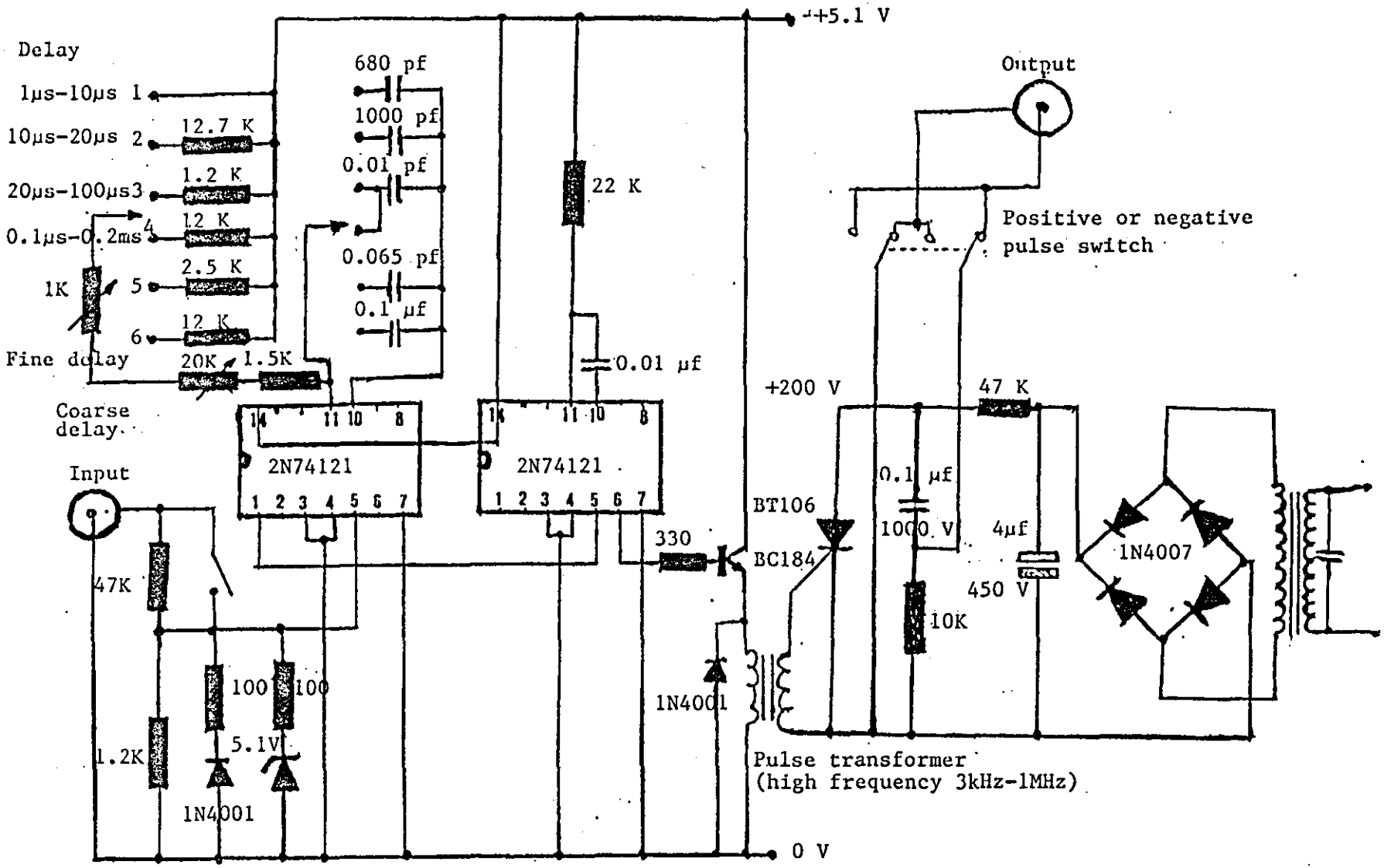

Figure (4.20) Circuit diagram of delay unit.

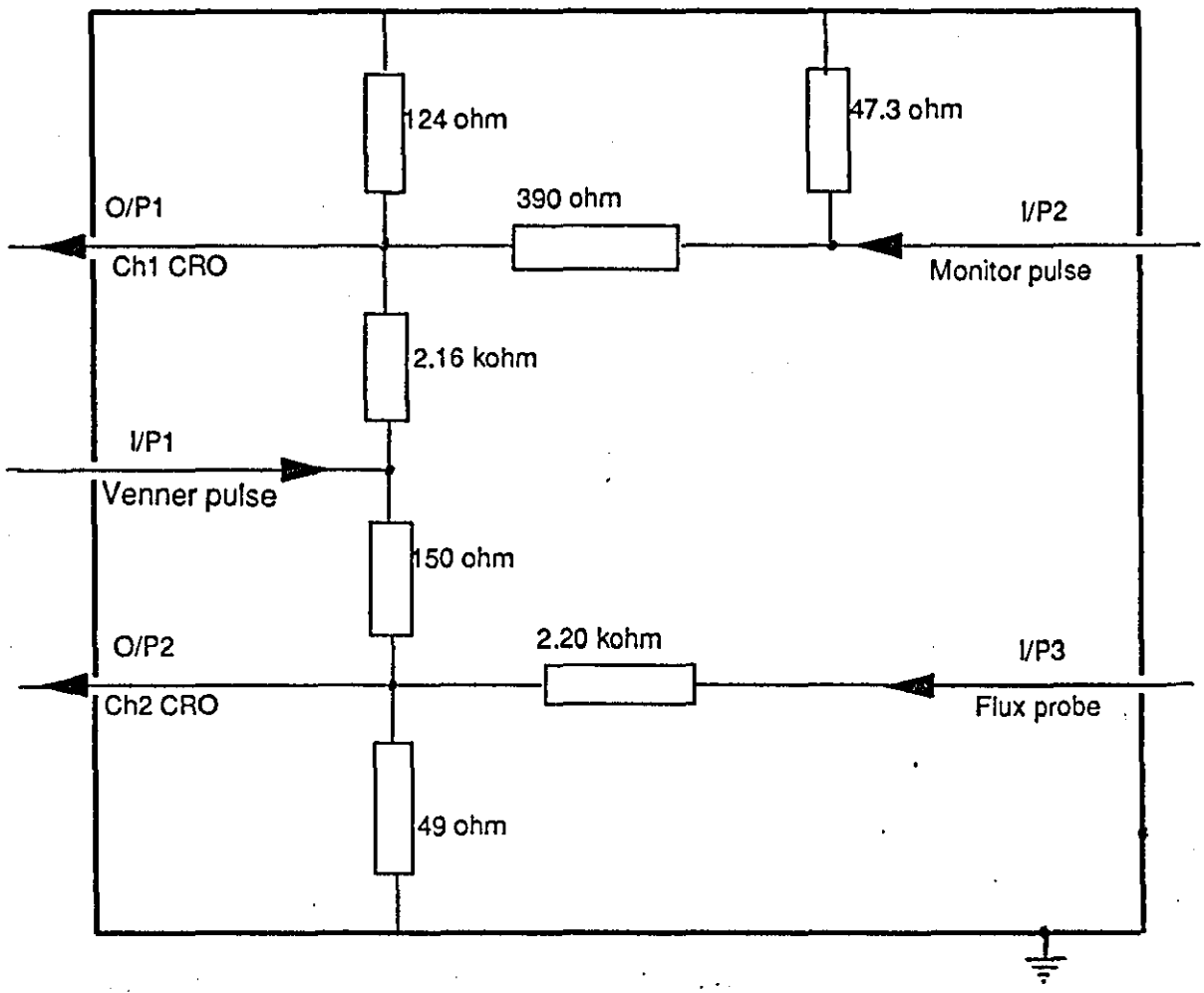

Figure (4.21) Circuit diagram of mixing unit.

CHAPTER 5
HIGH SPEED PHOTOGRAPHIC SYSTEM MEASUREMENTS

5.1 Xenon flash unit measurements

Figure (5.1) shows the present experimental set-up for the following measurements:

i) time constant of the flash unit,

ii) output duration, and

iii) the dependence of the intrinsic delay in the flash output upon the flash tube voltage and the triggering pulse amplitude. These measurements are essential for the best object illumination in the exploding wire experiments. A 9 V battery was used for triggering the flash.

5.1.1 Time constant

The time-constant of the charging capacitor circuit in the xenon flash source may be defined as the time required to reach 63.2% of the final charging voltage according to the charging equation of the capacitor circuit which is:

$$V = V_0(1-e^{-t/\tau})$$

where V is charging voltage at any time t, V_0 is the final voltage, and τ is the time-constant. To calculate the time-constant from this equation put $t=\tau$ which gives

$$V = V_0(1-e^{-1}) = 0.632\ V_0$$

This has been applied to find τ from Figure (5.2), which shows a plot of the voltage in kV as a function of time in seconds (readings being taken every 10 seconds). Table (1) shows results of several setting voltages.

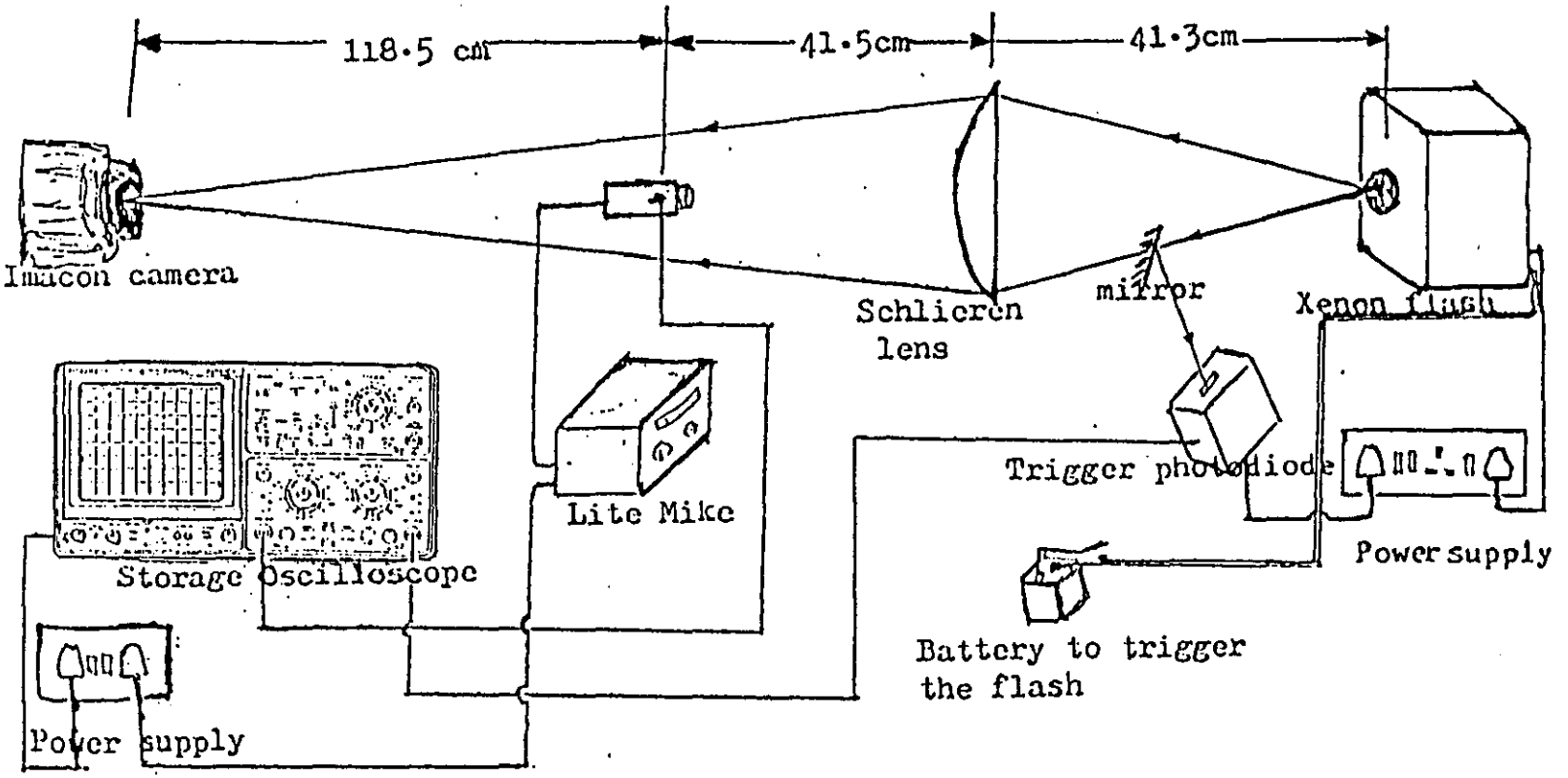

Figure (5.1) Block diagram of experimental set-up for flash output mesurements.

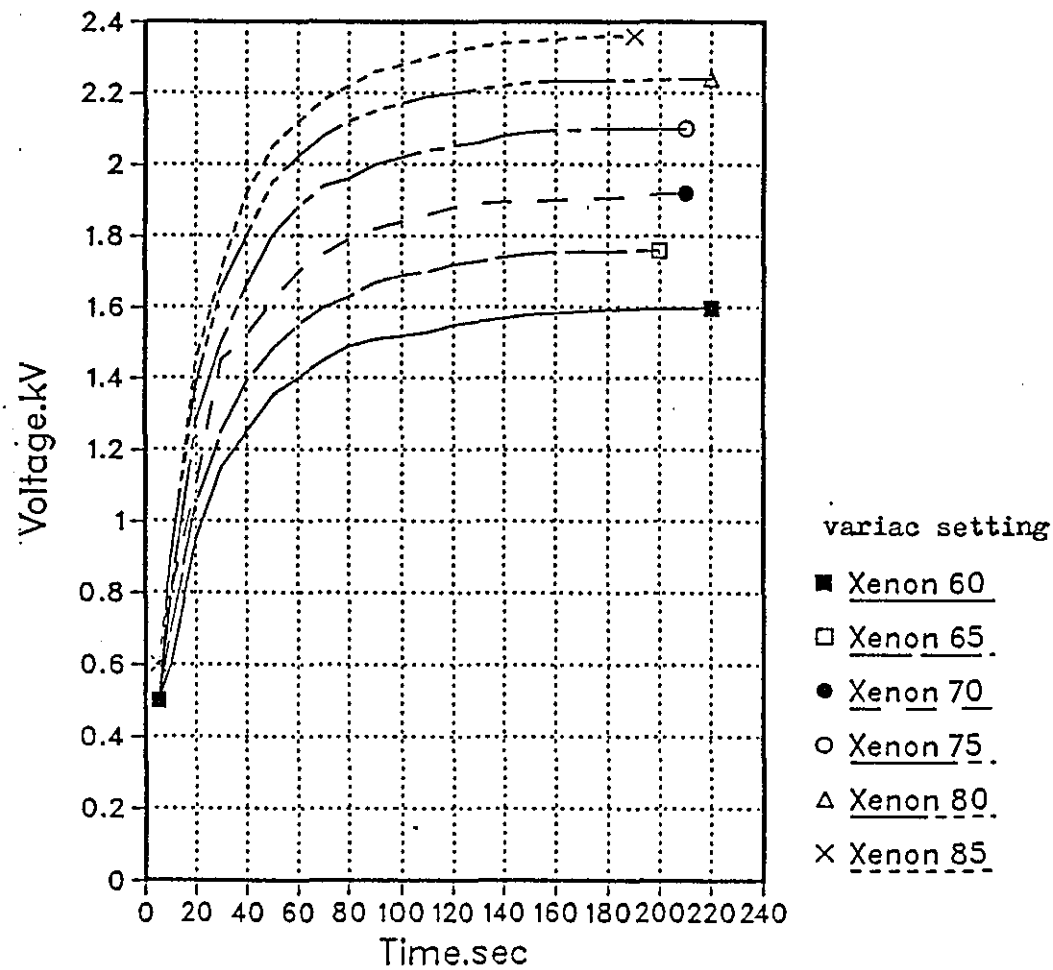

Figure (5.2) A plot of flash charging voltage against time.

Table (1)

Variac setting	V_0 (kV)	τ (+/- 0.05) s
60	1.60	26
65	1.76	25
70	1.92	25
75	2.10	25
80	2.25	24
85	2.36	24

5.1.2 Flash output

Flash output duration and delay measurements, which are required for the high speed photography system have been made by using the trigger photodiode and Lite-Mike detectors. From Figure (5.3) it is seen that the intrinsic delay between the trigger pulse to the flash unit and the output flash pulse recorded by the Lite Mike decreases as the xenon set voltage increases. The half peak duration increases to output 50 μs as the set voltage increases. The results are tabulated in Table (2).

Table (2)

Voltage (kV)	delay (μs.)	half-peak duration(μs)
1.25	103.1	26.0
1.50	35.3	28.0
1.75	27.0	31.2
2.00	15.5	35.0
2.30	12.0	45.0

The output pulse measurment at the input of the flash unit contains a small pulse of about 8 μs duration due to the battery trigger pulse followed by a large sharp pulse of 1.2 μs total rise time and 168 V amplitude. This large pulse is due to a pulse that is fed back from the input of the flash.

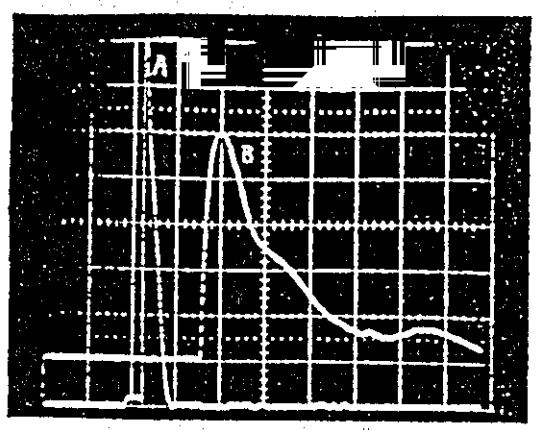

a) trigger pulse (A), Lite-Mike pulse (B), Horz: 20 μsec/div, Vert: 20 V/div (A), 5 V/div (B), flash voltage 1.5kV.

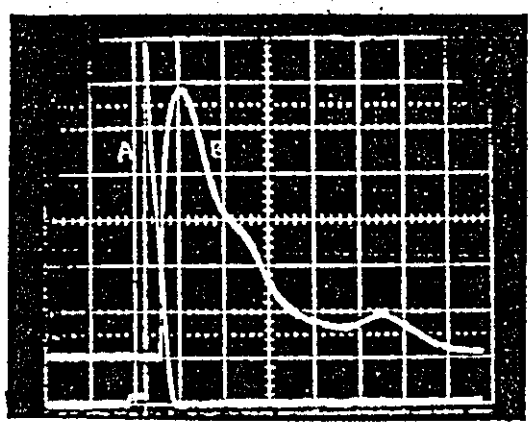

b) A, trigger pulse, B, Lite-Mike pulse, Horz: 20 μsec/div, Vert: 20 V/div (A), 5 V/div (B), flash voltage is 2kV.

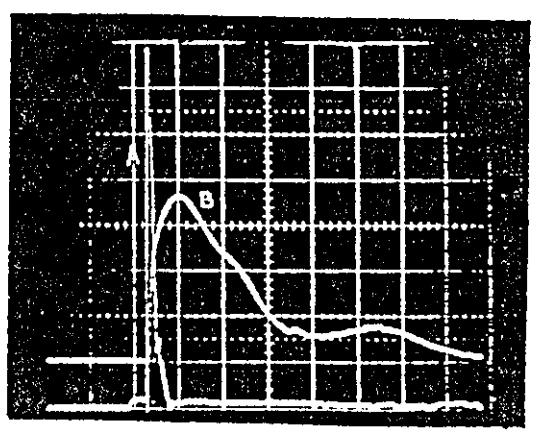

C) A, trigger pulse, B, Lite-Mike pulse, Horz: 20 μsec/div, Vert: 20 V/div (A), 10 V/div (B), flash voltage is 2.3kV.

Figure (5 . 3) Flash output at different setting voltages.

The delay measurements were taken between the beginning of the small pulse and the beginning of the output flash pulse recorded by the Lite-Mike detector. Ignoring the constant 8 μs duration of the small pulse, and starting from the sharp pulse, the results agree well with the manufacturer's stated delays for the xenon tube which is used in this flash unit.

The delay also decreases with increasing triggering pulse amplitude, which can be varied between 6 – 200 V by using different pulse generators instead of the battery like Farnell pulse generator or the output of the delay unit, which is 260 V or the pulse produced by the control unit which is 250 V.

5.2 Photodiode and opto–isolator trigger unit output

A trigger photodiode or an opto–isolator trigger unit are required to synchronize the camera with the flash unit.

Figure (5.4) shows the trigger photodiode output. This has an initial sharp part with a total rise time of 0.2 μs, 74 V height, and half peak duration of about 0.33 μs. This pulse is used for triggering the camera at a time such that the flash output reaches a suitable level to illuminate the object. The trigger delay of this depends however on the position of the photodiode with respect to the light source, so this can cause difficulty in triggering the camera at the right time when the light from the wire explosion is used. To avoid this, an opto–isolated trigger unit with the same output level and variable time–delay was designed to trigger the camera as described in Chapter 4.

The opto–isolator output and its triggering pulse from the Farnell pulse generator are shown in Figure (5.5) which shows that the intrinsic delay of this unit is 0.2 μs, the rise time is 0.3 μs, and the amplitude is +70 V peak.

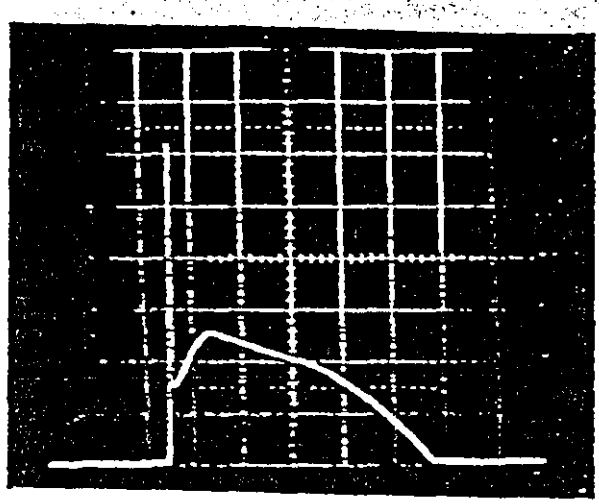

a) Trigger Photodiode pulse with flash voltage of 2kV.
Horz: 10 μsec.div, Vert: 10 V/div.

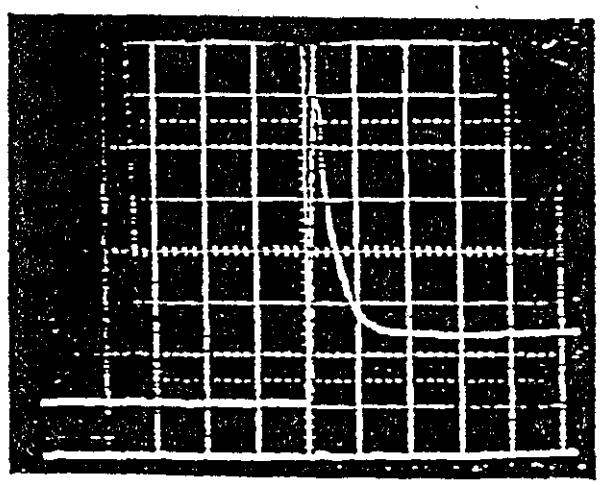

b) The first part of the photodiode pulse. Horz: 1 μsec/div,
Vert: 10 V/div.

Figure (5.4) Trigger photodiode output.

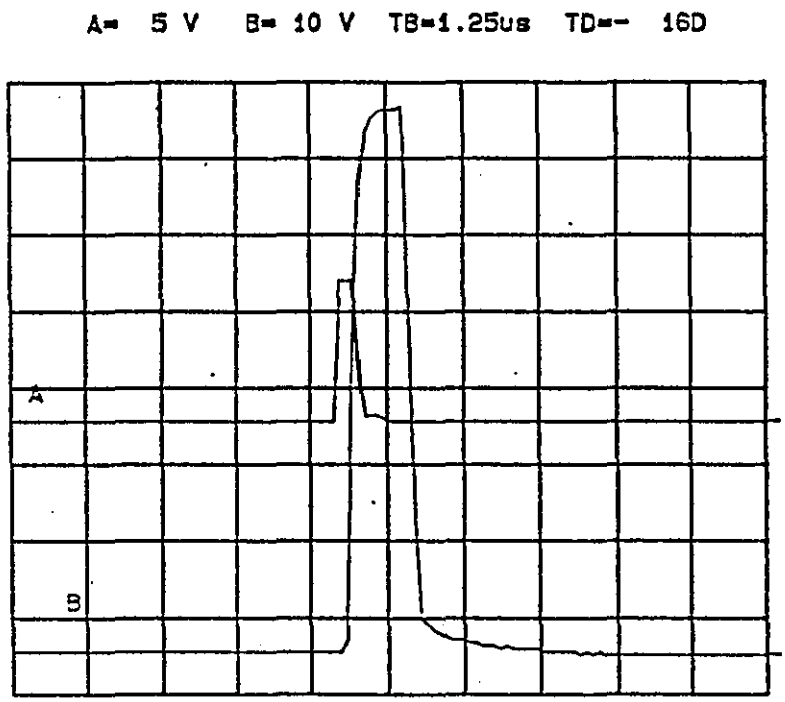

Figure(5.5) Opto-isolator output(B), and a trigger pulse(A).

5.3 High speed camera measurements

5.3.1 Time interval calibration and intrinsic delays

Figure (5.6) shows the calibration of the time interval between the photograph frames of the Imacon by using an output from a standard 1MHz crystal oscillator in a time counter unit. In this figure the upper traces show the monitor output of the Imacon camera. The monitor pulses are related to the frames 1, 3, 5, 7, 9 etc. The first and second monitor pulses are combined together in one large pulse in the case of 10^6 f/s framing rate. By comparing these monitor time intervals with the standard 1 MHz, the true frame interval was found.

From the trace of the 10^6 f/s framing rate, where the interval between the monitor pulses should be 2 μs, the measured time between the monitor pulses 1–3, 3–4, 4–5 etc are 2.33, 1.93, 1.93 μs etc respectively. Thus the true timing interval is 96.5% of the manufacturer's value for the plug–in which controls the framing rate in the camera. The delay in this unit between the triggering pulse (lower trace) from the opto–isolator and the first pulse of the monitor is about 450 ns as shown in Figure (5.7). The input impedance of the camera, which is connected in parallel with the CRO reduces the triggering pulse to a small pulse. The delay to the first picture is 595 ns as stated by the manufacture.

For the 5×10^5 f/s framing rate unit the time interval should be 4 μs between the monitor pulses but the measured values are 3.9 μs between 1–2, and 3.86 μs between each pair of the succeeding pulses, making the time interval 96.5% of the stated value for this plug–in unit. The delay to the first monitor pulse is 0.7 μs from the triggering pulse.

framing rate

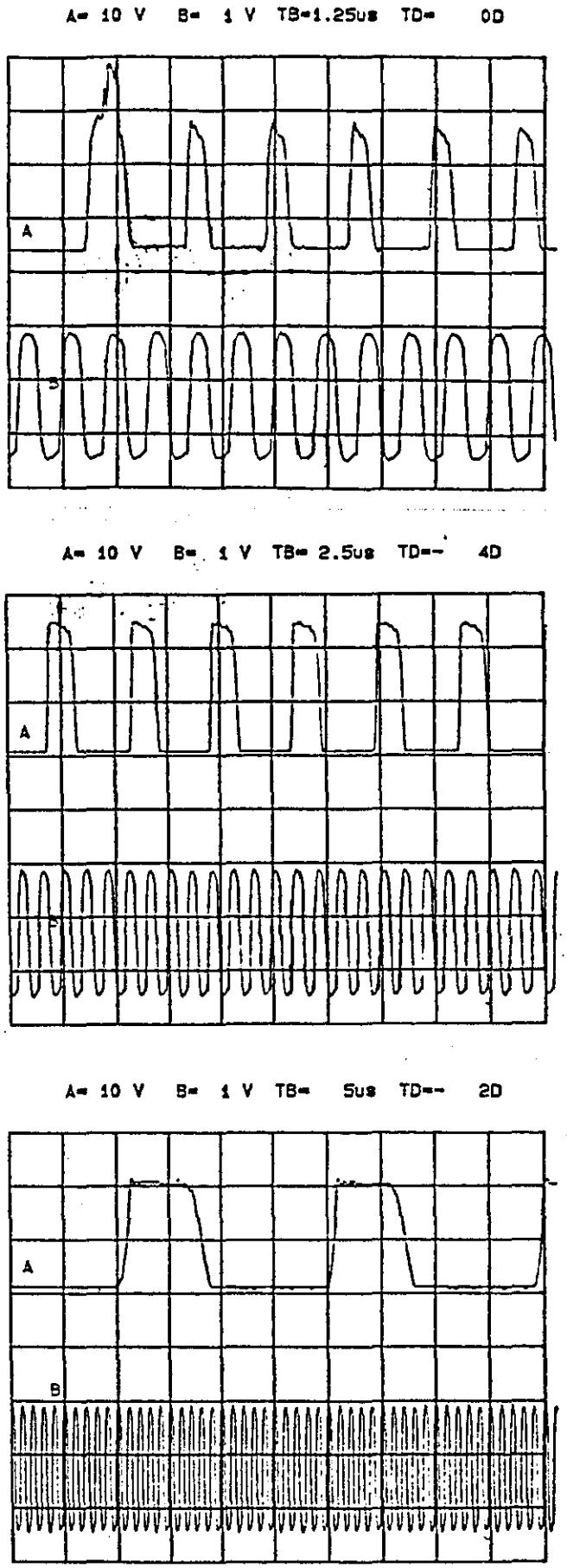

Figure (5.6) Monitor pulses of Imacon camera with crystal oscillator (1MHz) output.

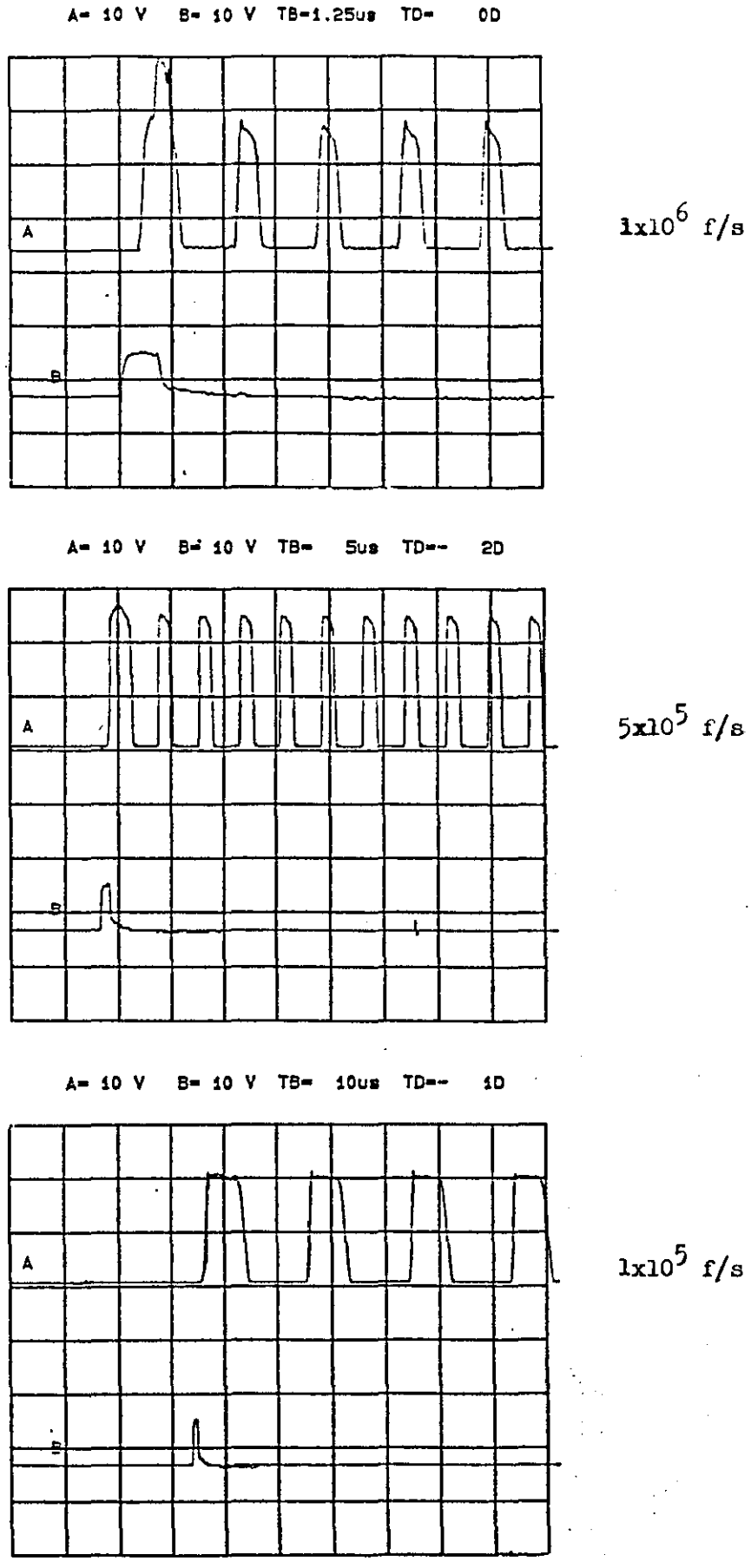

Figure (5.7) Intrinsic delay time of Imacon camera .

(A) Monitor pulses , (B) Opto-isolator pulse.

The framing unit of 10^5 f/s was checked, giving 20 μs interval between the first and the second monitor pulses, and 19.3 μs between each pair of the following pulses, making the time interval 96·5% of the stated value of this unit. The delay between the trigger pulse and the first monitor pulse is 1.7 μs.

5.3.2 Image size measurement and amplification

Figure (5.8) shows a photograph of a grid and wire, at the framing rate of 10^6 f/s, with the xenon flash at 2 kV by using (green + blue + black) filters in front of the objective lens of the camera. The distances are as following: lens–grid =32.5 cm, grid–camera=131.5 cm, and flash–lens =44 cm. The grid which is used is divided into centimetres, and each centimetre is subdivided into five divisions, each division equalling 2 mm. The field of view is 6.4 cm in the vertical direction and 4.4 cm in the horizontal direction. The measurements were taken of 4 cm in the vertical direction and 2 cm in the horizontal direction covering the middle of the field of view.

The magnification M is giving by:

$$M = \frac{\text{picture dimension}}{\text{actual dimension}}$$

which gives an equivalent magnification of 0.25. The overlapping was caused by the large number of frames in the photograph and the large field of view (a smaller field of view and/ or fewer frames would gives no overlap).

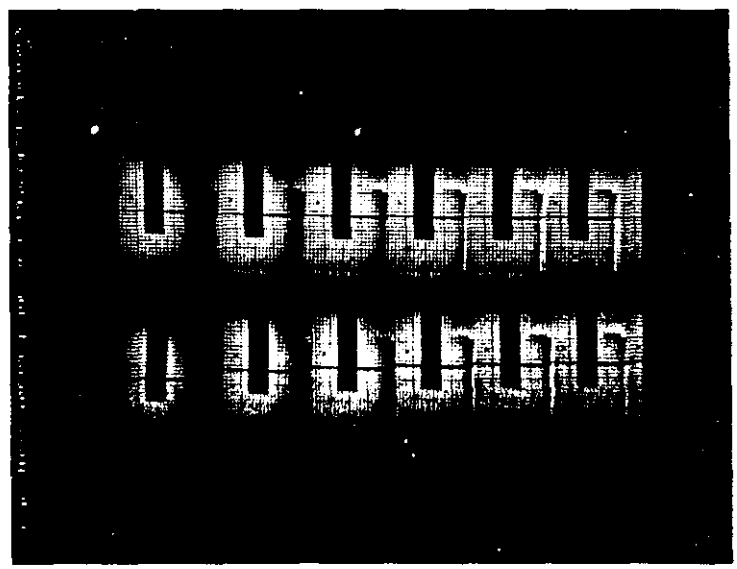

Figure (5.8) Calibration photograph for a grid and wire by Imacon high speed camera at framing rate of 10^6 f/s with xenon flash at 2 kV.

5.4 Synchronization measurements

In examining the oscilloscope traces of an exploding wire experiment several signals are seen which belong to different devices connected together and which operated at various times. Correct synchronization is required for a successful experiment. Figure (5.9) shows that the process starts working by using the signals from the control unit.

The control unit gives two pulses at the same time. One of them, of 250 V amplitude, triggers the E.H.T. pulse generator which then triggers the spark gap after a delay time of 20 μs. The second pulse of 6 V triggers both the Farnell and Venner pulse generators. This pulse is delayed by the pulse generators as required. It is delayed by 20 μs before it goes in the opto-isolator, 1 μs for the CRO reference pulse and the flash unit, and without delay to the CRO external trigger through the Farnell pulse generator.

As described previously, with a 2 kV operating voltage the flash unit has an intrinsic delay in its input circuit of 8 μs, and about 8 μs more to give the light output, so the total intrinsic delay is about 16 μs until the light output. Actual delay to reach the suitable flash output for photograph is 18 - 20 μs.

The intrinsic delay of the opto-isolator is 0.21 μs after the triggering pulse as shown in Figure(5.5), and the intrinsic delay of the camera with the framing unit of 10^6 is 0.47 μs compared with the manufacturer's value of 0.595 μs. Table (1) shows the various pulse values with the actual delays between the units.

Table (1)
The present pulses and delay settings.

pulse value	from	to	delay time(μs)	width(μs)
250 V	cont. unit	delay unit	0	——
260 V	delay unit	E.H.T.	20	——
20 kV	E.H.T	spark gap	0	——
6 V	cont. unit	Farnell p.g	0	1
6 V	cont. unit	Venner p.g.	0	1
23 V	Farnell	CRO.	0	5
10 V	Farnell	opto-isolator	20	0.3
80 V	Opto-isolator	camera (T1)	0.2	0.78
18 V	Venner p.g.	flash	1	5
18 V	Venner p.g.	mixing unit	1	5

Figure (5.10) shows the signals at the trigger input (a) of the xenon flash unit, and the monitor pulses (b). The first part of the signal (a) being the trigger pulse from the pulse generator (5 μs width). There is a clear delay between the trigger pulse and the monitor pulses of the camera, which is itself triggered by the opto-solator trigger unit directed towards the flash. The delay time between the initiating trigger pulse and the first monitor pulse is about 20.98μs. This delay is caused mainly by a combination of (i) the delay in the input circuit of the flash unit before a flash starts, (Al-maliky, Aug.1989), (ii) a delay of the opto-isolator to let the flash output reach its suitable level for photography. Also there is 0.47 μs delay between the opto-isolator pulse and the monitor pulse as shown in Figure (5.7). The opto-isolator trigger unit was used to trigger the camera instead of the trigger photodiode.

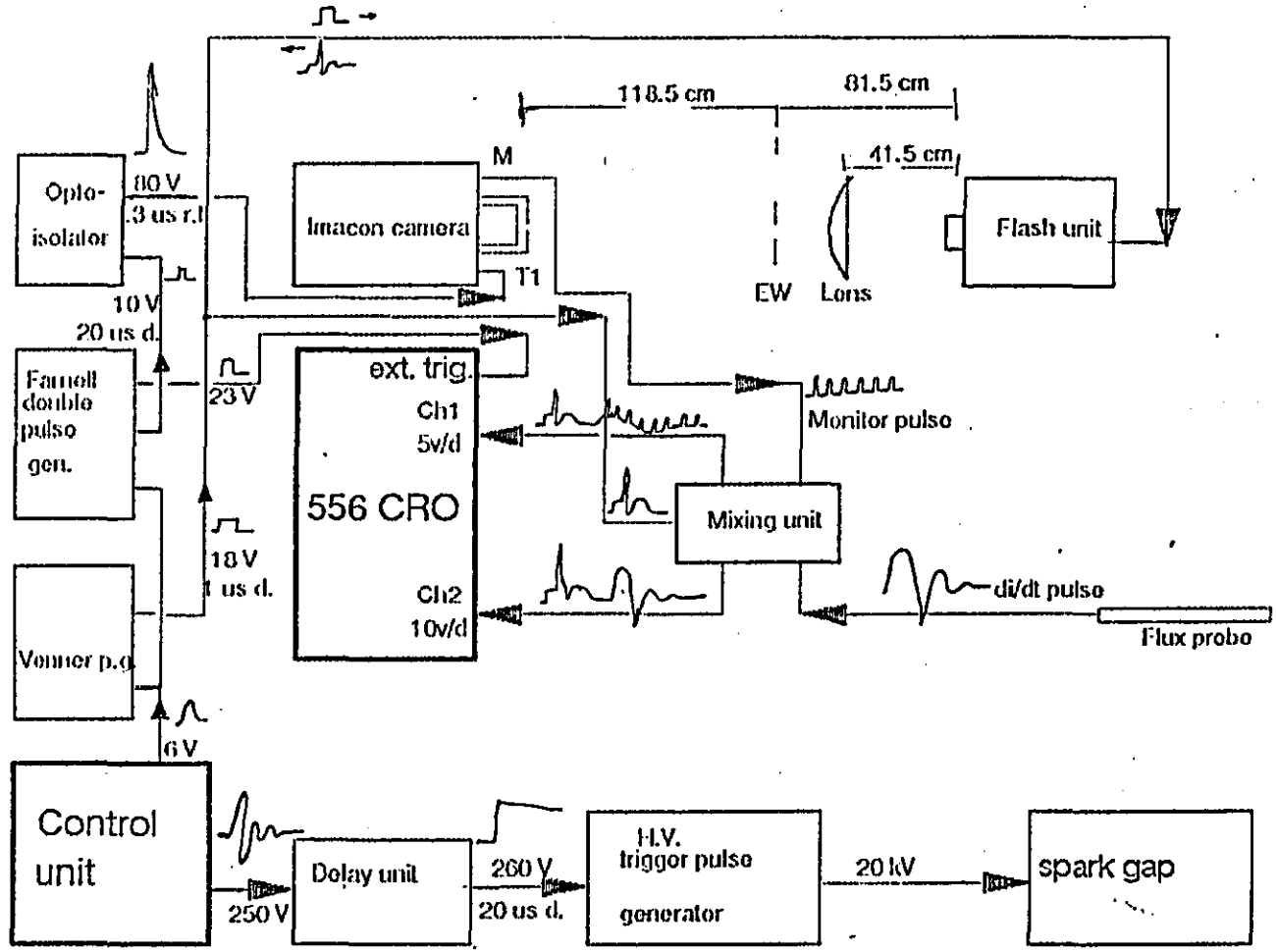

Figure (5.9) Block diagram for synchronization of exploding wire system.

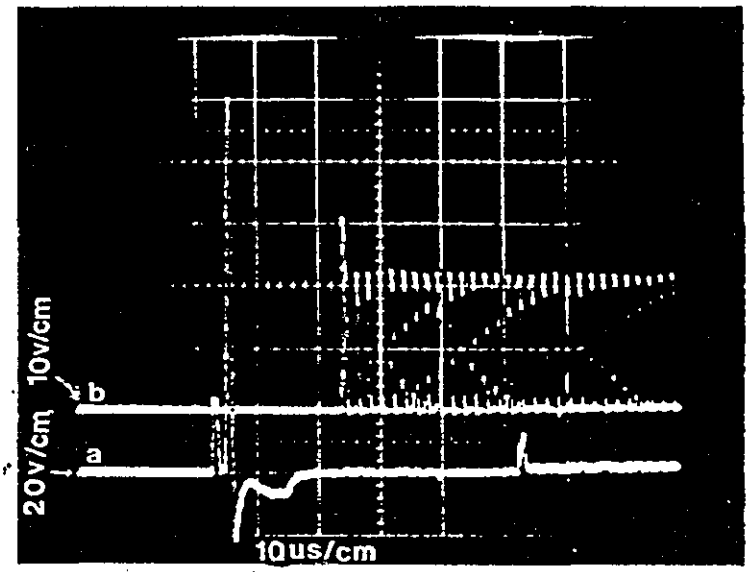

Figure (5.10) a, signals at the flash input
b, monitor pulses.

5.5 Discussion

Figure (5.2) shows that the charging of the xenon flash capacitors is initially fast but when the voltage reaches about 63.2% of the final value, the rate is much slower. The time for the flash unit to be ready to give its full illumination is then > 25 sec.

The half-peak output duration of the flash unit has been measured as 50 μs, which agree with the specification of 50μs.

The Imacon camera is designed to be triggered by a short rise time pulse. This pulse has been obtained using a trigger photodiode or an opto-isolator, the latter being better because of the easy variability of delay time, and the stability of its output level.

Image size measurements of a grid placed where an exploding wire would later be situated were made to calibrate the optical magnification of the camera. There was no difference in the magnification in any direction.

Measurements of true framing intervals are required to give accurate measurements of blast wave velocity and energy, which are related directly to the time intervals between the frames. The calibration showed that the framing intervals were about 4% lower than stated on the camera. Velocity and blast wave energy would then be significantly higher than the values using the manufacturer's data.

The measurements described in this chapter are all essential pre-requistes for the application of this system, as in the next chapters.

CHAPTER 6
EXPLODING WIRE MEASUREMENTS

6.1 Electrical characteristics of the exploding wire circuit

Figure (6.1) shows the present set-up of the complete system for measuring the exploding wire (EW) circuit characteristics by using a thick copper wire. This system as described in Chapter 5 includes a control unit which controls the charging and discharging of the bank as well as triggering the other devices. Three delay units are used to trigger the E.H.T trigger unit, the flash, opto-isolator, and the ocsilloscope. The opto-isolator, flash and the camera are not used in measuring the electrical characteristics of the EW circuit.

The basic electrical characteristics of an exploding wire circuit have to be measured using a thick wire which does not explode, ie. one for which the energy input is insufficient to cause melting and vaporisation. The basic circuit and its typical current waveform are shown in Figure (6.2).

In discharging the capacitor through the wire, the circuit may be assumed to behave as an RLC circuit where R is the total resistance of the circuit including the exploding wire as a load, L is the total inductance, and C is the capacitance.

Assuming (Stewardson 1984) that the effect of the transient process can be ignored after the first half cycle, and that

$$R_T^2 \ll 4L_T/C \quad ,$$

the time expression for the discharge current i is then a lightly damped sine wave as in the following equation :

$$i = Ae^{-\alpha t}\sin\omega t$$

where $\omega = (L_T C)^{-\frac{1}{2}}$

$\alpha = \dfrac{R_T}{2L_T}$, the damping factor

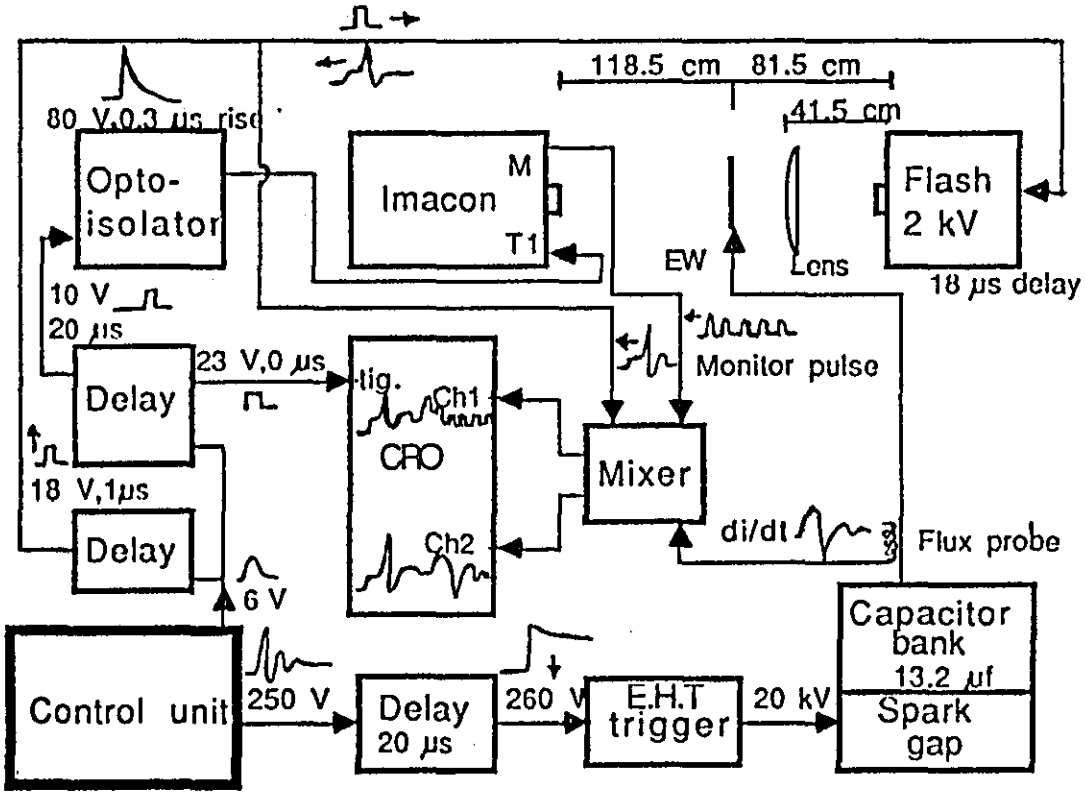

Figure (6 . 1) Block diagram for the exploding wire operating system.

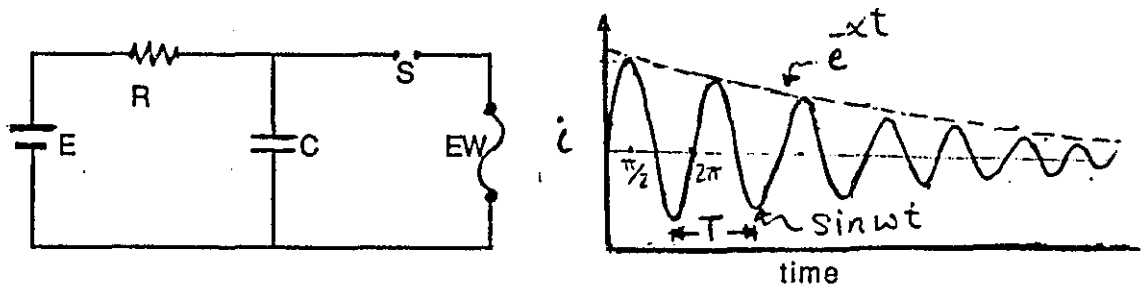

Figure (6.2) Basic diagram of discharge circuit of exploding wire with its typical output.

$T = \frac{1}{f}$, the period

$\omega = 2\pi f$ frequency

L_T = total inductance

R_T = total resistance of the discharge path

C = bank capacitance.

By differentiating the equation for i and putting the initial condition ($di/dt = V_0/L_T$ at t=0) to find A gives:

$$i = V_0 (\frac{C}{L_T})^{\frac{1}{2}} e^{-\alpha t} \sin\omega t$$

where V_0 is initial bank voltage.
Assuming $e^{\alpha t} = 1 + \alpha t$ for $\alpha t < 0.34$ the equation can be simplified to give values accurate to within 5%. It is then reduced to be (Stewardson 1984):

$$i = \frac{V_0 (\frac{C}{L_T})^{\frac{1}{2}} \cdot \sin\omega t}{[\ 1 + (\frac{R_T}{2L_T})t\ ]}$$

and $i_{max} = V_0/(\pi R_T/4 + (L_T/C)^{\frac{1}{2}})$, where $\omega t = \pi/2,\ 3\pi/2$, etc.

To obtain the constants of the discharge circuit, the period and ratios of the peak values of the output waveform of the inductance flux probe (lower trace in Figure (6.3)) were measured and used in the above equations to get L_T, α, and R_T.

The waveform of di/dt contains two functions of time which are the $\cos\omega t$ that causes the cosine wave oscillation, and the exponential function $e^{-\alpha t}$ that causes the decay in the signal. Assuming the exponential function is

$$V_p = a\ e^{-\alpha t}$$

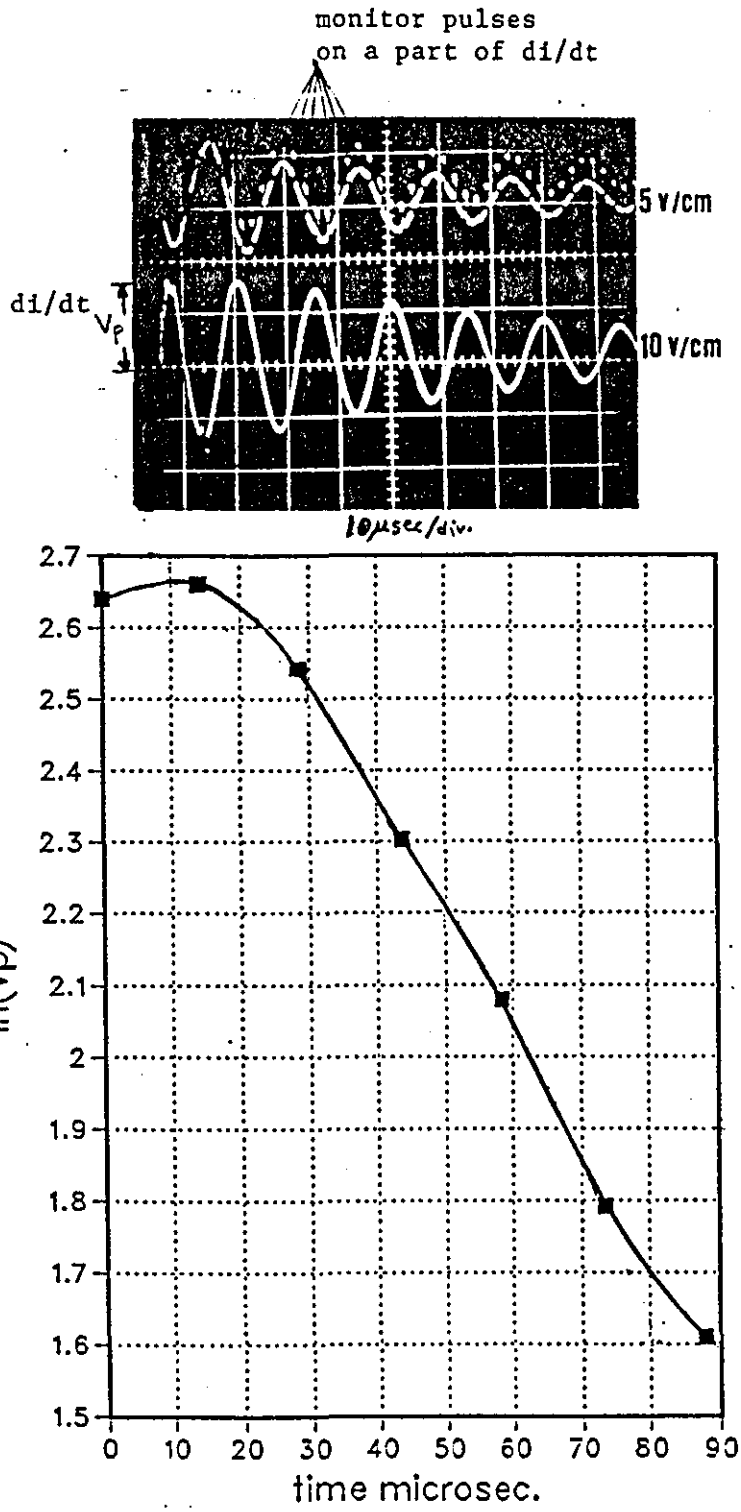

Figure (6.3) CRO record of di/dt (lower trace) and a part of di/dt (upper tace), and ln(Vp)-time plot to measure the damping factor of capacitor discharge, at 20 kV discharged through 16cm long copper wire with 6.3 mm diameter.

then $\ln(V_p)=\ln(a)-\alpha t$

and the slope of $\ln(V_p)$ versus time t equals $-\alpha$, the damping factor of di/dt.

A thick copper rod with diameter of 6.3 mm, and 16 cm length was used as a low resistance load to the bank. The rod was clamped directly into the electrode holders. Figure (6.3) shows a CRO record for di/dt waveform (lower trace) from the bank discharge at voltage (V_0) of 20.107 kV. The upper trace is a part of the di/dt picked up by the mixer unit, and monitor pulses appear on this signal. The di/dt signal is attenuated by the ratio of 47. A graph of $\ln(V_p)$ against time is also shown in Figure (6.3).

From the record
period T = 14.5 μsec .
frequency f = 68.62 kHz
$\alpha = 1.570\times10^4$ s^{-1} damping factor (from the graph)
L_T = 407.5 nH total inductance obtained from $2\pi f=(L_TC)^{-\frac{1}{2}}$, where C=13.2$\mu$F
$R_T = 2L_T\alpha = 0.0127955\ \Omega = 12.79\ m\Omega$
m = 8.74 nH mutual inductance obtained from

$$m = \frac{4\pi NA}{W}\times10^{-7}$$

(where from design the number of turns N=150, cross section of the coil A with diameter of 3 mm, and width of the strip line W=15.25cm)

$$di/dt=\frac{V_p}{m}=8.01\times10^{10}\ \text{amp/s}$$, where V_p=14×47 V=658 V the first peak.

To calculate i_{max}, i, and V_L(the voltage across the load) the following expressions were used:

$$i_{max} = V_o(C/L_T)^{\frac{1}{2}}\, e^{-\alpha t}, \text{ which gives } I_{max}=114.44 \text{ kamps}$$

$V_L=V_o e^{-\alpha t}(1-L_B/L_T)$, where L_B is the bank inductance (20 nH from the manufacturers).

$\therefore$ $V_L=19.12$ kV at t=0, and 20 kV bank voltage.

At t_0, the first peak, $di/dt = 8.01\times10^{10}$ amp/s from $di/dt=V_p/m$. The second +ve peak ($t=14\mu s$), $di/dt_{2\pi} = 8.18\times10^{10}$ amp/s, and the third peak ($t=28.6\mu s$), $di/dt_{4\pi} = 7.26\times10^{10}$ amp/s. So the first peak is smaller than the second one .

In the case of a damped sine wave discharge current through a thick-wire, if the dynamic circuit resistance is larger than the steady-state value by a factor of 2.5 in the first quarter-cycle, the first current peak will be too low by 25% (Bennet 1962). It follows that a higher average resistance over a shorter time interval can accomplish the same result.

6.2 Blast wave measurements

To produce blast waves a thin copper wire was used as a load in the high voltage capacitor discharge. The wire explodes rapidly when the discharge current passes through and produces a cylindrical blast wave pushing the vapour symmetrically outside with it. By using the Schlieren method, this blast wave could be photographed by the Imacon high speed camera to show the fast expansion of the wave.

For calibrating the time interval and the synchronization of the system, the corresponding CRO records were used. A typical CRO record is described in Figure (6.4).

6.2.1 Blast wave velocity

Blast wave velocity measurement is desirable in exploding wire applications (Dirwish 1979), since it enables a theoretical determination to be made of the pressure produced by a wire explosion inside a hollow cylinder. This method involves the measurement of the shock front with respect to radial distance. This is facilitated by the large and rapid change in pressure, density, and temperature associated with the shock front (Ahmad 1988). Voltages of 20, 25, and 30 kV have been used to explode copper wires of sizes 22 and 24 swg (standard wire gauge) of diameters 0.71 and 0.559 mm respectively. The lengths of the wire used were 8 and 13cm.

The measurements were made by measuring the increasing diameter of blast wave fronts from high speed photographic records. High speed photographic records of typical exploding wires together with their corresponding oscillograms are shown in Figures (6.5) to (6.10). Graphs of radii of the shock fronts versus time have been drawn for each wire. The corresponding oscillogram includes two traces, the lower one showing from left to the right the reference pulse from the Venner pulse generator, a large pulse from the flash, and the di/dt pulse from the flux probe. The upper pulse contains extra pulses which are from the camera monitor placed on the part of di/dt pulse which is picked up by the mixer unit. Monitor pulses are used for calibrating time intervals of high speed photographs, as shown in Figure (6.4).

The blast wave velocity is obtained by calculating the slope of radius–time graph. This has been done by drawing tangents to the graph at various points or by differentiating a polynomial equation which is fitted to this graph; both methods give the same results. Figures (6.11 to 6.16) show velocity versus radius plots which will be discussed later.

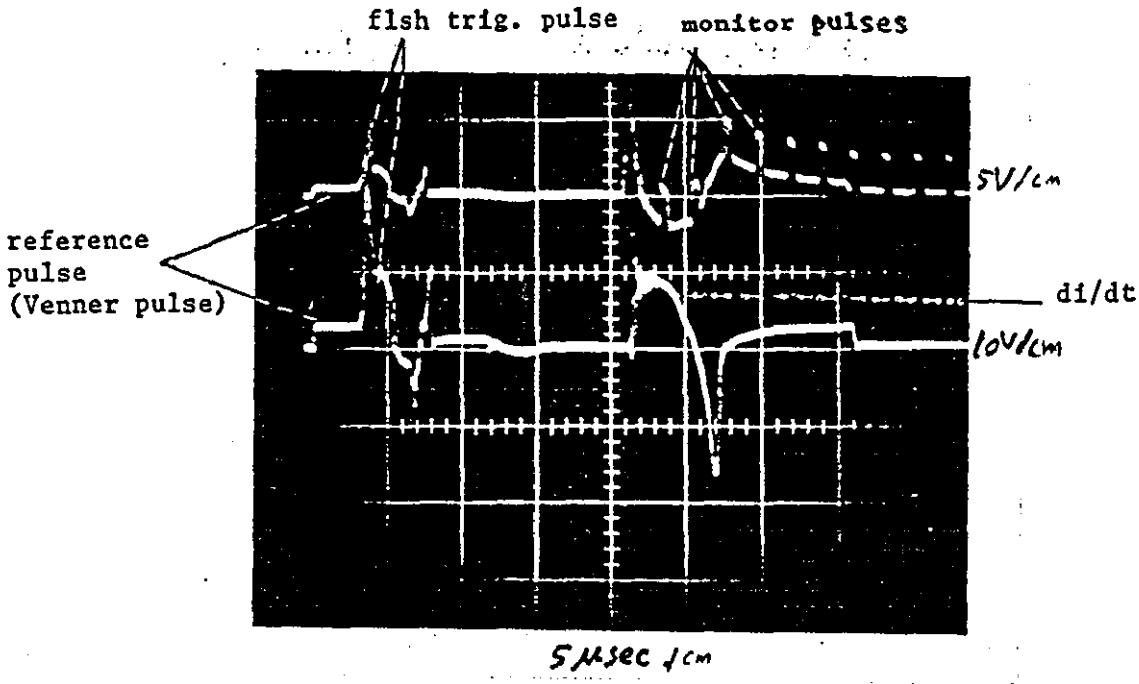

Figure (6.4) CRO record for an 8cm/22swg exploding wire at 20 kV.

The cylindrical blast wave generated by a wire explosion has a Mach number (M) which can be calculated by dividing the wave velocity by the sound speed in air at room temperature, e.g. the sound speed is 345 m/s at 20 ^{0}C. High speed camera times were calibrated as in Chapter 5 to give the exact time intervals, which are 0.96 μs for 1μs– camera interval, and 1.96 μs for 2 μs camera interval. Using this calibration the result Tables (1), and (2) show the true calibrated results of the measurements.

6.2.2 Calculation of blast wave energy

Strong blast waves from wire explosions were treated theoretically by Lin (1954), who established a relation between the time and position of the cylindrical shock wave front as shown in the following formula:

$$t = \frac{1}{2} \left(\frac{B\rho_0}{E}\right)^{\frac{1}{2}} R^2$$

where t is the time, R is the distance from the explosion to the shock front, ρ_0 (=1.205 kg.m^{-3} at 1 atm, 20 ^{0}C) is the density of air ahead of the shock, E is the energy in the explosion per unit length, and B is a dimensionless energy parameter of constant value 3.94 for air, dependent on γ, the ratio of specific heats. Therefore, a linear relationship between t and R^2 is predicted. The conditions for the validity of the above equation are :

1) the energy is assumed to be suddenly released and the shock disturbance is similar at all times,

2) the gases are supposed to be perfect with constant specific heat ratios, and

3) the energy losses from ionization and radiation are neglected.

Shock wave data corresponding to the 22 and 24 swg wires have been fitted to the Lin equation by plotting R^2 versus time, and then the best straight line after about 6 μs (linear R^2-t relationship) was selected graphically that has a slope m equal to:

$$m = \frac{R^2}{t} = 2\left(\frac{E}{B\rho_0}\right)^{\frac{1}{2}}$$

From the slope the axial energy E (joule per unit length) can be obtained.

Typical examples of R^2/t plots in the present study are shown in Figures (6.17 to 6.22), which will be discussed later. From these figures can be seen that the early part of the graphs show a slow rise in R^2, and indicates that as the wire explodes, 2 – 6 μs elapse while energy is being fed into the explosion before the shock front reaches its maximum velocity. Therefore, the shock wave behaviour accords with blast wave theory after this initial period.

6.2.3 Determination of the efficiency of the exploding wire

The highest velocity of the blast waves produced by the wire explosions usually corresponds to the highest energy transfer process from the capacitor. For 30 kV the stored energy in the 13.2μF capacitor is 5.94 kJ with the discharge current reaching its peak after about 3 – 5 μs as shown in the CRO records (e.g. Fig(6.9), Fig(6.23c), and Fig(6.27c)). The 13cm/24swg wire requires about 1.72kJ to be vaporized (Stewarson 1984), which means that vaporization and blast wave formation are so rapid that only part of the stored energy is available for the formation of the blast wave. The energy needed for vaporization depends on the wire material and its diameter. The 13cm/22 swg wires need 2.7 kJ for complete vaporization. Therefore, the blast wave formation for the 22swg wire occurs later than for the 24 swg in the discharge process. The 24swg wire gives the highest velocities and highest blast wave energies as

shown in the velocity/time and R^2/time graphs. For wires of greater diameter, more of the energy is used for vaporization, such as in 22swg wire which requires 2.7 kJ, leaving less energy to energize the blast wave. From the di/dt signal in the corresponding CRO records, at 20 kV there is only a small residual current in the circuit as indicated after the negative peak of di/dt. At the higher voltages (e.g. Fig 6.7) greater energy in excess of vaporization energy is supplied. The current then will continue to pass through the plasma under 're-strike' conditions as described in Chapter 2. The plasma has a low resistance and the circuit behaves as an LC circuit.

The explosion efficiency can be defined as the ratio of the output energy (blast wave energy) to the input energy from the capacitor. The blast wave energy can be found by the theory of strong blast waves (Sakurai 1965 and Lin 1954) as described before in Section (6.2.2). Graphs of R^2 versus time give the output energy of the blast waves. The input energy is $(CV^2/2)$, where C and V are the bank capacitance and voltage respectively. Tables (1) and (2) show the results for 24 and 22 swg wires with 13 and 8 cm lengths respectively by applying 20, 25, and 30 kV.

6.2.4 Pressure determination

The pressure generated on the inside wall of cylindrical specimens is that due to the reflected shock wave (Dirwish 1979). The peak pressure can be determined from blast wave theory. The reflected pressure can be obtained by knowing the Mach number (as in Section 6.2.1) and by applying standard plane shock wave theory (Gaydon and Hurle 1963). However at the high temperatures associated with the reflected shock wave at high Mach number air does not behave as an ideal gas.

Figure (6.34) shows the theoretical curves of reflected shock pressure as a function of Mach number of the incident shock for air as a real gas taking into account changes in γ caused by vibration and dissociation (Law and Bristow 1969). Another method can be used for measuring the reflected pressure directly, e.g. by using a piezoelectric pressure probe which measures the pressure from the wave reflection off the inside of a cylinder placed symmetrically around the wire. Such a probe, as shown in Figure (6.35) (Griffiths et al 1986), consists mainly of a piezoelectric crystal sandwiched between two high strength stainless steel bars. The wave transit-time of about 0.1 μs through the crystal ensures a fast response while the steel bars reduce radial oscillation (Parry 1988). The bar system is enclosed within an earthed brass housing which reduces the electromagnetic noise to a low level. Such direct measurements of pressure have not been made in the present work.

6.2.5 Electrode and effects

Figure (6.32) shows a plot of the propagation of the shock wave between the electrodes around the exploding wire. The photographs in Figure (6.31) show that the wave front is not plane near the holders which were flat ended. The small ripple in the graph is because of the small different in the timing of the two shots. The shots were taken by applying 20 kV to 24 swg wires with lengths of 8 cm, and photographed from the right and the left sides of the wire.

During photographing the shock waves near the ends of the wire holder two features have been seen. These are the effect of shape of holder end on the shape of the shock wave front, and the short spark which starts before the explosion takes place. If the same voltage is applied to the exploding wire, but with a variation in the shape of the holder, differences clearly appear in the end of the shock wave between the exploding wire and its holders. The shock wave front has curved edges with different radii corresponding to the different

shapes of holder as shown in Figure (6.33). The best cylindrical shock wave front is given by the wire holder with the hemispherical shaped end. To reduce the effect of the holder shape slightly, high voltage would be applied to give a cylindrical shock wave. The second feature is the short spark which starts about 1 μsec before the explosion. It causes a spherical shock wave faster than the cylindrical shock wave, which then decays quickly. The first time it was observed, it was not clear if it was because the melting point of the soft solder is less than of the copper. The shot was repeated several times and gave the same result.

Hard silver brazing solder, less hard brazing solder , aluminium metal, and the soft ordinary solder (multicore 60/40 tin/lead alloy solder with melting point of 188 ^{0}C) were then used to connect the exploding wire into the holders. All gave the same little circular spark before the expansion takes place. The only difference between them as shown in Figure (6.33) (records 3, 4, and 5) is that the spark starts 1 μsec earlier for the aluminium with respect to the brazing solder, and in the soft solder it starts earlier than in aluminium. It is clear that the occurrence of the spark is related to the fact that the solder melts and vaporises before the copper: the harder the solder the more time is required before melting. The melting points of silver brazing , aluminium, and ordinary soft solder are about 1230, 930, and 460 ^{0}K respectively. The intense electric field at the end of an electrode will then generate a spark at a time which depends on the solder. The resistance of the contact region of the wire with solder and the solder with the holder may be added to the previous reasons.

6.3 Discussion

Figures (6.5) and (6.6) show photographs of the explosion and the corresponding CRO records of syncronization and calibration signals. Graphs of distance versus time are also shown. The experiments were done by applying a 20 kV voltage to explode 24 swg and 22 swg copper wires of 13 cm length. The photographs were taken by the Imacon high speed camera with a nominal 1 μs interval. All the graphs use the nominal time intervals. The true time intervals, however, were used for subsequent calibration. The graphs give a maximum velocities of 3.16 and 2.1 km/s (max. M. no. of 9.2 and 6.1) for 24 and 22 swg wires respectively as shown in Figures (6.11) and (6.12). This means the 22 swg wire produces slower blast waves than the 24 swg because the 22 swg wire requires more energy for vaporization leaving less energy to energize the blast wave.

Figures (6.7) and (6.8) show the photographs, corresponding CRO records as well as graphs of the radial expansion of the blast waves from 24 and 22 swg wires exploded at 25 kV giving maximum velocities of 4.14 and 3.58 km/s respectively, as shown in Figures (6.13) and (6.14).

Figures (6.9) and (6.10) show photographs and graphs of the radius against time of 24 and 22 swg wires exploded at 30 kV. These give maximum blast wave velocities of 4.58 and 4.08 km/s respectively, as shown in Figures (6.15) and (6.16). The velocity plots versus radius show that the blast velocity goes up quickly to reach a maximum vlaue and then decays slowly.

Figures (6.17), (6.18), and (6.19) show plots of R^2 versus time for exploding wires with conditions of 24 swg and 13 cm length exploded at 20, 25, and 30 kV. Calculations from these graphs give blast wave energies of 102.43, 156.94, and 211.07 J/cm respectively. The same voltages were applied to 22 swg wires. The graphs of R^2 against time

are shown in Figures (6.20), (6.21), and (6.22) and give blast wave energies of 54.2, 101.82, and 133.08 J/cm respectively.

In addition 8 cm long wires were used to generate blast waves by using 20,25, and 30 kV to explode the wires. Figure (6.23) shows the photographs and CRO records for 8 cm/24 swg exploding wires at the above voltages. The photographs show that at higher voltages, the wire exploded faster. Also at 30 kV the vapour emits light because of the high energy which it receives after re-strike.

Figure (6.24) shows graphs of radius versus time of blast waves generated by the above voltages applied to 24 swg wires. Maximum velocities of 4.42, 4.90, and 5.03 km/s respectively are achieved as shown in the velocity versus radius plots in Figure (6.25). The slope of graphs of R^2–time as shown in Figure (6.26) are 120×10^4, 167×10^4, and 152×10^4 cm^2/s for 20, 25, and 30 kV respectively to give efficiencies of 51.85, 64.48, and 37.31 per cent.

Figure (6.27) shows photographs and CRO records for 8 cm/22 swg wire at 20, 25, and 30 kV, while Figure (6.28) shows the corresponding radius versus time plots. These plots give maximum velocities of 3.10, 4.04, and 4.95 km/s respectively as shown in Figure (6.29) (Mach no. of 9.01, 11.73, and 14.36). The photographs and the corresponding oscillograms give a good guide of the start of the bursting of the wire which coincides with the maximum negative value of the di/dt pulse.

Figure (6.30) shows the graphs of R^2–time for 22 swg wires exploded at 20, 25, and 30 kV from which it can be seen that the slope increases in accord with increasing applied voltage. Efficiencies of 29.3, 29.5, and 41.6% respectively are produced. The results are tabled in Tables (1) and (2).

Table (1)

Shock wave results from 13cm exploding wire.

Print no.	swg	D (mm)	Voltage (kV)	Max. v (km/s)	Temp C	Max. M no.	Slope 10^4 (cm^2/s)	Output energy (J/cm)	Input energy (J/cm)	Eff. (%)	Max. refl. pressure (kbar)
72	24	0.559	20.0	3.18	20	9.25	91.2	98.6	203.1	48.5	0.92
73	=	=	=	3.17	=	9.24	88.5	92.8	=	45.8	0.92
75	=	0.55	=	3.04	21	8.82	91.3	98.9	=	48.7	0.82
77	=	0.54	=	3.17	=	9.15	92.6	101.7	=	50.0	0.89
78	=	=	=	3.10	20	8.93	92.2	100.9	=	49.6	0.84
86	=	0.549	25.0	4.13	22	12.00	114.6	155.8	317.3	49.1	1.78
89	=	0.55	=	4.38	=	12.73	118.9	167.8	=	52.9	2.09
92	=	0.54	30.0	4.56	24	13.19	132.9	209.6	456.9	45.9	2.31
79	22	0.692	20.0	1.40	=	4.04	62.6	46.5	203.1	22.9	0.12
83	=	0.678	=	2.10	25	6.07	67.3	53.8	=	26.5	0.35
84	=	0.700	=	1.45	=	4.20	44.1	23.0	=	11.3	0.14
85	=	0.694	25.0	3.57	21	10.37	97.5	112.9	317.3	35.6	1.22
88	=	0.699	=	3.14	=	9.14	112.2	149.4	=	47.1	0.90
90	=	=	30.0	3.67	=	10.67	127.7	193.7	456.9	42.4	1.31
91	=	0.702	=	4.06	22	12.34	127.5	193.0	=	42.2	1.92

Table (2)

Shock wave results from 8cm exploding wire.

Print no.	swg	D (mm)	Voltage (kV)	Max. v (km/s)	Max. M no.	Slope x 10^4 cm^2/s	Output energy (J/cm)	Input energy (J/cm)	Eff. (%)	Max. refl. pressure (kbar)
94 a	24	0.54	20.0	4.85	14.12	115.8	159.2	330.08	48.2	2.79
97 a	"	0.534	"	3.84	11.14	116.5	161.2	"	48.8	1.46
98 b	"	"	"	4.82	13.87	121.6	175.6	"	53.2	2.66
100 c	"	"	"	4.65	13.43	119.4	169.2	"	51.3	2.43
103 d	"	"	"	4.42	12.84	119.4	169.4	"	51.3	2.14
105 c	"	"	"	4.97	14.45	124.0	182.5	"	55.3	2.98
116 g	"	"	"	4.39	12.74	106.6	154.0	"	46.7	2.10
117 f	"	"	"	4.37	12.67	118.6	166.9	"	50.5	2.10
118 e	"	"	"	4.27	12.38	113.2	152.1	"	46.1	1.94
99 b	"	"	25.0	5.01	14.52	137.8	225.5	515.64	43.7	3.02
107 c	"	"	"	5.09	14.76	131.4	205.0	"	39.7	3.17
119 e	"	"	"	4.90	14.19	166.5	329.1	"	63.8	2.83
120 e	"	"	"	4.63	13.45	168.2	335.9	"	65.2	2.44
112 c	"	"	30.0	5.71	16.56	144.8	248.9	742.42	33.5	2.40
113 c	"	"	"	5.03	14.59	151.9	274.2	"	36.9	3.10
101 c	22	0.702	20.0	3.10	8.87	74.6	66.1	330.08	20.0	0.83
108 c	"	0.695	"	3.10	9.01	90.3	93.3	"	29.3	0.86
110 c	"	"	25.0	4.25	12.35	114.1	154.6	515.64	29.9	1.93
111 c	"	"	"	4.04	11.73	113.3	152.3	"	29.5	1.70
114 c	"	"	30.0	5.03	14.61	163.1	315.8	742.42	42.5	3.07
115 c	"	"	"	4.95	14.36	161.2	308.5	"	41.6	2.93

Shots conditions:

a Lefthand side, flat ended holder, soft solder.
b Righthand side, " " " " "
c Middle " " " " "
d Righthand side, hemi-spherical ended holder, soft solder.
e " " " " " , silver solder.
f " " " " " , aluminium solder.
g " " , pointed end holder, silver solder.

6.4 Conclusion

High speed Schlieren photography has been used for showing that blast waves generated by exploding copper wires are both radially and axially symmetric over most of their lengths for the wire sizes and capacitor voltages used. This study shows that 8cm/24 swg wires give the highest blast wave velocities up to 4 – 5.5 km/s (Mach no. about 13) at 30 kV discharge voltage. The exploding wire technique has been shown to produce symmetrical blast waves of sufficiently high pressure to satisfy the requirements of impact loading of hollow cylindrical specimens, which will be described in next chapter.

The exploding wire technique involves a fast discharge capacitor bank providing energy via a pressurized triggered spark gap to explode the wire, which is soldered to brass electrodes with diameter of 6.3 mm, and usually with flat ends. These electrodes are attached to the bank terminals. Figure (6.36) shows the electrodes and the electrode holders. Flat ended electrodes have been used as well as hemispherical and pointed ends to give more uniform cylindrical blast waves. Different types of solder also have been used to fix the exploding wires into a small hole in the electrodes, e.g silver brazing solder, aluminium, and ordinary soft solder. These types of solder used to study their effect on the shape and delay of the blast wave as well as studying the short spark before the wire explosion. The results in Table (2) shows there is no big difference caused by using different types of solder.

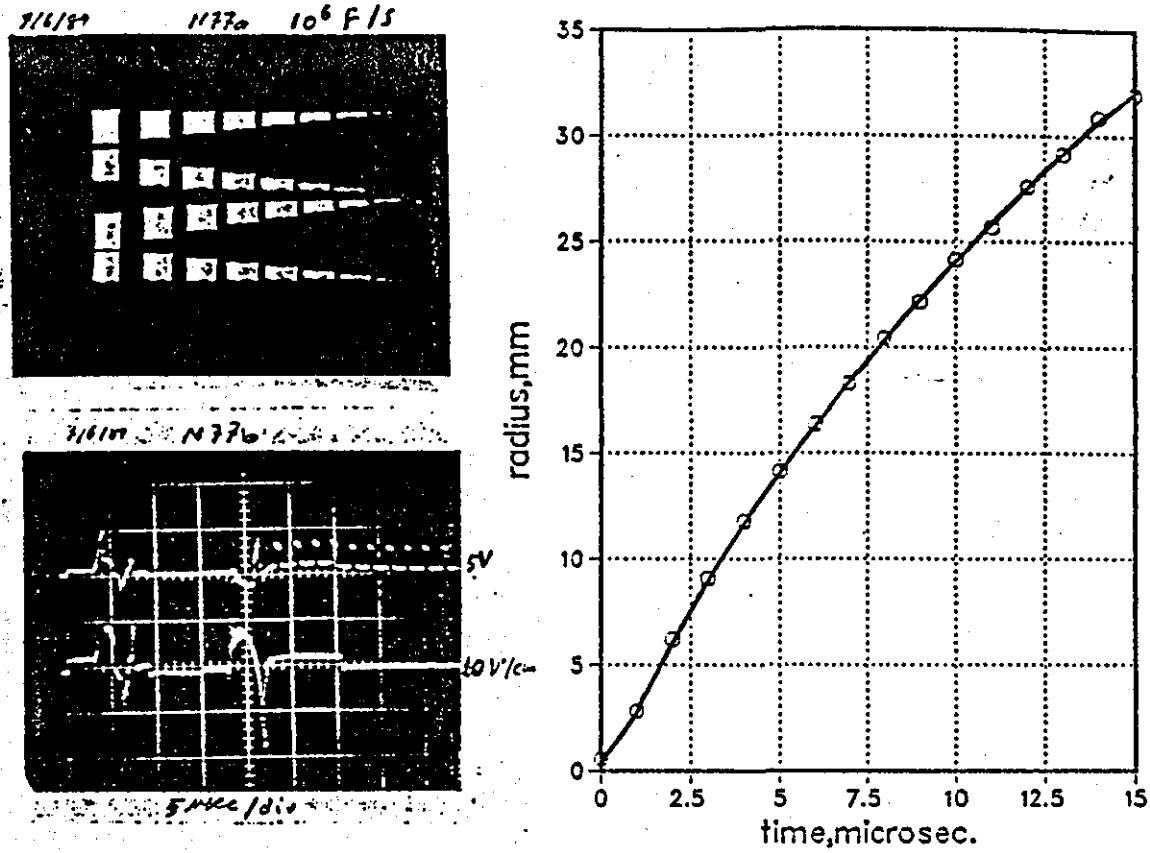

Figure (6.5) High speed photograph (10^6 f/s) of shock wave, corresponding CRO record, and radius of shock front against time graph for 13cm/24 swg wire at 20 kV.

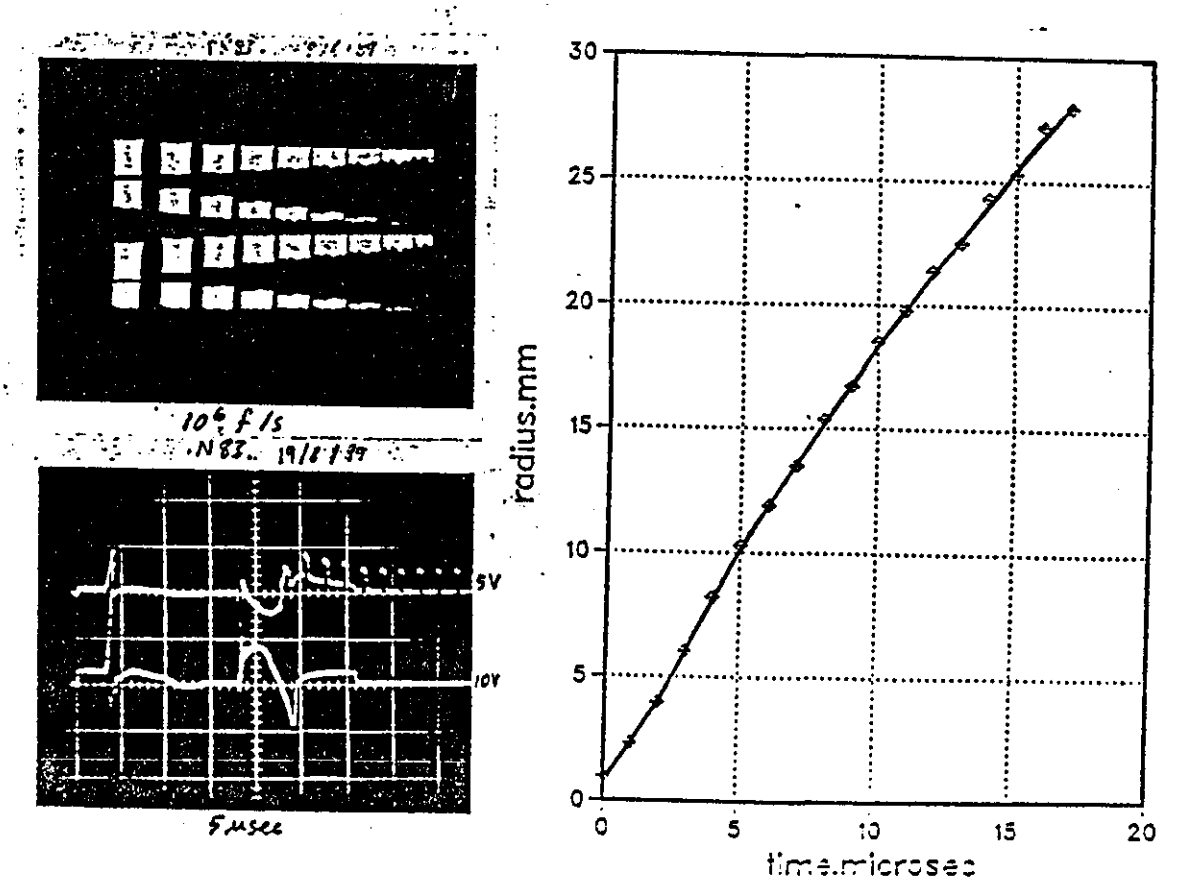

Figure (6.6) Photograph (10^6 f/s) ,CRO record and radius of shock front against time for 13cm/22swg wire at 20 kV.

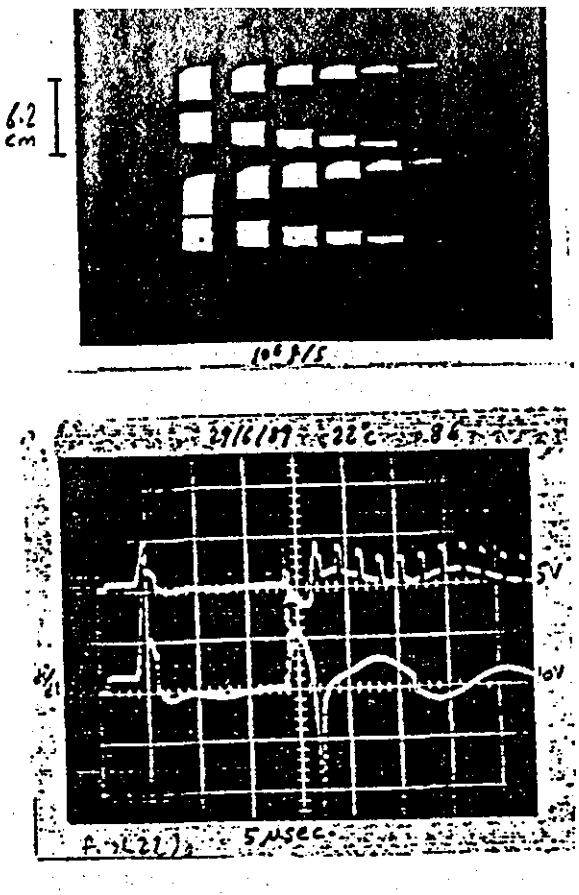

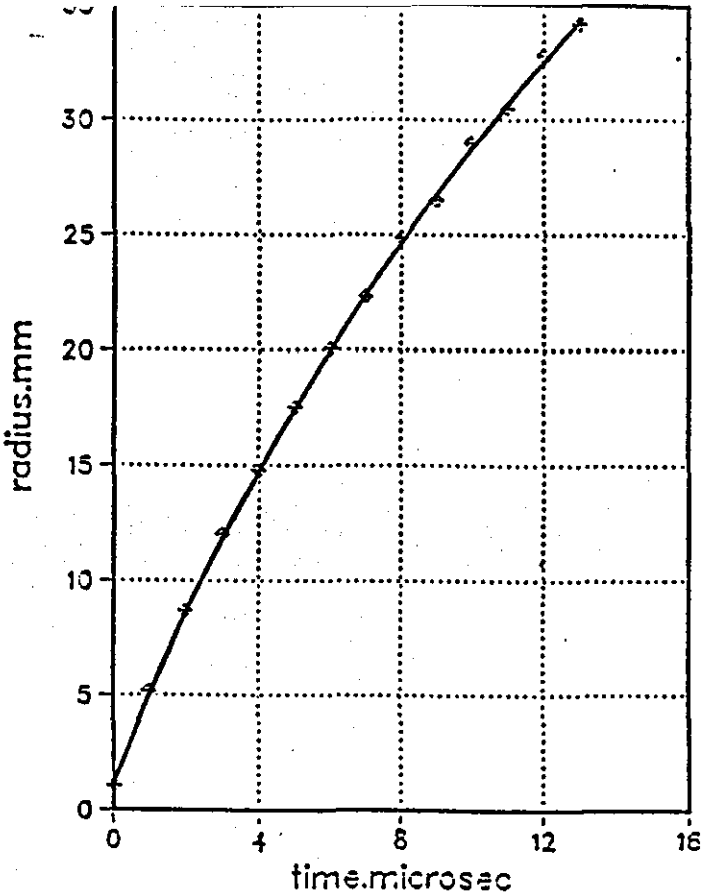

Figure (6.7) High speed photograph (10^6 f/s), CRO record and plot of shock front radius against time for 13cm/24swg wire at 25 kV.

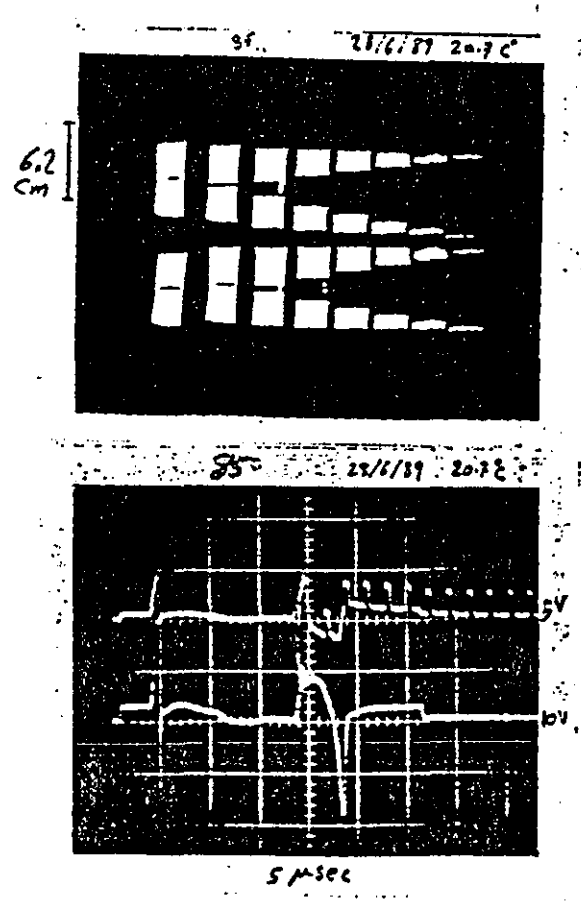

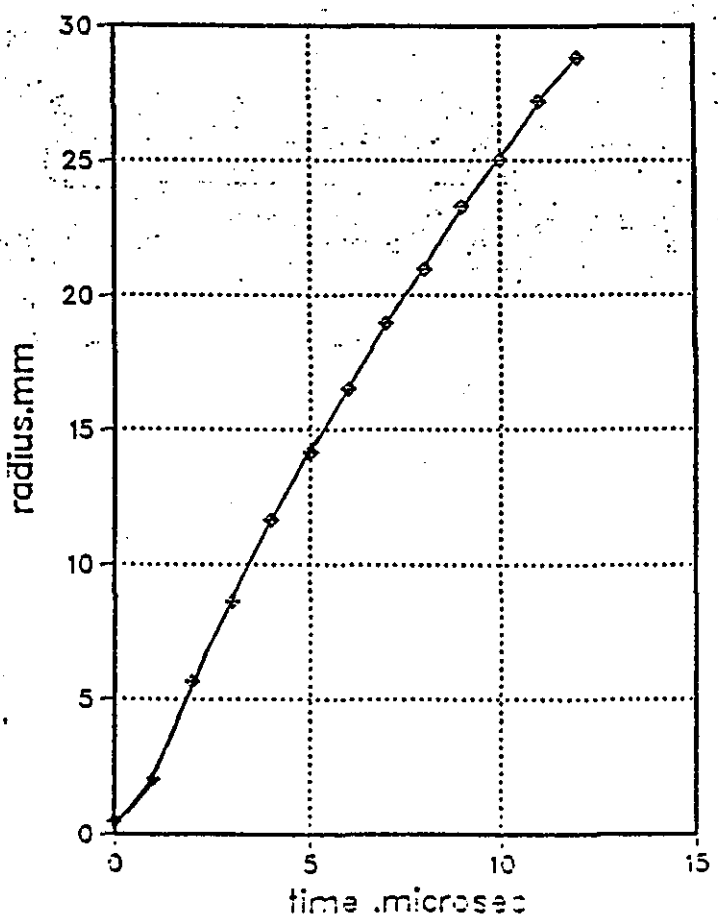

Figure (6.8) High speed photograph (10^6 f/s), CRO record , and plot of shock front radius against time for 13cm/22swg wire at 25 kV.

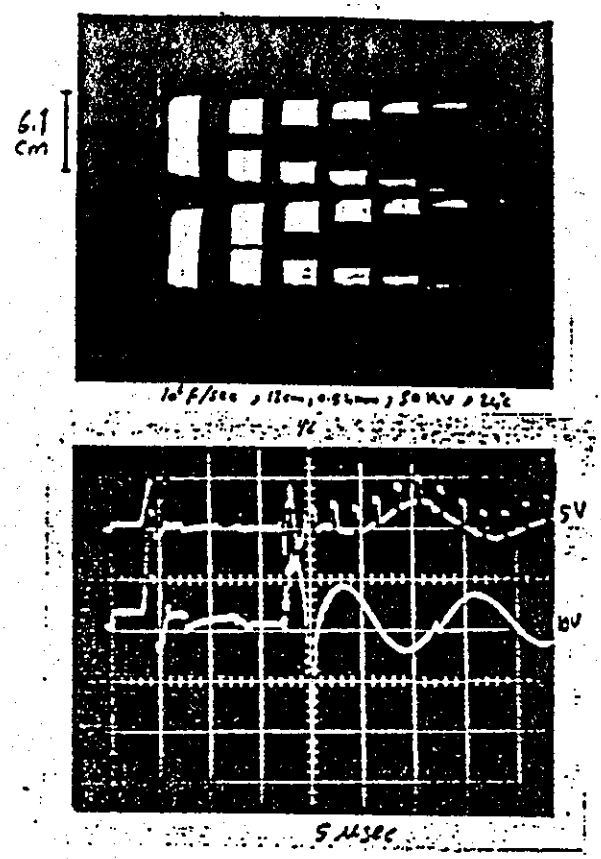

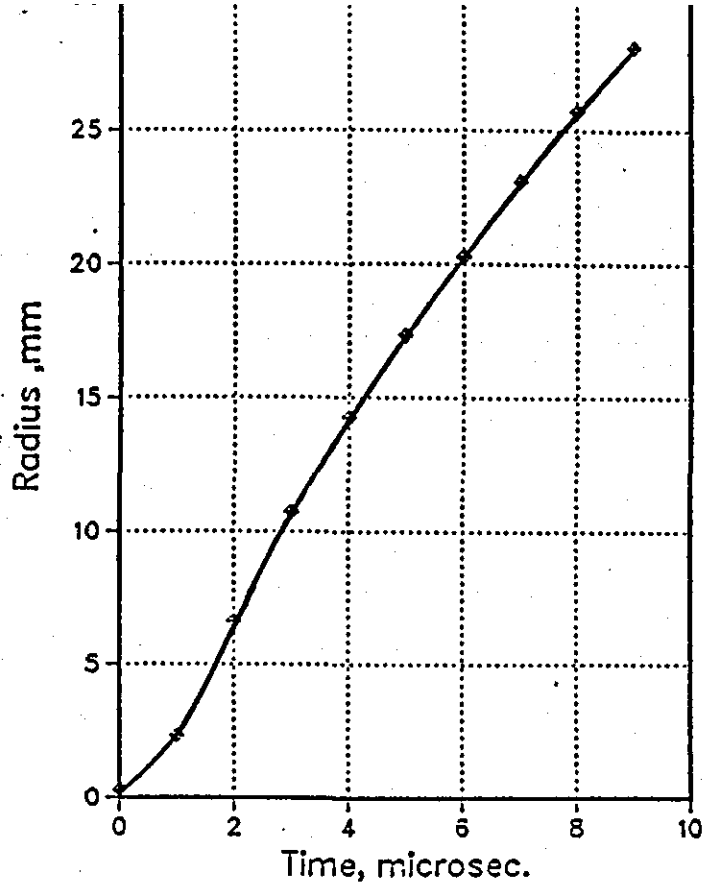

Figure (6.9) High speed photograph, CRO record, and graph of shock front against time for 13cm/24swg wire at 30 kV.

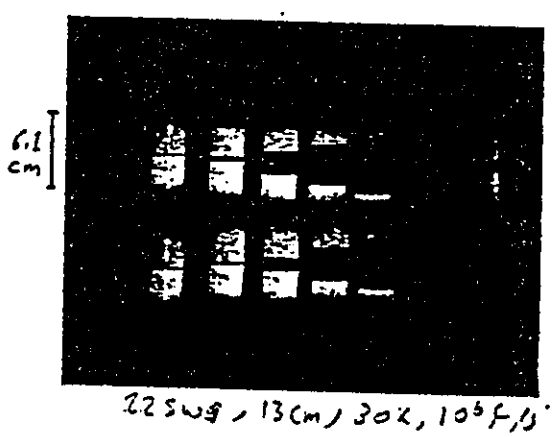

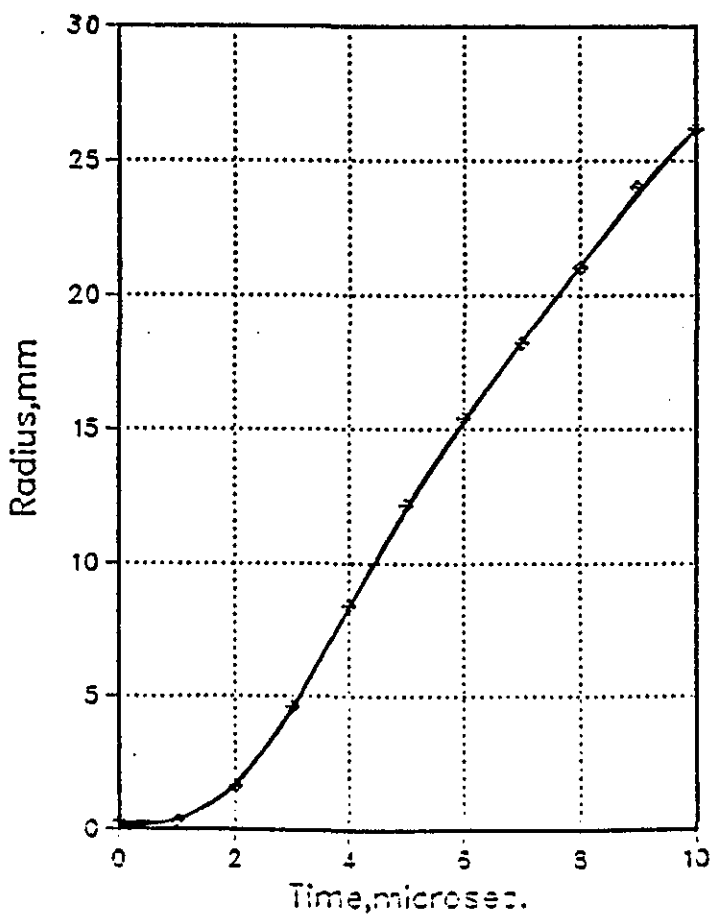

Figure (6.10) High speed photograph (10^6 f/s) and graph for radius of shock front against time for 13cm/22swg 30 kV.

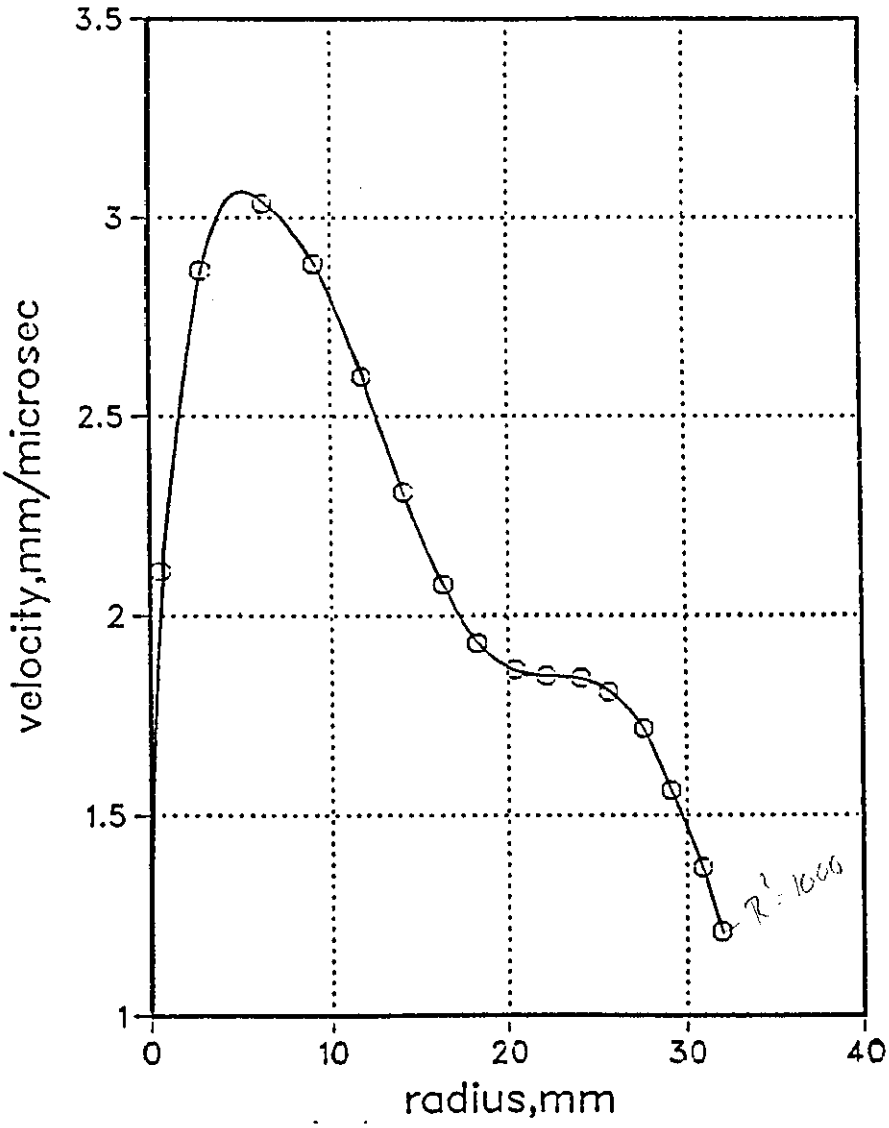

Figure (6.11) Shock wave velocity against shock front radius for 13 cm/24 swg wire at 20 kV.

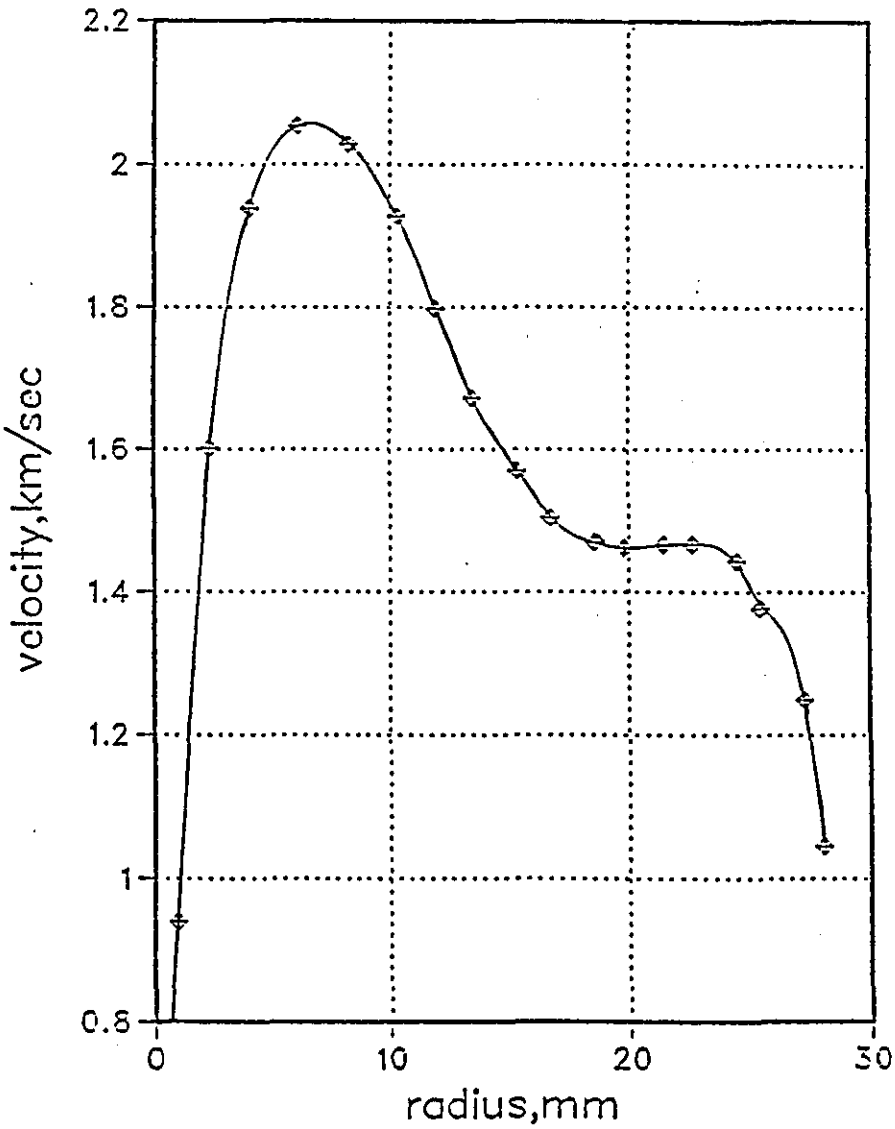

Figure (6.12) Shock wave velocity against shock front radius for 13 cm/22 swg wire at 20 kV.

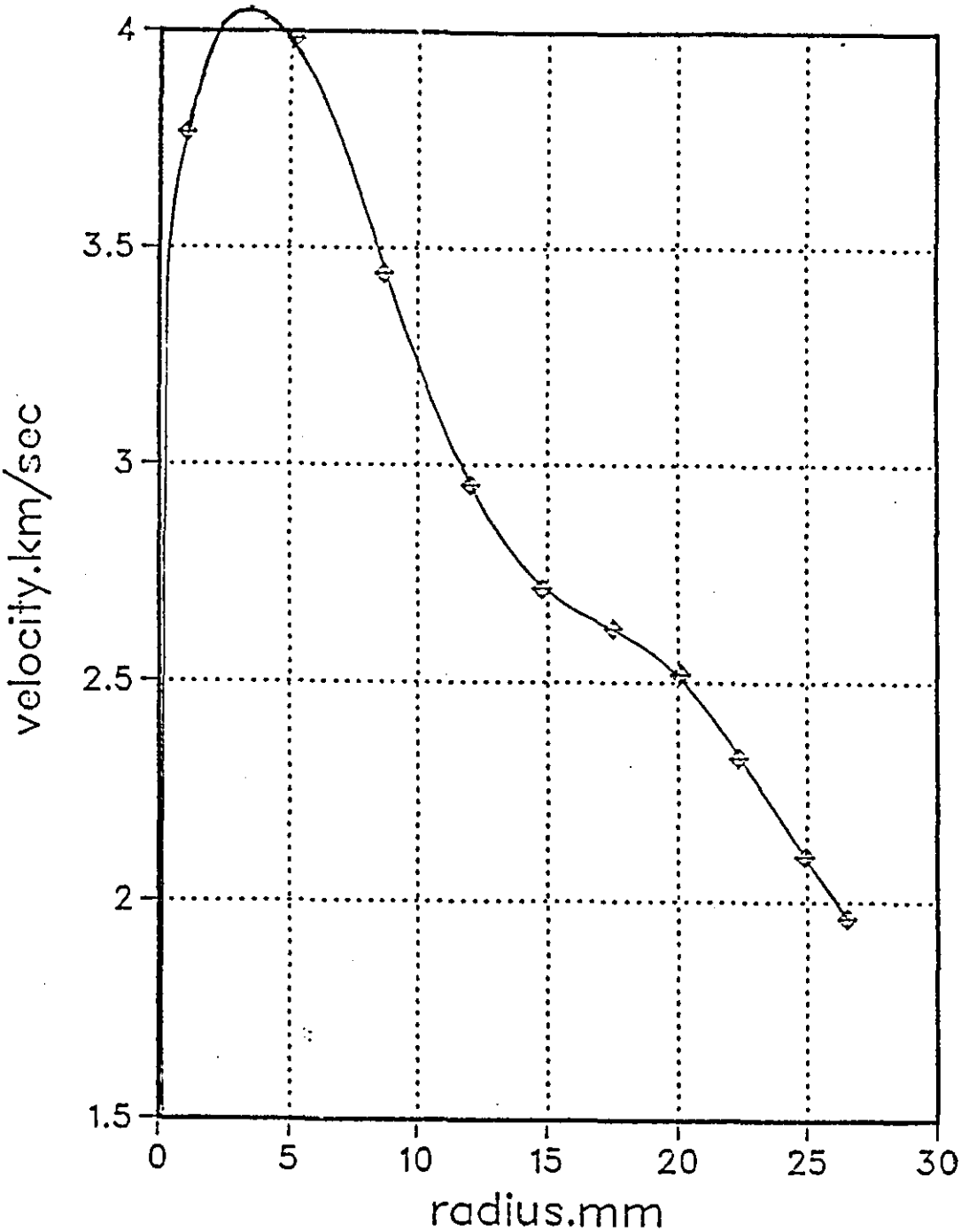

Figure (6.13) Shock wave velocity against shock front radius for 13 cm/24 swg wire at 25 kV.

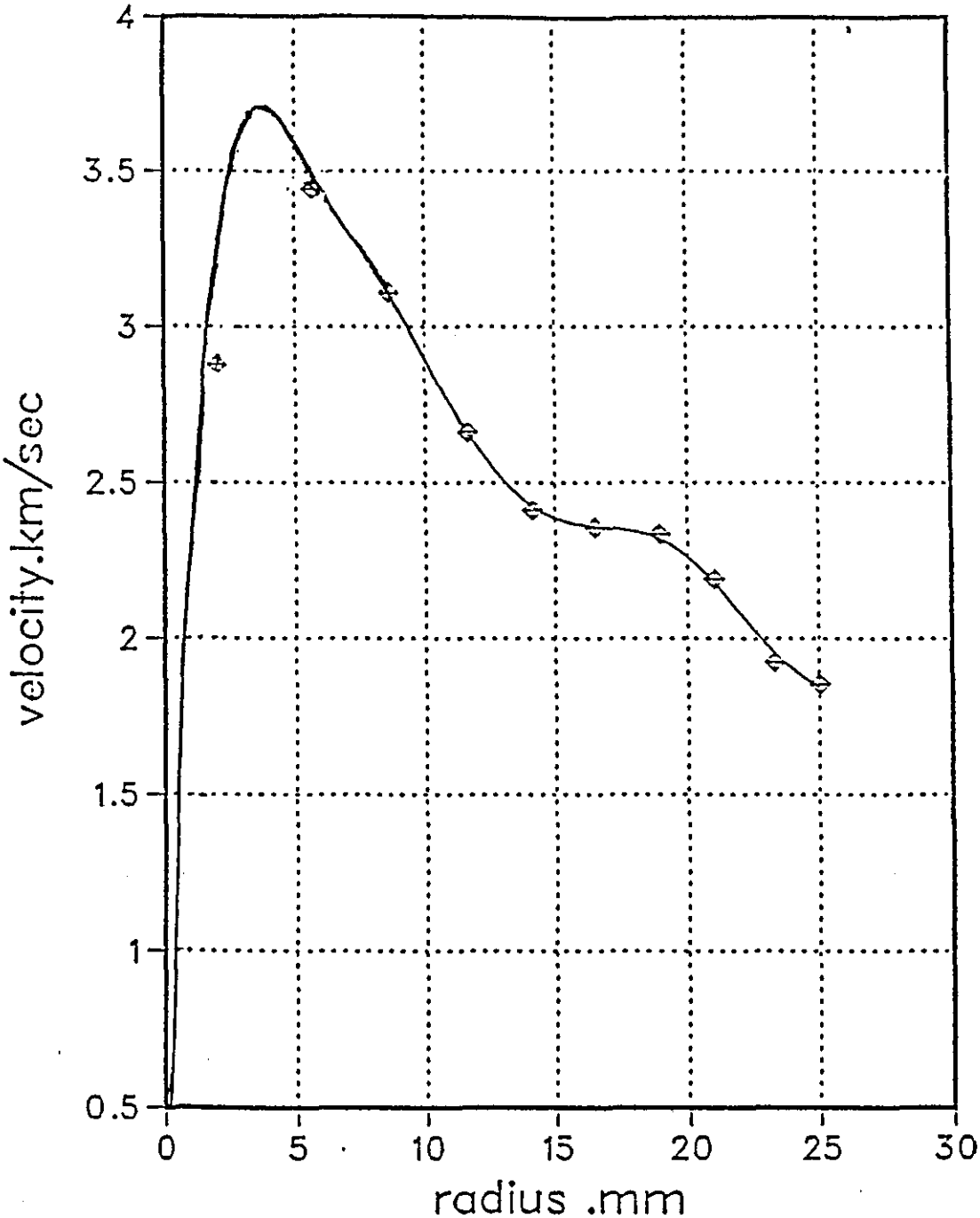

Figure (6.14) Shock wave velocity against shock front radius for 13 cm/22 swg wire at 25 kV.

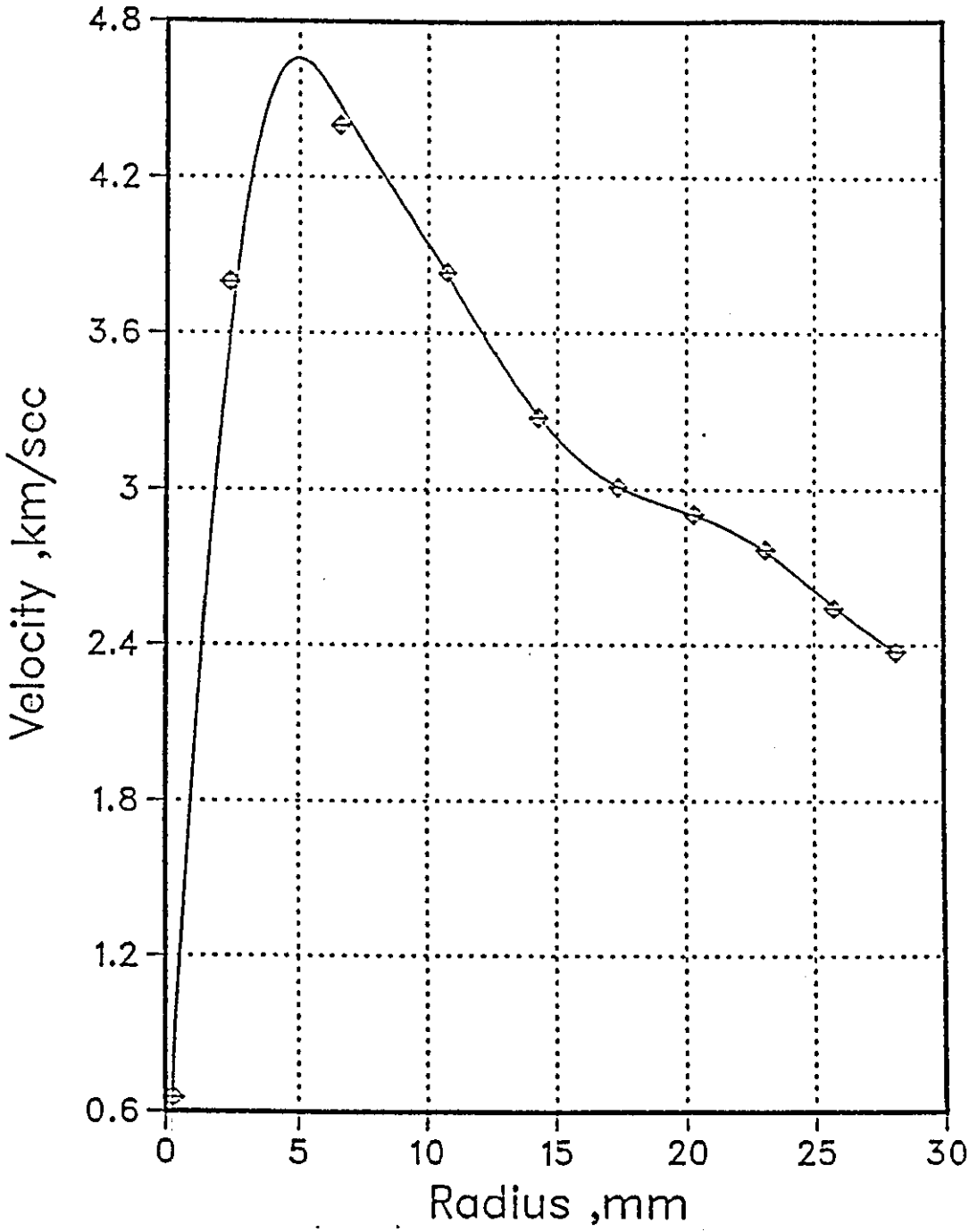

Figure (6.15) Shock wave velocity against shock front radius for 13 cm/24 swg wire at 30 kV.

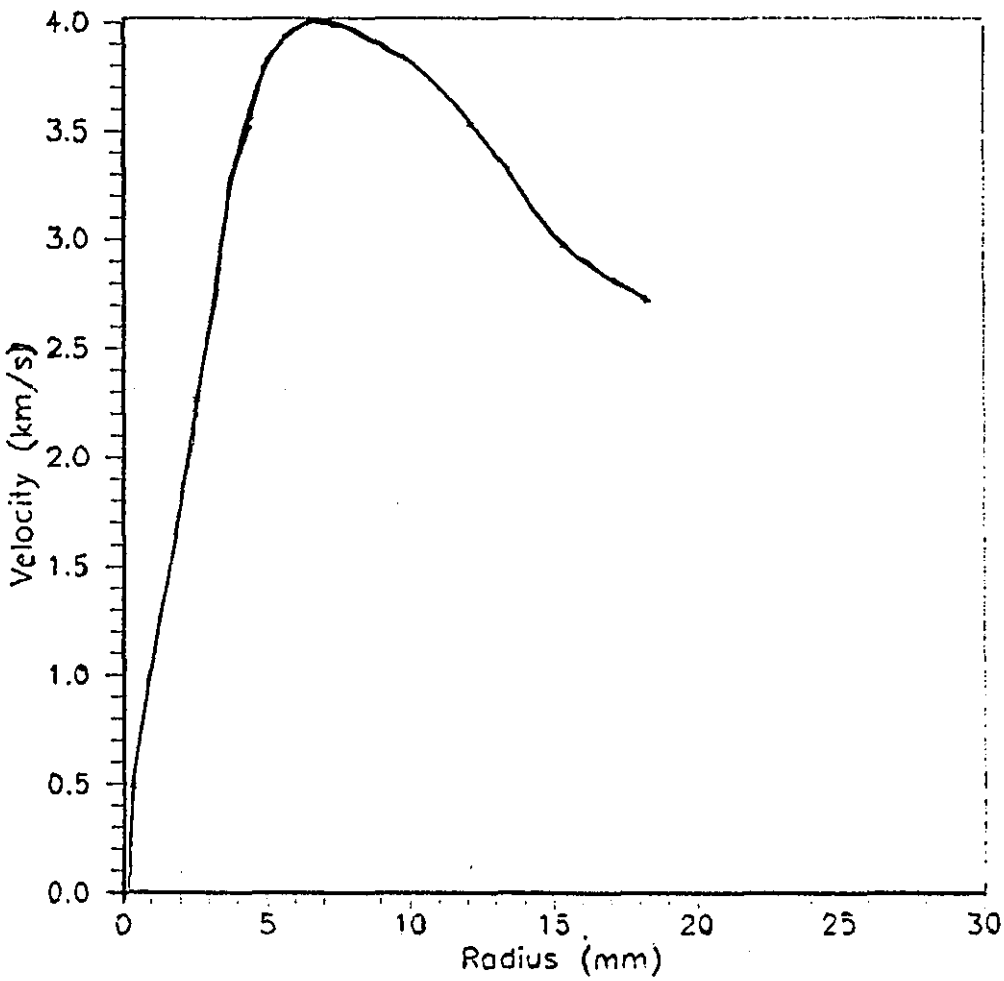

Figure (6.16) Shock wave velocity against shock front radius for 13 cm/22 swg wire at 30 kV.

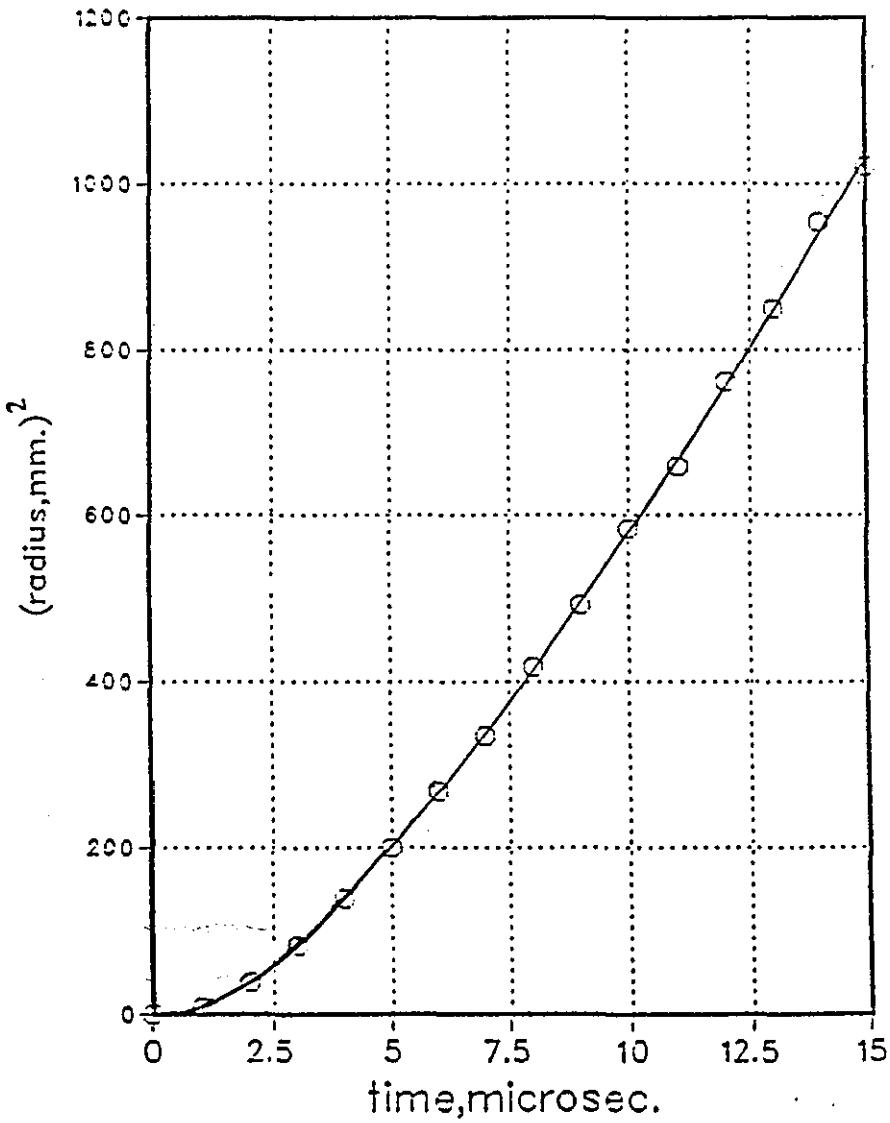

Figure (6.17) Radius squared as function of time for 13 cm/24 swg wire at 20 kV.

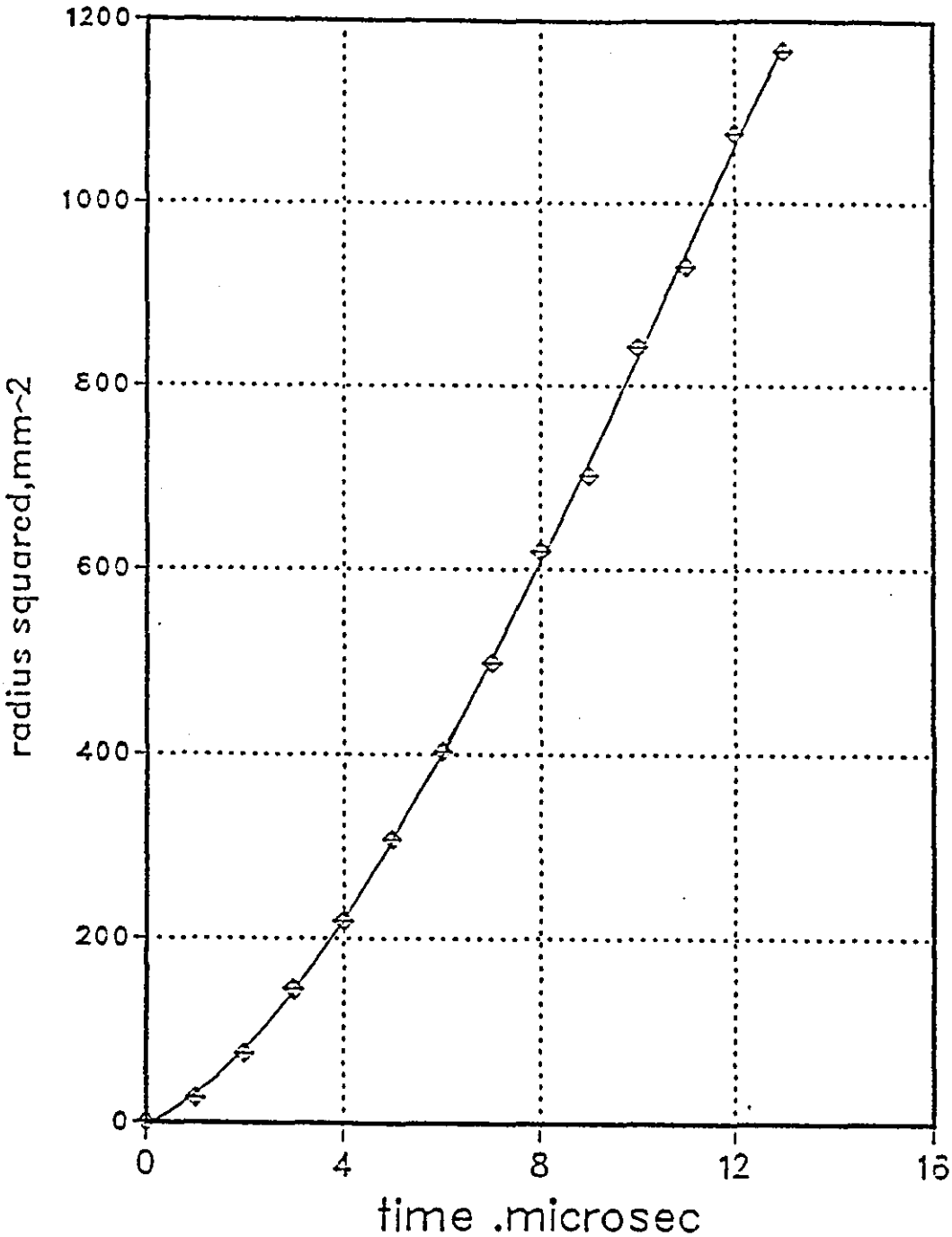

Figure (6.18) Radius squared as a function of time for 13 cm/24 swg wire at 25 kV.

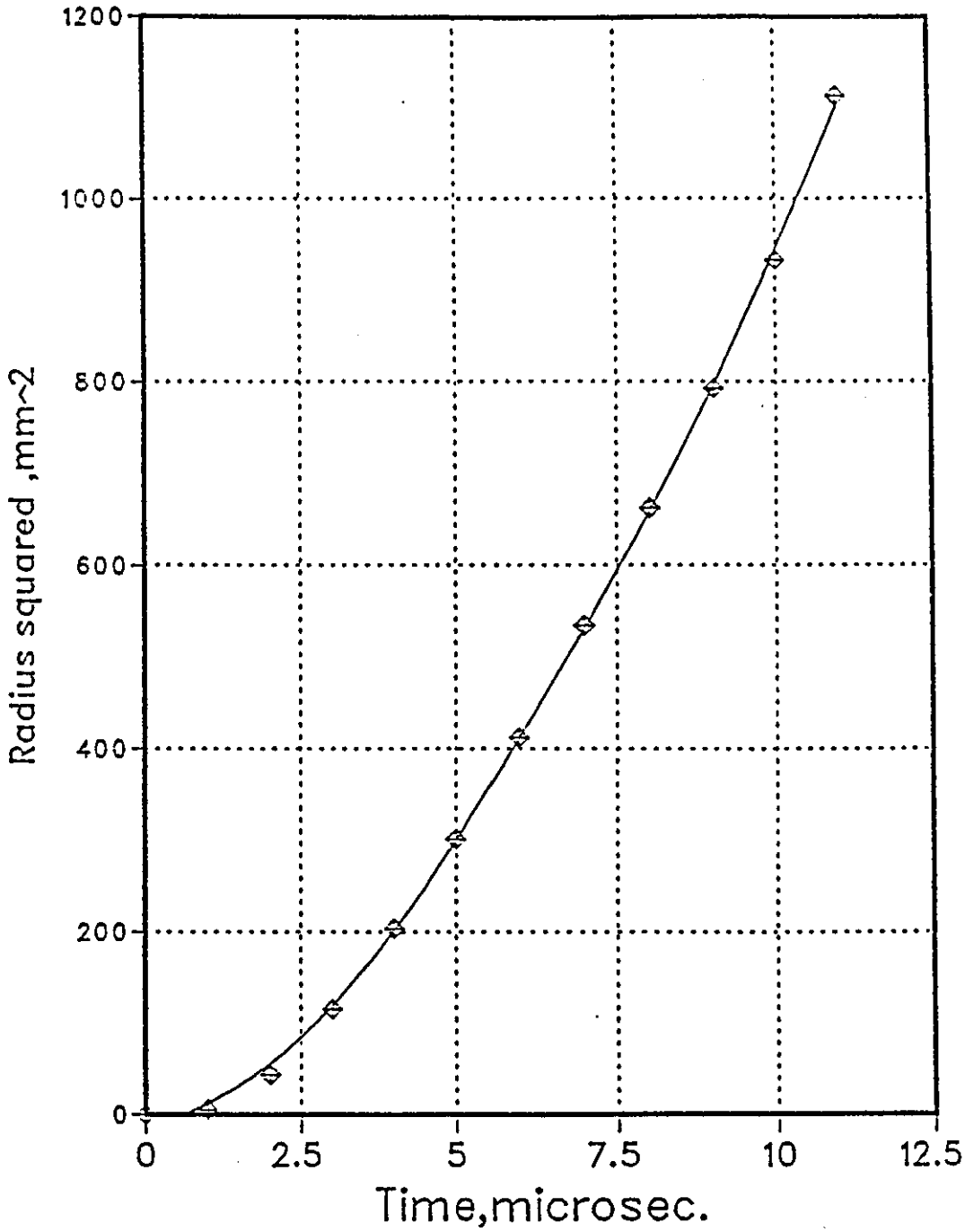

Figure (6.19) Radius squared as a function of time for 13 cm/24 swg wire at 30 kV.

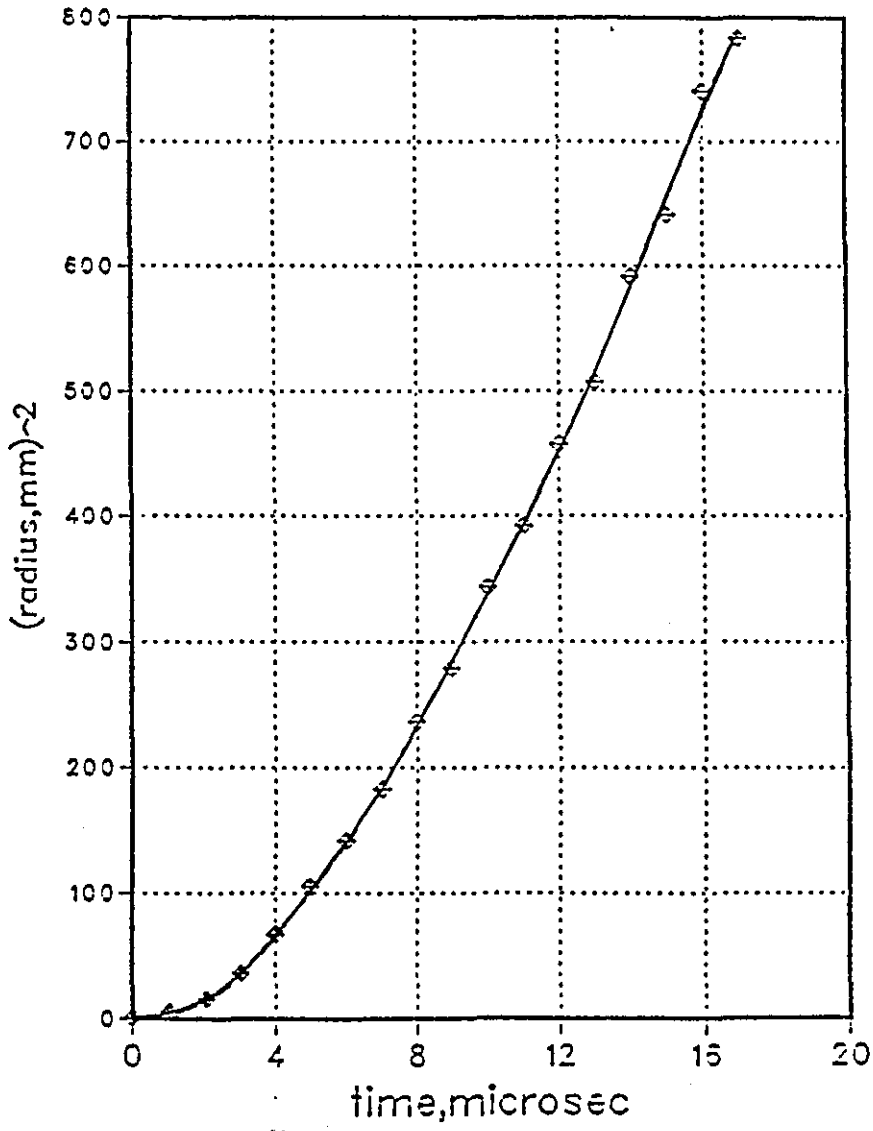

Figure (6.20) Radius squared as a function of time for 13 cm/22 swg wire at 20 kV.

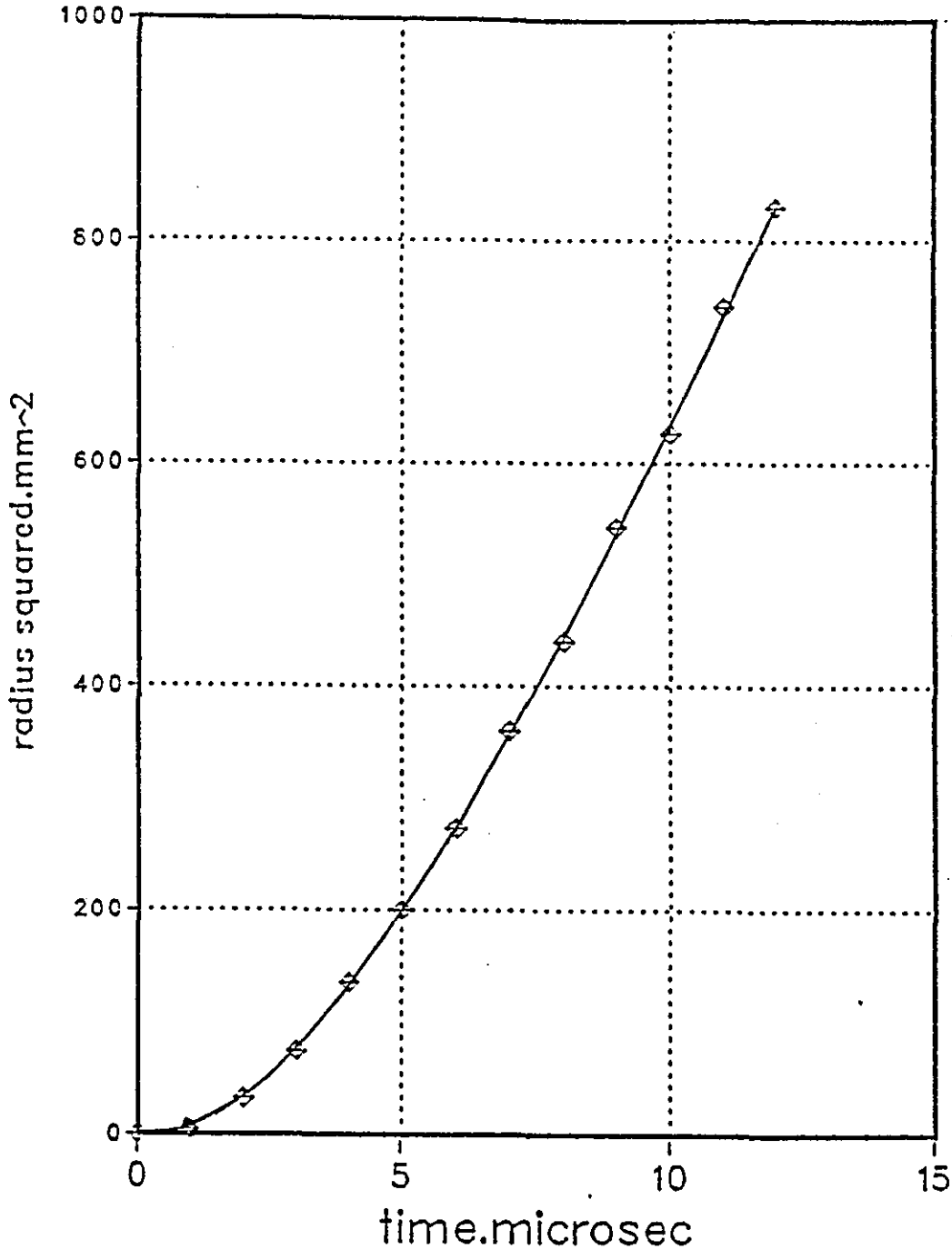

Figure (6.21) Radius squared as a function of time for 13 cm/22 swg wire at 25 kV.

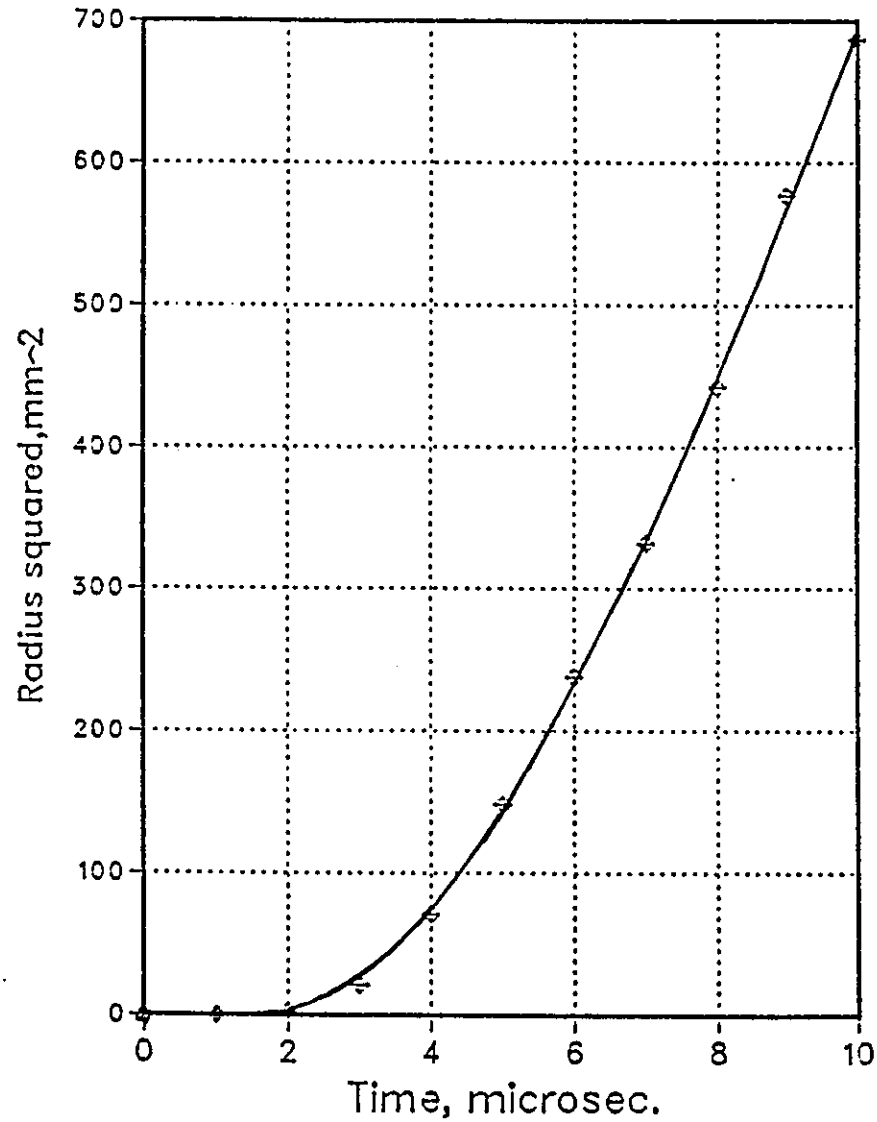

Figure (6.22) Radius squared as a function of time for 13 cm/22 swg wire at 30 kV.

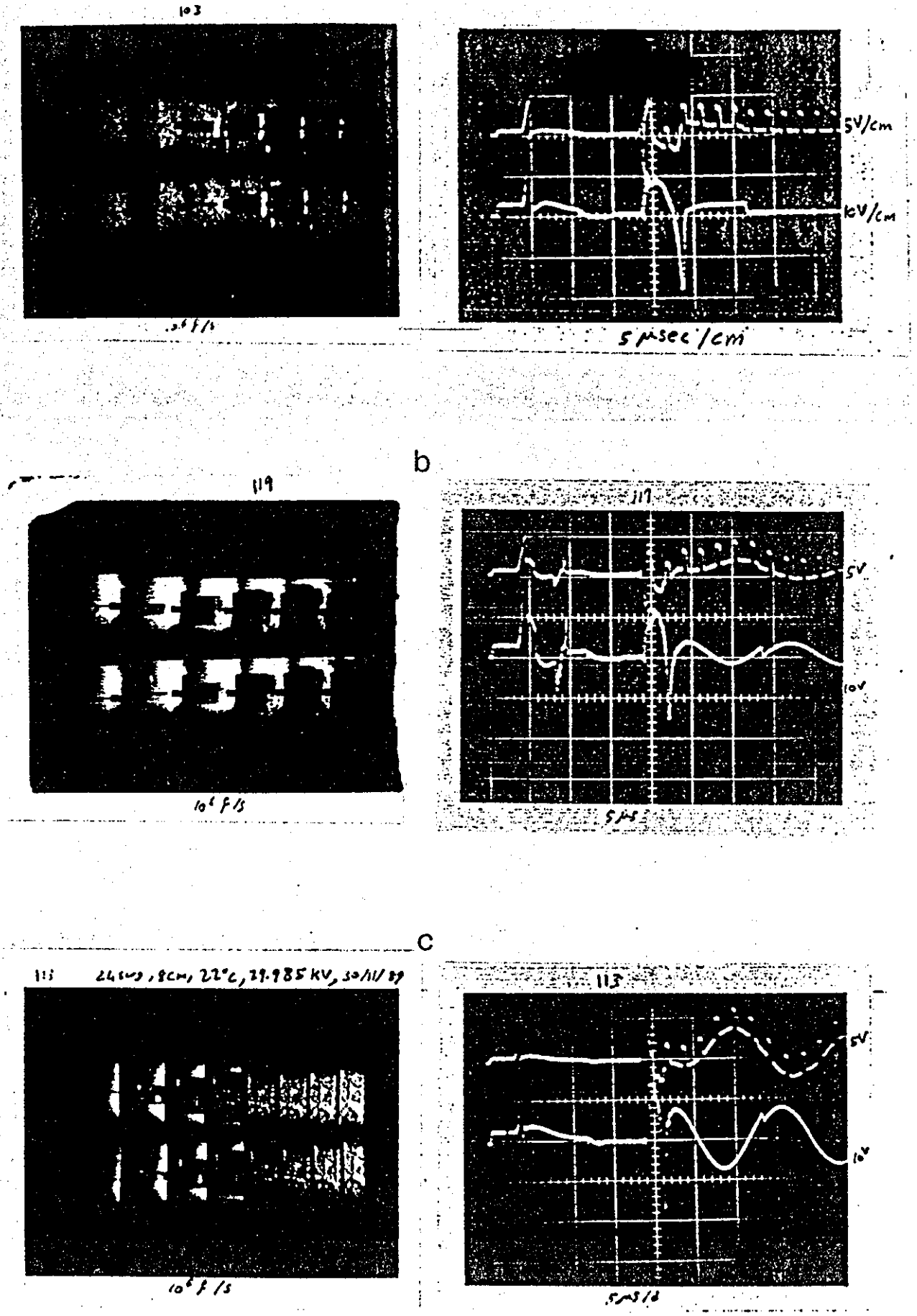

Figure (6.23) High speed photographs and CRO records of 8 cm/24 swg wire exploded at (a) 20 kV, (b) 25 kV, and (c) 30 kV.

(framing rate 10^6 f/s)

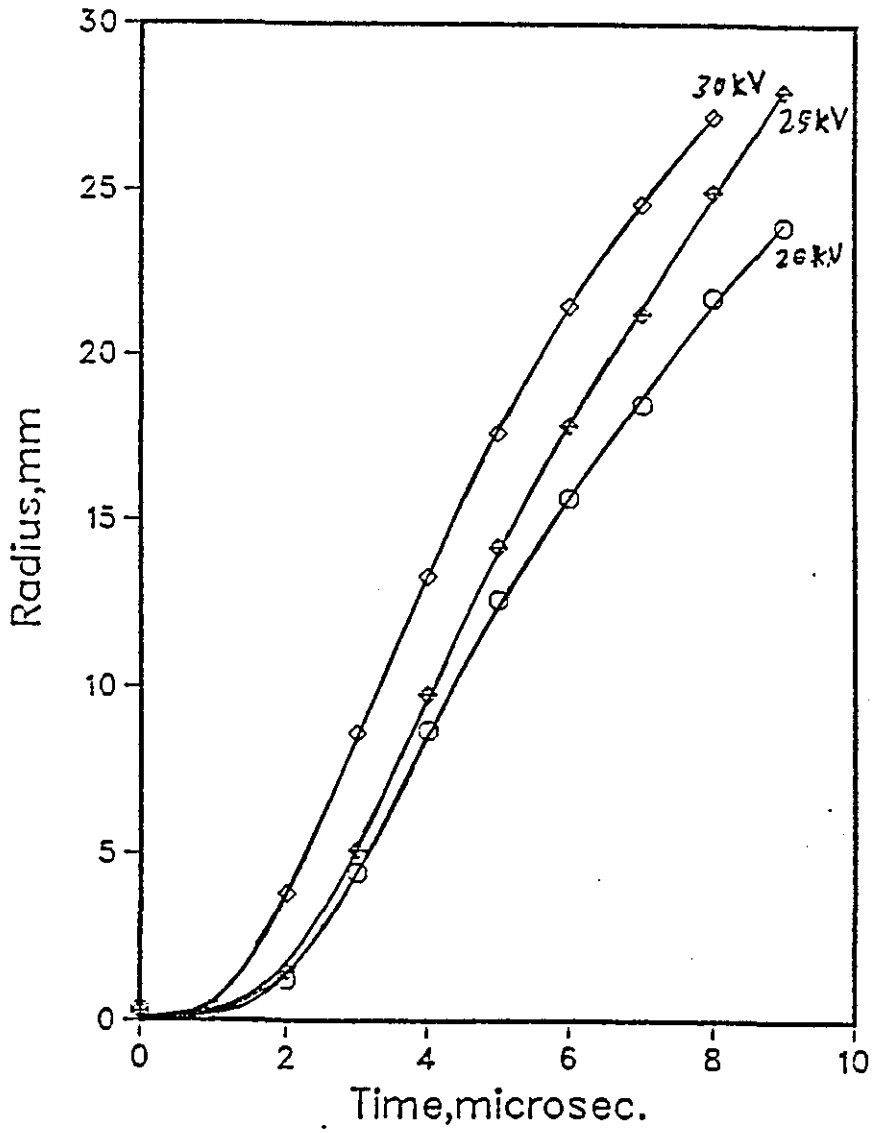

Figure (6.24) Shock front radius against time for 8 cm/24 swg wires at 20, 25, and 30 kV.

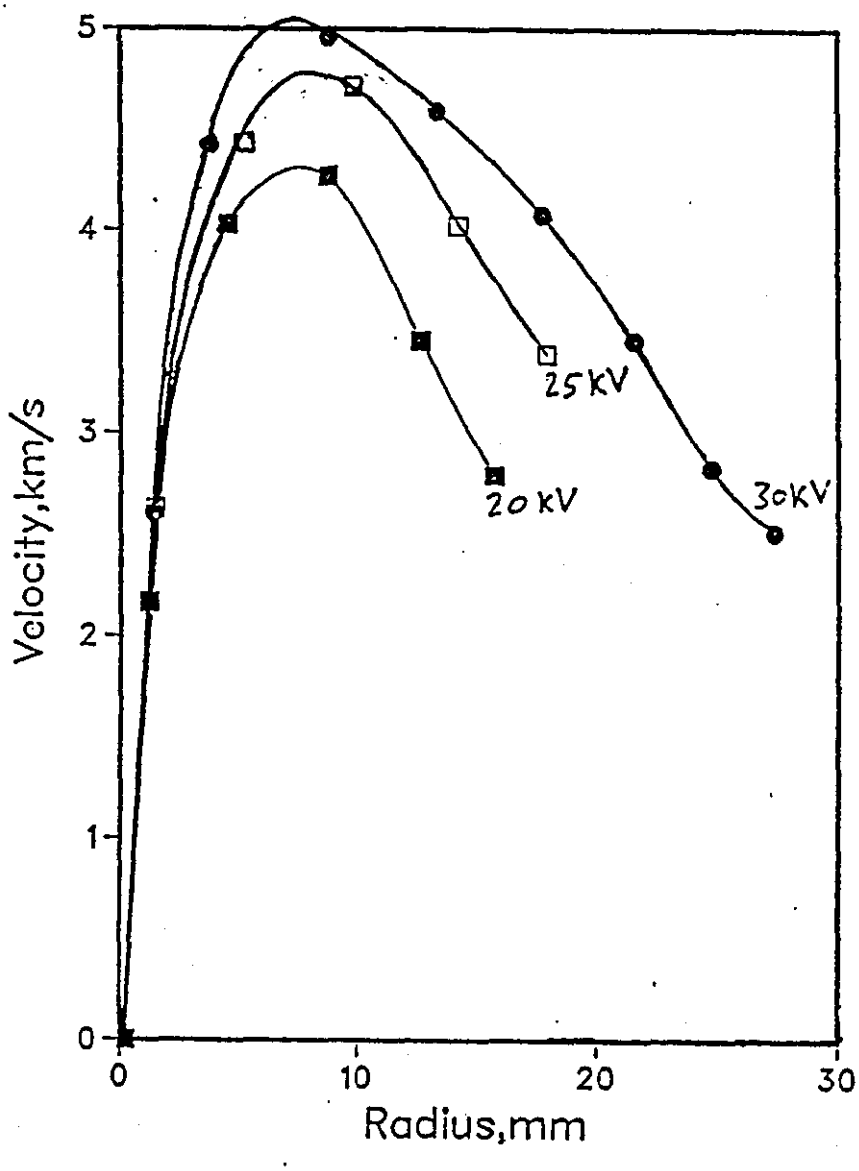

Figure (6.25) Shock wave velocity against shock front radius for 8cm/24swg at 20, 25, and 30 kV.

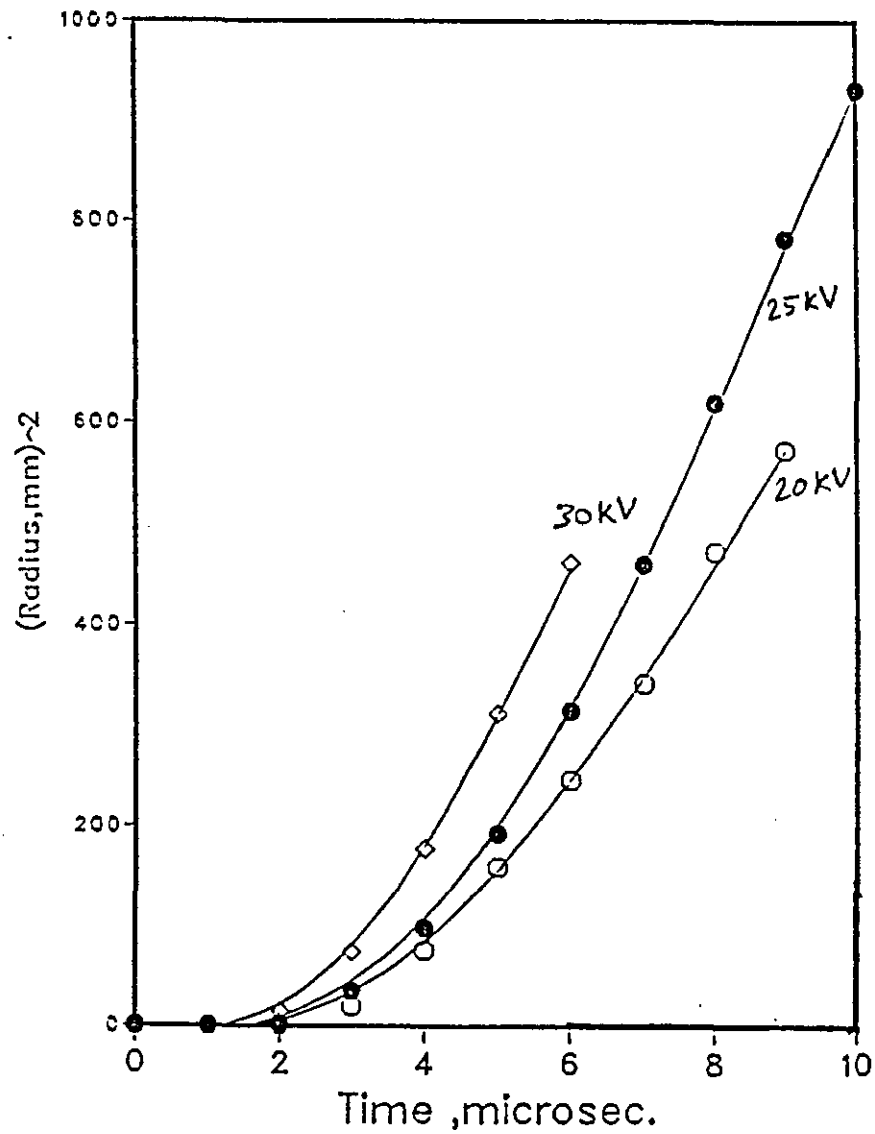

Figure (6.26) Radius squared as a function of time for 8cm/24swg wire at 20, 25, and 30 kV.

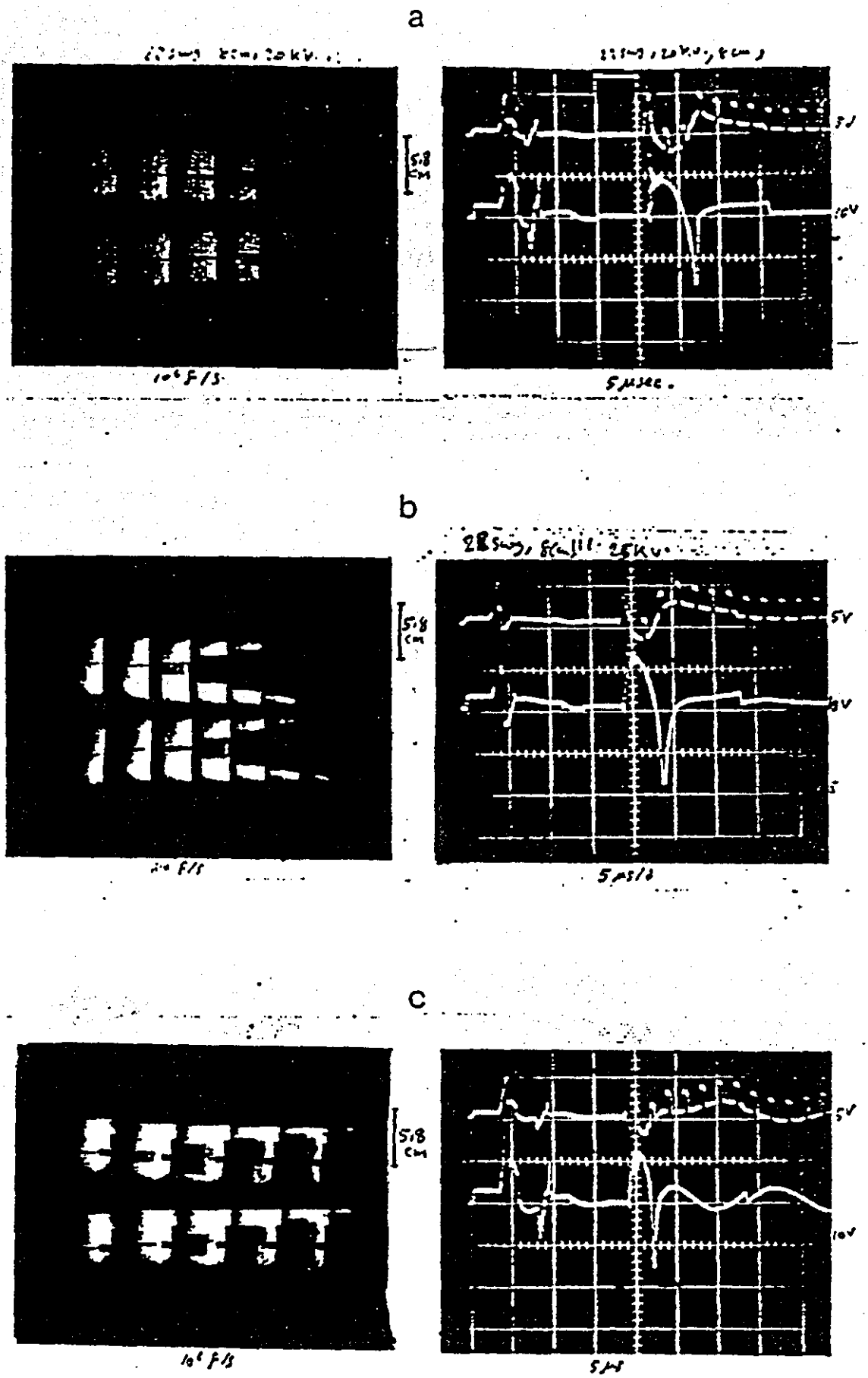

Figure (6.27) High speed photographs and CRO records for 8cm/22swg wire at (a) 20 kV, (b)25 kV, and (c) 30 kV.
(framing rate = 10^6 f/s)

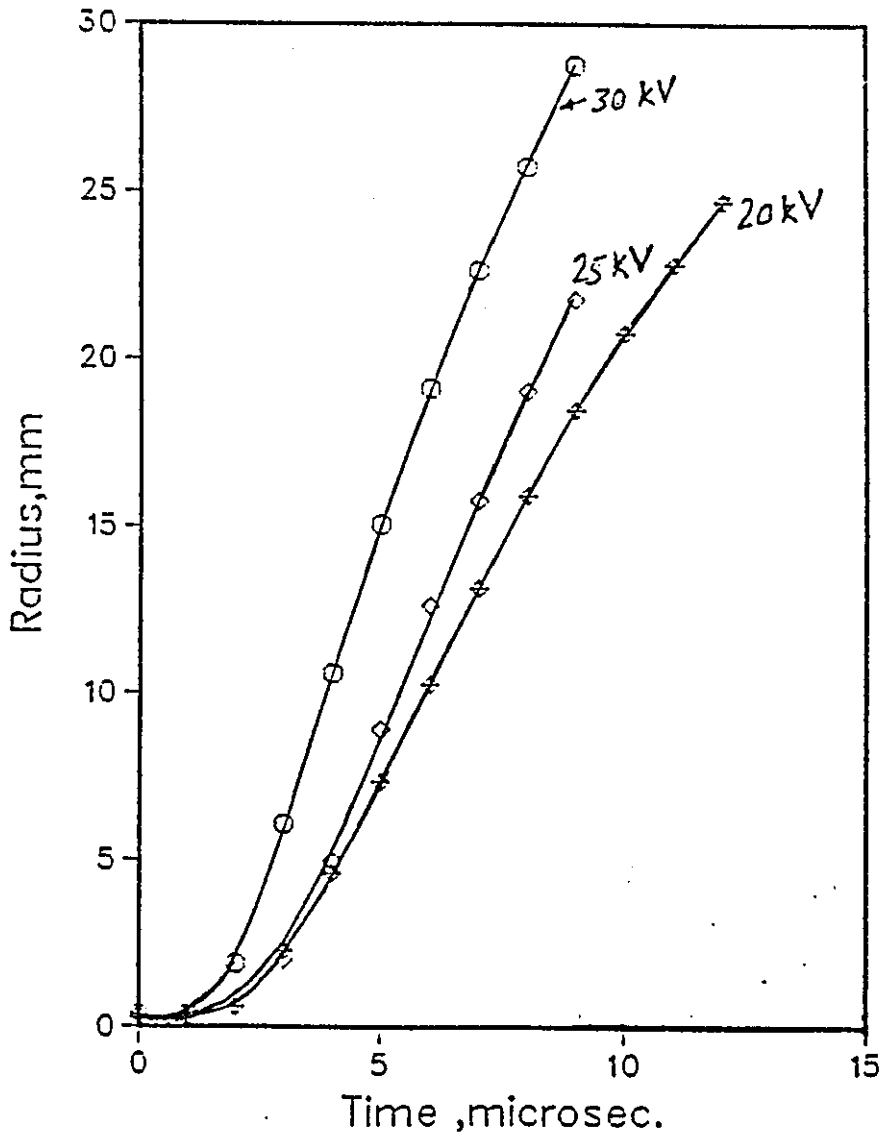

Figure (6.28) Shock front radius against time for 8cm/22swg wire at 20, 25, and 30 kV.

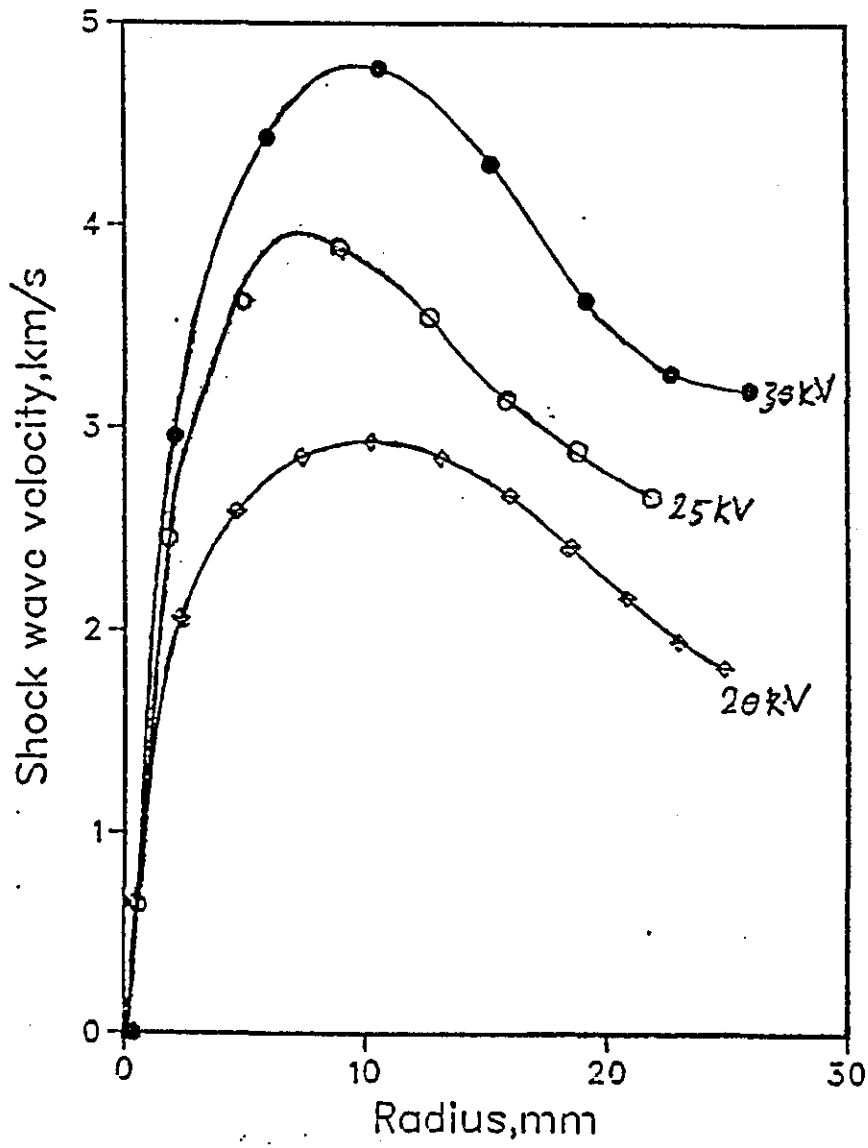

Figure (6.29) Shock wave velocity against shock front radius for 8cm/22swg at 20, 25, and 30 kV.

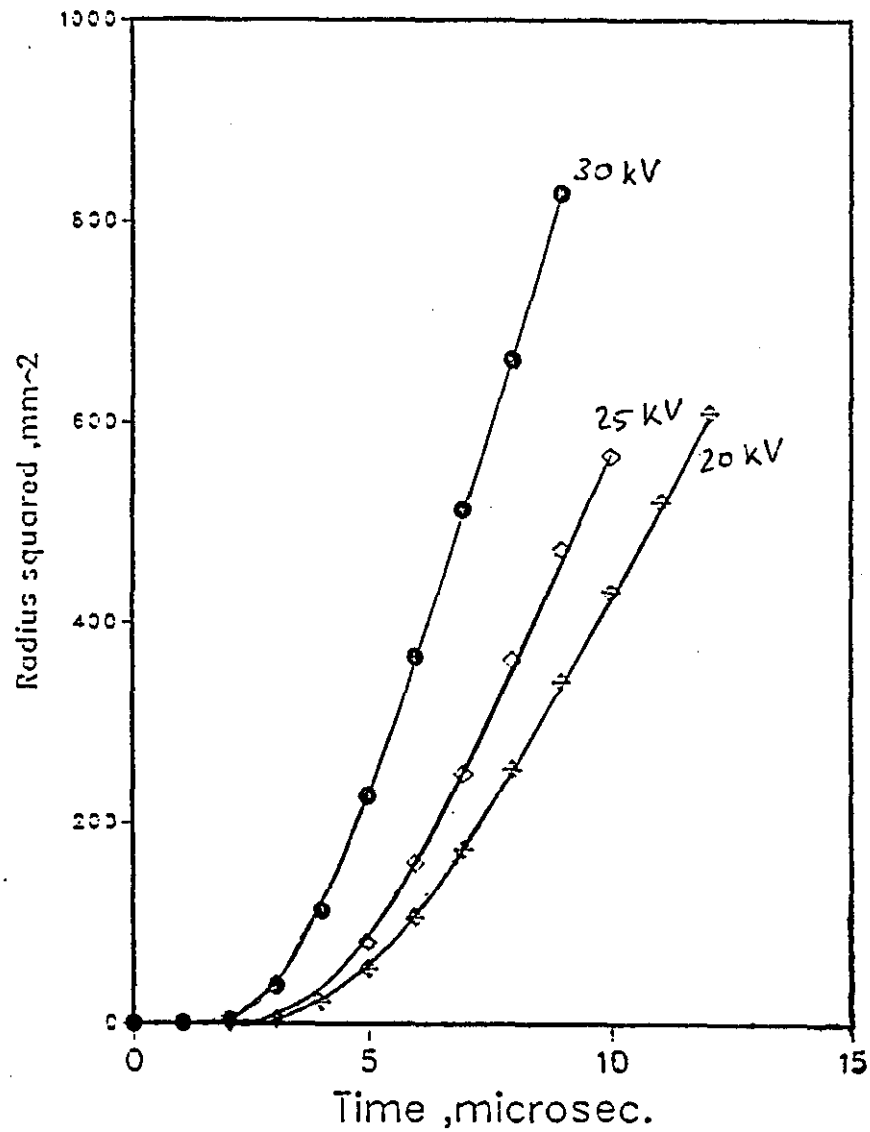

Figure (6.30) Radius squared as a function of time for 8cm/22swg wire at 20, 25, and 30 kV.

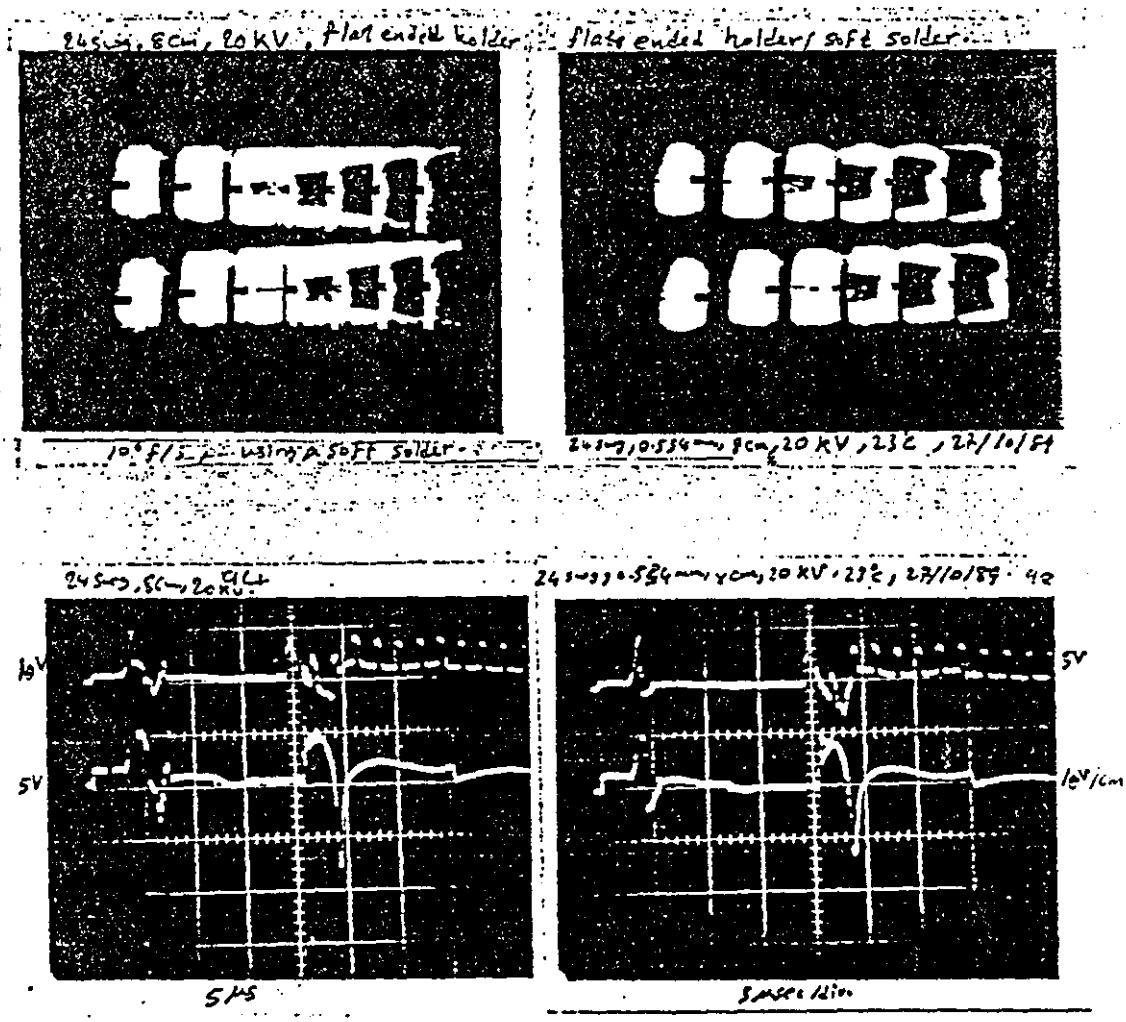

Figure (6.31) High speed photographs (10^6 f/s) of shock wave propagation around the right and the left holders of 8cm/24swg exploding wire at 20 kV. Both holders are flat ended and connected with the wire by a soft solder.

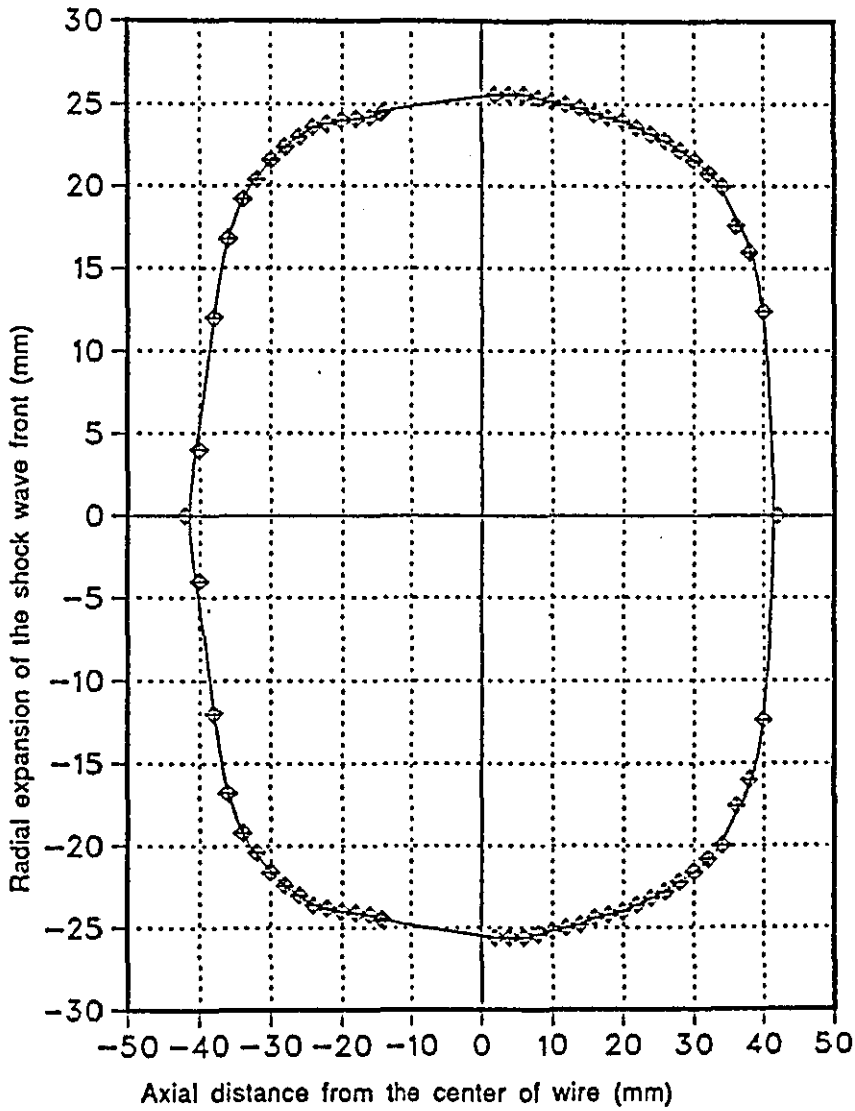

Figure (6.32) XY plot of shock wave propagation around an 8cm/22 swg exploding wire at 20 kV, 7μs after the explosion.

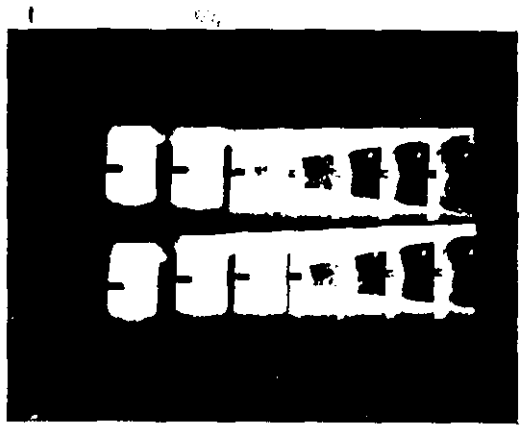

8cm/24swg, 20 kV, left side flat ended holder with soft solder.

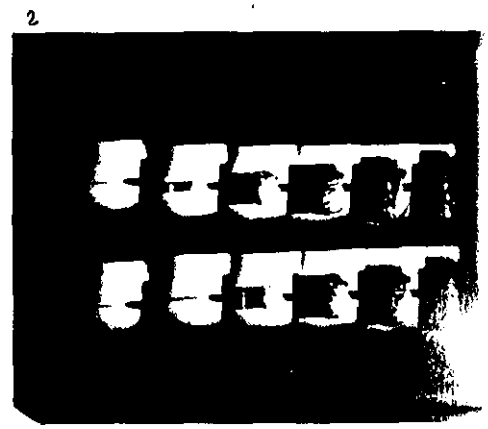

8cm/24swg, 20 kV, right side point ended holder, brazing (silver solder).

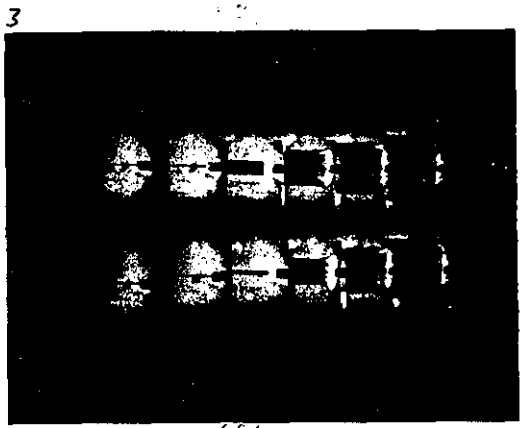

8cm/24swg, 20kV, hemi-spherical ended holder, soft solder.

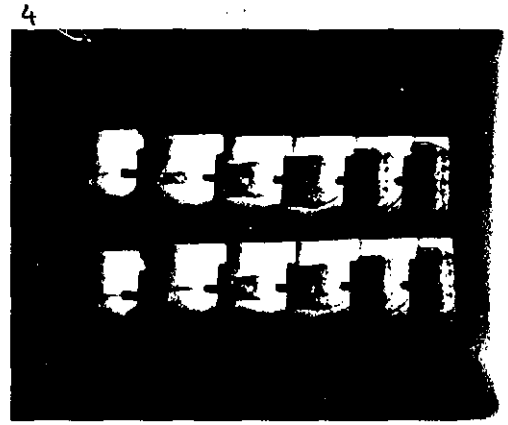

8cm/24swg, 20 kV, hemi-spherical ended holder, aluminium solder.

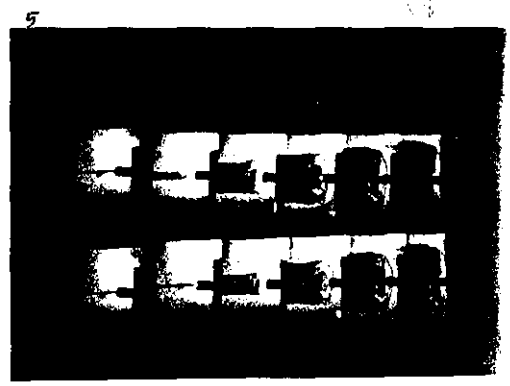

8cm/24swg, 20 kV, hemi-spherical ended holder, hard brazing solder.

Figure (6.33) High speed photographs (10^6 f/s) shows the shock wave propagation and the small spark near the holder of the exploding wire with different end shapes and solders.

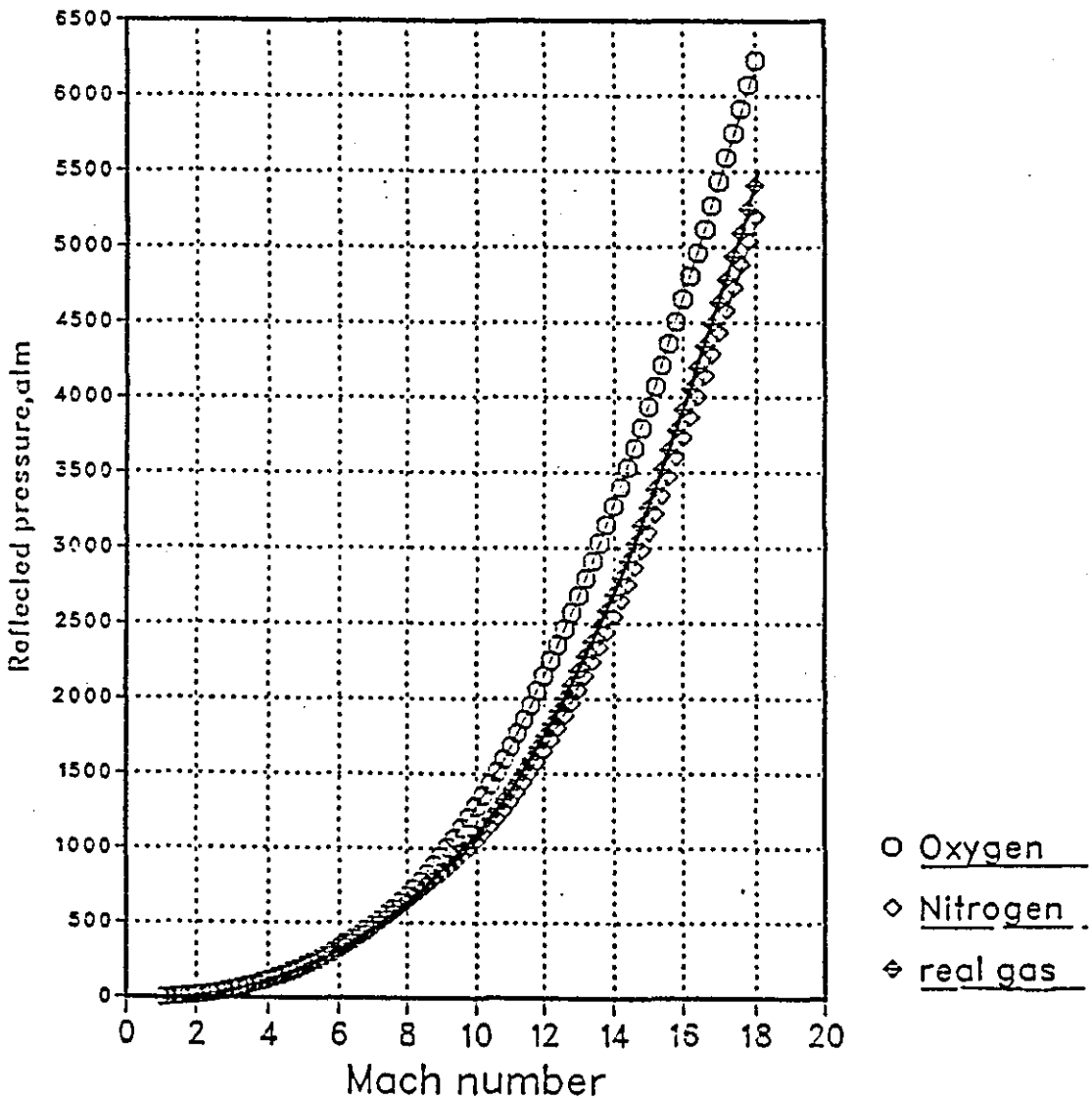

Figure (6.34) Reflected shock front pressure against Mach number.

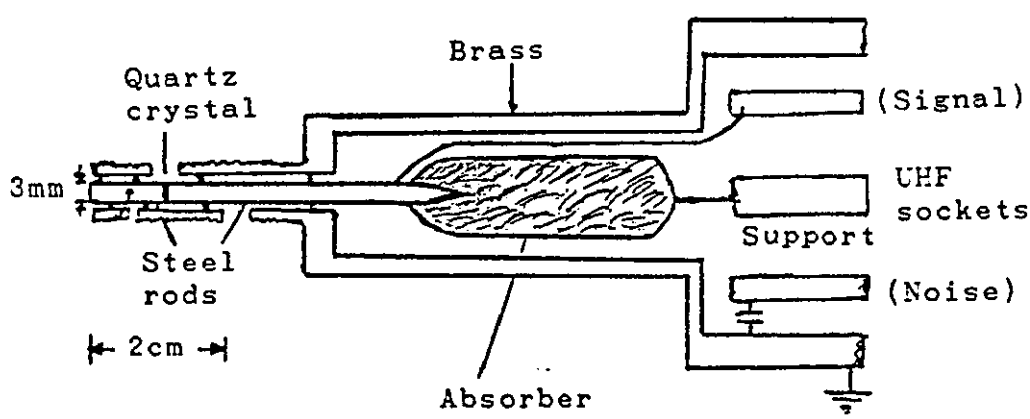

Figure (6.35) Piezoelectric pressure gauge.

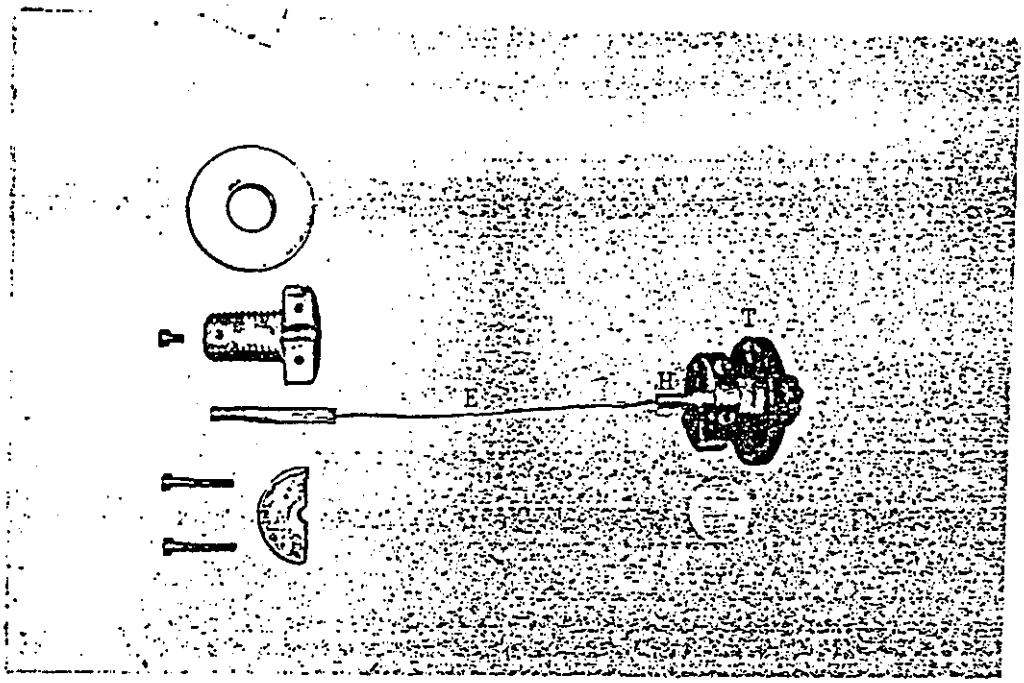

E : Exploding wire (copper, 13cm/22swg)
H : Electrode (brass, 6.3mm. diameter)
T : Electrode holder

Figure (6.36) Exploding wire with electrodes and the electrode holders.

CHAPTER 7
EXPANDING CYLINDER TESTING

7.1 Introduction

The mechanical behaviour of materials at high rates of strain has importance to many practical and theoretical problems (Ahmad 1988). One of the methods used to determine the mechanical behaviour of materials is that of a hollow cylinder expanded by means of an internal pressure applied rapidly.

Several investigators have used the expanding cylinder method to study different materials at high strain rates. Swift and Fyfe (1970) carried out two distinct types of experiment using the exploding wire technique to examine an elastic/viscoplastic constitutive theory in a radial cylindrical configuration. One experiment examined the plane-strain plastic response of thick hollow cylinders subjected to an internal finite-rise-time pressure; the other examined the decay behaviour of the cylindrical elastic precursor associated with high stress level impact loading. A linear and an exponential form of the viscoplastic strain-rate function were considered.

Schmit and Fyfe (1973) used the exploding wire technique to study the dynamic fracture of thick hollow cylinders. This experiment investigated the influence of biaxial strain on the dynamic fracture of metals.

Dirwish (1979) used a method, proposed by Ensminger and Fyfe (1966), to measure the small displacements of the outer surfaces of thick nylon cylinders subjected to internal pressure waves due to the reflection of blast waves from an exploding wire. This involved monitoring the displacement by using a laser beam which is intercepted by the outer surface of a cylinder.

Ahmad (1988) used a strain gauge method to study plastic deformation of polymer cylinders also by using exploding wires to provide high pressure internal impact loading.

Fyfe and Rajendran (1980, 1982) combined experiment and theory to examine the influence of strain-rate inertial effects and dynamic pre-strain on the ductile fracture of thin cylinders and thin rings. High speed photography was used to study the deformation of cylindrical specimens of high density polyethylene (HDPE) at high strain rates of 10^4 s^{-1}.

Forrestal, et al (1980) applied a high explosive loading technique to study the uniform plastic expansion and fracture initiation of stainless steel cylinders.

In this chapter, a prelimary study of the expansion of high density polyethylene (HDPE) tubes is described. High speed photography in association with the Schlieren technique is employed to monitor the radial displacements of the tubes. The expansion of the specimens has been produced by using an exploding wire inside a hollow cylinder along its axis.

7.2 Experiments and discussion of results

Figure (7.1) shows a simple diagram of the exploding wire system used for loading hollow cylindrical specimens. The cylinder is placed symmetrically around an exploding wire by using two nylatron holders which are fitted on the wire holders and the cylinder as shown in Figure (7.2).

High density polyethylene (HDPE) tube expansion was studied using a 10^5 f/s framing rate in an Imacon camera with 10 μs nominal intervals and 2 μs framing exposure, the illumination being provided by a small electronic flash of half-peak output duration of 204 μs as shown in

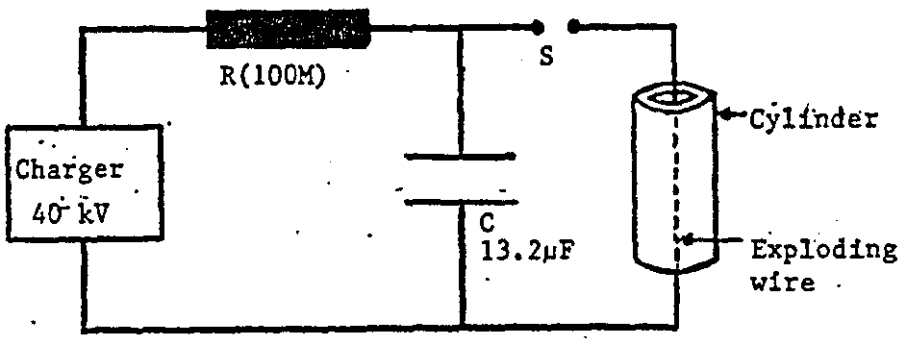

Figure (7.1) Simple diagram of exploding wire system employed for testing cylindrical specimens.

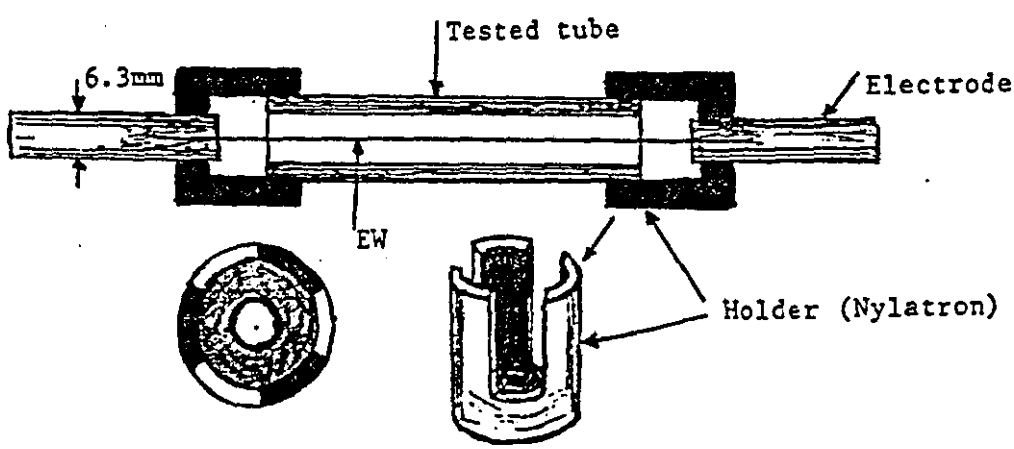

Figure (7.2) Mounting arrangement of thin-walled expanding tube.

Figure (7.3). The flash unit could be triggered either manually by pressing a push-button to short the flash circuit, or by an external pulse (in this case a 10 V pulse from a pulse generator) to fire a solid state thyristor, which does the same job of shorting the trigger circuit of the flash. As the oscilloscope record in Figure (7.3) shows the flash has delay of 18 μs from the triggering pulse to reach half-peak output.

The experiments were carried out mainly for HDPE-thin-walled cylinders subjected internally to an 8cm/22swg wire explosion using capacitor voltages of 20, and 25 kV. The outer radius of the tube surface was measured and plotted with respect to time in order to determine the velocity by differentiating the polynomial fit equation of the graph. Engineering hoop strain has been measured directly from the photographs and plotted against time to calculate the strain rate from the polynomial equation of the graph.

The tube wall thickness at break was measured after the experiment by using a digital micrometer for the middle part of the fractured tube. Also the breaking thickness was measured from the particular Imacon photograph which indicated the fracture starting, by measuring the outer radius (R_0) of the tube and assuming the volume is constant during the deformation of the tube. The inner radius can then be calculated by the following method:

For a length L of tube, assuming plane strain,

$V_1 = \pi(r_0^2 - r_i^2)L$ initial volume

$V_2 = \pi(R_0^2 - R_i^2)L$ final volume

where $V_1 = V_2$ constant volume for plastic flow.

$\therefore \quad R_i^2 = R_0^2 - (r_0^2 - r_i^2)$,

where r_0 and r_i are the initial outer and inner radii,

R_0 and R_i are the final outer and inner radii.

The wall thickness is then $\Delta R = R_0 - R_i$.

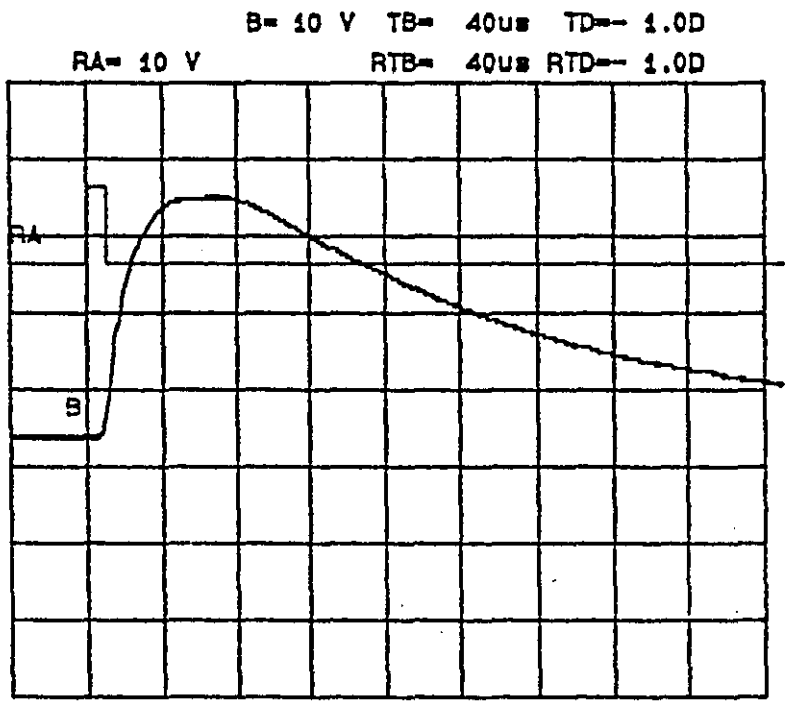

Figure (7.3) Elèctronic flash output (B), and the triggering pulse (RA).

The direct measurements from the photographs are usually smaller than the measurement by micrometer for the tested tube because of the recovery of the tube radially after the experiment.

The estimation of the values of the thickness is made by drawing slopes before and after the fracture from the radius-time or the velocity-radius graphs which show a large increase in the radius after the fracture, the mean of the radius being used to give the outer radius of the tube at the fracture point. The above expressions are then used to determinate the breaking thickness.

The measurements have been made from the Imacon photographs by using an eye-piece magnifier which can be used to measure small distances to about ± 0.2 mm, and these measurements are converted to the actual values by multiplying them by the magnification ratio of the camera optics. The error bars which are drawn on the radius-time curves indicate the maximum error variation.

Figure (7.4a) shows a graph of outer radius–time of an HDPE tube of 13.56 mm outer diameter with thickness of 3.5 mm, and length of 8cm. This tube was loaded by an 8cm/22swg wire explosion at 25kV. From the fourth order polynomial equation of this graph, the outer surface velocity was obtained by differentiation. The velocity-radius graph is shown in Figure (7.4b). The engineering hoop strain against time graph is shown in Figure (7.4c). The calculations from this experiment give the maximum velocity of the outer surface of the tube as 404 m/s before the fracture, as shown in Figure (7.4b). The tube has fractured at an engineering hoop strain of 340%, engineering strain–rate of 4.94×10^{4} s^{-1}, velocity of 200 m/s, and radius of 29.5mm at 80 μs after the explosion. The breaking thickness of this tube has been estimated to be 0.6 mm compared with the measured value of 0.74 mm. Figure (7.4d) shows the tube after the test. The fracture appears ~ 80 μs after the expansion starts at radius of about 30 mm as shown in high speed photograph in Figure (7.4a). The

fractured part of the cylinder has about same thickness throughout except the ends which remain intact with a small deformation. The feature of plane strain is clear in this case causing uniform deformation in the middle part of the cylinder.

Figure (7.5a) shows the outer radius–time graph of an HDPE cylinder of 6.78 and 3.39 mm outer and inner radii respectively with a length of 8cm. It has been loaded by an explosion from an 8cm/22swg copper wire fired at 25 kV. From the first differentiation of the polynomial fit equation of the graph, the velocity of outer surface of the cylinder was obtained, which increases rapidly at the fracture point, as shown in Figure (7.5b). This also shows the velocity keeping at a constant value of 450 m/s before the fracture. First differentiation of the polynomial equation of the engineering strain–time graph (Figure (7.5c)) gives the peak engineering strain–rate of 8.71×10^{4} s^{-1}, and a maximum engineering strain of 334%. This cylinder fractured at an engineering strain of 232% with an estimated thickness of 0.83 mm compared with the final measured value of 1 mm. The outer radius was 21 mm at the fracture point 35μs after the explosion. The fractured tube is shown in Figure (7.5d).

In the above experiments the direct blast wave loading creates a high temperature on the inner surface of a cylinder. To protect the tested HDPE cylindrical specimen from the high temperatures of the explosion, experiments have been done where the thin–walled tube specimen has been placed as a sliding fit on another tube. The inner tube's dimensions are 7, 3.9, and 9.9 mm outer, inner radii and length respectively, while the tested tube's dimensions are 9 and 7 mm outer and inner radii respectively with a length of 8 cm. Loading by an 8cm/22swg wire at 25 kV produced the record in Figure (7.6a). The estimated thickness at the fracture point is 0.6 mm and the final measured value is 1.1 mm. As shown in Figure (7.6a) the tube fractured at radius 27.9 mm at 105 μs after the explosion. The

velocity at the fracture point is 379 m/s as shown in Figure (7.6b), and the engineering hoop strain is 212% as shown in Figure(7.6c) which gives a strain-rate of 4.24×10^4 s^{-1}. The peak engineering strain-rate is 6.3×10^4 s^{-1}, and the maximum engineering strain is 264.3%. The double tubes are fractured symmetrically as shown in Figure (7.6d). The photograph shows the breaks in all the direction around the tubes.

In addition to the possible temperature rise from the explosion, tube temperature can increase due to its strain. Assuming that the hoop stress is uniform for a thin-walled tube with short rise time at high rate of plane strain, and considering that volume V remains constant, the work done on the tube can be found. Equating the mechanical to the thermal energy, then

$$V\int\sigma d\epsilon = ms\Delta T$$

$$\Delta T=(V/ms)\int\sigma d\epsilon = (1/\rho s)\int\sigma d\epsilon$$

where m is the mass of the material, ρ is the density, s is the specific heat, and ϵ is the true strain.

For HDPE (Ahmad 1988), flow stress of 45 MPa. For a true fracture strain of ϵ=157%

then $\Delta T=\frac{45\times10^6\times1.57}{955\times2400} = 31\ ^{0}C$

This value is the temperature rise due to the strain of the tube. Thus, the temperature of the tube for a room temperature of 21 ^{0}C will be at least 52 ^{0}C. The temperature increase causes an increase in the elongation of the polymers (Higgins 1977). Such a temperature rise of the tube would effect its material behaviour.

Results of the expanding tubes experiments are shown in Table (1), which show that the estimated thicknesses of cylinders are less than

the measured ones. This because of the thickness measurements have been made some time after the experiment letting the fractured cylinders recover. The maximum strain rate is about 6×10^4 s^{-1}.

7.3 Conclusions

The thin expanding tube method has been employed to study HDPE cylindrical specimens subjected to a high pressure pulse from exploding wires. The expansion was photographed by using the high speed photography system, which was described before, but with slower framing rates and using an electronic flash of long duration to provide enough illumination of the tested tubes. Measurements have been carried out to study the conditions that affect the fracture behaviour of the above material. These are the impact velocity (>200m/s), the strain and the strain-rate. The tubes have been broken at engineering hoop strains between 212% and 380% compared with the supplier's typical quasistatic values of about (100-500)%.

From table (1) the results indicate that the breaking thickness of the tubes decreases when the engineering hoop strain at the fracture point increases, and that the tubes are broken at engineering hoop strain-rates above 4×10^4 s^{-1}. Velocities of the outer surfaces of the tubes which have been broken are more than 200 m/s.

The pressure pulse amplitude inside a thin tube decreases with time because of the expansion of the cylinder and the variation of temperature with time, so it is not possible to make an accurate estimation of the pressure to calculate the stresses on the tube wall. Another method has been investigated to study HDPE tubes which can allow measurements of stress to be made. This method is the freely expanding ring technique which will be described in the next chapter.

Table (1)
Expanding tube results.

Print number	Material	Outer radius mm	Inner radius mm	Length cm	Voltage kV	Outer R. at break mm	Breaking thickness measured mm	Breaking thickness estimated mm	Eng. hoop strain %	Eng. hoop strain rate(/s)	Velocity at break m/s	Max. velo. before break m/s
1	HDPE	7.04	3.93	10	20	8.73 *	no	break	19.64 *	1.93×10^4	116.2 *	------
2	HDPE	7.01	4.06	9.95	25	33.65	0.7	0.53	380	4.44×10^4	268.0	381
5	"	6.78	3.28	8.0	"	29.5	0.74	0.60	340	4.94×10^4	200.0	404
6	"	6.78	3.39	"	"	21.0	1.00	0.83	232	6.3×10^4	490.0	440
7	"	6.79	3.62	"	20	8.72 *	no	break	25.1 *	2.56×10^4	178.1 *	------
8	"	6.96	3.36	"	"	9.56 *	no	break	37.4 *	9.74×10^3	74.0 *	------
11 **	"	9.00	7.00	"	25	26.2	1.10	0.62	212.2	3.5×10^4	310.0	200

* maximum values.

** double tubes, the measurements have been made for the outer tube.

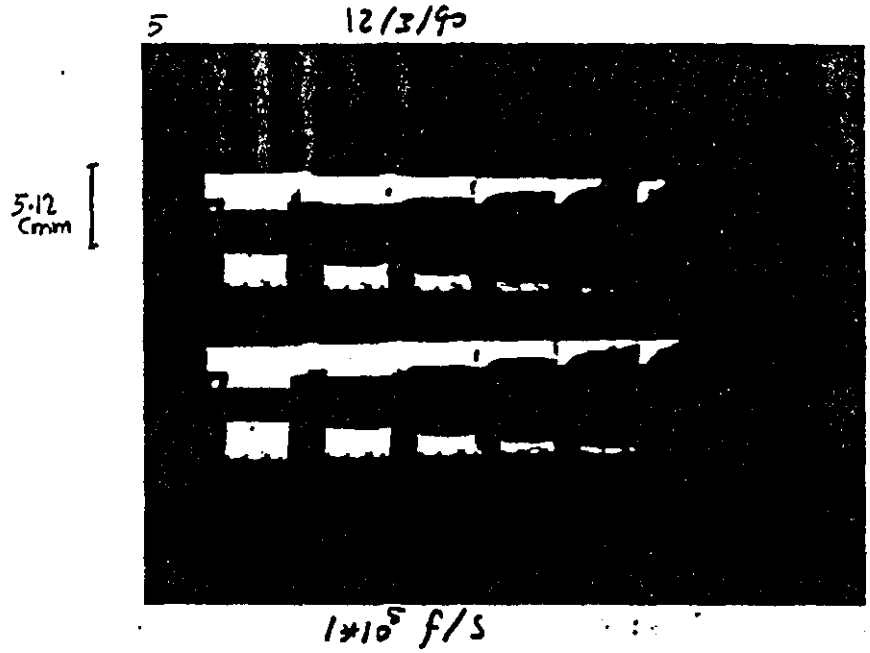

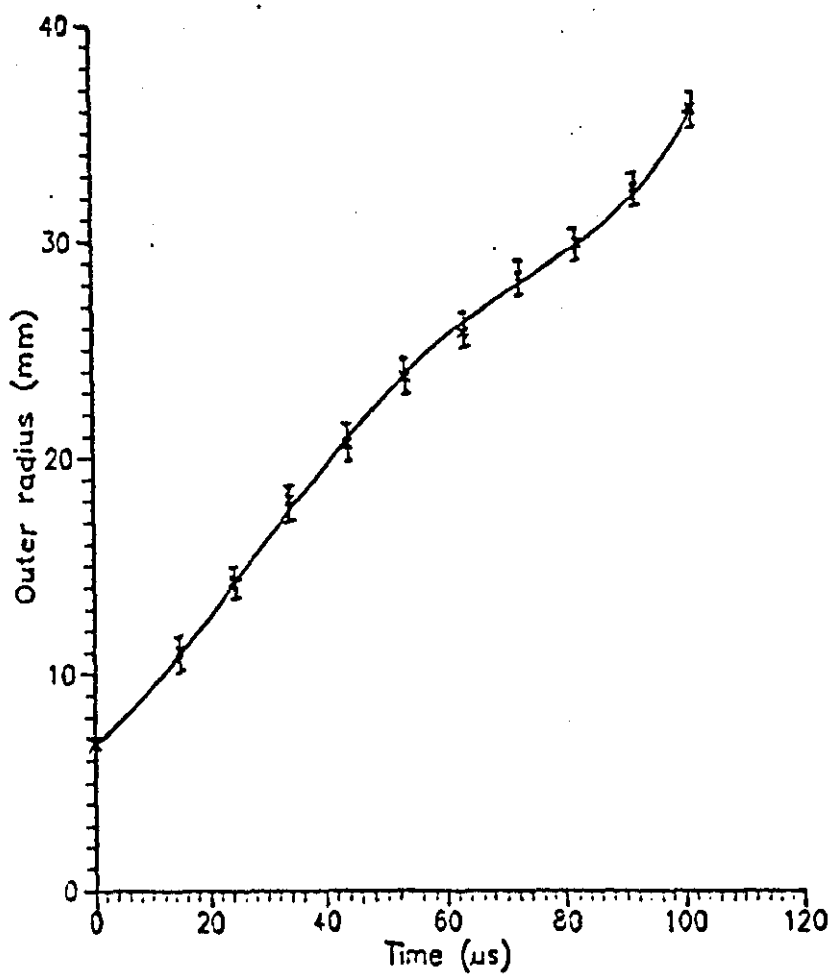

Figure (7.4a) Outer radius against time of HDPE tube, 13.56mm o.d., 3.5mm thick, and 8 cm long fired by an 8cm/22swg wire at 25 kV.

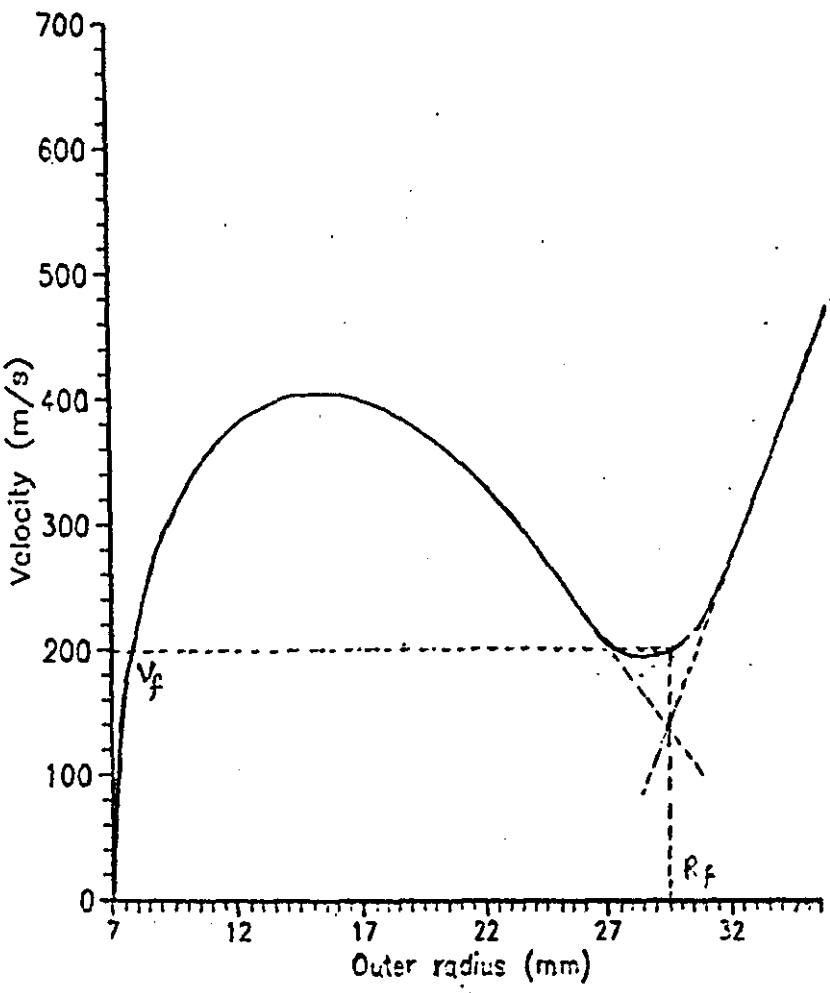

Figure (7.4b) Velocity against radius for HDPE tube of 13.56 mm o.d., and 3.5mm thick loaded by an 8cm/22swg wire explosion at 25 kV.

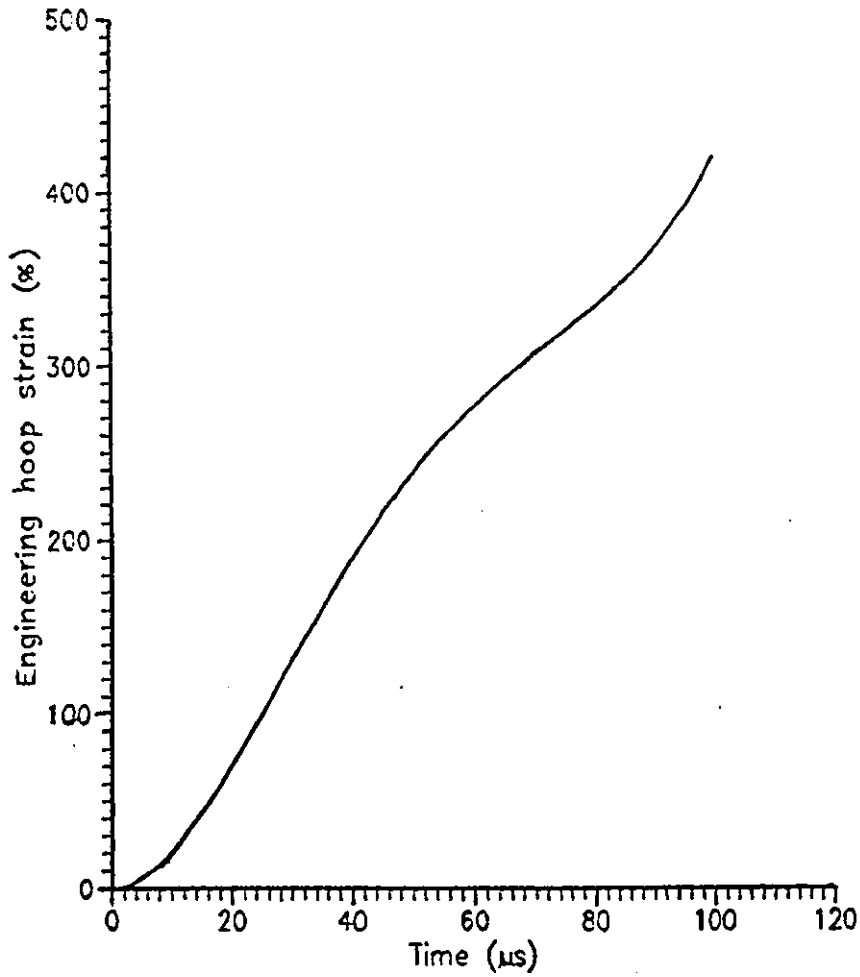

Figure (7.4c) Engineering hoop strain against time of HDPE tube of 13.56mm o.d.,and 3.5mm thick fired by an 8cm/22swg wire at 25 kV.

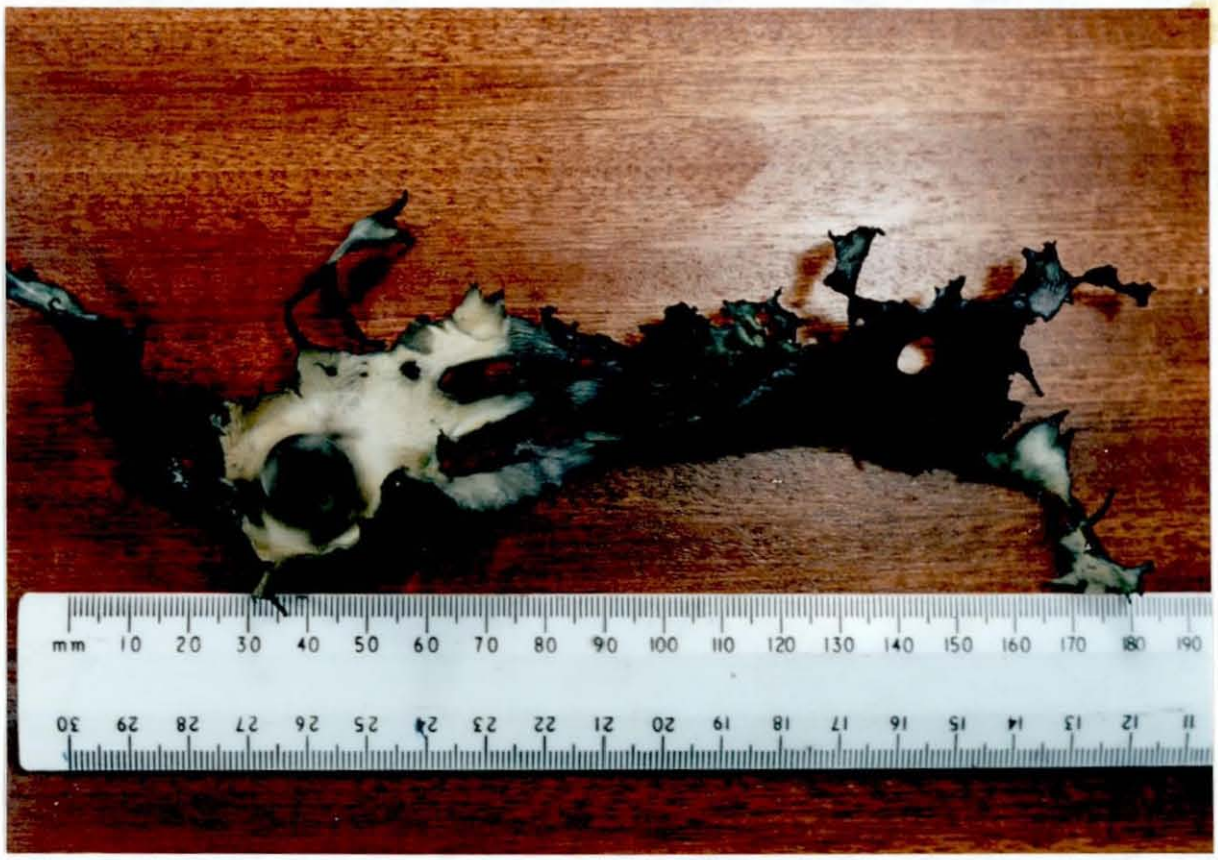

Figure (7.4d) Fractured HDPE tube, 13.56 mm o.d., and 3.5 mm thick fired by an 8cm/22swg wire at 25 kV.

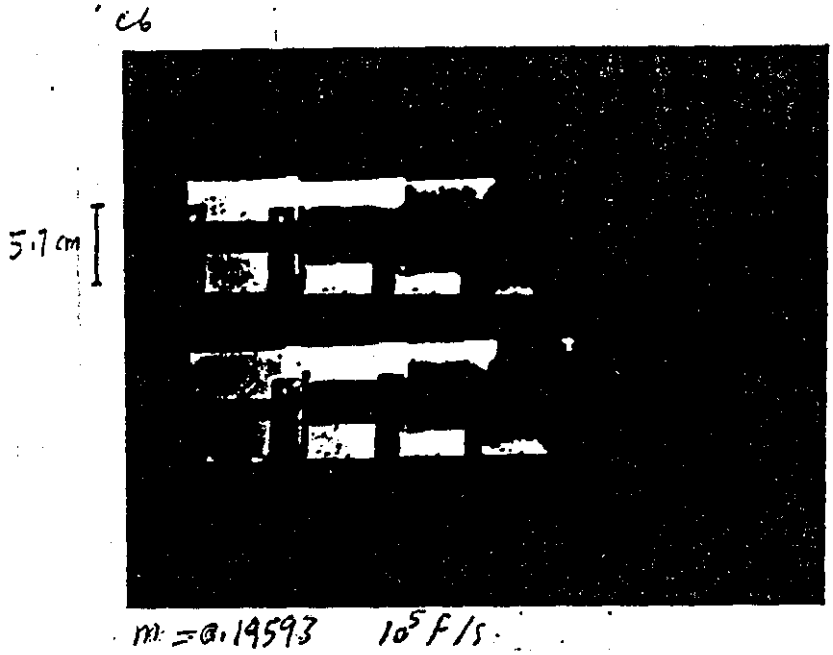

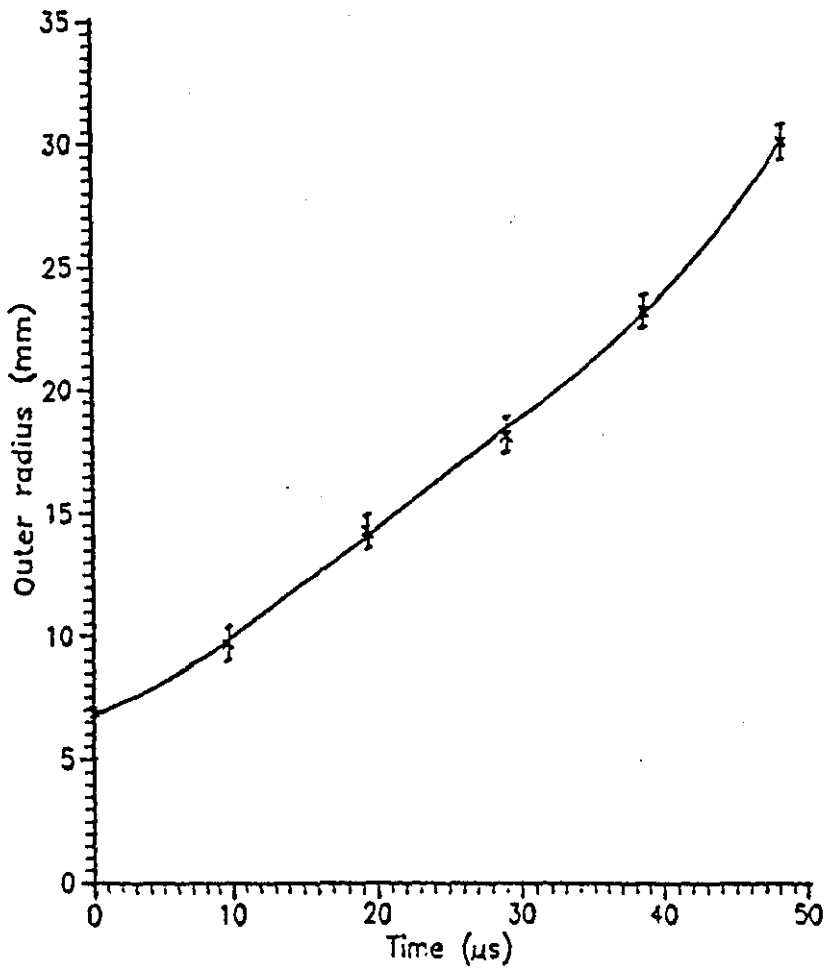

Figure (7.5a) Outer radius against time for HDPE tube of 6.78mm o.d.,3.39mm i.r., and 8cm long fired by 8cm/22swg wire at 25 kV.

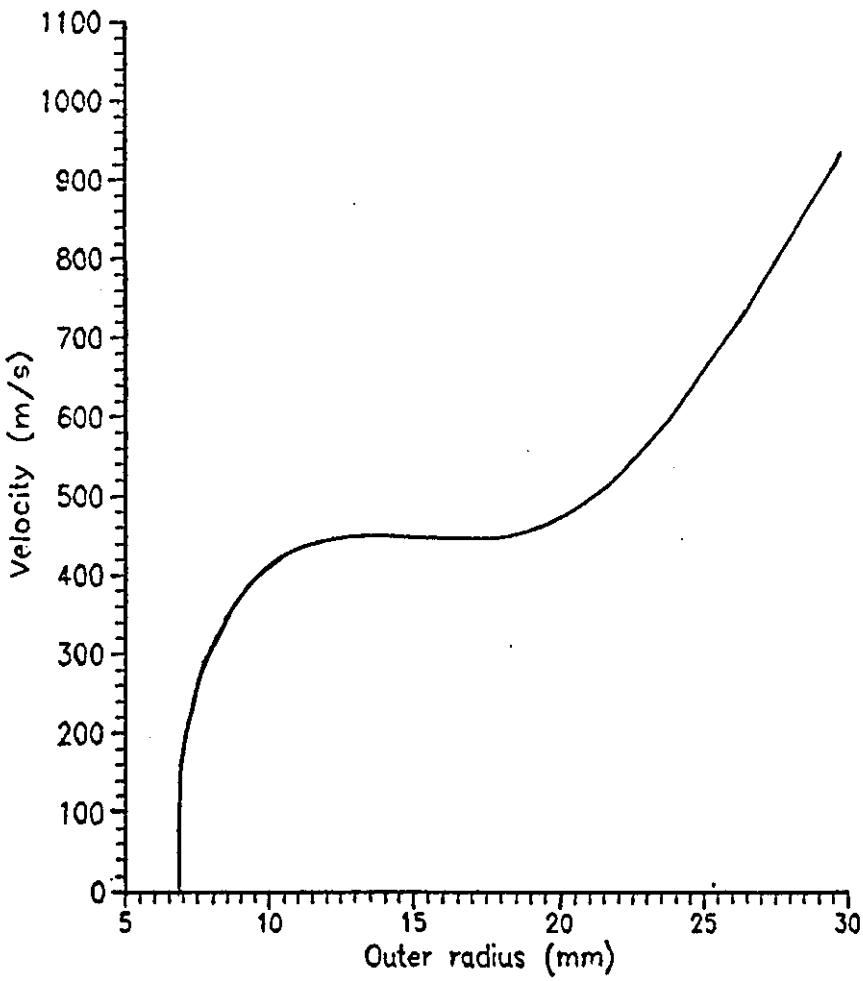

Figure (7.5b), Velocity-radius graph for HDPE tube of 6.78mm and 3.39mm outer and inner radii respectively fired by 8cm/22swg wire at 25 kV.

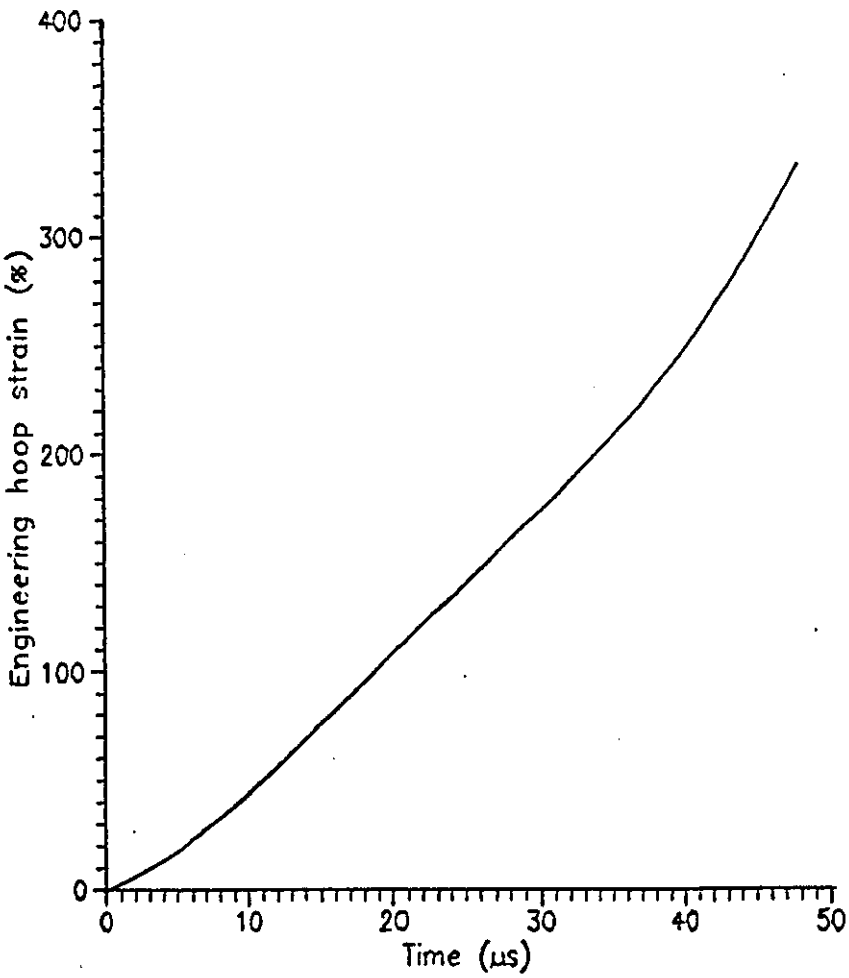

Figure (7.5c). Engineering-time graph for HDPE tube of 6.78 and 3.39 mm outer and inner radii fired by 8cm/22swg wire at 25 kV.

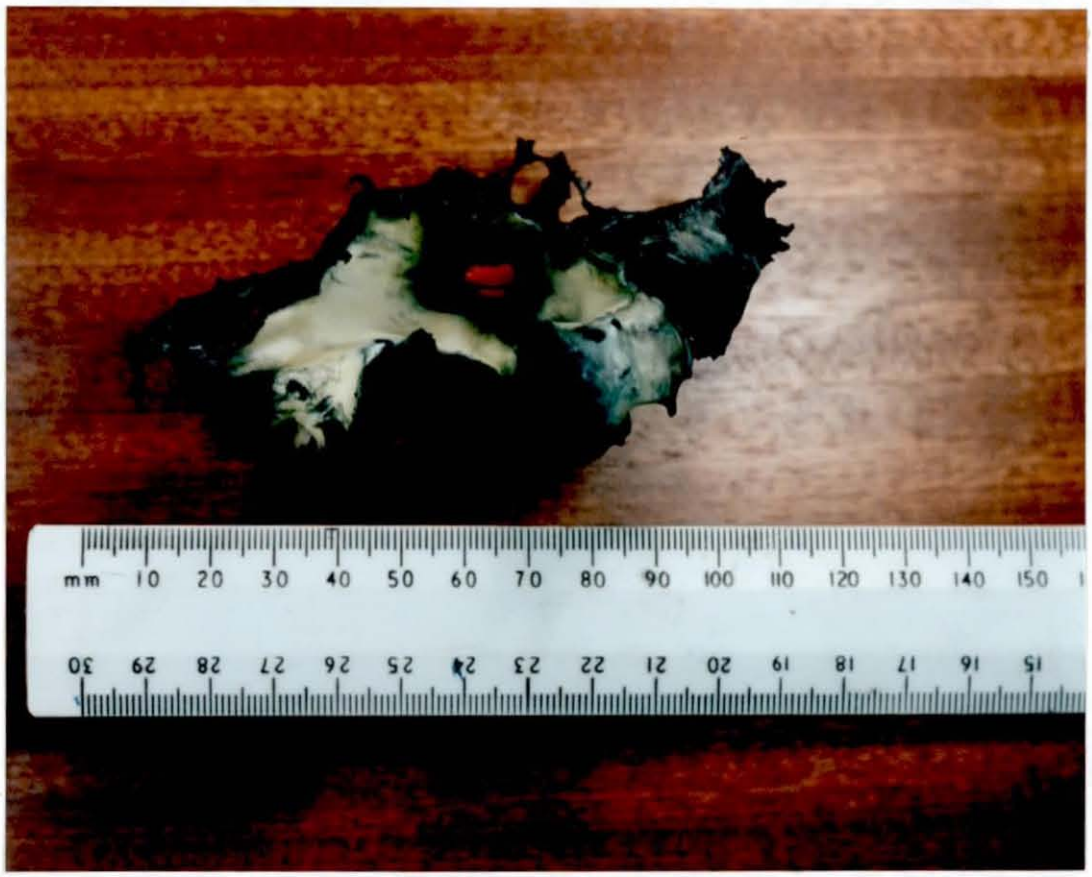

Figure (7.5d) Tested HDPE tube of 6.78 and 3.39 mm outer and inner radii fired by 8cm/22swg wire at 25 kV.

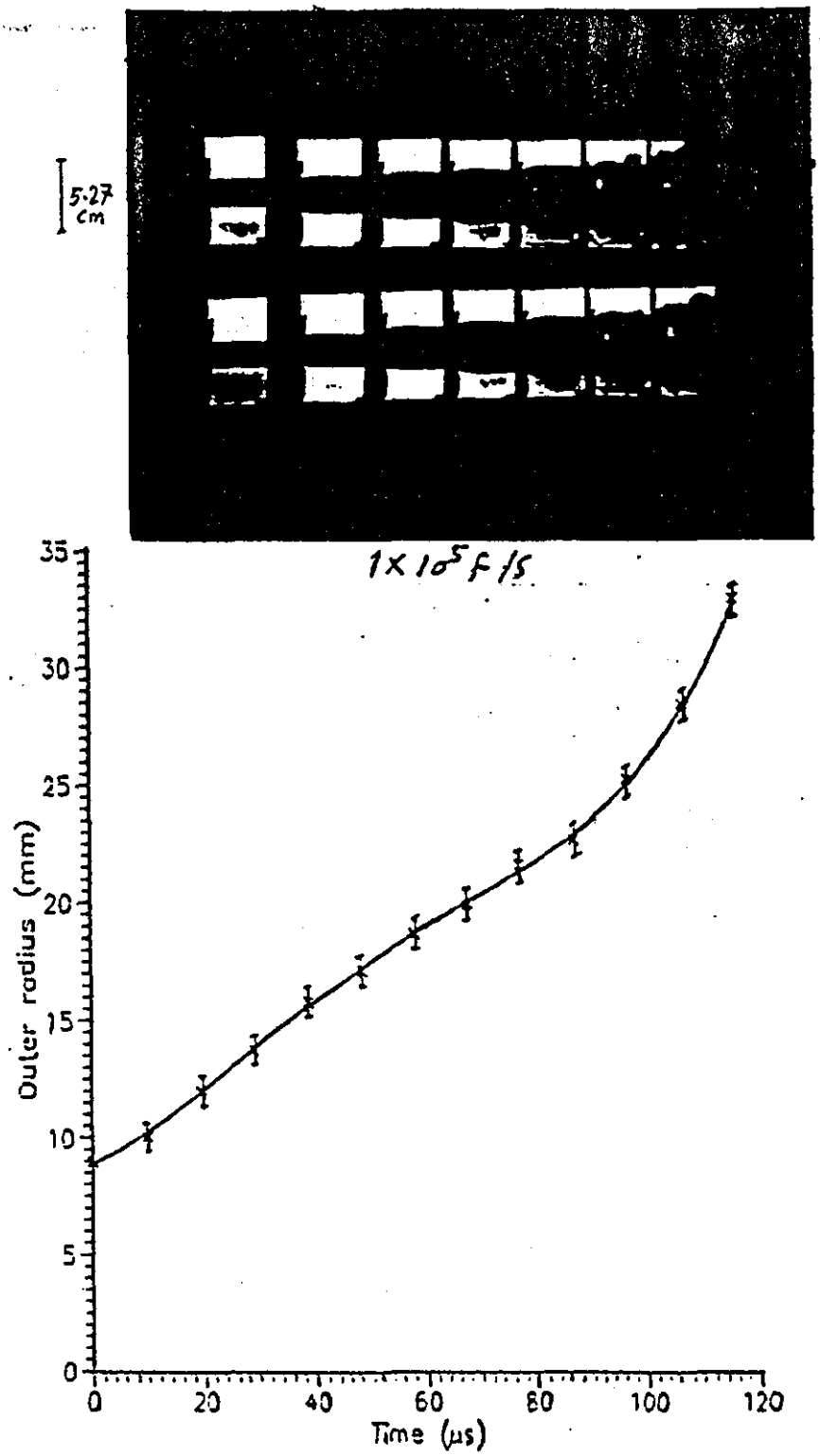

Figure (7.6a) Graph of outer radius against time for HDPE tube of 9mm o.r., and 7mm i.r fired by 8cm/22swg wire at 25 kV.

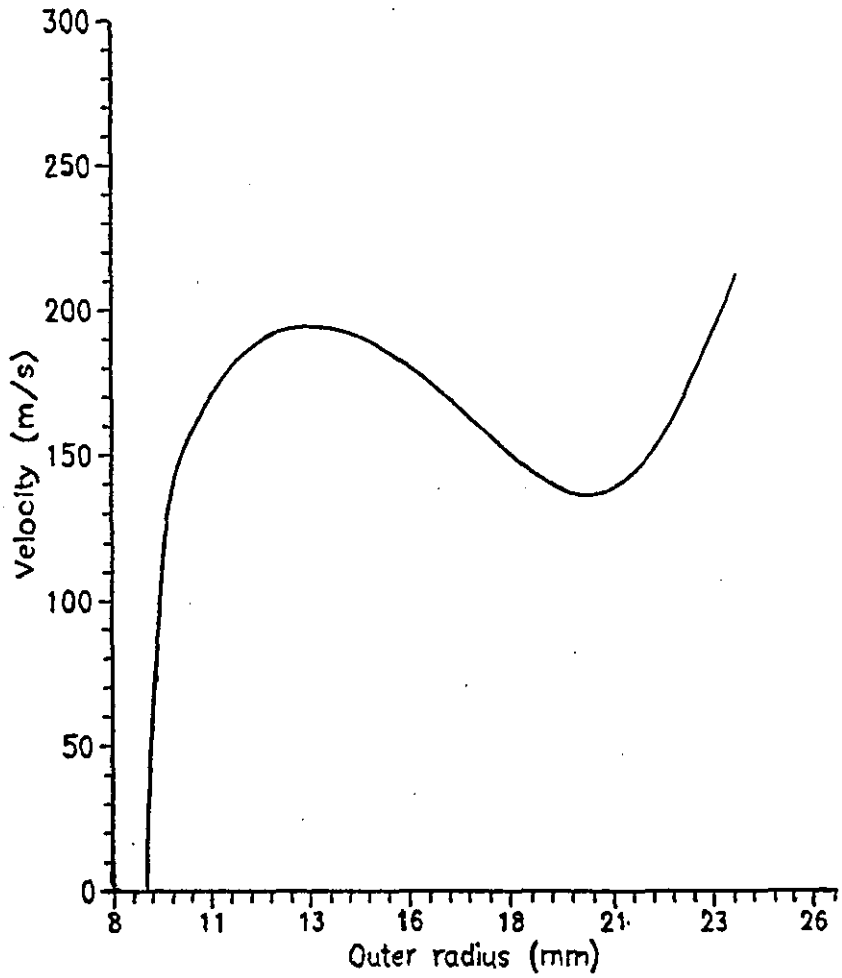

Figure (7.6b) Velocity-radius for HDPE tube of 9mm o.r., and 7mm i.r. fired by 8cm /22swg at 25 kV.

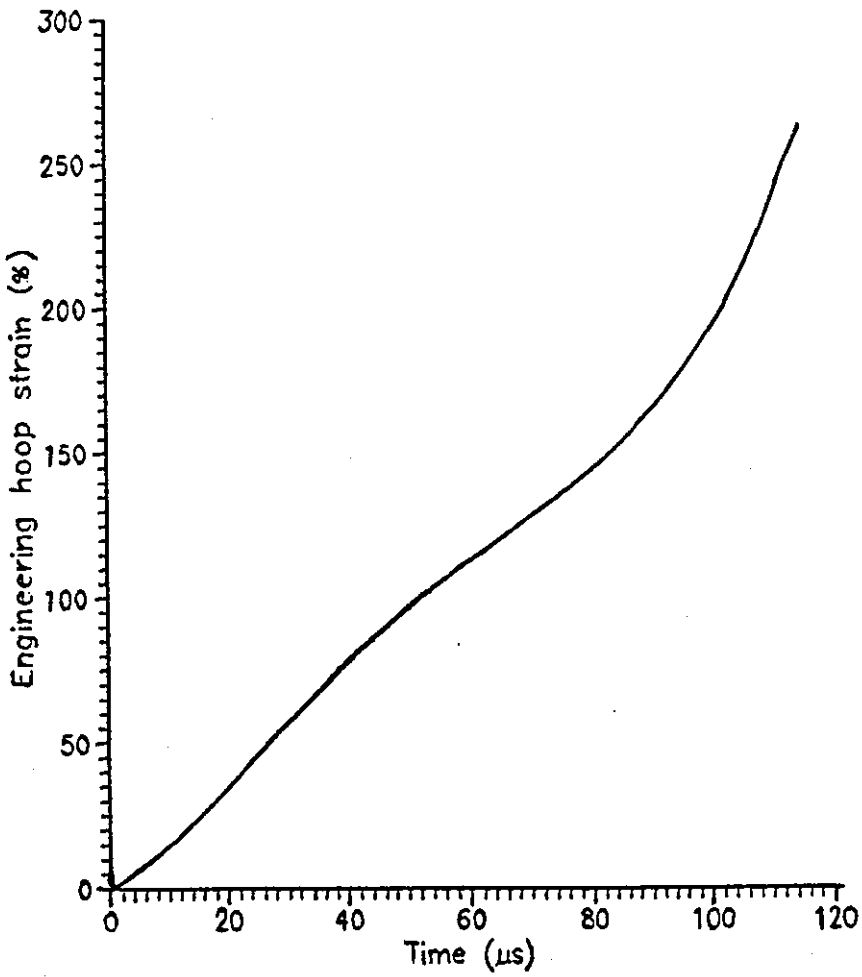

Figure (7.6c) Engineering hoop strain against time for HDPE tube with o.r. of 9mm, i.r. of 7mm fired by 8cm/22swg wire at 25 kV.

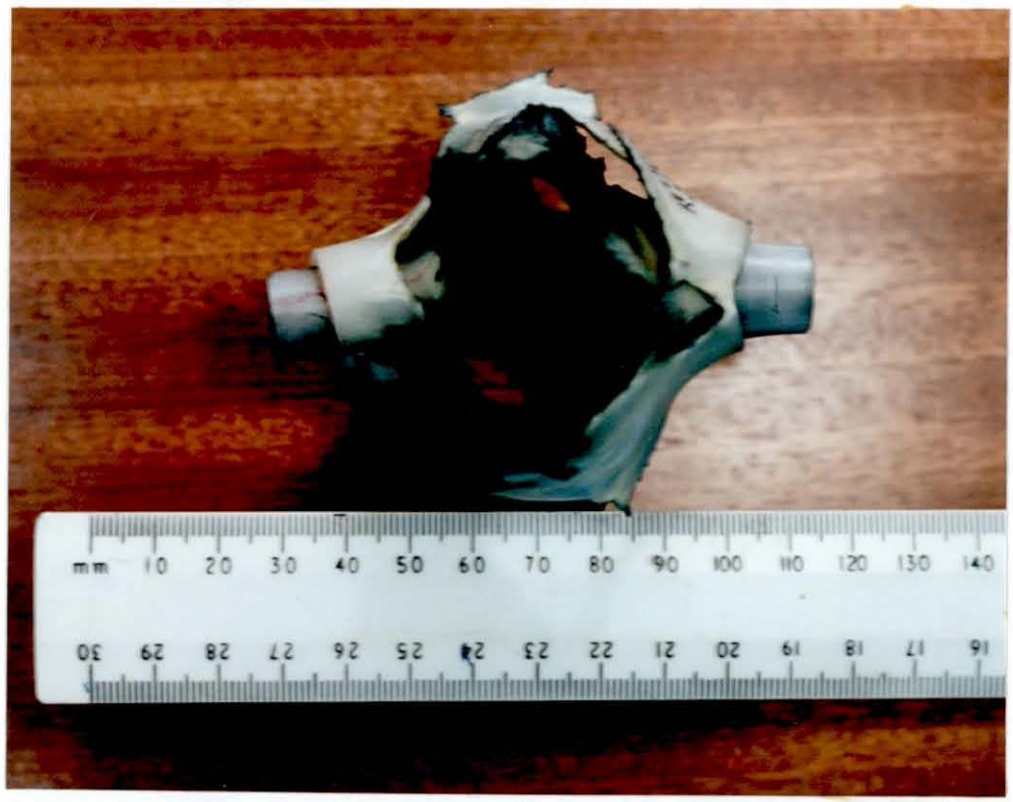

Figure (7.6d) Double HDPE tubes fractured by an 8cm/22swg wire explosion at 25 kV.

CHAPTER 8
EXPANDING RINGS

8.1 Introduction

The expanding ring technique is a method of obtaining high strain-rate properties of materials (Zukas 1982). The ring can be shown to be under a state of uniaxial stress, while a cylinder is in a state of plane strain, when loaded with a symmetrical radial pressure.

Clark and Duwez (1950) used the expanding ring as well as the cylinder geometry for testing materials at high-strain rate. Their method of securing a uniform high strain rate was to use a thin-walled hollow cylindrical specimen in which circumferential strain is induced by an internal fluid pressure by means of a piston moving at constant velocity. They computed the maximum fluid pressure from the value of the maximum force. The formula used to find the stress is

$$\sigma = p\frac{r_a}{d}$$

where p is the pressure, d the wall thickness, and r_a is the average radius of the cylinder.

Niordson (1965) developed a dynamic deformation method for a ring by using an electromagnetic force generated by a 24 windings coil supplied by a discharge current from 12 μF capacitor.

Hoggatt, et al (1967) used the deformation caused by explosive charge. In 1969 he and Recht approximated the true hoop stress of the thin rings by the following formula

$$\sigma = -\rho R \frac{\partial^2 R}{\partial t^2}$$

where ρ is the mass density of the material, R the outer radius of the ring, and $\partial^2 R/\partial t^2$ is the radial deceleration of the ring flight. They calculated the true strain rate from:

$$\dot{\epsilon} = \frac{\partial R/\partial t}{R}$$

where $\dot{\epsilon}$ is the strain-rate, and $\partial R/\partial t$ is the ring velocity.

Circular aluminium rings were impulsively loaded with axisymmetric short duration pressure pulses by Forrestal and Walling (1972) who compressed the rings into the plastic regime and measured their response by strain gauges. They did comparisons of the measured strain-time history with two theoretical predictions, one using an elastic-perfectly plastic stress-strain law, and the other using a strain-stress law suggested by Lindberg (1968), (1970). The closest comparison was the first prediction.

An experimental method for impulsively loading structural rings with a simultaneously applied, short duration pressure pulse has been presented by Walling, Forrestal, and Tucker (1972). They utilized a fast discharge capacitor bank and a current pulse shaping technique to provide a pressure pulse with a duration of about 2 μs, which is sufficiently short that loading can be considered impulsive for most structural ring experiments.

A magnetic pressure pulse has been used by Walling and Forrestal (1973) to expand 6061-T6 aluminium rings dynamically. The magnetic pressure pulse was used to load the ring for a short duration, and

the ring response was measured by strain gauges. The gauge output was subjected to interference for the first 20 μs from electrical noise from the capacitor bank switching and current shaping. The ring response depends on its geometry and the stress-strain law of the material. To avoid the noise they achieved a pulse of less than 10 μs duration that provided clean signals from the strain gauges that were used for measuring circumferential strain in the ring.

Wesenberg and Sagartz (1977) used the same technique of generating a magnetic pressure pulse from a capacitor discharge to study the dynamic fracturing process in aluminium cylinders at strain rate of up to $10^4\ s^{-1}$.

Fyfe and Rajendran (1980) used a thin cylinder configuration accelerated by an exploding wire system and laser-photomultiplier system for displacement measurements to study strain-rate and strain history effects on the fracture of metals.

Forrestal et al (1980) developed a new explosive loading technique for producing nearly uniform expansion of thick-walled cylinders. Strain-rates achieved on AISI 304 stainless steel cylinders were in axcess of $4000\ s^{-1}$.

The expanding ring method has been improved by Warnes et al in 1980 for determining dynamic material properties. This improvement is centred around the incorporation of a direct velocity-measuring device (velocity interferometer) to remove the necessity of double differentiation of the experimental data.

Carden, et at (1980) used the expanding ring method by subjecting a 6061 aluminium ring to uniaxial loading to obtain the stress-strain dependence from the radial-velocity versus time behaviour.

Daniel, LaBedz, and Liber (1981) tested a composite material at strain rates in the 100 s^{-1} to 500 s^{-1} regime. Their method employed a thin ring specimen loaded by an internal pressure pulse applied explosively through a liquid. They based their analysis on a numerical solution of the equation of the motion involving smoothing and approximation of the strain data, strain-rate and strain accelerations.

The freely expanding ring technique was used by Warnes, Karrp, and Follansbee (1985) for determining the stress-strain behaviour of materials at large strains and at high strain-rates. This technique consists of placing a thin ring of test material in a state of uniform radial expansion by pressing the ring carefully onto a high strength steel driving cylinder. The ring moves outward without the action of external forces. Radial ring velocity decreases, however, because of the action of internal circumferential flow stresses. By this technique they extended the test of the materials to strain rates of 2.3×10^{4} s^{-1}. The experiments used copper rings subjected to an internal explosion. The measurement of the expanding ring velocity $\partial R/\partial t$ was taken directly by a laser velocity interferometer. They used three thin rings instead of one to reduce the time required for the central ring (the ring to be tested) to achieve the one-dimensional motion necessary for the equation $\sigma=-\rho R\partial^{2}R/\partial t^{2}$ to be correctly applied.

Courdin (1989) has also used the expanding ring method to study the constitutive properties of copper and tantalum at high rates of tensile strain.

In the Physics department, Loughborough University, the freely expanding ring method has been examined since the expanding tube experiments require measuring the loading pressure accurately if the stress is to be found. So to avoid the difficulty of pressure measurement the free expanding ring was studied. The method involves

placing a thin ring around a thick-walled cylinder and subjecting the cylinder to internal blast wave loading. The shock wave propagates through the cylinder and is then partially transferred into the ring, which then moves at high velocity away from the cylinder and then decelerates under the action of the hoop stress. By measuring the displacements by high speed photography, the true stress can be determined by the equation which was used by Hoggatt and Recht (1967) ($\sigma=-\rho R\partial^2 R/\partial t^2$).

8.2 Expanding ring theory

The wire explosion has been used for providing an impulsive loading for a cylindrical specimen. The explosion produces a short duration pressure pulse. In the freely expanding ring system the energy propagates through the wall of the cylinder, and then transfers into the ring, which is a sliding fit on the cylinder. The ring expands at high initial radial velocity, and then decelerates because of the opposing radial component of the circumferential stress. This method has been used to produce a uniform deformation by a symmetrical expansion of a thin narrow ring or tube avoiding the problem of wave propagation.

The ring leaves the inner cylinder, which can be considered as a driver, the loading pressure being zero after the separating of the ring from the driver. The ring continues to expand by its own radial inertia. The movement of the ring is opposed by the radial component of the circumferential (hoop) stress, causing decelerating of the ring. Consider a ring as shown Figure (8.0), at zero driving pressure. The equation of motion is F=MA (Hoggatt and Recht 1969), where F is the force, M is the mass, and A is the acceleration.

For a small element of the wall of the ring:

$$dFi = dmA = \pi\rho(R_0^2 - r_0^2)L_0(d\theta/2\pi)(\partial^2R/\partial t^2)$$
$$dF\sigma = -2\sigma(R-r)L \sin(d\theta/2)$$

where dF_i - initial radial force
dF_σ - radial component of hoop stress
dm - element mass
$\partial^2R/\partial t^2$ - deceleration of the ring
σ - true hoop sress
ρ - density
R - external radius
r - internal radius
θ - solid angle
L_0 - initial length
and L - axial length

At all stages

$$dFi = dF\sigma.$$

By solving the equation for stress it becomes, for small θ,

$$\sigma = -\rho \frac{(R_0^2 - r_0^2)}{2(R-r)} \frac{L_0}{L} \frac{\partial^2 R}{\partial t^2}$$

For an isotropic material, the radial and axial strains are equal, which gives

$$\frac{L_0}{L} = \frac{R_0 - r_0}{R-r} .$$

and under uniaxial stress condition,

$$\frac{Vol}{(Vol)_0} = \left(1 + \frac{\sigma}{E}\right)\left(1 - \frac{\nu\sigma}{E}\right)^2$$

where $Vol = \pi(R^2-r^2)L$ the volume

E = Young's modulus

ν = Poisson's ratio.

By combining the above equations and simplifying, the resulting equation for true stress can be closely approximated for a thin ring to be :

$$\sigma = -\rho R \frac{\partial^2 R}{\partial t^2} \quad .$$

True strain is given by

$\epsilon = \ln(R/R_0)$, which gives a true strain-rate of

$$\dot{\epsilon} = \frac{\partial R/\partial t}{R}$$

By a polynomial curve fitting of the radius-time measurements and double differentiation of this curve, true stress can be obtained. Also from velocity a true strain-rate can be determined. The advantage of the expanding ring method is that stress can directly be evaluated and no pressure profile is required. Also the ring behaviour is not affected by the variation of the pressure pulse with time.

8.3 Experiments and discussion

As mentioned before, the freely expanding ring method has been used in order to avoid estimating the pressure pulse which is required to calculate the stress for the cylinder method. When the ring is in free flight it is in a state of uniaxial stress, and the stress can be found from the surface displacement, as shown previously.

Several experiments have been carried out to test different dimensions of tube and the ring to define the dimensions which enable the free expansion of the tested ring.

Figure (8.1) shows the mounting arrangement of the expanding ring placed as a sliding fit on a thick-walled tube.

In one experiment an HDPE ring 2mm thick, 5.8 mm wide, and 17.82mm outer diameter, has been placed on a thick HDPE tube 3.3 mm thick, 10 cm long, and 13.82 mm outer diameter. This ring has been fired by an 8cm/22swg wire at 20 kV inside and along the axis of the tube. The expansions of the ring and tube were photographed at a nominal interval of 10μs. The ring outer radius versus time graph with high speed photograph and CRO record are shown in Figure (8.2a). The first differentaition of this graph gives the velocity of the outer surface, which reaches a maximum value of 70.4 m/s and then decreases as shown in Figure (8.2b). The ring behaves together with the inner cylinder as one thick expanding tube. So the freely expanding ring method is not valid in this case. An engineering hoop strain-time plot is shown in Figure (8.2c). This graph gives a maximum hoop strain-rate of 7.9×10^{3} s^{-1}, and a maximum engineering hoop strain of 34.7%. The tested specimen is shown in Figure (8.2d).

Figure (8.3a) shows the high speed photograph, CRO record and the outer radius versus time plot for a 2mm-thick HDPE ring with a length of 5.89 mm, and outer diameter of 17.75 mm placed on an HDPE cylinder

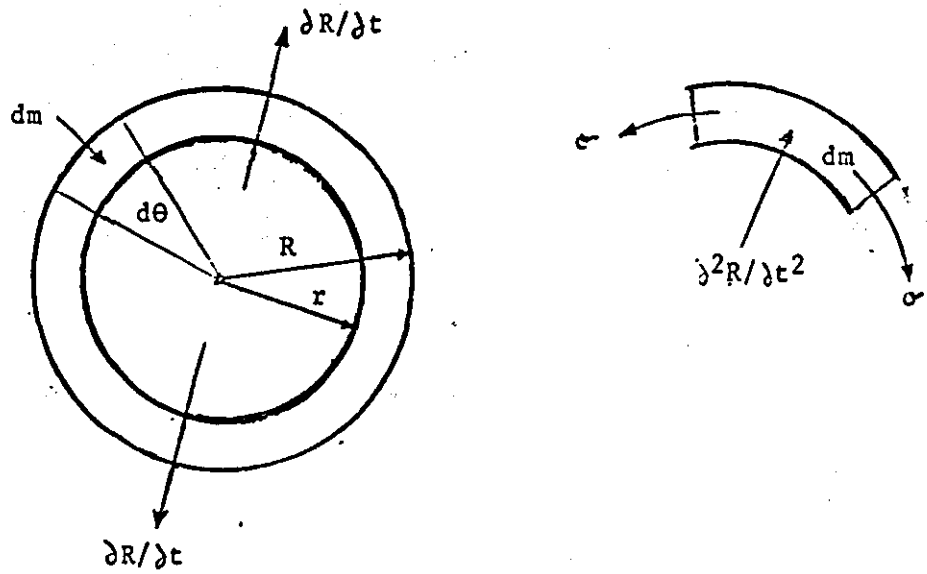

Figure (8.0) Dynamic symmetrical expansion of a thin ring.

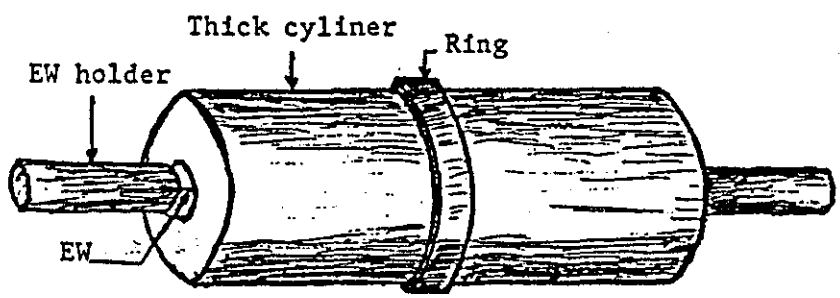

Figure (8.1) Mounting arrangement of a thin ring placed on a thick-walled cylinder.

of 13.75 mm o.d, 3.1 mm thickness, and 10 cm length fired by an 8cm/22swg wire at 25 kV. The first derivative of the polynomial fit equation of radius-time plot gives a maximum velocity of 186.3 m/s as shown in Figure (8.3b) of velocity vesus outer radius graph. Figure (8.3c) shows a graph of engineering hoop strain against time. This gives a maximum engineering hoop strain of 136.7%, and the first derivation of the plot polynomial equation of the degree 4 gives a maximum value of engineering hoop strain-rate of 2.1×10^4 s^{-1}. The ring strengthens the inner cylinder as shown in Figure (8.3d).

In the above experiments, the hoop stress can not be calculated because of the loading pressure is unknown and there is no free expansion condition.

Figure (8.4a) shows the high speed photograph, corresponding CRO record and the outer radius against time for a ring and cylinder. The measurements have been made for a 0.83 mm thick HDPE ring of 6.1 mm length, and 13.3 mm o.r, placed as a sliding fit on a thick HDPE tube of 12.43 mm o.r, 8.2 mm thickness, and 8 cm length fired by an 8cm/22swg wire at 25 kV. The separation between the ring and the outer surface of the cylinder is clear as shown in the high speed photograph and the r/t graph. Also as the graph shows the ring expands faster than the tube, which provides the free expansion condition that is required for calculating the stress directly without knowing the internal loading pressure.

The radius/time graph of the freely expanding ring in Figure (8.4a) has been made by fitting the measured values of the outer radius against time into a third order polynomial equation. The ring velocity has been determined and plotted against time in Figure (8.4b), giving a maximum velocity of 148 m/s. The second derivative of the radius-time polynomial equation is required to calculate the true hoop stress, which is plotted against true hoop strain in Figure (8.4c). This graph shows that the maximum true hoop strain is 34.1%

at a true hoop of 38.4 MPa. Figure (8.4d) shows a graph of engineering hoop strain against time, which gives a peak engineering hoop strain-rate of 1.12×10^4 s^{-1} and then decreases with time becoming zero at zero velocity when engineering strain is 40.6%. Figure (8.4e) shows a photograph of the tested ring around the unfractured cylinder. After the experiment, the inner diameter of the ring is larger than the outer diameter of the cylinder because of the free flight of the ring away from the cylinder, and the fast recovery of the cylinder. Several hours later the ring recovery is noticeable, becoming almost a sliding fit on the cylinder.

Figure (8.5a) shows outer radius-time plots of another thin ring and inner tube system. The dimensions of the HDPE ring are 13.3, 0.7, and 5.92mm outer radius, thickness, and length respectively. This ring was placed on an HDPE thick-walled tube of 12.6 mm outer radius, 9.41 mm thickness, with length of 63 mm. The ring moves outward without external forces by the energy which is received from the tube. The radial velocity of the ring decreases, however, because of the action of the circumferential flow stresses. The separating of the ring from the cylinder, which is shown in Figure (8.5a), provides the free expansion condition. The radius against time data have been fitted into a third order polynomial equation which is required to determine the velocity and the deceleration of the ring. The first derivative of the equation gives the ring velocity as shown in Figure (8.5b), which gives a maximum velocity of about 146 m/s, decreasing to zero after 62 μs. There is an almost constant deceleration. Figure (8.5c) shows the engineering hoop strain against time plot for the ring. There is a maximum strain-rate of 1.18×10^4 s^{-1}, and a maximum engineering strain of 36.8%. True hoop stress is obtained by double differentiation of a cubic polynomial R/t equation. True hoop stress against true strain has been plotted for comparison with quasi-static properties obtained using an Instron machine at strain-rate of 10^{-3} s^{-1} as in Figure (8.5d). This shows the marked increase of the strength of the material at higher strain-rates.

Figure (8.5e) shows a photograph of the tested ring and the cylinder. The volume of the ring has been measured before and after the experiment as 334.23 mm^3, which means that it remains at the same value without change after the deformation. This indicates that the ring deformation was in a plastic manner. The ring as in the previous test continues in slow recovery after the experiment.

8.4 Conclusion

The expanding ring test is a simple method of obtaining material properties in uniaxial tension at high strain-rate by monitoring the uniformly expanding ring. The stress-strain-strain rate response of the ring material can be calculated from the equation of ring motion and the recorded data. The true stress determination requires a double differentiation with respect to time of the ring displacement. Hence, great care must be taken in fitting a polynomial to the initial radius/time data from the photographic records. In order to achieve better resolution in the early stages of the expansion, future work should use a higher framing rate for the camera.

This method provides direct measurement of stress from the record avoiding the difficulty of measuring or estimating the internal pressure which is required to calculate the stress on the wall of the tube. To slow down the movement of the cylinder and leave the expanding ring to fly away, a thick-walled cylinder and a thin ring are required. The freely expanding ring method provides a strain-rate above 10^4 s^{-1} in the early part of the test, the rate then decreasing with time to become zero at zero velocity at a true strain of about 30%. A marked increase in material strength at these high strain-rates can be observed as shown in the comparison with conventional quasi-static tests at 10^{-3} s^{-1} using an Instron machine.

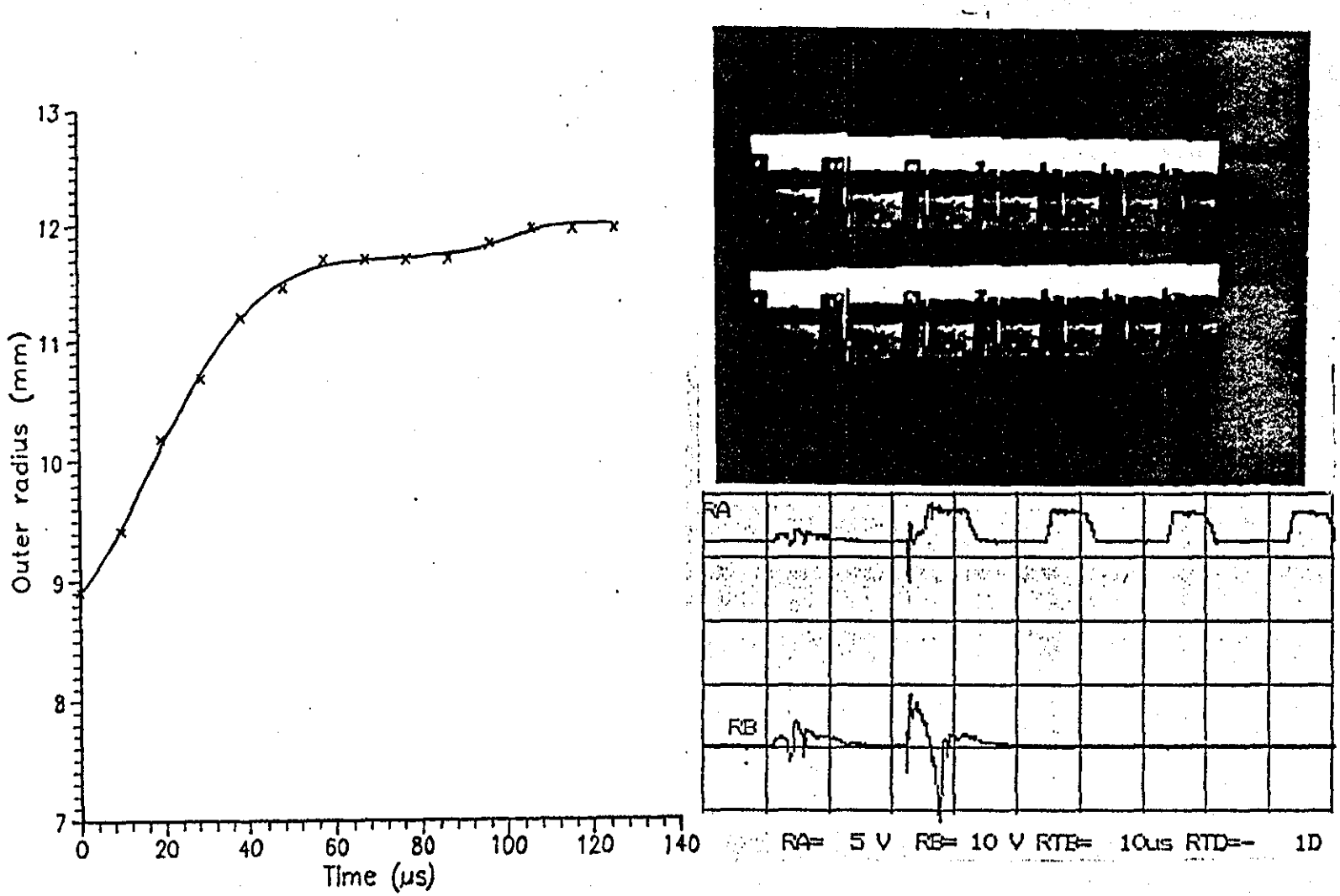

Figure (8.2a) High speed photograph(10^5f/s) with corresponding CRO record and outer radius/time graph for HDPE ring 8.91mm o.r., 6.91mm i.r., and 5.8mm length placed on HDPE cylinder 6.91mm o.r., 3.2mm thick, and 9.9 cm length fired by 8cm/22swg wire at 20 kV.

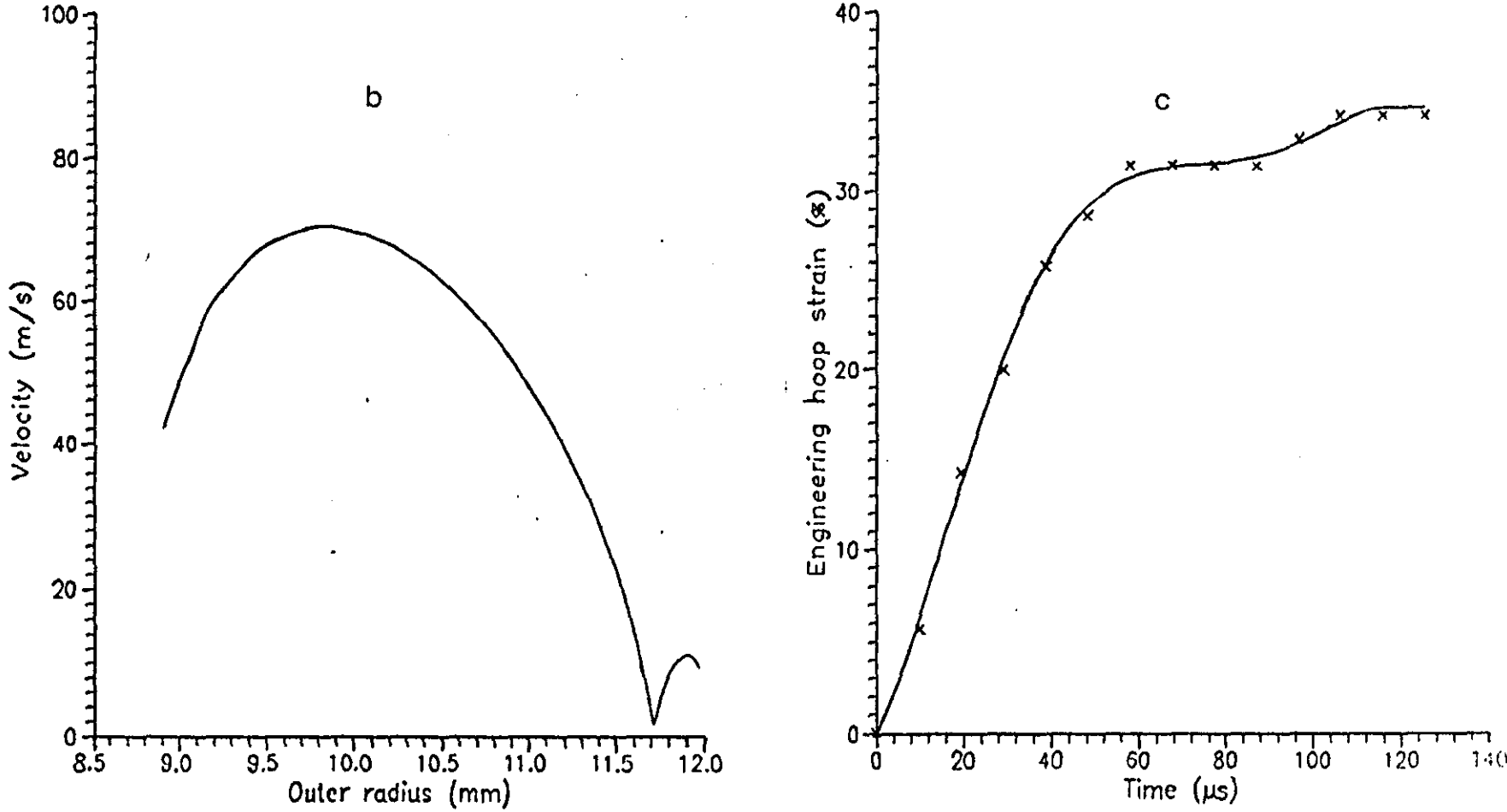

Figure (8.2) Velocity/radius (b), and engineering strain/time[(c)] plots for HDPE ring (8.91mm o.r, 6.91mm i.r, and 5.8mm length) placed on an HDPE cylinder, 9.9cm long, and 3.2mm thick fired by an 8cm/22swg wire at 20 kV, as in Figure (8.2a).

Figure (8.2d) Tested HDPE ring of 8.91mm o.r., and 6.91mm i.r, placed on an HDPE cylinder, 6.91mm o.r and 3.2mm thick fired by an 8cm/22swg wire at 20 kV.

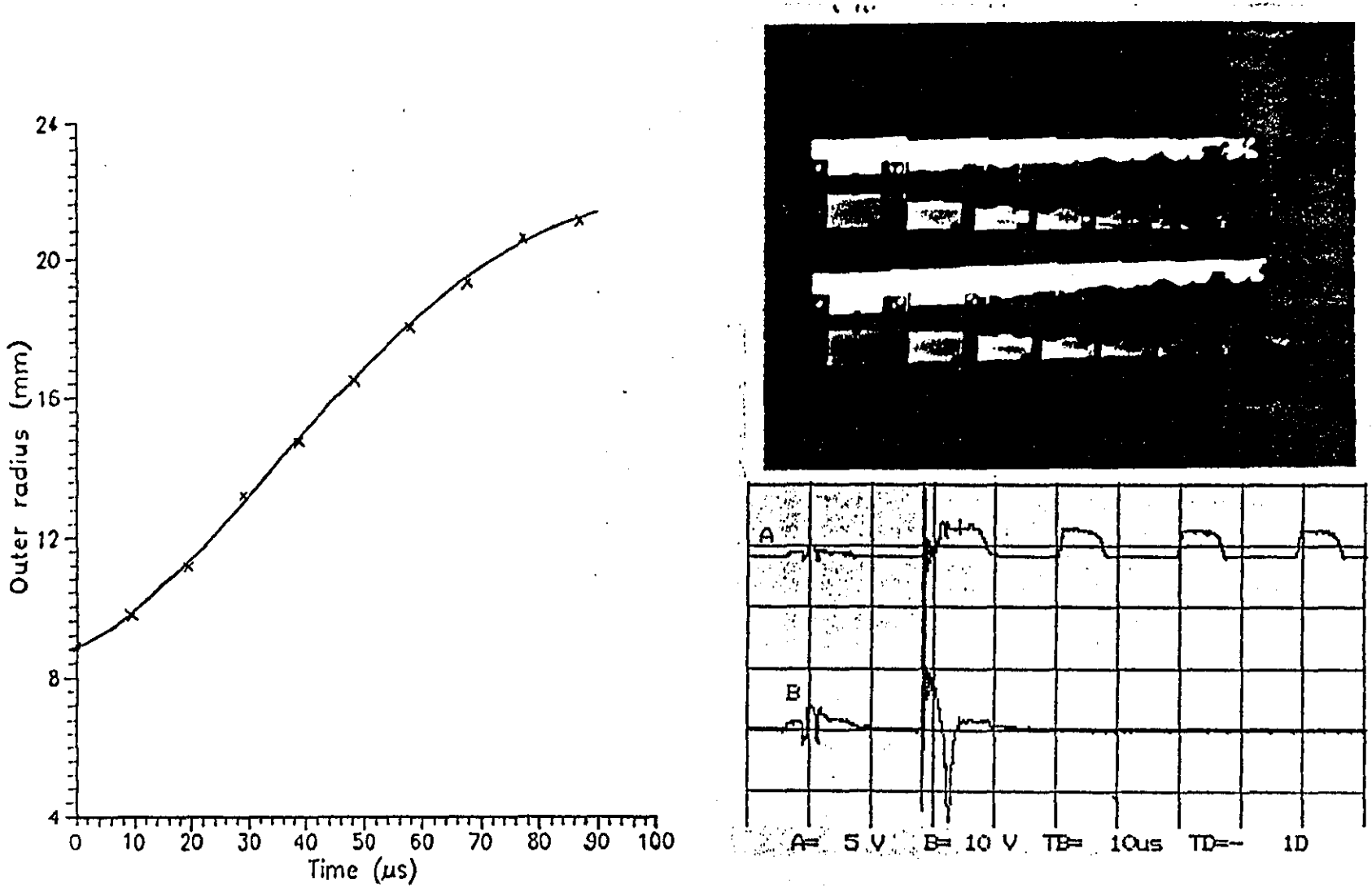

Figure (8.3a) High speed photograph(10^5f/s) and CRO record with outer radius/time plot for a 2mm thick HDPE ring of 5.89mm length and 17.75mm o.d, placed on a 10cm long cylinder of 13.75mm o.d, and 3.1mm thickness fired by an 8cm/22swg wire at 25 kV.

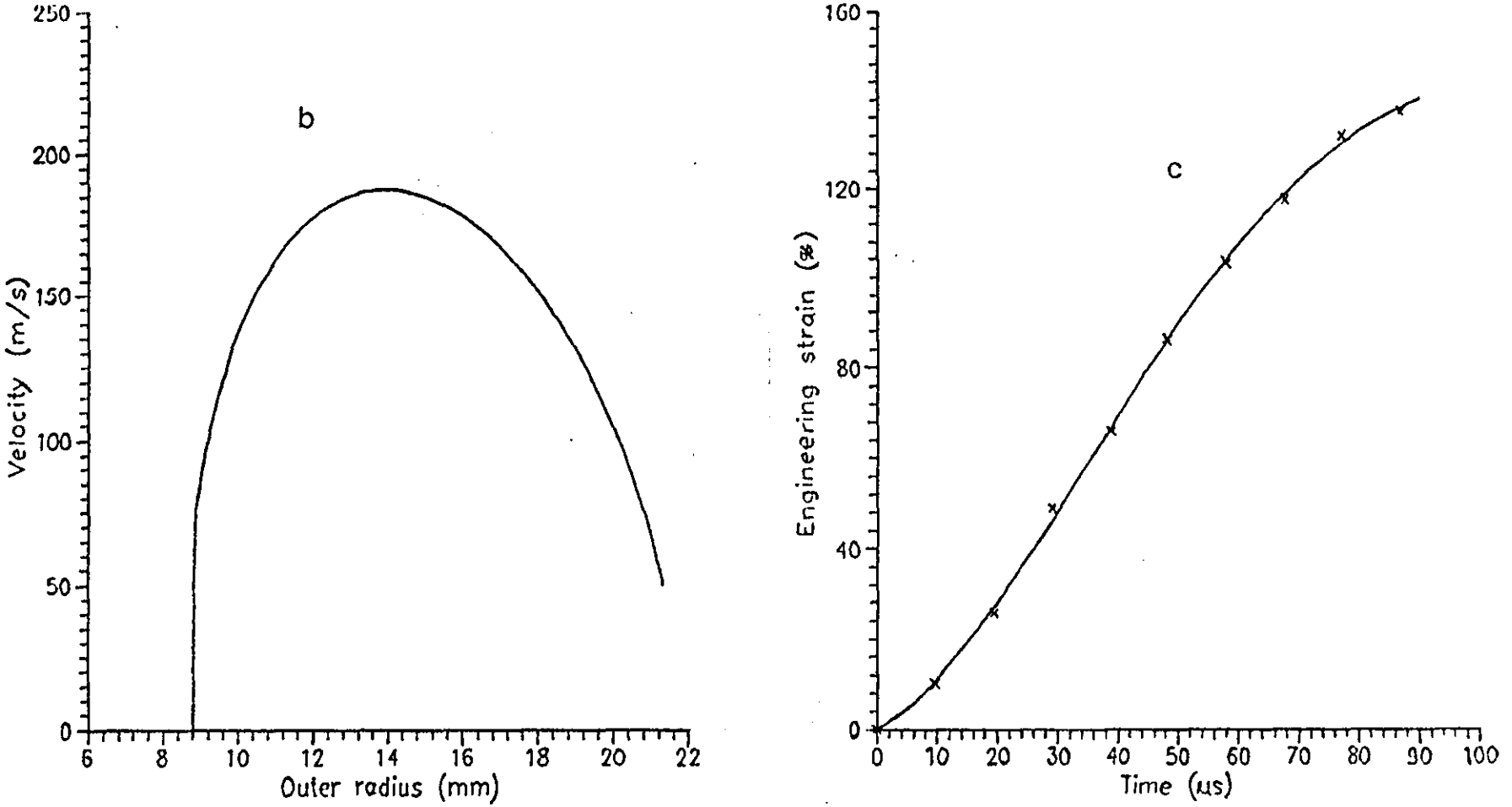

Figure (8.3) Velocity/radius(b), and engineering strain/time(c) plots for an HDPE ring of 2mm thick, 17.75mm o.d, and 5.89mm length, placed on a 10cm lon cylinder of 13.75mm o.r, and 3.1mm thickness fired by an 8cm/22swg wire at 25 kV.

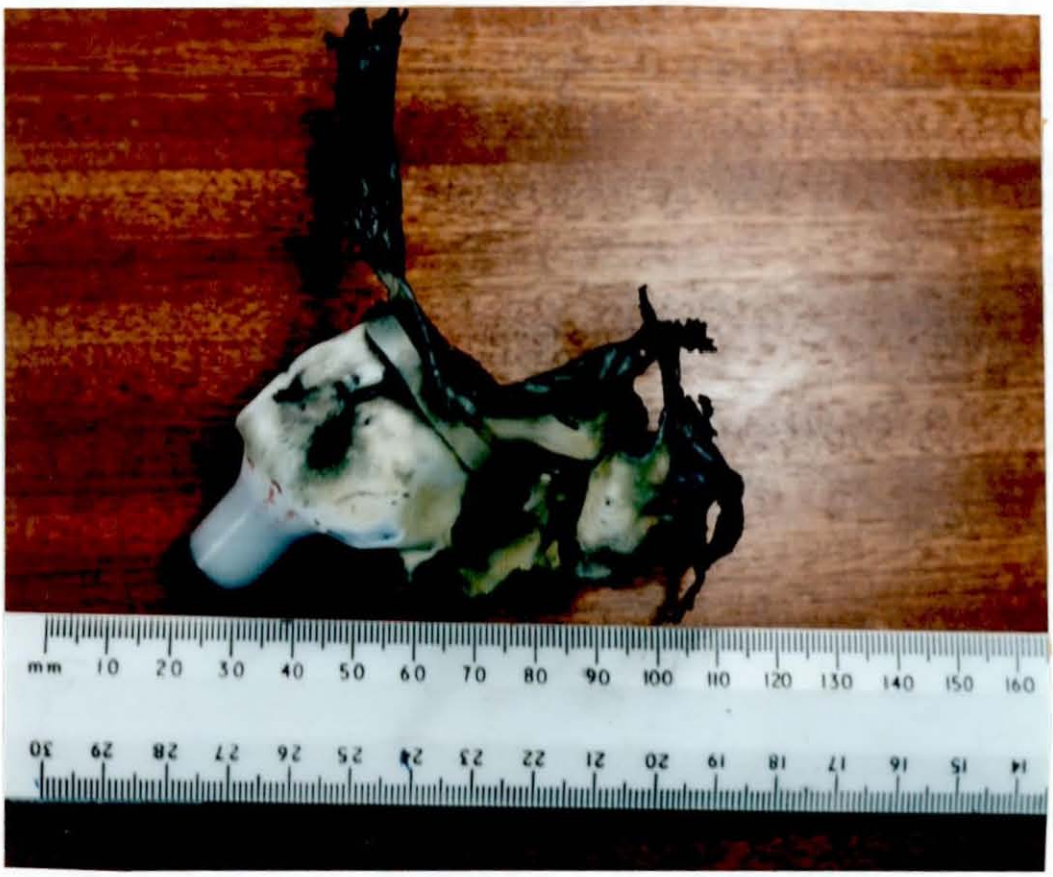

Figure (8.3d) Tested HDPE ring of 17.55 mm o.d, and 13.75 mm i.d placed on an HDPE cylinder of 13.75 mm o.d fired by an 8cm/22swg wire at 25 kV.

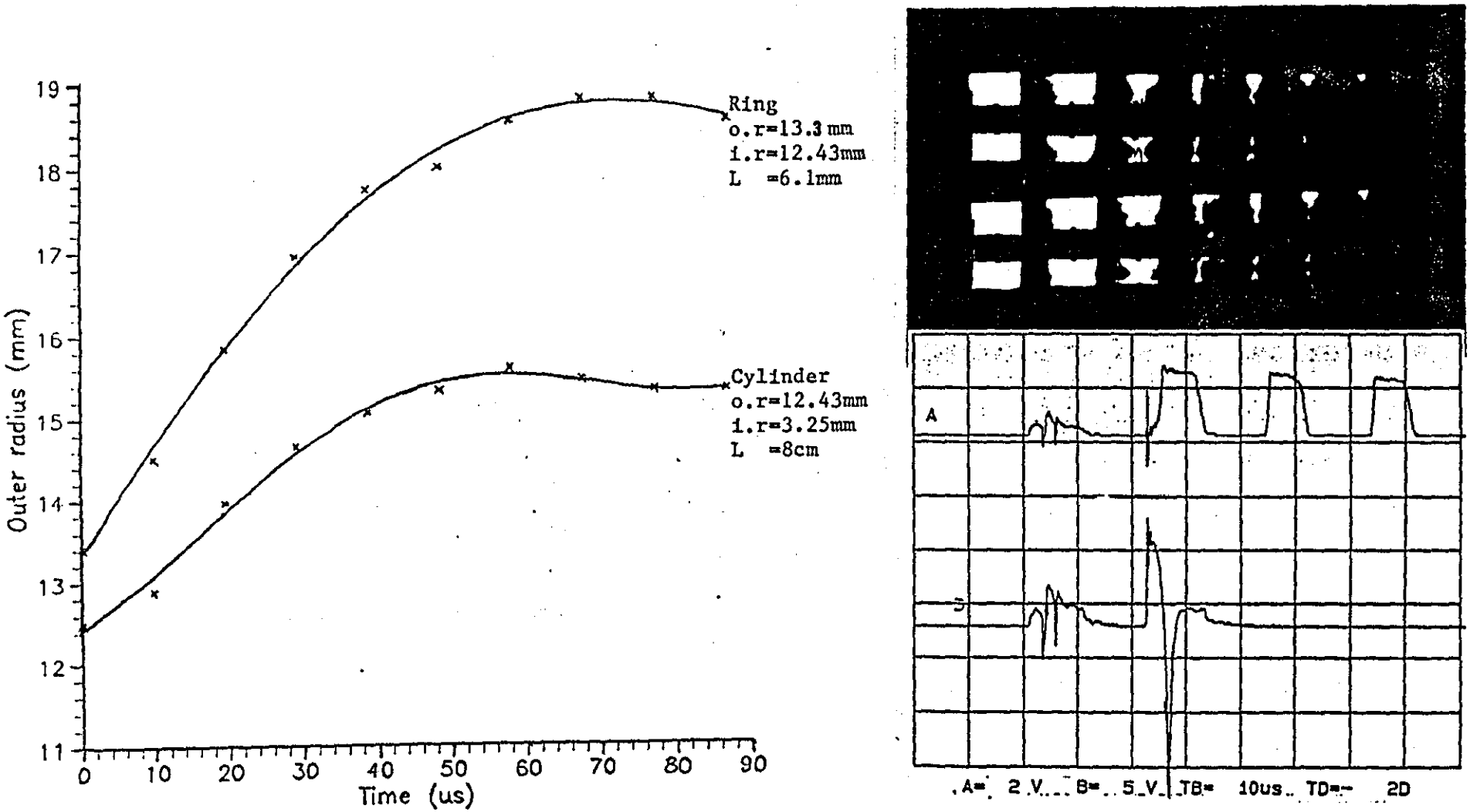

Figure (8.4a) High speed photograph(10^5f/s), CRO record, and outer radius/time plots for HDPE ring and thick-walled cylinder fired by an 8cm/22swg wire at 25 kV.

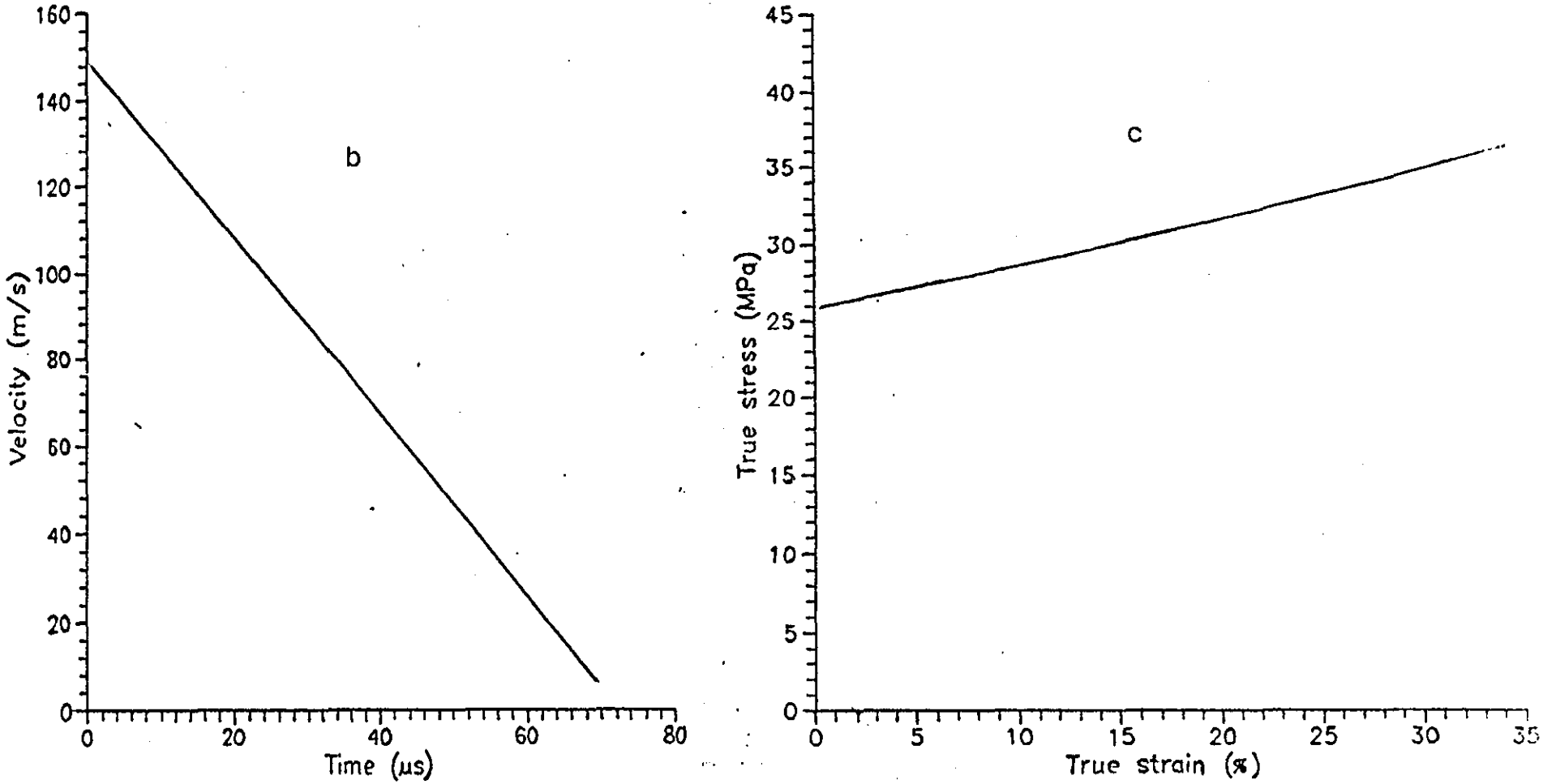

Figure (8.4) Velocity/time(b), and hoop stress/strain(c) plots for a freely expanding ring of 13.3mm o.r, and 12.43mm i.r, placed on a thick-walled cylinder of 9.18mm thickness fired by an 8cm/22swg wire at 25 kV.

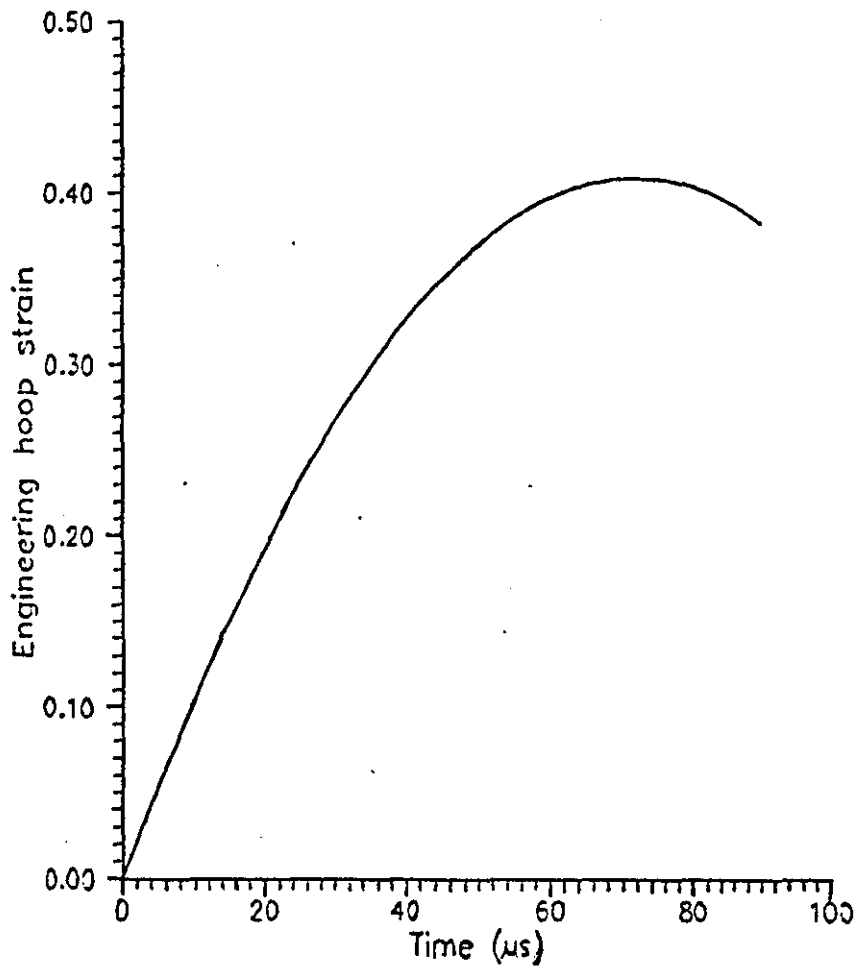

Figure (8.4d) Engineering hoop strain/time plot for a freely expanding ring of 13.3 mm o.r, and 12.43mm i.r, placed on a thick-walled cylinder and fired by an 8cm/22swg wire at 25kV.

Figure (8.4e) Tested HDPE thin ring of 13.3mm o.r, and 12.43mm i.r, placed on a thick cylinder of 12.43mm o.r, and 3.25mm i.r, fired by an 8cm/22swg wire at 25 kV.

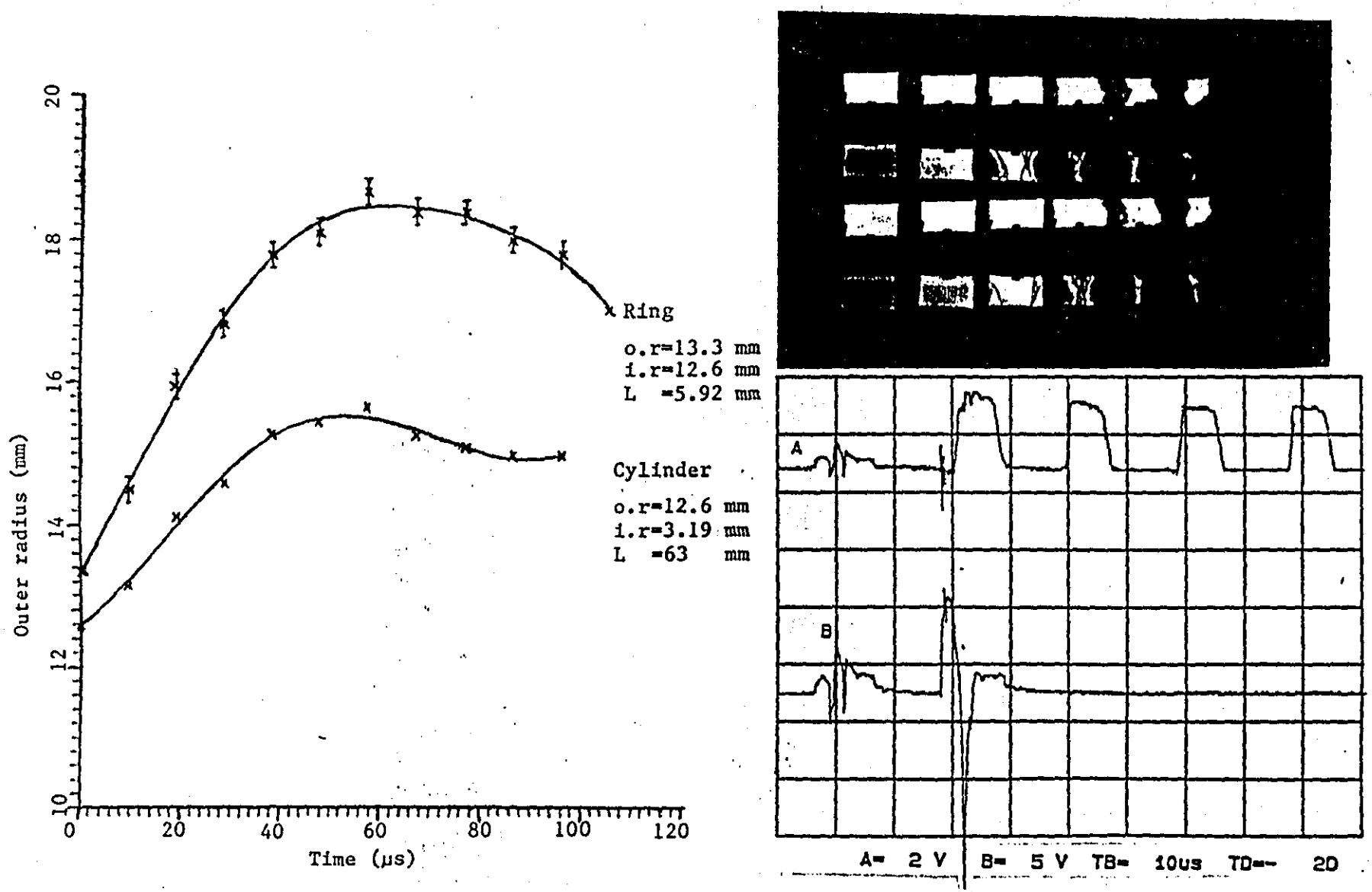

Figure (8.5a)High speed photograph and corresponding CRO record with outer radii against time plot of HDPE freely expanding ring and a thick cylinder fired by an 8cm/22swg wire at 25 kV.

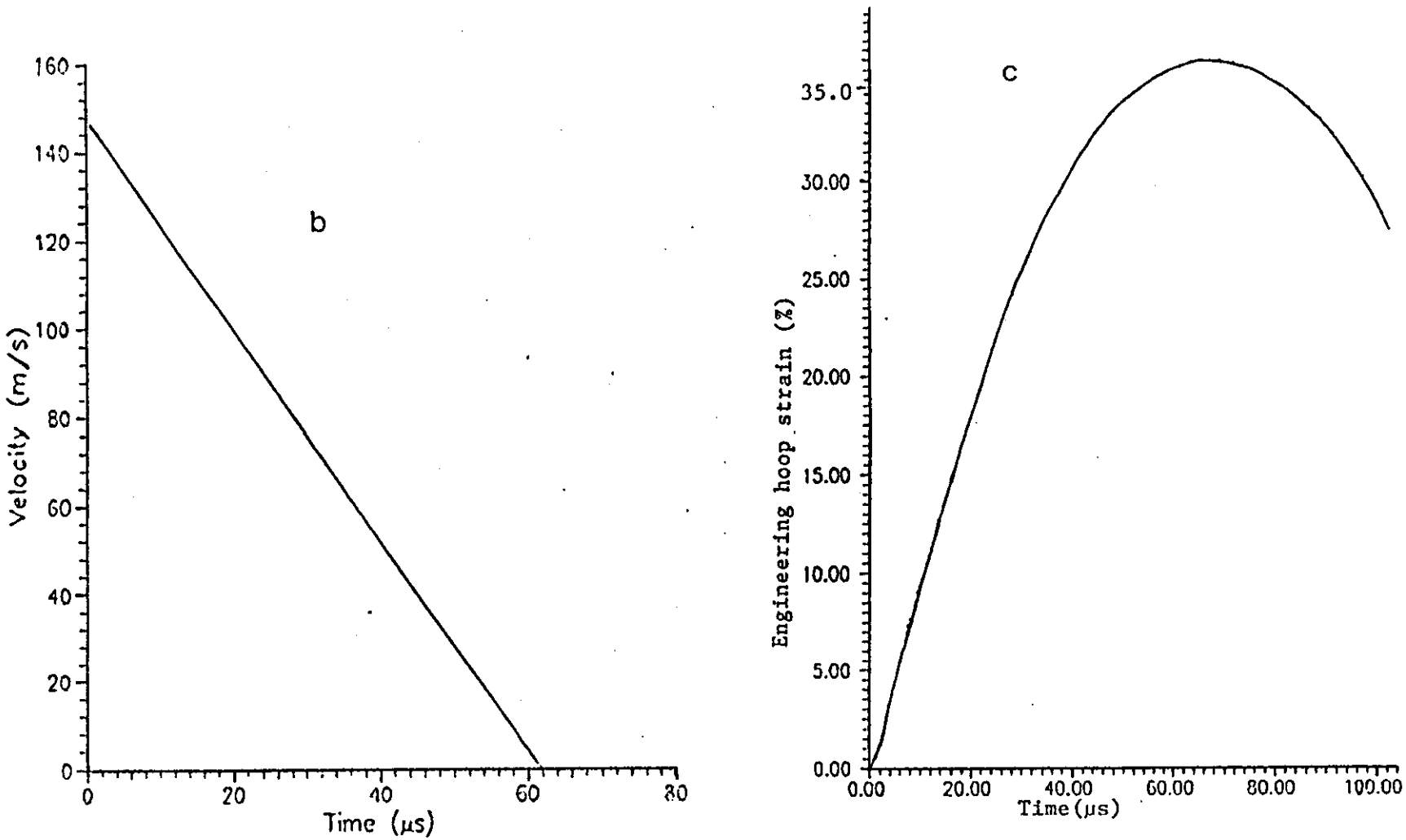

Figure (8.5) Velocity/time(b) and engineering strain/time(c) plots for an HDPE ring of 13.3mm o.r, 0.7mm thick, placed on a thick-walled cylinder of 9.41mm thick fired by an 8cm/22swg wire at 25 kV.

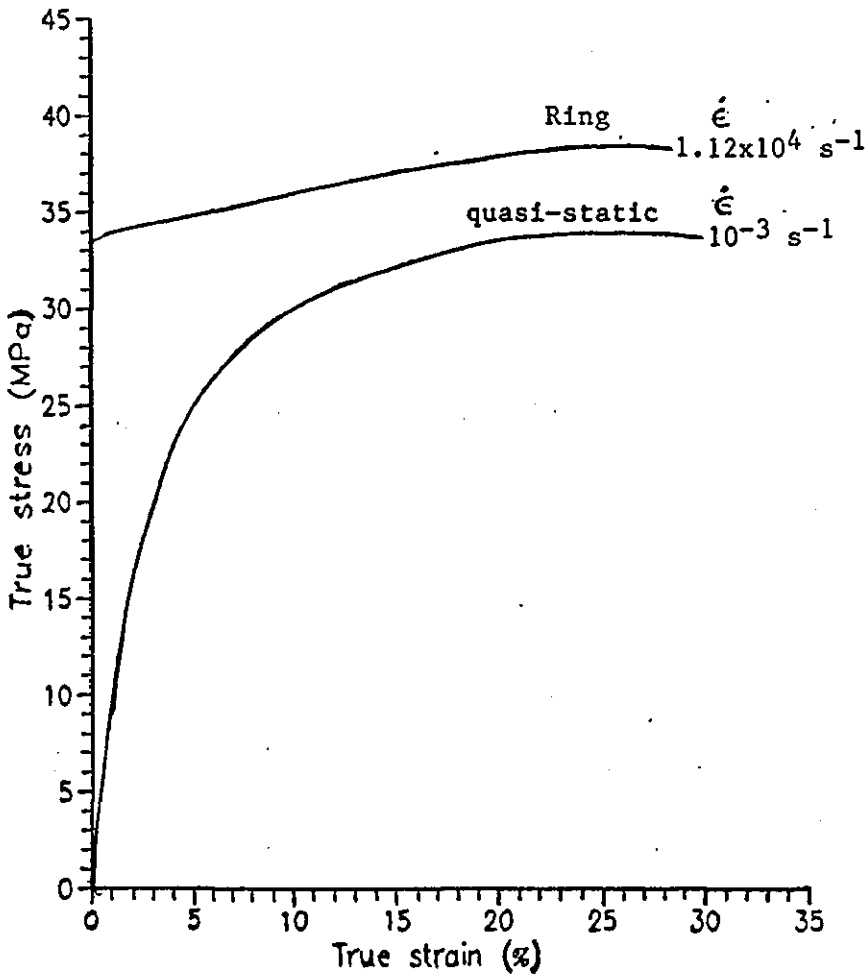

Figure (8.5d) True stress/true strain curves of expanding ring (0.7mm thick, and 13.3 mm o.r) and quasi-static curve of HDPE material.

Figure (8.5e) Tested HDPE thin ring of 13.3 mm o.r, and 0.7 mm thick placed on a thick-walled cylinder 9.41 mm thick, fired by an 8cm/22swg wire at 25 kV.

CHAPTER 9

CONCLUSIONS AND RECOMMENDATIONS

9.1 General conclusions

The work described in this thesis relates to the study of blast waves and their use in impact loading of materials to high strain-rates up to and beyond 10^4 s^{-1}.

The exploding wire technique (EWT) has been used to produce cylindrical, axially symmetrical, blast waves. The exploding wire was photographed before and during the explosion by a high speed camera with a short duration flash. The blast wave generated by the explosion is a high pressure pulse of low rise time and short duration, which is applied to a hollow cylindrical specimen in order to study the response to impact.

The wire explosion takes place when a heavy discharge current of up to about 100 kA passes through a copper wire in approximately 5 μs. This causes rapid vaporisation and a consequent explosion.

In order to generate a wide range of blast wave energies a 13 μF capacitor is used at different voltages of 20, 25, 30 kV, and discharged through 22 swg or 24 swg copper wires of lengths 8 or 13cm.

High speed photography of the exploding wire was executed using the schlieren technique in conjunction with an Imacon high speed image-converter camera operated at the nominal framing rate of 10^6 f/s with exposure time of 0.2 μs. The object was illuminated using a 50 μs duration xenon flash.

The 13.2 μF capacitor was fired by triggering a 20 kV step pulse, initiated by a 250 V pulse from a control unit across an asymmetric spark gap containing pressurised dry air. The 250 V pulse was delayed by 20 μs before it reached the EHT trigger unit, while at the initial time another pulse of 6 V triggered a pulse generator to fire the flash to let it reach a usable output before the wire explosion.

The camera was triggered by a 70 V pulse of short rise time from an opto-isolator after a 20 μs delay by a pulse generator. The charging and discharging of the capacitor was operated by a pneumatic control system controlled by an efficient control unit.

The review of high speed photographic techniques in Chapter 3 shows the electronic framing camera is the ideal instrument for photographing the rapidly expanding blast waves generated by the exploding wire. The time interval calibration of the camera indicated that the true time interval is about 96.5% of the nominal time marked on the unit.

The xenon flash unit used for the illumination was shown to have a charging time constant of about 25 s and duration of about 50 μs with the delay time depending on the triggering pulse level and the operating voltage.

A vital step in this work was the synchronization measurements required for setting the delays and the voltages of the high speed photography and the exploding wire systems as described in Chapter 5.

A thick non-exploding copper wire of 6.3 mm diameter was used as a load in the discharge current circuit for studying the electrical characteristics of the exploding wire circuit. The study indicated that the damping factor of the damped sine waveform of the discharge current was about $1.57\times10^{4}s^{-1}$, the current frequency is 69 kHz, and the total resistance of the circuit was 12.8 mΩ. The capacitor discharge at 20 kV gave a maximum current of about 114 kamps and the voltage across the wire was about 19.12 kV. The maximum di/dt was 8.18×10^{10} amp/s.

Thin copper wires were made to explode in a few microseconds by high voltage capacitor discharge. The wire explodes rapidly when the discharge current passes through it. Its vaporisation causes intense heating of the surrounding air, generating high velocity cylindrical

blast waves (up to ≈ Mach 15) of high energy, and short duration. This pulse was used for loading hollow cylindrical specimens to study the material's response to impact loading.

The blast waves were observed to expand in a cylindrically symmetric manner with maximum Mach numbers of up to 15. The 24 and 22 swg copper wires of 8 and 13 cm lengths were used to give different blast wave velocities and energies, the energy being calculated by using strong shock wave theory. From the calculation of the blast wave energy, the efficiency of the energy transfer from the capacitor to the wire varied from a maximum of 64% to a minimum of about 29%. The 24 swg copper wires gave greater blast wave energies for all lengths and discharge voltages. The shorter length of wire gave greater blast wave energy because a smaller proportion of energy is required for the vaporisation.

The exploding wire technique has been employed for studying material behaviour at high strain-rates. The exploding wire produces axial and radially symmetrical blast waves which load the inside wall of a test cylinder giving a reasonable duration (about 20 μs) of plane strain in the middle of the cylinder. The high stress is capable of causing fracture in the cylinder at high rates of loading. Studies have been carried out on high density polyethylene (HDPE) thin-walled cylinders, the outer surface expansions, velocities, and hoop strains being determined up to and beyond fracture from the high speed photography. Velocities up to 500 m/s, and hoop strain-rates up to 10^4 s^{-1} were measured with fracture engineering hoop strains of about 380%. These fracture strains were less than the quasi-static values quoted by the supplier. For tube expansion the high speed photography was carried out at lower framing rates of 10^5 f/s, with a long duration electronic flash (≃ 200 μs) used for illumination.

It was not possible to measure the loading preasure on the expanding cylinder wall because of the pressure variation with time and distance. To avoid this difficulty, the freely expanding thin ring method was used for studying stress-strain behaviour of HDPE material.

The freely expanding ring technique has the advantage of enabling the specimen stress to be obtained directly from the high speed photographs of the expansion. This method involved placing a thin ring on to a thick-walled cylinder and subjecting the cylinder internally to blast wave loading from the wire explosion. Measurement of the deceleration of the ring from radius/time was used to determine the stress.

Several experiments have been made to establish the dimensions of the rings (0.8 or 0.7 mm thick, and 13.3mm o.r) and the cylinders (8 or 9mm thickm, and 3.2mm i.r) required for free expansion conditions. The maximum true stress obtained using this method was about 38 MPa, which gave 34% true strain. The ring velocity reached a maximum of about 150 m/s within a time of 5-10 μs and decreased with a constant deceleration. The engineering hoop strain-rate was about 1.2×10^{4} s^{-1} at the start and eventually became zero at zero velocity, after about 62 μs.

The flow stress which is given by freely expanding HDPE rings at ititial strain-rates of about 1.12×10^{4} s^{-1}, is about 13% higher than that given by quasi-static testing at 10^{-3} s^{-1} strain-rate.

9.2 Recommendations for future work

1) The present work was carried out without direct pressure measurements of the pressure loading of the cylinders. Future work should include measurement of the blast wave pressure profile on the inner wall of thick cylinders by using a piezoelectric pressure gauge. This could then be used in a finite element program to predict the stress-strain behaviour of the material in the form of a thick cylinder.

2) In addition to multiple-framing high speed photography, strain-time measurement using a different optical method could be used for measuring the displacement of the expanding ring and the cylinder. This method could employ a laser beam scanning the outer surface to give a continuous record of the displacement.

3) Further work is needed on the freely expanding ring technique using higher voltages for the wire explosion to give even greater strain rates.

4) Measurements of temperature variation through a test sample could be attempted by inserting at least two fast response thermocouples inside the cylinder wall.

5) A variety of polymers and metals could be examined using the freely expanding ring method since this is one of the few techniques available for obtaining tensile properties of materials at very high strain rates.

REFERENCES

Ahmad, S.A., 1985. "Optical studies of cylindrical blast waves produced by exploding wires". Internal report.

Ahmad, S.H., 1988. Ph.D thesis, Department of physics, Loughborough university.

Alfery, J., and Gurnee, E.F., 1967. "Organic polymers", Prentice-Hall, Inc, Englewood Cliffs, New Jersey, pp 54-75.

Al-maliky, N.S., 1989. "Introduction to high speed photographic technique", Internal report, Department of Physics, Loughborough university.

Andreson, J.A., 1920. Astrophys. J., Vol. 51, 37.

Azarkevich, E.I., Kotov Yu.A., and Sedoi V.S, 1975. "Conditions for the current pause in exploding wires". Sov. Phys. Tech. Phys., Vol. 20 (1), pp111-112.

Bell, J.F., 1982. "On dynamic elastic limit". Exp. Mech., Vol. 22, pp270- 276.

Benham, P.P., and Warnock, F.V., 1979. Mechanics of solids and structures, Pitman press.

Bennett, F.D., 1958. "Cylindrical shock wave from exploding wire". Phys. Fluids, Vol 1 (4), pp 347.

Bennett, F.D., 1958. "Energy partition in the exploding wire phenomena". Phys. Fluids, Vol. 1 (6), pp 515.

Bennett, F.D., Burden, H.S., and Shear, D.D., 1962. "Correlated electrical and optical measurements of exploding wire". Phys. Fluids, Vol. 5 (1), pp 102.

Bennett, F.D., 1962. "Shock producing mechanisms of exploding wires". Phys. Fluids, Vol. 5 (8), pp 891.

Bennett, F.S., and Marvin, J.W., 1962. "Current measuremenet and transient skin effects in exploding wire circuit". Rev. Sci. Instr., Vol. 33 (1), pp 1218.

Bennett, F.D., Burden, H.S., and Shear, D.D., 1963. "Two-wavelength streak interferometry of an ionized heavy gas". Phys. Fluids, Vol. 6, pp 752-753.

Bennett, F.D., 1964. "Initial heating rates and energy inputs for exploding wires". Phys. Fluids, Vol. 7, pp 147-148.

Bennett, F.D., 1965. "High- temperature cores in exploding wires". Phys. Fluids, Vil. 8 (6), pp 1106 8.

Bennett, F.D., Kahl, G.D., and Weber Jr., F.N., 1970. "Quantitative interferometry of expanding metal vapour". Phys. Fluids, Vol. 13 (7), pp 1725- 30.

Bennett, F.D., 1971. "Current diffusion in cylindrical exploding wires and fuses during microsecond electrical pulses". J. Appl. Phys., Vol. 42 (7), pp 2835- 39.

Bennet, F.D., Burden, H.S., and Shear, D.D., 1974. "Expansion of superheated metals". J. Appl. Phys., Vol. 45 (8), pp 3429-38.

Bisplinghoff,R.L, Mar, J.W., and Pian, T.H.H., 1965. "States of deformable solids", Addison-Wesley, USA, pp 168 - 230.

Bradley, J.N., 1962. "Shock waves in chemistry and physics", Methuen & Co. Ltd, London, and Wiley & sons Inc New York.

Brown, E., 1965. "Modern optics", Chapman & Hall Ltd., London, pp 464.

Burtsev, V.A., Dubyanskii, V.A., Egorov, N.P., Kasatkina, M.P., and Broduvnov, I.V., 1979. "Electrical explosion of a cylindrical foil in air. Current distribution in the high-current shunting discharge". Sov. Tech. Phys. Lett., Vol. 4 (6), pp 264.

Carden, A.E., Williams, P.E., and Karpp, R.R., 1980. in "Shock wave and high strain-rate phenomena in metal, concepts and applications". ed., Meyers, M.A., and Murr, L.E., Plenum press, New York, pp 37-50.

Cassidy, E.C., Abramowitz, S., and Beckett, C.W., 1968. "Investigation of the exploding wire process as a source for hogh temperature studies", NBS Monograph 109, US Dept of Cammerce National Bureau of Standards.

Chace,W.G., and Moore, H.K., 1964. "Exploding wire", Vol. 3, Plenum press, New York.

Clark, D.S., Duwez, P.E., 1950. "The influence of strain rate on some tensile properties of steel". Proc. ASTM, Vol. 50, pp 560-575.

Cristescu, N., 1972. "A procedure for determining the constitutive equations for materials exhibiting both time-dependent and time-independent plasticity", Int. J. Solids Structures, Vol. 8, pp 511-31

Daniel, I.M, LaBedz, R.H., and Liber, T., 1981. "New method for testing composites at very high strain rates", Exp. Mech., Vol. 21, pp 71.

Dirwish M., 1979. Ph.D thesis, Department of physics, Loughborough university.

Duggin, B.W., Forrestal, M.J., and Butler, R.I., 1978. "Impulse from an electrically exploded etched copper mesh", AIAA J., Vol. 16 (8), pp856-7.

Edelson, H.D., and Korneff, T., 1966. "A comarative study of exploding wire in air and water", J. Appl. Phys., Vol. 37 (5), pp 2166.

Edgerton, H.E., and Killiam, J.R., 1953. "Flash ! (seeing the unseen by ultra high speed photography", Charles,T., Branford Co., Boston.

Edgerton, H.E., 1979. "Electronic flash, Strope", 2nd ed., The MIT press, Canbridge.

Ensminger,R.R., and Fyfe, I.M., 1966. "Constitutive model evalution using cylindrical stress wave propagation", J. Mech. Phys. Solids, Vol. 14, pp 231-8.

Forrestal, M.J., and Walling, H.C., 1972. "Axisymmetric plastic response of rings to short duration pressure pulses". AIAA J., Vol. 10 (10), pp 1382-4.

Forrestal,M.J., Tucker,W.K., and Von Riesemann,W.A., 1975. "Impulse loading of finite cylindrical shells". AIAA J., Vol. 13 (10), pp 1396-1398.

Forrestal, M.J., Duggin, B.W., and Bulter, R.I., 1980. "An explosive loading technique for the uniform expansion of 304 stainless steel cylinders at high strain-rates". J. Appl. Mech. trans. ASME, Vol. 47, pp 17-19.

Fyfe, I.M., and Ensminger, R.R., 1964. "Explodive wire induced cylindrical waves in solids". in Exploding wire, Vol. 3, ed. Chace, W., and Moore, H., Plenum press, New York, pp 257-265.

Fyfe, J.M, 1968. "Plane-strain plastic wave propagation in a dynamically loaded hollow cylinder", Mechanical behavior of material under dynamic loads, conf., 314-28.

Fyfe, I.M, and Rajendran, A.M., 1980. "Dynamic pre-strain and inertia effects on the fracture of metals", J. Mech. Phys. Solids, Vol. 28, pp 17-26.

Fyfe,I.M., and Swift,R.P, 1969. Report 69, 3, University of Washington, Department of Aeronautics and Astronautics.

Gaydon,A.G, and Hurle,I.R, 1963. "The shock tube in high temperature chemical physics", Chapman and Hall, London.

George A. Jones, 1952. "High speed photography", Chapman & Hall, London.

Gourdin, W.H., 1989. " Constitutive properties of copper and tatalum at high rates of tensile strain: expanding ring result", Ins. Phys. Conf. Ser.No.102, section 5, pp221.

Griffiths, L.J., Parry, D.J., and Stewarson, H.R, 1986. "Cylindrical blast waves for materials testing", Proc. Int. Symp. on Intense Dynamic loading and its effects, pp 269-75, Beijing.

Heiman, J.H., and Kolsky, H., 1966. "The propagation of elastic waves on thin cylindrical shell", J. Mech. Phys. Solids., Vol. 14, pp 121-130.

Higgins, R.A., 1977. "Properties of engineering materials", Hodder and stoughton, London.

Hoggatt,C.R, Orr,W.R, and Recht,R.F., 1967. "The use of an expanding ring for determined tensile stress-strain relationships as a functions of strain-rate", Proc. First Int. Conf. Center for high energy forming, Estes Park, Dover.

Hoggatt, C.R. and Recht, R.F., 1969. "Stress-strain data obtained at high rates using an expanding ring". Exp. Mech., Vol. 9, pp 441-8.

Huston, A.E., 1978. "High speed photography and photonic recording". J. Phys. E: Sci. Inst., Vol. 11, pp 601-9.

Hwangbo, C.K., and Kong, H.J., and Lee, S.S., 1980. "Inhomogeneous wire explosion in water". New Phy. (Korean Phys. Sco.), Vol. 20 (3), pp 149-53.

Hyzer, W.G., 1962. "Engineering and scientific high speed photography". Macmillan co., New York.

Isuzugawa, K., and Fujimura, T., 1982. "Studies of exploding wires", Bull Univ., OSAKA, PREFEZI.SER., Vol. 31, part 2, pp 111-6.

Jones,D.L., and Callet,R.M., 1962. "Microwave Doppler measurement of the ionization front in cylindrical shock waves from exploding wires", Exploding wires, Vol. 2, pp 127-144.

Kang, C.Y., Lee, M.H., and Lee, S.S., 1979. "Optical flashes from double wire explosion". Can.J.Phys., Vol. 57, pp 1439-1443.

Kelly, J.M., and Gillis, P.P., 1970. "Shock thickness in viscoplastic solids". J. Appl. Mech.,tran. ASME, Vol. 37 (1), pp 163-70.

Kinloch, A.J., and Young, R.J., 1983. "Fracture behaviour of polymers", Applied Scince Publishers, London, pp 23.

Kolsky, H., 1953. "Stress waves in solids", Clarendon Press, Oxford.

Lavrentyuk,V.E., Rogovtsev,P.N., Sobolev,V.F., and Starchenko,V.A., 1987. "Formation of a stratifield pulsed discharge under current-pause conditions". Sov. Phys. Tech. Phys. (USA), Vol. 32 (1), pp 38-43.

Law, C.K., and Bristow, M., 1969. "UTIAS Tech. Note 148", Toronto.

Lee, W.M., 1988. "Pressure measurements correlated with electrical explosion of metals in water". J. Appl. Phys., Vol. 64 (8), pp 3851.

Leonard, T.A., 1973. "Observation of a core in an exploded lithium wire plasma by reflection of laser light". J. Appl. Phys., Vol. 44 (3), pp 1380-1.

Lindberg, H.E., and Anderson, D.L, 1968. "Dynamic pulse backing of cylindrical shells under transient lateral pressres", AIAA J., Vol.6 (4), pp 589-98.

Lindberg, H.E., 1970. "Dynamic pulse of cylindrical shells", TR 001-70, April 1970, Poulter Lab., Stanford Research Inst., Menlo Park, Calif., pp 36-38.

Lin, S.C., 1954. "Cylindrical shock waves produced by insantaneous energy release". J. Appl. Phys., Vol. 25 (1), pp 54.

Lipson, S.G., and Lipson, H., 1964. "Optical Physics", FRS, Cambridge University press.

Megson, T.H.G., 1980. "Strength of materials", Van Nostrand Reinhold (UK) Co., Ltd., pp 50.

Muller, W., 1937. Physik, 149, 396.

Muller, W., 1959. Exploding wires, Vol. 1, Plenum Press Inc., New York, pp 186.

NcVeagh, J.S., and Newbery, H.W., "A high speed mechanical shutter driven by a gas motor", ET1.

Nakajima, T., 1979. "Shock propagation in the circular hollow cylinder". Sci. Univ. Tokyo, Vol. 15, part 1 (A), pp1-11.

Nakamura, Y., and Tsuno, T., 1980. "High speed Schlieren system as applied to measure high velocity flow". Annu. Rep. Eng. Res. Inst. Fac. Eng. Tokyo Univ., Vol. 39, pp 151-4.

Niordson, F.I., 1965. "A unit for testing materials at high strain rates". Exp. Mech., Vol. 5, pp 29.

Parry, D.J., 1976. "One day short course on high speed photography", Department of Physics, Loughborogh university.

Parry, D.J., Stewardson, H.R., Ahmad, S.H., 1988. "Measurement of high strain rate properties of materials using an exploding wire technique". J. de Physique, C3, Vol. 49, pp 689.

Pollard, F.B., and Arnold, J.H., 1966. "Aerospace ordnance handbook", Prentice-Hall, Inc., Englewood Cliffs, New Jersey.

Probe, D.G., Michalopoulos, C.D., and Muster, D., 1975. "Transit response of ring-stiffened thin cylindrical shell with symmetric mass loading", AIAA J., Vol. 13 (11), pp1423-4.

Quick, J., and LaBau, T., 1972. "Handbook of film production", The MacMillan Co., New York.

Rajendran, A.M., and Fyfe, I.M., 1982. "Inertia effects on the ductile failure of thin rings". J. Appl. Mech., Vol. 49, pp 31.

Ralph, L. 1959. "Electronic flash photography", Temple-press, LMT, London.

Reich, L., and Stivala, S., 1971. "Elements of polymer degradation", McGRAW-HILL Book Co., USA, pp 44.

Ritchie, R.D., 1965. "Physics of plastics", ILiffe Book Ltd., London.

Roark, R.J., 1956. "Formulas for stress and strain", 4th ed., McGRAW-HILL Book Co., New York.

Ron, R.H., Rohatgi, V.K., and Rau, R.S.N., 1983. "Rise time of a vacuum gap triggered by an exploding wire", IEEE trans. Plasma Sci., Vol. PS-11, No. 4, pp 274-8.

Rose, J.L., and Chou, P.C., 1972. "Energy of cylindrical stress waves generated by exploding wires". Exp. Mech., Feb. 1972, pp 104.

Ryszard Malewski, 1968. "New device for current measurement in exploding wire circuits2, Rev. Sci. Inst., Vol. 39 (1), pp 90-4.

Shin-Ichi Lin, 1979. 13th International conference on high speed photography, pp 504.

Schmit,R.M., and Fyfe,I.M., 1973. Exp. Mech., Vol. 13, pp 163-7.

Schofer, R, Seydel, V., and Jager, 1977. "On the propagation of shock waves of wire explosions in water", Z. Naturfosch, Vol. 32 A, Part 7, pp736-45.

Smith, S.H., 1970. "Origin of straitions due to mechanical effects in fast wire explosion". J. Appl. Phys., Vol. 41 (10), pp 3918-21.

So-Young Song, and Kim, U., 1984. "Oscillographic and Schlieren streak photographic investigations of exploding wire discharge", J. Korean Phys. Soc., Vol. 17 (2), pp 167-9.

So-Young Song, and Kim, U., 1984. " A physical interpretation of metal expantion phenomena". J. Korean Phys. Soc., Vol. 17 (1), pp63.

Stewardson, H.R., 1984. "Energy and pressure measurements in programme to establish an exploding wire facility for testing materials at high rates of strain", Internal report.

Suhara, K., 1986. "V-I characteristics measurements for short gap arcs initiated by wire explosion", IC-CEMCA Conf., Nagoya, Japan, pp167-174.

Swift, R.P, and Fyfe, I.M., 1970. "Elastic/viscoplastic theory examined using radial cylindrical stress waves", J. Appl. Mech., Vol.37 (1), pp 1134.

Vlostos, A.E., 1973. "Electrical explosion of tungsten wires in a vacuum", J. Appl. Phys., Vol. 44 (1), pp 106.

Wakefield, G.K., and smith, N.W., 1952. "Syncro-flash photography", The Fountain Press, London.

Walling, H.C, Forrestal, M.J, and Tucker, W.K., 1972. "An experimental method for impulsively loading ring structures". Int. J. Solids Structures, Vol. 8, pp 825-831.

Walling, H.C., and Forrestal, M.J., 1973. "Elastic-plasticic expansion of 6061-T6 aluminum rings". AIAA J. Vol. 11 (8), pp 1196-7.

Warnes, R.H., Duffey, T.A., Karpp, R.R., and Carden, A.E., 1980. "An improved technique for determining dynamic material properties using the expanding ring". in Shock waves and high-strain rate phenomena in metal, ed. Meyers, M.A., and Murr, L.E., Plenum press, New York, pp 23-36.

Warnes, R.H., Karpp, R.R., and Follansbee, P.S., 1985. "The freely expanding ring test- A test to determine material strength at high strain rates". J. de Physique, C3, Vol. 46, pp 583-590.

Wesenberg, D.L., and Sagartz, 1977. "Dynamic fracture of 6061-T6 aluminium cylinder". J. Appl. Mech. trans. ASME, Vol. 44 (4), pp 643-6.

Wingrove, A.L., 1971. "A device for measuring strain-time relationships in compression at quasi-static and dynamic strain rates". J. Phys. E: Sci. Ins., Vol. 4, pp 873-5.

Wulf, G.L, and Rechardson, G.T., 1974. "The measurement of dynamic stress-strain relationships at very high strains", J. Phys. E: Sci. Inst., Vol. 7, pp 167-169.

Yakimura, 1987. "Shock wave energy of wire explosion in air". Sci. and Eng. Rev. of Doshiska Univ., Vol. 28 (2), pp 63-73.

Youngdahl, C.K., 1990. "Dynamic plastic deformation of a tube loaded over a time - dependent region". Int. J. eng., Vol. 9 (1), pp 71-88.

Zukas, J.A., 1982. "Impact dynamics", Wiley, New York, pp 241-332.